Preparation of a Fibre Optic Sensor based on AgNp/silica Composite for pH Measurement

A Thesis Submitted By

Shaon Debnath

For the Degree of Doctor of Philosophy

Department of Chemical and Process Engineering

University of Strathclyde

November 2023

DECLARATION OF AUTHENTICITY AND AUTHOR'S RIGHTS

This thesis is an original work carried out by the author. It has not been previously submitted to any institution which led to the award of a degree.

The copyright of this thesis belongs to the author under the terms of the United Kingdom Copyright Acts as specified by the University of Strathclyde Regulation 3.50. Any information derived from this thesis must be adequately acknowledged.

Signed: Shaon Debnath

Date: 16/11/2023

ABSTRACT

The measurement of hydrogen ion concentration in a solution, commonly referred to as pH, holds significant importance in various industries. However, measuring pH under high-temperature and high-pressure (HTHP) conditions has posed a formidable challenge due to the lack of reliable sensors and instrumentation. Recent research has demonstrated the potential of utilising the localised surface plasmon resonance (LSPR) phenomenon seen by gold nanoparticles deposited on optical fibres for pH detection under varying temperature and pressure conditions. Using this reported stability of optical fibres in HTHP conditions, this project aimed to create an optical fibre-based pH sensor using silver nanoparticles (AgNp) embedded within a silica matrix, which is suitable for use under HTHP conditions. In this work, a AgNp/silica coating is applied on a glass optical fibre to create an optical pH sensor.

The initial stage of the project involved the preparation of colloidal silver nanoparticles and silica gel as separate entities, with a focus on stabilising the colloidal solution and optimising silica gel production. Subsequently, setbacks were overcome in creating the AgNp/silica coating, refining the sol-gel method, and enhancing adhesion through careful adjustments of gelation temperature and heat treatment procedures. The project optimised the gelation process to achieve good adhesion on the glass while maintaining sufficient silver nanoparticles for pH sensitivity. Characterisation through UV-Vis spectroscopy indicated an extinction peak at 400 nm, which confirms the presence of silver nanoparticles. Afterwards, the AgNp/silica coating was applied to the optical fibres.

In the preparation of the optical fibre, the fibre was etched using 7 M sodium hydroxide (NaOH). This marked a successful milestone in utilising NaOH as an etchant for optical fibres. The coated optical fibre reached an ideal core diameter of 104 ± 1 microns, which was required for pH sensitivity. Extensive experimentation led to fine-tuning the sensor setup, ensuring optimal sensitivity while emphasising the delicate balance between light source voltage and detector integration time.

Durability testing revealed susceptibility to acidic environments, underscoring the need for coating improvement. The project explored pH measurement under ambient conditions, demonstrating the sensor's accuracy and stability in various chemical conditions. A calibration curve was constructed, and the coating's reproducibility and repeatability were thoroughly analysed, further validating its reliability as a pH sensing tool. The calibration curve provided insights into pH measurement using the optical method. Additionally, the performance and sensitivity of the sensor were investigated and compared between sensors prepared in the same batch and those from batch-to-batch production, offering insights into the sensor's characteristics. Furthermore, an evaluation was conducted to assess the accuracy of the sensor in comparison to the potentiometric pH measurement technique.

The project's most challenging phase involved testing the sensor in HTHP conditions, revealing issues related to the stability of the AgNp/silica coating at higher temperatures and pressures. It was observed that the pH decreased as the temperature of the solution increased. The experimental apparatus was constructed, which allowed experiments up to a gauge pressure of 5 bar, equivalent to 156 °C temperature, where a higher dissolution of the coating was observed. Nonetheless, the sensor was stable at lower gauge pressures, such as 2 bar, even during multiple heating and cooling cycles. Despite these challenges, the inclusion of silver nanoparticles showed promise in improving the sensor's consistency and stability.

In conclusion, this project represents a significant effort in developing a robust optical pH sensor with potential applications in industries such as oil and gas, chemicals, and environmental monitoring. The work underscores the ongoing challenge of maintaining sensor integrity under HTHP conditions, showing the need for further research to enhance coating resilience and a more robust calibration technique. Despite these challenges, this project pushes the boundaries of pH measurement technology and contributes substantially to the field of optical pH sensing. It is an exciting step towards overcoming the limitations of pH measurement in extreme environments, opening new avenues for precise monitoring and control in critical industries.

ACKNOWLEDGEMENTS

Contents

List of Figures

List of Tables

List Of Abbreviations

HTHP	High temperature and high pressure
TEOS	Tetraethyl orthosilicate
AgNp	Silver nanoparticle
AuNp	Gold nanoparticle
LSPR	Localised surface plasmon resonance
UV-Vis	Ultraviolet-Visible
SEM	Scanning Electron Microscopy
EDX	Energy Dispersive X-ray Spectroscopy
ST	Straight tip
SMA	Sub-miniature version A
FWHM	Full width at half maximum

CHAPTER 1 : Introduction & Background

Chapter 1: Introduction & Background

The primary objective of this investigation is to develop a pH sensor utilising an optical fibre that has been enhanced with silver nanoparticles and incorporated into a silica matrix. This approach is proposed as a potential resolution to the difficulties encountered when attempting to measure the pH of aqueous solutions in environments characterised by elevated temperature and pressure. In this chapter, the background information on pH, its importance in industry, traditional methods of measuring pH, and limitations of the available measurement techniques are described. Thereafter, the background information on fibre optics in relation to the measurement of pH is provided.

The discussion is mainly focused on the importance of pH measurement in the oil and gas industry, the challenges encountered with traditional pH sensors, and the different types of coating used on optical fibres for applications towards pH sensing. In addition, the reasons for choosing silica obtained from tetraethyl orthosilicate (TEOS) and silver nanoparticles (AgNp) and their role when decorated on an optical fibre for the determination of pH are explored. This is followed by the presentation of the problem statement as well as justification for the research, which indicates the relevance of the research. The aims and objectives of the research, as well as the scope of the study, are presented, which puts the research into context.

In some of these sections, the fundamental theories associated with the measurement of pH, such as the relationship between the dissociation constant of ionic salts and pH, the working principle of the traditional pH measurement technique (potentiometric pH measurement), and corresponding calibration methods are provided. The types of optical fibre as well as the working principle are discussed. Furthermore, the theory behind the formation of the silver nanoparticle embedded in silica coating (AgNp/silica) coating, including the mechanism of pH measurement using the coated optical fibre is discussed, which will provide the basis for understanding why an optical fibre-based sensor may succeed where traditional methods may be less useful.

1.1 Background on pH

The pH of a solution is the property that gives information on the extent of acidity or alkalinity of the solution. The pH scale comprises a range of values from 0 to 14, with pH values below 7 being classified as acidic and pH values over 7 being categorised as alkaline. By mathematical definition, pH is the negative logarithm of hydrogen ion activity or concentration, as shown in equation 1.1 [1]

$$pH = -\log [H^+] \qquad\qquad (1.1)$$

This definition raises two important questions: why is pH expressed as a logarithm function, and why does it have a negative sign? To answer these questions, there is a need to assess the concentration of hydrogen ions in a given solution in order to understand why a negative logarithmic function is applied to it in order to deduce the pH values. The concentration of hydrogen ions in a neutral solution is always very low in the order of 10^{-7}. The fact that the molar concentration of hydrogen ions in solution is a very small number and less than 0 explains why a logarithm function is used. Also, the logarithm of numbers less than 1 will give a negative number, therefore, using a negative logarithm will convert it to a positive number, which is quite convenient.

The mathematical expression of pH extends beyond solely hydrogen ion concentrations, as the concentrations of both hydrogen and hydroxyl ions in a specific solution remain constant under a specific set of conditions. Consequently, if the concentration of one ion is known, the concentration of the other ion may also be determined [1,2]. Determination of the pH of solutions, therefore provides a quantitative measure of assessing the degree of acidity or alkalinity of a solution. This has great significance in chemical processes that are highly pH dependent especially in pharmaceutical, cosmetics and other chemical industries [3–5].

As mentioned, the pH of a solution represents the degree of acidity. If this were to be expressed in terms of alkalinity (pOH), then pOH would be the negative logarithm of the hydroxyl ion concentration since its molar concentration in solution is also less than 0 and needs to be converted to a positive number. The mathematical expression of pOH is given in equation 1.2 [2], while the relationship existing between pH and pOH is shown in equation 1.3.

$$pOH = -\log[OH^-] \tag{1.2}$$

$$pH + pOH = 14 \tag{1.3}$$

The values of pK_a and pK_b are related through the pK_w, where a and b denote acid and base. The equilibrium constant for acid is K_a, and for the base is K_b.

In water, the pK_b scale extends from 0 to 14 with low values representing the strongest bases. Since the pH of a solution only indicates whether the solution is acidic or alkaline, it is different from assessing the strength of an acid or alkali. When assessing the strength of an acid or alkali/base, the dissociation constant K_a for acid or K_b for alkali or base is used. A weak acid dissociates partially in solution, for example, all organic acids such as acetic acid, butanoic acid, etc., are weak acids, while a strong acid dissociates completely in solution for example sulphuric acid, perchloric acid, hydrochloric acid etc., are strong acids [2]. The higher the K_a value, the stronger the acid. This can also be expressed in terms of pK_a, the higher the pK_a value, the weaker the acid.

Conversely, when a molecule of a weak acid (AH) is deprotonated, the acid dissociation constant can be expressed in terms of both the dissociated and undissociated components, as shown in equations 1.4 – 1.7.

$$AH \leftrightarrow H^+ + A^-$$
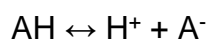
$$K_a = \frac{[H^+][A^-]}{[AH]} \tag{1.4}$$

Where K_a is the dissociation (equilibrium) constant

Taking the log of both sides

$$Log\ K_a = log[H^+] + log\frac{[A^-]}{[AH]} \tag{1.5}$$

Since,

$$pK_a = -logK_a\ and\ pH = -logH^+$$

$$pK_a = pH - log\frac{[A^-]}{[AH]} \tag{1.6}$$

4

Or that
$$pH = pK_a + log\frac{[A^-]}{[AH]}$$
(1.7)

Equation 1.7 is called the Henderson-Hasselbach equation, which shows the relationship between pH and pK_a. The equation suggests that the conjugate base form or the deprotonated form is the dominant form in solution when the pH is greater than the pK_a [1]. Likewise, the undissociated form will predominate if the pH is less than the pK_a [1]. Hence, the relation between pK_a and pK_b is as follows,

$$pK_w = pK_b + pK_a = 14$$
(1.8)

1.2 Acid-base theories

Acid-base theories are concepts that aim to provide coherent definitions of acids and bases [1]. The exact definition of these theories has been controversial. The initial definition was mainly focused on their properties, which cannot be generalised to all acids and bases [1]. The early misconception of acids was that acidity results from the presence of oxygen, as reported by Lavoisier in the 18th century [1,6]. However, it later became clear that if there was an essential element in acids, it was hydrogen, not oxygen [1]. Some of the generally accepted acid-base theories that are used currently after concepts have been developed are provided in the following sections.

1.2.1 Arrhenius-Ostwald theory

The Arrhenius-Ostwald definition of acids includes partial or complete ionization in water, giving out hydrogen ions in the process, while a base ionizes in water to produce hydroxyl ions [1], as shown in the chemical equations below.

$$HA + H_2O \rightarrow H_3O^+ + A^-$$
(1.9)

$$B + H_2O \rightarrow BH^+ + OH^-$$
(1.10)

This theory introduces the discussion of acid-base equilibrium as well as the strength of acids and bases, which is related to its degree of ionization. Partial ionization would imply that the acid is weak, while complete ionization suggests that it is a strong acid. It must be noted that water itself ionised to protons (or hydronium ions) and hydroxyl ions, as shown below [1]

$$H_2O \leftrightarrow H^+ + OH^-$$
(1.11)

The acidity or basicity of an aqueous solution is dependent upon the concentration of free hydrogen (H^+) ions and hydroxyl (OH^-) ions inside the solution. In pure water, which is completely neutral, the concentration of free hydrogen ions is equivalent to the concentration of hydroxyl ions [1]. The concentration of the ionic product of water K_w is defined by the water dissociation constant, which is given in equation 1.12 [1].

$$K_w = [H^+][OH^-] \qquad (1.12)$$

In pure water $[H^+] = 10^{-7}$ mol/l, and also $[H^+] = [OH^-]$

Then, $K_w = [H^+][OH^-] = 10^{-14}\, mol/l$, which gives rise to equations 1.3 and 1.8 shown previously.

The Arrhenius theory of acids and bases proposes that their behaviour is contingent upon their presence in aqueous solutions rather than their intrinsic properties as substances. Consequently, its scope is confined solely to the examination of acids and bases within aqueous environments, rendering it inapplicable to gaseous and non-aqueous solutions. However, there are several limitations of the Arrhenius theory. For instance, the theory specifically addresses acids with the chemical formula HA (e.g., HCl, HBr) and bases with the formula BOH (e.g., NaOH, KOH) while excluding substances such as SO_2, CO_2, $AlCl_3$, Na_2CO_3, NH_3 [7,8]. Notably, the formulation NH_4OH was postulated to clarify the relationship between bases and hydroxide ions (OH^-) in water despite its discrepancy with the actual composition of ammonia (NH_3). Arrhenius theory disregards the influence of solvents on acid-base behaviour, as evidenced by the discrepancy between the strength of hydrochloric acid when dissolved in water versus benzene [9]. This theory falls short in explaining acid-base phenomena in solvents other than water, such as benzene or acetone, and in gaseous states. Furthermore, while Arrhenius asserts that all salts should yield neutral solutions, exceptions exist, as demonstrated by the slightly acidic nature of solutions resulting from equal amounts of HCl and ammonia and the slightly basic nature of those from acetic acid and sodium hydroxide [7]. Critically, Arrhenius' premise that hydrogen ions are liberated in aqueous solutions and persist therein to elevate hydrogen ion concentration is challenged by the reality that hydrogen ions do not exist independently but rather as hydronium ions (H_3O^+).

1.2.2 Bronsted-Lowry acid-base theory

The Bronsted-Lowry theory of acids and bases is shown in the reaction below. This is based on the transfer of protons leading to the formation of conjugate acids and bases. The role of acid in this process is to donate protons forming a conjugate base, while the base accepts the proton and forms a conjugate acid, as shown in Figure 1.1 [1].
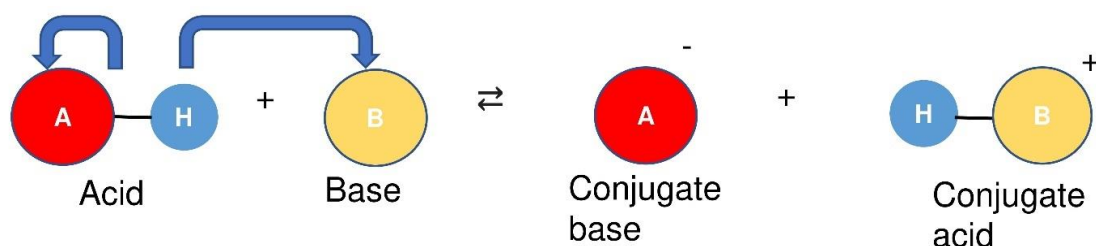
Figure 1.1: Illustration of the Bronsted-Lowry theory showing the formation of conjugate acid and conjugate base.

The Brønsted-Lowry theory offers notable advantages in elucidating the behaviour of acids and bases across diverse solvent environments, encompassing both aqueous and non-aqueous solvents. Additionally, it provides insight into the basic characteristics of substances such as Na_2CO_3, devoid of the hydroxyl (OH) group, thus defying categorisation as a base under the Arrhenius framework due to its inability to accept protons. Despite these merits, the theory exhibits several limitations. Notably, it lacks the capacity to delineate the acidic and basic properties of organic compounds and fails to characterize the acidic, basic, and amphoteric nature of gaseous molecules [8,9]. Furthermore, the theory's conceptualisation introduces complexities in predicting a compound's role as either an acid or a base within different reaction contexts. Moreover, its explanatory scope is insufficient in detailing acid-base interactions within certain solvents such as benzene and dioxane [8,9].

Additionally, the Brønsted-Lowry theory fails to account for reactions involving acidic oxides (e.g., CO_2, SO_2, and SO_3) and basic oxides (e.g., BaO, CaO, and Na_2O), where proton transfer mechanisms are absent. Furthermore, it overlooks the acidic attributes of proton-deficient compounds like $AlCl_3$, $FeCl_3$, and BF_3, thereby

underscoring its limitations in comprehensively describing the acid-base behaviour of diverse chemical species [8].

1.3 Importance of pH?

pH measurement is important in diverse sectors such as petroleum engineering, food manufacturing, health, and medicine, among others [10,11]. This is because it is a primary determinant of the stability and activity of some products as well as an index of regulatory compliance. It is also one of the indices of the quality of a product in several industrial applications [5,12–14]. In many instances, a stable pH can be an indication of good quality during quality control tests of a product [5,12–14]. For instance: orange juice, lemon juice, beer, cheese, bleach etc., all require a constant pH to maintain its quality, as shown in Figure 1.2 [15] In Biotechnology, pH control is essential, for example, bacterial growth depends on a specific pH value [5]. Also, pH control is an important determinant in a quality test of water [16,17]. The variety of products where pH features in quality control is shown in Figure 1.2.
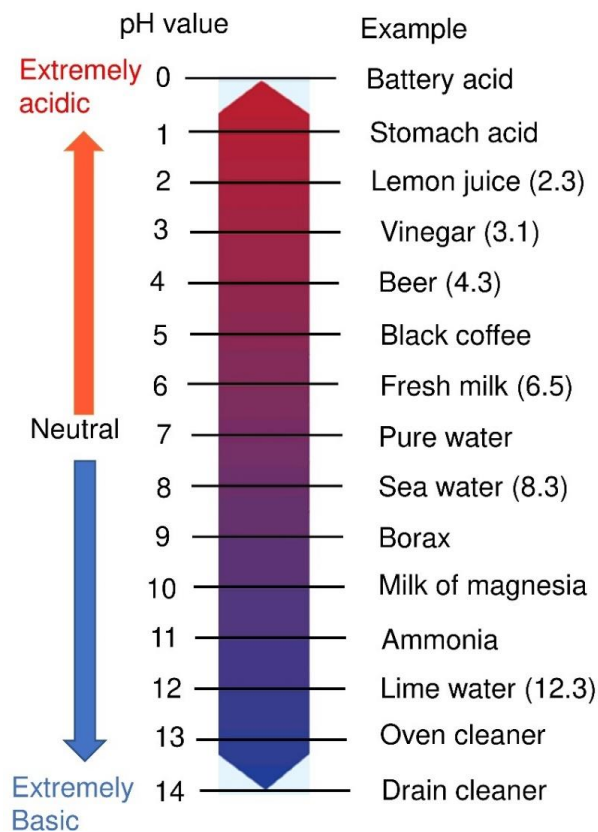
Figure 1.2: An illustration of the pH of different fluids from extreme acidic pH to extreme basic pH range [15].

During production, control over pH is important to obtain the desired quality and to ensure conformity and manufacturing to the required standard. Therefore, a slight change in pH can have a profound effect on a product, such as a change in appearance or taste [2]. In addition, pH is a useful parameter in the maintenance of industrial equipment, which comes into contact where reagents may cause corrosion during production processes [16–18].

1.4 Measurement of pH

An instrument that is sensitive to changes in hydrogen ion concentration from which the pH value can be derived is required in order to successfully detect pH. It is not sufficient to qualitatively assess the acidity or basicity of a solution, but it is vital that this be measured in order to guarantee that strict compliance in terms of quality is maintained.

The measurement of pH has been and will continue to be used extensively as a method of determining the level of acidity of fluids of different types [1,2]. Colourimetric techniques, employing indicator liquids or papers, and electrochemical methods, utilising electrodes and a voltmeter, represent the primary approaches for pH measurement. Colourimetric methods are less accurate because they are based on visual inspection of the colour change and corresponding match with some reference colour chart, which can be prone to human error [1,19]. The utilisation of pH measurement and regulation on a large scale has been facilitated by the advancement of the glass electrode, which is employed in conjunction with a voltmeter. The implementation of these advancements was imperative to facilitate the extensive utilisation of pH measuring and regulation.

1.4.1 Measurement of pH using colorimetric method

Certain kinds of paper or fabric that are impregnated with colour carriers, called chromophores, can be used as pH indicators. A chromophore is a functional group existing within a molecule that absorbs light within the visible spectrum resulting in the emission of colour characteristic of the compound [20]. For example, the carbonyl, hydroxy, nitro, azo, and conjugated alkene groups are responsible for different indicators of colours such as phenolphthalein, methyl red, and bromothymol blue.

Indicator (Colourless when 0 < pH > 8)
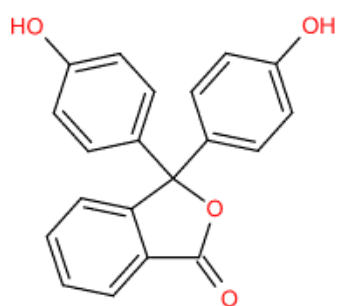
Indicator (Pink in colour when 8 < pH > 12)

OH⁻

H⁺
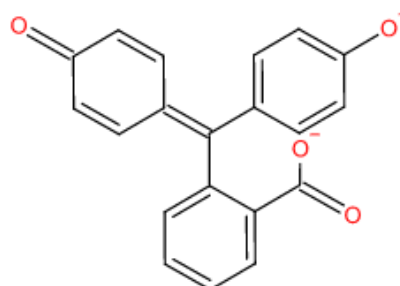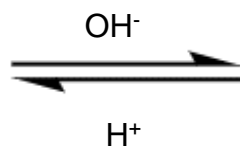
Figure 1.3: Image showing the colour change and chemical structures of phenolphthalein indicator in acidic and basic solutions [21].

Phenolphthalein has a structure that contains carbon, hydrogen, and oxygen chains, as shown in Figure 1.3. The two different structures shown in Figure 1.3 are a chemical transformation observed as a result of a change in pH. The structure of the deprotonated form of the phenolphthalein indicator is responsible for the absorption of visible light. In this case, the electrons in the molecule are more delocalized due to ionization than in the protonated form. The hydroxyl group is deprotonated when the pH increases to the alkaline range, resulting in a change in structure which also absorbs light in the ultra-violet (UV) range. In addition, the pink form also absorbed light in the visible light spectrum. In a basic solution, the molecule will lose one of its hydrogen ions. The phenolphthalein indicator changes more as the solution becomes more alkaline, resulting in a deeper pink colour.

Sometimes, a universal indicator consisting of two or more dyes may be used to obtain a broader and improved pH measurement. The different dyes that could be used in a universal indicator include: phenolphthalein, methyl red, bromothymol blue, and thymol blue. The pH papers are usually impregnated with one or more of these

indicator dyes, which are covalently linked to the strip. The dyes are organic molecules that can undergo colour change depending on the pH of the solution. In general, the strips can be used with a variety of solutions ranging from acidic to alkaline range.

pH range	Colour
< 3	Red
3-6	Yellow
7	Green
8-11	Blue
> 11	Violet
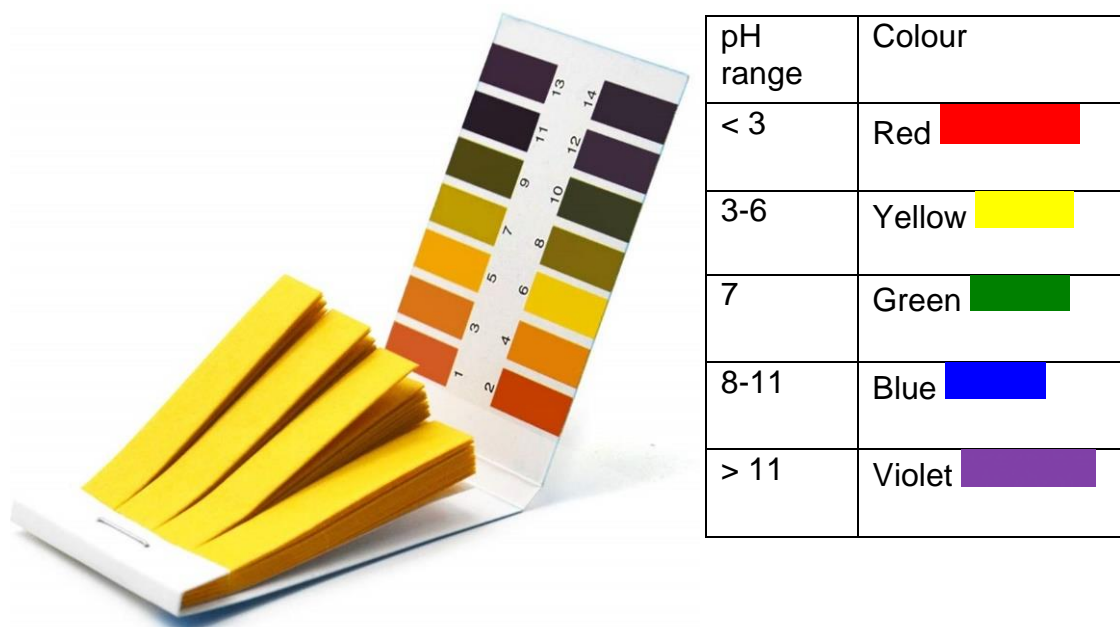
Figure 1.4: Image of pH strips and reference pH charts.

In most instances, a shift in pH of two units is required for a full-colour transformation to take place. This method involves submerging a strip of paper in a liquid and watching out for a colour change after a few seconds. Then, the colours on the strip are compared with a reference colour scale, as shown in Figure 1.4. This may be regarded as a crude estimation of pH as it is prone to human bias and other factors. However, strips that are used to test the pH of highly pigmented solutions may cause the colour output to be inaccurate [19]. In addition, they have a limited shelf-life and can also leach into solutions which are being tested.

1.4.2 Measurement of pH using the potentiometric technique

Potentiometric techniques provide another method for pH measurement. The traditional measurement technique consists of the glass electrode, which is shown in Figure 1.5. This involves the measurement of the potential of a test solution, which can be compared with the potential of a known solution [1]. The principle of

measurement is based on the presence of a sensor embedded in the glass membrane, which is sensitive to hydrogen ions. The schematic representation of the traditional pH meter is shown in Figure 1.5. The device has two electrodes: the pH electrode, which serves as the working electrode, and the reference electrode, which is integrated into a single unit. The working electrode is inserted into the test solution while the reference electrode is in the reference solution. The reference electrode of a glass pH meter usually consists of an Ag/AgCl electrode, while the reference solution is potassium chloride with a pH of 7 [1,19]. The pH meter measures the potential of the test solution and compares it with the potential of the known solution (KCl), the difference in potential between the two solutions is expressed in terms of the hydrogen ion concentration from which the pH of the test solution can be deduced [1,22].
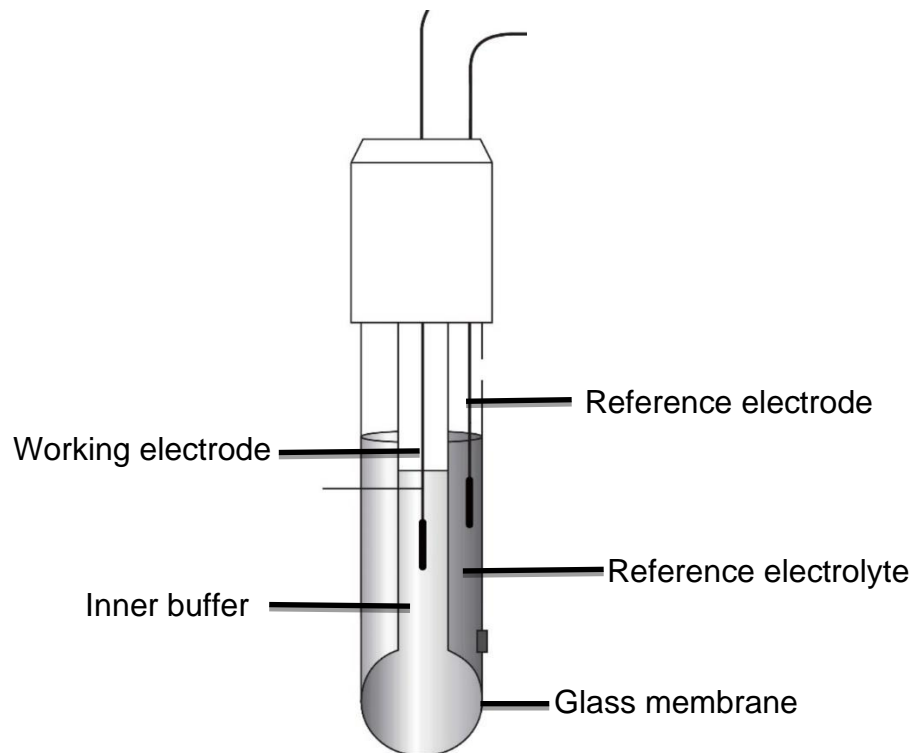
Figure 1.5: Instrumental setup showing the incorporation of the sensing and reference electrodes in one device for use as a pH meter [1].

The glass electrodes consist primarily of SiO_2 [1,23]. When glass electrodes are submerged in aqueous solution, the outermost layer of the membrane's surface gets hydrated. This leads to the development of negatively charged sites, which are denoted by the symbol —SiO– [24]. Counter ions are typically sodium ions, denoted by the symbol Na^+, which is being displaced by hydronium ions. This results in the

membrane having a selectivity for hydrogen ions due to the fact that hydrogen ions bind to —SiO– more strongly than sodium ions [25,26]. The Na^+ ions are responsible for carrying the charge across the membrane in this process, as shown in the reaction below [25], which may be attributed to Gibbs–Donnan equilibrium.

$$H^+ + - SiO^- Na^+ \leftrightarrow - SiO^- H^+ + Na^+ \qquad (1.13)$$
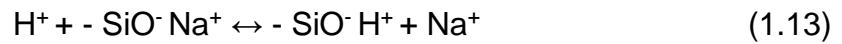
The Gibbs–Donnan equilibrium is often used to explain the exchange of such charge between particles that are in proximity to a semi-permeable membrane which does not distribute themselves uniformly on both sides of the membrane. The most common reason for an uneven electrical charge is the presence of a different charged material that is unable to flow through the membrane and, as a result, causes the charge to become uneven [27].
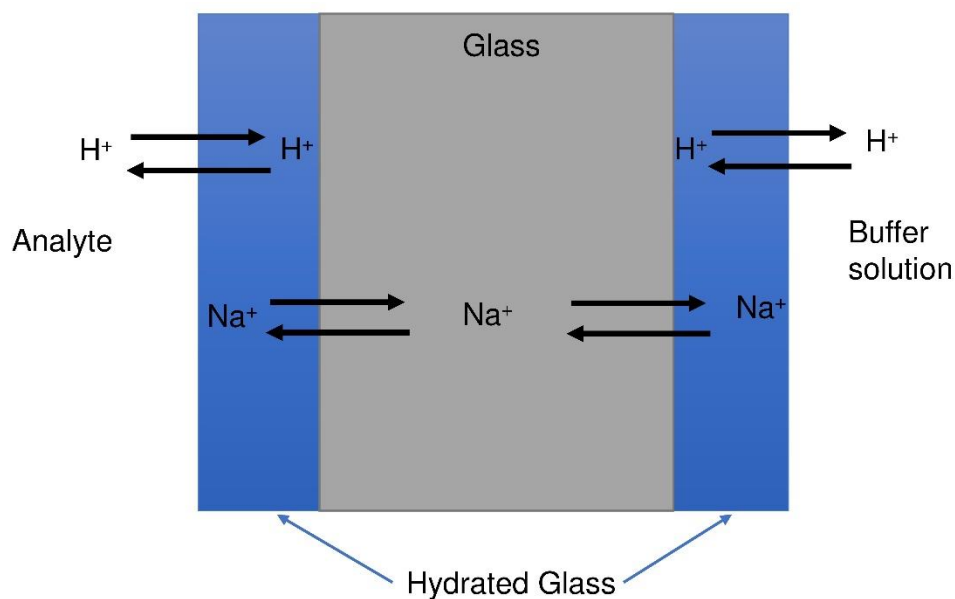
Figure 1.6: Schematic representation of ion exchange through a hydrated glass membrane [28].

The working principle of the hydrated glass membrane is shown in Figure 1.6. This suggests that the potential exists for hydrogen ions present in the solution to undergo migration into the glass material, displacing sodium ions that are confined within the glass membrane. The amount of H^+ ions present in the solution has a direct relationship with the number of H^+ ions that are able to pass through the glass membrane and enter the solution. Due to the fact that the concentration of H^+ in the

buffer solution is always the same, a predetermined quantity of the Na$^+$ ions in the glass membrane is replaced by H$^+$ ions, as shown in Figure 1.6. Since the quantity of H$^+$ ions in the test solution varies as a function of pH, the number of Na$^+$ ions that are displaced from the glass membrane also varies with pH.
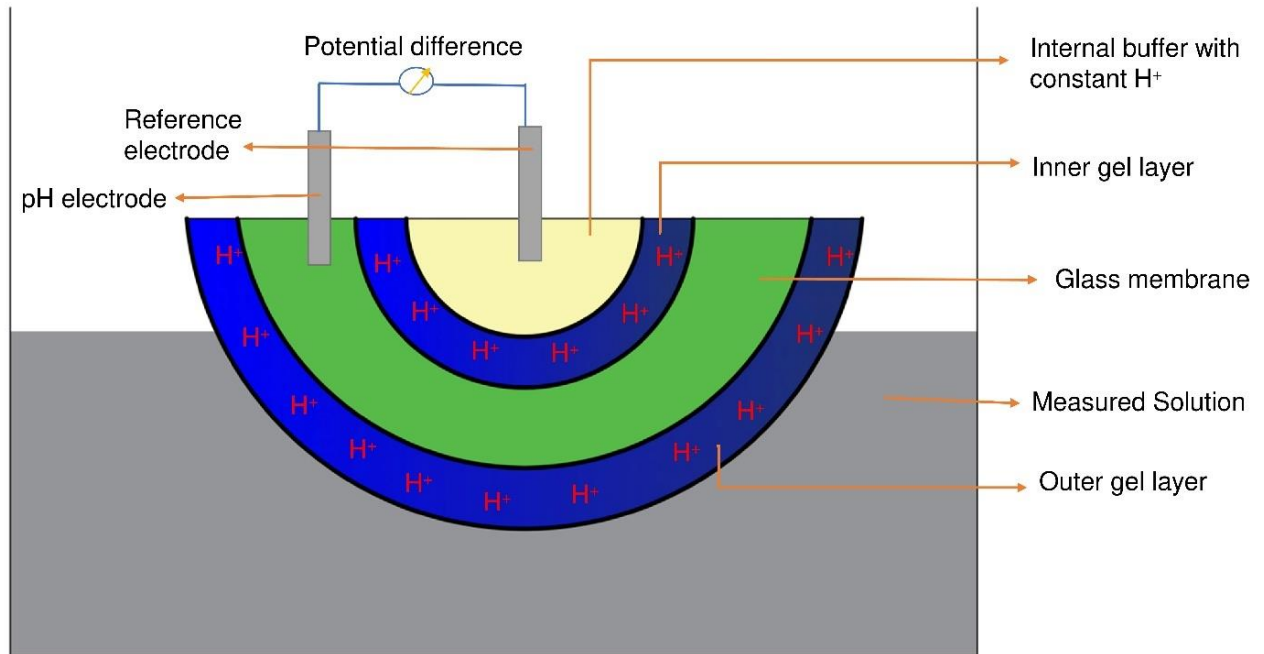
Figure 1.7: Schematic representation of a potentiometric pH meter showing the working principle of the glass membrane for the determination of the potential difference of different solutions from which pH can be deduced.

The potential difference between both electrodes in a measured solution and a sample solution determines the pH value of the measured solution, as shown in Figure 1.7. The working electrode depends on the hydrogen ion concentration. This gives the degree of acidity or alkalinity of the solution. On the other hand, the reference electrode does not respond to changes in H$^+$ ion concentration in the sample solution [1,2,19]. This implies that it will always produce a constant potential when pH is measured. The pH measurement is conducted using the glass electrode, which determines the potential differences between the working electrode and the reference electrode.

The pH of a test solution X is a linear function of the measured potential. The response of the pH electrode is defined by the Nernst Equation [1], which is

$$pH(X) = Constant + \frac{Ex}{2.3026*RT/F}$$ (1.14)

For a standard solution (S)

$$pH(S) = Constant + \frac{Es}{2.3026*RT/F}$$ (1.15)

Subtracting Equation (1.15) from (1.14)

$$pH(X) = pH(S) + \frac{Ex-Es}{2.3026*RT/F}$$ (1.16)

Where E_X= measured potential of solution (V),

E_S = measured potential of standard solution (V),

R = molar gas constant (8.3144 J mol^{-1} K^{-1})

T = Temperature (K),

F = Faraday constant (96485 C mol^{-1})

pH = the pH of the standard solution is 7

In order to convert the potential difference of the test solution to pH, a calibration plot of the potential difference against pH is required. This enables the potential difference of the test solution to be traced to the corresponding pH value on the plot. Figure 1.8 shows the calibration plot for buffer solutions at 3 different pHs at 20 °C. The calibration curve shows the relationship between the potential difference and pH at room temperature.
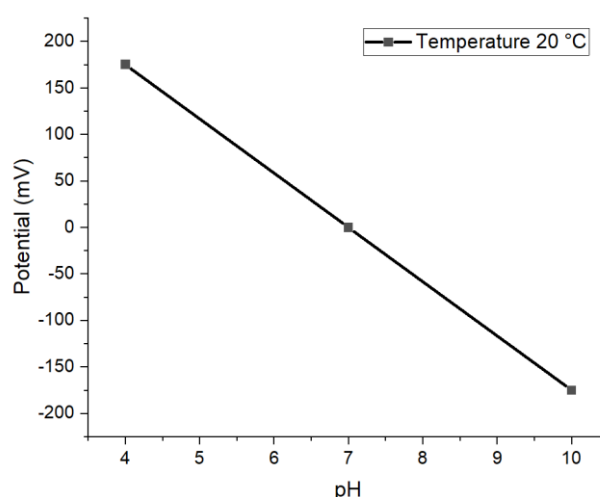
Figure 1.8: The pH calibration plot of a standard buffer solution at 3 different pHs at room temperature (20 °C), the closed squares are calculated values using equation 1.16.

The potential difference-pH calibration plot at two different temperatures is shown in Figure 1.9. As equation 1.16 is dependent on temperature, it suggests that the pH measurement is influenced by a change in temperature. The calibration plot in Figure 1.9 consists of three pH values 4.01, 7.00 and 10.0, which were taken at different temperatures of 20 °C and 40 °C respectively. It can be seen that the slope of the curve is observed to increase as temperature increases.
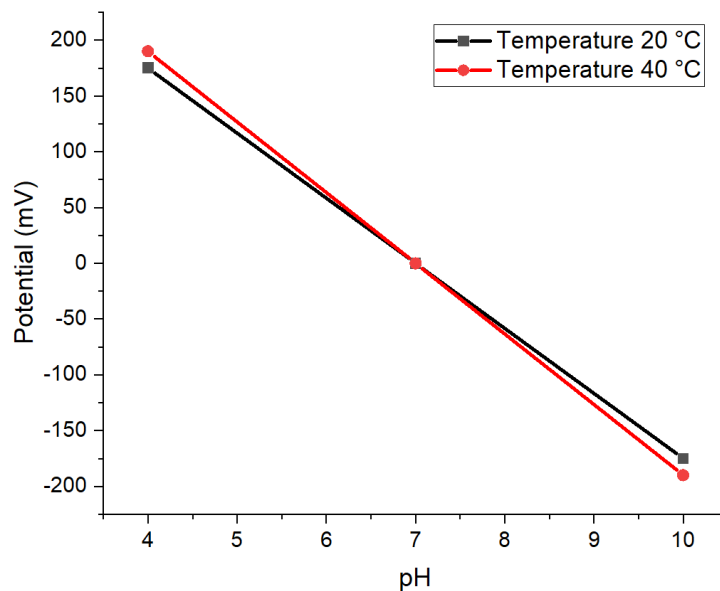
Figure 1.9: A potential difference-pH calibration plot at different temperatures of 20 °C and 40 °C, illustrating a change in the slope of the curves.
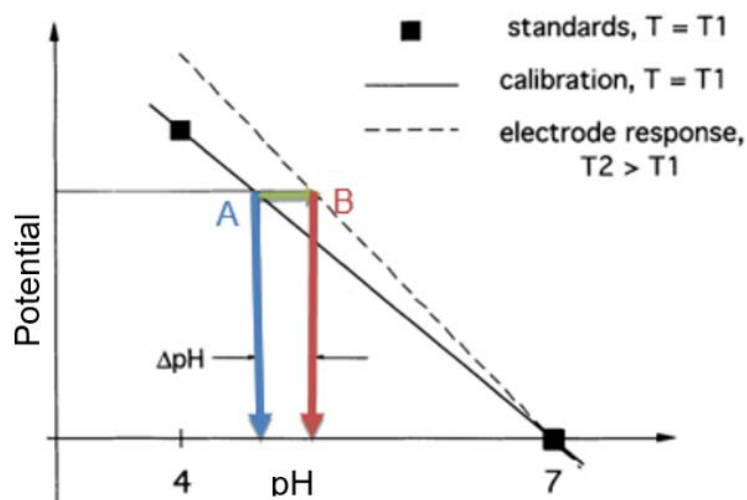
Figure 1.10: A potential-pH plot showing the change in slope due to temperature change during the pH calibration. A pH shift from A to B would occur.

These changes in temperature from day to day can lead to errors in interpreting pH data. For example, when the pH measurement was carried out at 40 °C, a certain change in slope, as shown in Figure 1.10 is observed, with a corresponding shift in the pH value. The change in the experimental temperature tends to cause a change in the potential difference, resulting in a deviation from the calibration curve.

Consequently, in order to provide standardised pH readings, pH measuring devices need to adjust to different temperature settings. This is because pH measurements are dependent on the prevailing temperature. For manual pH regulating devices, the user is usually required to input the temperature of measurement for pH meters and controllers prior to computing the pH of the medium.

Advanced pH devices are already equipped with automatic temperature compensation (ATC), which allows direct measurement of the temperature when the pH electrode contacts the test solution [29]. It is widely agreed that these devices, which automatically adjust the pH value depending on the temperature of the solution are more useful for carrying out the majority of pH measurements in the laboratory [29]. The automatic temperature compensation simply corrects for variations in the electrode output and does not consider any real changes in the pH of the solution that may have occurred as a result of the temperature. In an ideal situation, both the temperature and the pH of the solution should be measured at the same location, but since the temperature sensor is often positioned inside the electrode itself, near the glass membrane, it may not be possible to make adequate corrections to the measurement.

1.5 Importance of pH measurement in the oil and gas industry

The issues mentioned in the previous paragraph have special significance in the oil and gas industry [14,30,31]. For the oil and gas industry, the study of pH is useful in determining the acidity or basicity levels of an oil well. Accurate determination of pH is essential in deciding the appropriate pretreatment processes that should be followed prior to sending crude oil to the refinery for processing. For offshore applications, the pH of seawater depends on the anionic content (mostly sulphates

and fluorides), changes in temperature and pressure as well as the amount of dissolved CO_2 or H_2S [30,32], which worsens when considering the pH in geological fluids.

Furthermore, the pH determination in reservoir conditions may be at higher temperatures and pressure in downhole conditions. Safety in downhole drilling, as well as overcoming the problems of corrosion and scaling [33,34]. It is quite difficult to develop techniques and sensors that meet all the criteria for pH measurement under downhole conditions compared to the currently available techniques for pH measurement. In the downhole conditions, there are aggressive conditions like high temperature and high-pressure environments. The most of the problems faced under these aggressive conditions are stability based [13,35,36].

1.5.1 Challenges associated with pH measurement in the oil and gas industry

In the oil and gas industry, the determination of pH is essential during oil extraction and processing [37–39] because the pH of an oil well gives preliminary information on the chemical characteristics, which determines the protocols to be followed in the purification process. For example, scale formation and corrosion problems are some of the issues encountered in the oil and gas industry [14,37]. Acidic pH increases the concentration of hydrogen ions in solution culminating in the dissolution of these scales and the corrosion of metals on the pipelines, which causes problems for oil and gas workers safety [38].

The formation of mineral deposits on the interior surfaces of containers may be referred to as scales. This is often observed in oilfields during drilling and has been attributed to various factors, such as incompatible anionic and cationic components in water [40,41]. For example, scales have been reported to form when water containing carbonates and bicarbonates of calcium and magnesium are heated, these are the so-called stalactites and stalagmites usually observed at the top and bottom parts of oil reserves respectively [42].

The production of scale in the oil and gas sector is subject to various influencing elements, including pH levels, temperature, salinity of the aquifer, penetration rate, flow velocity, and the existence of additional salts or metal ions [37-40]. This usually

occurs in pipes carrying fluids, which are predominantly water with some mineral salts usually pumped into oil wells to release oil from the underground rock [43]. Although waters in different oil fields have been reported to have different compositions [40,44], it is important that the properties associated with these aquifers be controlled prior to the injection of water to access the oil trapped within the rock.

Iron sulphide is an example of a scale that forms in oil and gas wells, and it has been responsible for the production of sour oil and gas [45]. These scales may be found deposited at the top parts of the well, the control valve for the generated water, and the subsurface safety control valves [46]. The iron sulphide scale is a consequence of the reaction between hydrogen sulphide and iron, as shown in equation 1.17 [47].

$$H_2S + Fe \rightarrow FeS + H_2 \qquad (1.17)$$

The iron sulphide scale poses many operational issues during oil extraction and purification. These include loss of injectivity of power water injectors and water disposal wells, difficulty in operating the wireline, and lowering the amount of fluid that can be extracted from an oil well. Scale development exhibits notable variations among different wells, and it can even exhibit variations along the vertical depth inside the same well [48]. Scales have the potential to accumulate in various components and infrastructure like oil wells, including downhole, tubing, and other production equipment and facilities. The prevalent scales encompass a range of compounds, including, but not restricted to, sulphides (mostly iron sulphides), oxides (primarily iron oxides), sulphate, and carbonate scales [38].

1.5.1.1 Corrosion issues in the oil and gas industry

Corrosion within the oil and gas industry might arise due to the existence of carbon dioxide (CO_2) or hydrogen sulphide (H_2S) [49]. The phenomenon of corrosion induced by carbon dioxide is commonly referred to as sweet corrosion, whereas corrosion resulting from the presence of hydrogen sulphide (H_2S) is commonly referred to as sour corrosion [50]. The occurrence of sweet corrosion can be attributed to the chemical reaction between carbon dioxide (CO_2) and water,

resulting in the formation of carbonic acid, as depicted in Figure 1.11. The dissolution of carbon dioxide (CO_2) in water leads to the formation of carbonic acid (H_2CO_3), which then undergoes interactions with metal surfaces, resulting in the occurrence of corrosion. This creates acidic conditions required to facilitate the dissolution of iron to ferrous ions (Fe^{2+}), which takes place at anodic sites of the metal. The electrons given off at the anode migrate to the cathodic region and reduce protons to hydrogen, which adheres to the surface of the metal. In addition, the hydrogen bubbles which accumulate on the iron surface may further weaken the metal and accelerate corrosion [51,52].
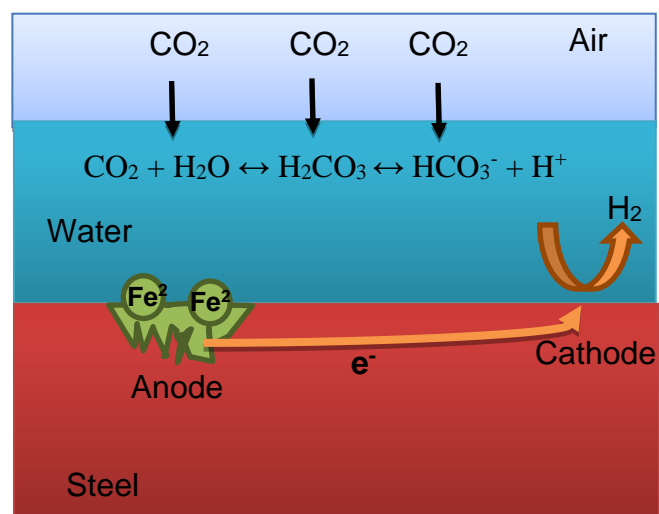
Figure 1.11: Mechanism of sweet corrosion showing how CO_2 dissolves in water resulting in increased H^+ in solution.

Sweet corrosion begins with the dissolution of CO_2 in water produced by the reservoir, which results in the formation of carbonic acid. The presence of carbon dioxide (CO_2) in water, leading to the formation of carbonic acid, as depicted in equation 1.18, enhances the likelihood of corrosion and increases the possibility of corrosion [38,53,54]. These processes can be influenced by pH [12,37], hence the need to determine the pH of oil wells. The acidification mechanism is given by the following steps:

$$H_2O + CO_2 \leftrightarrow H_2CO_3 \tag{1.18}$$

The subsequent procedure involves a two-step dissociation mechanism, leading to the production of bicarbonate and carbonate, as depicted in equations 1.19 and 1.20 [54], respectively.

$$H_2CO_3 \text{ (aq)} \leftrightarrow H^+ \text{ (aq)} + HCO_3^- \text{ (aq)} \tag{1.19}$$

$$HCO_3^- \text{ (aq)} \leftrightarrow H^+ \text{ (aq)} + CO_3^{2-} \text{(aq)} \tag{1.20}$$
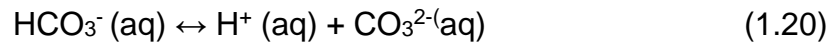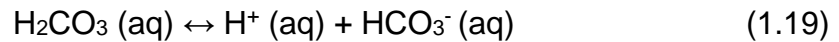
Based on the findings of Dugstad [55], it can be shown that the involvement of carbon dioxide (CO_2) in the occurrence of sweet corrosion is not attributed to a singular mechanism. Instead, it emerges from a wide range of simultaneous electrochemical, chemical, and mass transport phenomena that occur at the interface of the corroding steel in an electrolytic environment. The phenomenon of carbon dioxide (CO_2) corrosion has been associated with chemical and electrochemical mechanisms, including the dissociation and reduction of water, the reduction of hydrogen ions, and the subsequent creation of hydrogen and iron carbonate [51,56].

The extent to which CO_2 contributes to the corrosion of steel in oil wells is often contingent upon alterations in fluid properties, including temperature, pressure, salt concentration, and flow characteristics such as velocity and flow regime. Moreover, this contribution exhibits variability across diverse geographical regions [52,54]. The collective response resulted in the occurrence of CO2 corrosion and the subsequent creation of $FeCO_3$, as shown by the scale formation described in equation 1.21.

$$Fe + CO_2 + H_2O \rightarrow FeCO_3 \downarrow + H_2 \text{ (g)} \uparrow \tag{1.21}$$
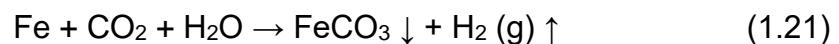
The existence of $FeCO_3$ scale on the surface of steel at a pH of 6.0 and room temperature may offer sufficient protection for the surface, as stated by Videm and Dugstad [57]. Experimental evidence has shown that the solubility of Fe^{2+} reduces in an acidic environment with a pH range of 4 to 5, in relation to the production of $FeCO_3$. Furthermore, it has been discovered that there is a notable decrease in the solubility of Fe^{2+} when the pH is raised from 5 to 6 [54]. Hence, it is probable that the pH factor exerts an influence on the rate at which $FeCO_3$ is formed. Moreover, it is probable that the characteristics of corrosion products could be impacted under low

pH conditions, resulting in the commencement and expansion of corrosion pits [33,58]. The aforementioned traits are prone to be impacted by the pH and other chemical attributes of the bulk solution [59,60]. Hence, it is imperative to accurately determine the pH of water.

On the other hand, "sour corrosion" refers to corrosion that takes place in oilfields due to the presence of H_2S [38,45] as shown in Figure 1.12. The mechanism of sour corrosion is believed to involve a two-step dissociation process involving hydrogen sulphide to give bisulphite ion and further dissociation to sulphide ion, as shown in equations 1.21 and 1.22, respectively [54]. The hydrogen ions can react with the iron to form ferrous ions (Fe^{2+}) and hydrogen gas (H_2). The ferrous ion can also react with sulphide ions (S^{2-}) to form ferrous sulphide (FeS). Corrosion of iron may be made severe by the formation of ferrous sulphide (FeS) by continuous depletion of sulphide ions (S^{2-}) in solution, thereby promoting the formation of hydrogen sulphide.

$$H_2S \text{ (g)} \leftrightarrow HS^- \text{ (aq)} + H^+ \text{ (aq)} \tag{1.22}$$

$$HS^- \text{ (aq)} + H^+ \text{ (aq)} \leftrightarrow S^{2-} \text{ (aq)} + H^+ \text{ (aq)} \tag{1.23}$$
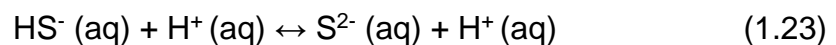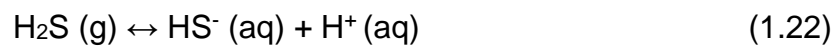
Hydrogen sulphide is commonly encountered in oil and gas reservoirs, often coexisting with other acidic gases, such as carbon dioxide, organic acids, and a diverse range of free radicals and ions resulting from the dissolution of salts [49,61]. Moreover, mackinawite ($FeNi)_9S_8$ is one of the varieties of iron sulphide that may be found in a sulphide laden environment [45,48]. It is believed that mackinawite initially forms on the surface of the steel via a direct surface reaction [48].
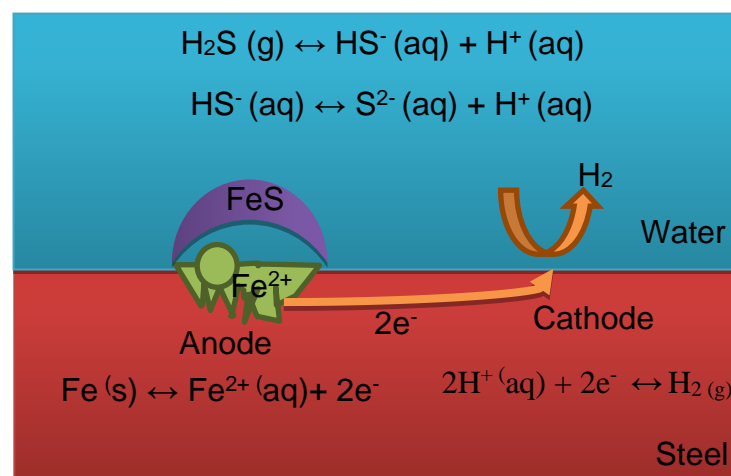
Figure 1.12: Mechanism of sour corrosion showing how H_2S dissolves in water thereby increasing hydrogen ion concentration in solution.

In a general context, it can be observed that under constant temperature and pressure conditions, the corrosion rates tend to decrease with an increase in the pH of the aqueous solution [32,53]. This phenomenon can be attributed to the inverse relationship between pH levels and the concentration of H^+ ions at cathodic sites [34,54]. Besides, the solubility of iron and most metals increases as pH decreases [48]. As a result, iron sulphide does not precipitate on the surface of the metal at a pH less than 2. With further increase in pH up to 5, the formation of a protective coating on the electrode surface consisting of ferrous sulphide (FeS) has been reported [62]. This tends to protect the metal against further corrosive effects of hydrogen sulphide.

1.5.2 Challenges of pH measurement in downhole conditions

In spite of the available techniques for measuring the pH of solutions at room temperature, such lab-based techniques are not usable in downhole conditions due to the high temperature and high pressure (HTHP) observed in this environment [31,39,63,64]. The environment expected in a downhole is presented in Table 1.1. The limitations of the traditional pH measuring techniques in such an environment, which are discussed in the following paragraphs, show the need for our work.

Table 1.1: The physical conditions of the downhole drillings [65].

Conditions	Temperature (°C)	Pressure (Bar)	pH
Downhole drilling	≥ 245	≥ 700	4 to 8

As mentioned, the traditional method of determining the pH of solutions involves the use of glass electrodes to measure the potential difference between the sensing and reference electrodes. This is based on the attraction of hydrogen ions of the test solution to the surface of the probe of the pH meter, resulting in a change in electrochemical potential at different pH. Although this has been widely used in determining the pH of solutions in various applications, glass electrodes are fragile and could easily break on application of slight stress. In addition, they have a low

temperature and pressure range, and the hydronium ions might irreversibly adsorb to the glass electrode, leading to erroneous results among other limitations [26,66]. Colorimetric methods, which use dyes are also restricted to the temperature range of room temperature or lower temperatures since most organic dyes decompose at elevated temperatures. Therefore, there is a need to fabricate an instrument that can determine pH under harsher conditions of high temperature and pressure (HTHP).

1.6 Optical fibre technology as a pH sensor

The optical fibre is a light sensitive material that has wide applications in telecommunications as well as data transfer [67,68]. A fibre optic can be prepared by drawing silica (glass) or plastic to a diameter of 9 µm for single-mode and 50 µm to 1500 µm for multi-mode fibre optics [69] The optical fibre consists of a core, then a cladding followed by a coating, which offers additional protection, as illustrated in Figure 1.13. The optical fibres offer excellent illumination, where they transmit light even in confined spaces [70].
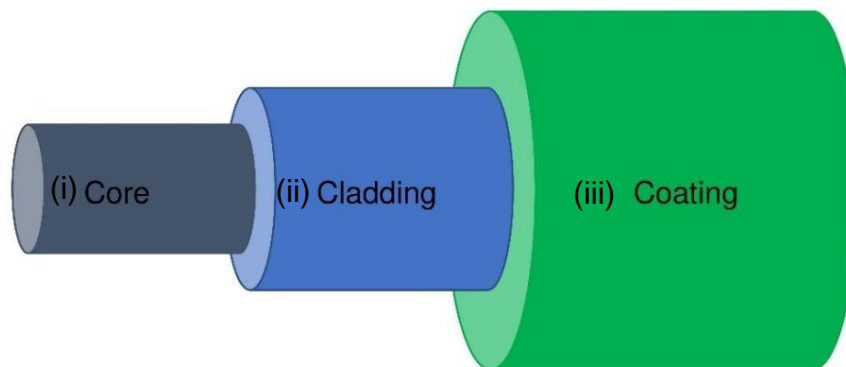
Figure 1.13: Schematic representation of an optical fibre showing the three important layers: (i) core, (ii) cladding and (iii) coating.

The inner part of the fibre where light is transmitted is called the core. This is followed by the middle cylindrical structure, which surrounds the core and is called the cladding. It has a lower refractive index than the core. Finally, the outer component of the optical fibre is known as the coating and consists of one or more polymeric layers. The coating protects the cladding and helps to prevent the optical fibre from any environmental damage [71].

The application of optical fibre as a sensor for measuring pH is a new technique which is still under exploration. It is believed that the optical properties of these sensors could be employed in determining the pH of solutions, especially in environments where conventional pH electrodes cannot be used, such as those observed in harsh environments, which are usually at high temperatures and pressure [72–75]. Besides, the fact that optical fibre can be used over long distances makes it quite interesting for remote monitoring of pH. Therefore, optical pH sensors may have several advantages compared to traditional glass electrodes. This also includes cost-effectiveness since fibre optic technologies are not as expensive as reference electrodes used in traditional pH meters [76–78]. However, more work is required to test their usefulness on an industrial scale [3,76,79,80]. This project is focused on fabricating an optical fibre pH sensor for the measurement of pH for a variety of reference chemical systems, especially high-temperature and high-pressure environments, which are usually experienced in oil wells.

1.7 State of the Art

In recent years, some research has been directed towards the utilisation of a fibre optic sensor for pH measurement at HTHP conditions [81–83]. For example, gold nanoparticles embedded in silica has been decorated on optical fibre, and its sensitivity for pH measurement has been assessed [82,83]. The incorporation of metal nanoparticles in a silica matrix has been reported to improve the stability and sensitivity of optical fibres for pH measurement [84]. In this case, the gold nanoparticle is believed to have a surface plasmon resonance property, which plays a significant role in the optical response required for pH measurement [82]. This technique was proposed as an alternative for pH measurement using the traditional glass electrode, which seems to be the way forward to overcoming the high temperature and high-pressure requirements observed in oil environments.

1.7.1 Working Principle of optical fibre

A fibre optic device is a device that contains strands of glass fibres used for transmitting data in the form of light over long distances [67]. The key mechanism that enables this phenomenon is the modulation of the refractive index, which is defined as the ratio of the speed of light in a vacuum to the speed of light when it

passes through the substance. This relationship can be mathematically represented by equation 1.24. [67].

$$n = \frac{c}{v}$$ (1.24)

In this context, the variable "c" represents the speed of light, while "v" denotes the speed of light within a dielectric or non-conducting medium.
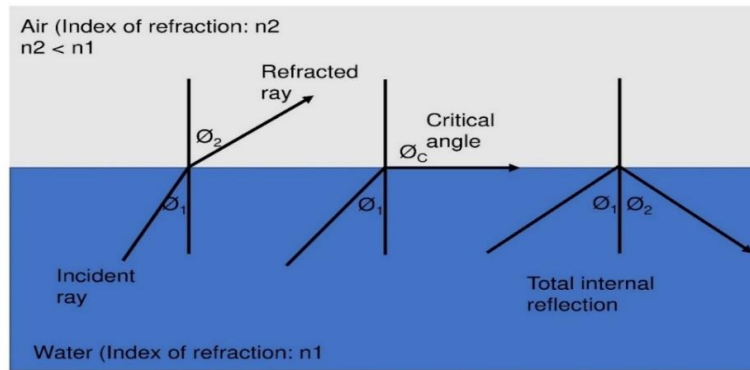
Figure 1.14: Schematic representation of light transmission in different media resulting in total internal reflection.

As shown in Figure 1.14, when the light ray is incident on a surface, refraction occurs when $n_2 < n_1$. The difference in densities of the two media causes the bending of the light rays while travelling from one medium to the other. The relationship existing between the incident ray and the bent ray is given in Snell's law (equation 1.25) [67].

$$n_1 \sin\phi_1 = n_2 \sin\phi_2$$ (1.25)

Where the symbol ϕ_1 represents the angle of incidence, while ϕ_2 represents the angle of refraction, the refractive indices of the two materials are denoted as n1 and n2.
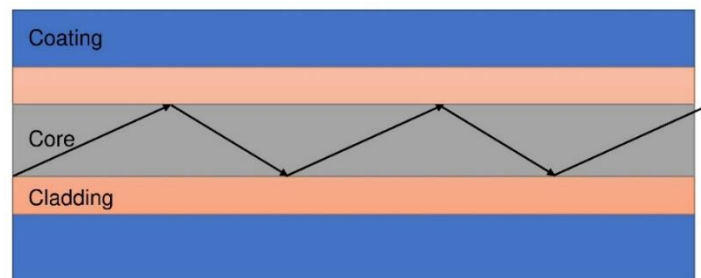
Figure 1.15: Schematic representation of the mechanism of total internal reflection in an optical fibre.

The cladding contributes to the retention of the light signals inside the core. It is constructed out of a unique glass material that has a lower refractive index compared to the core of the glass. This is the region where total internal reflection takes place. According to Snell's law, total internal reflection is observed when light transitions from a medium characterised by a lower density to a medium characterised by a higher density, as illustrated in Figure 1.15. Due to total internal reflection, when a light signal is transmitted at one end of an optical fibre, the light enters the fibre and travels along the core of the fibre. This occurs as a result of the light travelling back and forth from the walls of the fibre. The core of the optical fibre is denser than the cladding; therefore, light can travel along the core of the fibre without a significant loss of energy. The cladding encircles the core and performs the function of a protective covering, thereby preventing any external interference, such as bending or pressure that could result in loss of incident light.

1.7.2 Types of Optical Fibres

Optical fibres may be classified into different types according to the refractive index or the type of material used. For classification based on refractive index, optical fibres may be classified into single mode, multimode graded index and multimode step index [85]. The type of optical fibre depends on the refractive index, materials used, and mode of propagation of light [67]. A schematic diagram showing the three types of optical fibres is shown in Figure 1.16.
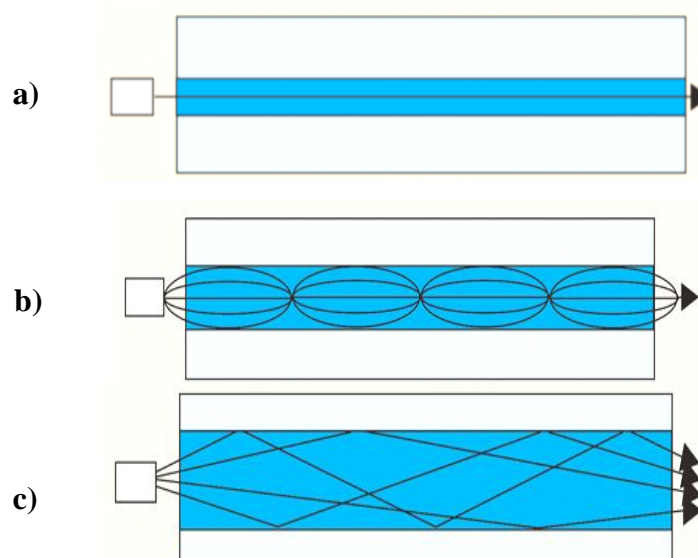
Figure 1.16: Different types of optical fibre: (a) single mode, (b) multi-mode graded index and (c) multimode step-index optical fibre [85].

The single-mode optical fibre, as the name implies means that it operates in one mode only due to the small diameter of its core. The speed of transmission of a single-mode optical fibre is greater than multimode optical fibres. For multimode graded-index optical fibre, the diameter of the core is greater than single-mode optical fibre. In addition, light transmission at the edges of the core is faster than the transmission at the centre due to a continuous decrease in the refractive index from the centre of the core to the cladding surface [85]. Unlike the multimode-graded index, the multimode step index has a uniform refractive index from the core of the optical fibre to the cladding surface [85]. Beyond the cladding, the refractive index increases in a stepwise pattern, which has different path lengths through the optical fibre, causing the transmission of data in this mode to be kept at short distances to avoid mode dispersal issues.

For classification based on the type of material, optical fibres may be classified into plastic and glass optical fibres. The glass optical fibres are usually made from silica [67]. Glass fibres are used for longer-wavelength infrared and other specialised applications. Glass fibre cables could be used for high-temperature (HT) applications up to 500 °C including extremely low-temperature (-40 °C) [78]. Glass cores are effective in transmitting light, and its transfer speed is quite high; therefore, glass optical fibres can be used as a sensor over long distances. On the other hand, plastic optical fibre (POF) or polymer optical fibre is an optical fibre that is made from a polymer. The core is prepared from polymethyl methacrylate or polystyrene, and the cladding is prepared from polysiloxane or fluorinated polymers. Plastic optical fibre has some advantages over glass optical fibre, such as reduced fragility and robustness during stretching and bending [75,78]. In addition, the polymer optical fibre is cheaper than the glass optical fibre.

1.8 Statement of research problem and justification

The traditional glass electrode has significant limitations, such as the inability to determine pH at high temperatures and high pressures greater than 100 °C and 1 bar, respectively, which is usually encountered in oil wells. Therefore, there is a need to develop a sensor that can measure the pH of fluids at high temperatures and high pressure, which would be suitable for oil wells operating under such conditions.

Research conducted on the efficacy of gold nanoparticles incorporated within silica as the active component in optical fibres for pH detection has been somewhat restricted, primarily focusing on temperatures up to 80 °C [82]. Moreover, it should be noted that the temperature range within a conventional oil well has been reported to reach as high as 370 °C [86], with typical values falling between 50 and 200 °C [30]. Consequently, there exists a significant disparity between the experimental conditions of existing studies and the actual operational temperatures encountered in oil well environments. Therefore, this study seeks to develop a fibre optic pH sensor based on silver nanoparticles embedded in silica, which could possibly be used in measuring pH at high temperatures and pressures.

In this work, gold nanoparticles are replaced with silver nanoparticles. This is because silver nanoparticles have also been reported to possess the LSPR property, and it is less expensive compared to gold [87–89]. A similar investigation was carried out using palladium nanoparticles embedded in silica, but no peak which could serve as evidence of LSPR property was observed [90]. To the best of our knowledge, there has been a dearth of information regarding the effectiveness of decorating silver nanoparticles on optical fibres for the determination of the pH of solutions, even though silver is much cheaper than gold and palladium. Apart from cost, the excellent LSPR property of silver nanoparticles and the novelty of the work are the key reasons that influenced the choice of silver as the target metal to be embedded in silica for this application. The substitution of gold nanoparticles with silver nanoparticles encapsulated within a silica matrix represents a strategic hypothesis shift that presents multiple advantages across diverse domains. Silver nanoparticles, distinguished for their robust optical characteristics, emerge as a compelling substitute owing to their prominent localised surface plasmon resonance (LSPR) phenomena discernible within the visible electromagnetic spectrum. Additionally, the greater abundance and relatively lower cost of silver (i.e. 1/10th) in comparison to gold provide it with enhanced economic feasibility, particularly conducive to large-scale production endeavours. The tunability of silver nanoparticle plasmonic resonance within silica matrices facilitates tailored optical responses, which are pivotal for sensor applications. The integration of silver nanoparticles into silica matrices exhibits compatibility with various fabrication methodologies [91–93], ensuring scalability and adaptability. Nonetheless, the utilization of AgNp/silica

coating under conditions of high pressure and temperature remains an area demanding further investigation and exploration.

This study will focus on the synthesis of silver nanoparticles incorporated within a silica matrix. Initially, the investigation will involve the synthesis of gold nanoparticles encapsulated within a silica coating [90,94,95], serving as a precursor to replicate the aforementioned methodology. However, it is anticipated that the fabrication protocol for the gold nanoparticle/silica composite and subsequent coating procedures, including the requisite heat treatment temperatures, will necessitate adjustments for the preparation of silver nanoparticle/silica coatings. Furthermore, the literature on the preparation of gold nanoparticle/silica coatings lacks comprehensive and detailed procedural information, thereby confounding replication efforts, which may entail considerable time investment for optimization. Consequently, the current endeavour commenced directly with the preparation process, incorporating an optimization phase to elucidate the methodology for fabricating silver nanoparticle/silica coatings within the scope of this thesis.

1.9 Aims and Objectives

The main aim of this work is to fabricate a pH sensor based on silver nanoparticles embedded in silica and decorated on an optical fibre. The key objectives of this work targeted at achieving this aim include the following:

- ➢ To determine the suitability of silver nanoparticles when embedded in silica matrix for use as an optical sensor.
- ➢ To assess the reproducibility and repeatability of the response of silver nanoparticle-silica coated optical fibre for pH measurement.
- ➢ To assess the stability and performance of the sensor under different chemical environments such as sulphuric acid, phosphoric acid, hydrochloric acid, sodium chloride, etc.
- ➢ To establish an apparatus to incorporate a fibre optic sensor in a high temperature and pressure system.
- ➢ To establish a calibration process at higher temperatures and pressures, which will lead to the optical pH measurement technique.
- ➢ To assess the stability and performance of the sensor at high pressure and high-temperature conditions.

1.10 Structure of the thesis

This thesis consists of seven chapters organised to provide an overview of the fabrication of a fibre optic pH sensor for the determination of pH at high temperature and pressure conditions.

Chapter 1 presents the Introduction and Background of pH measurement, which begins with an overview of the background of pH and its relevance to the oil and gas industry. The traditional pH measurement technique and its limitations, including theories of pH measurement as well as working principles of optical fibre sensors are also covered. In addition, the problems encountered within the oil and gas industry regarding pH measurement are also highlighted, as well as the justification and objectives of the research.

Chapter 2 is the Literature review on pH measurement using glass optical fibres. It describes previously published information on the formation of silica coating, including the stability of fabricated optical fibres and research on gold nanoparticles in silica coating. It discusses the preparation of silica coating, including gel formation, and the parameters that control them.

Chapter 3 is the experimental chapter, which is structured into two main sections: preliminary experiments involving the preparation of silver nanoparticles embedded in silica coating on glass slides and the preparation of coating on the optical fibre to enable it to function as a pH sensor. It provides a detailed description of the preparation process, covering the preparation of AgNp/silica coating on optical fibre, the etching process of optical fibre, and the optical fibre connections, including the coated optical fibre, with the detector and light source. It also addresses the challenges associated with the experiments and ways to overcome them.

Chapter 4 is the first Results chapter that describes the preparation of AgNp/silica coating on a glass slide. This is followed by the decoration of the coating on the optical fibre to enable it to function as a pH sensor. Additionally, the chapter explains the preparation of an AgNp/silica-coated optical fibre, optimizing conditions for gelation and heat treatment. The adhesion of the coating is improved through optimization experiments, and selective etching of the optical fibre's cladding and coating layers is reported. Durability tests on the AgNp/silica coating under different

31

conditions are also documented, providing insights into the coating's stability. Also, the characterisation of the coated glass slides using scanning electron microscopy to assess the coating's surface morphology are discussed.

Chapter 5 is the second Results chapter, where the results of the performance of the optical pH sensor under different chemical conditions at room temperature are presented. It covers the reproducibility and repeatability of the optical pH measurements. This chapter encompasses several key aspects, including optimising the light source and detector arrangement for maximum optical pH sensitivity, determining the ideal etched optical fibre diameter for sensitivity at varying pH levels, conducting optical pH measurements in diverse chemical environments (phosphate ions, sulphate ions, and chloride ions), evaluating the reproducibility of sensors within the same and different batches, and establishing calibration procedures for optical pH measurements. A comparison of pH measurements with the optical pH measurement and potentiometric methods is provided to assess the accuracy of the sensor.

Chapter 6 is the third Results chapter, presenting the results of the performance of the optical pH sensor at higher temperatures (up to 156 °C) and pressures (up to 5 Bar) in different chemical conditions. It compares the stability of the AgNp/silica coating under HTHP conditions and investigates the stability of the sensor for multiple cycles in HTHP conditions, providing insights into the capabilities and limitations of the sensor.

Chapter 7 contains the major conclusions, including limitations of this AgNp/silica optical fibre pH sensor, as well as recommendations for future work.

CHAPTER 2 : Literature Review

CHAPTER 2: Literature Review

This chapter covers the research that has been carried out in fabricating pH sensors using optical fibres, including some modifications that would enable its usage as a pH sensor. This review aims at assessing the work carried out in fabricating optical fibres as a sensor for pH measurement and helps identify areas that still need more investigation as well as gaps that this study seeks to fill. Although there are several publications on fibre optic sensors for pH measurement at room temperature, there is a paucity of reports on methods of fabrication, especially those applicable to high-temperature and high-pressure measurements. Therefore, this section also discusses some of the technical constraints associated with optical pH measurement at high temperatures and high pressure (HTHP), which will explain our contribution to solving the problems of pH measurement under HTHP conditions usually observed in some oil wells.

2.1 Formation of silica coating

This section begins with reports on the preparation of silica coating, this includes gel preparation and factors that influence gel formation. The silica coating is usually prepared using the sol-gel technique. Therefore, adequate information on gel formation is important in obtaining a good adhesive coating. In addition, the preparation of silica coating and factors such as concentration, temperature, and presence of metal nanoparticles are also covered. This work highlights the optimum conditions required for the preparation of silica coating with the properties required for a coating, such as good adhesion to the optical fibre, as well as good stability and sensitivity in determining pH at HTHP conditions.

Silica coatings have been used in various applications due to its adaptability and versatility [96,97]. The coating process involves the application of a layer of silica precursors on the external surface of a targeted substrate such as metals, ceramics, polymers, and even biological materials. Coatings made of silica-based materials are often used to enhance biocompatibility and resistance to substrate corrosion. Additionally, silica coatings are utilised to enhance the substrate's mechanical, chemical, and thermal characteristics. The deposition of silica coatings may be

accomplished using a number of processes, including sol-gel, chemical and physical vapour deposition, as well as electrochemical deposition.

Sol-gel processing is a typical technique used for the deposition of silica coatings in most studies reported in the literature [76,98–100], and it involves hydrolysis of a silica precursor and subsequent condensation of the resulting intermediate to form a sol. This sol is then used in the processing of sol-gel materials. A typical sol-gel route for the preparation of silica coating is the Stöber process. This involves five different steps: hydrolysis, condensation, polymerisation, gelation and drying [101]. The hydrolytic step is usually applied to the precursor to generate intermediates that undergo further reactions to yield other products. In this study, the silica coating was prepared from tetraethyl orthosilicate as the source of silica. Other researchers have used tetraethoxysilane as well [102,103]. Some of the chemical reactions involved in the synthetic steps regarding the formation of silica coating are explained in the forthcoming paragraphs.

Hydrolysis is the splitting of a molecule using water. Tetraethyl orthosilicate (TEOS) can be hydrolysed in the presence of water and alcohol at acidic or basic pH to form silanol, as shown in the reaction below (equation 2.1) [103].

$$Si(OC_2H_5)_4 + H_2O \rightarrow HO\text{-}Si(OC_2H_5)_3 + C_2H_5OH \qquad (2.1)$$
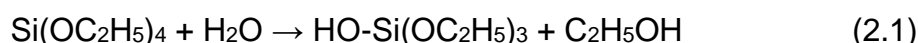
The pH level of the solution is one of the factors that can impact the reaction rate, alongside other parameters. If the solution is acidic, the rate of hydrolysis increases; however, if the solution is alkaline, the condensation reactions (equations 2.2 and 2.3) will be favoured. The reaction can also be influenced by the type of catalyst present. For example, acid catalysts such as hydrochloric and nitric acid will favour hydrolysis, while alkaline catalysts such as ammonia will enhance the condensation reaction [103]. The newly formed $HO\text{-}Si(OC_2H_5)_3$, as shown in equation 2.1, then undergoes condensation reactions, as shown in equations 2.2 and 2.3.

Condensation reactions involve chemical reactions of two molecules to form a single molecule with the elimination of small molecules such as water or alcohol [103]. If the molecule eliminated is alcohol, then this is referred to as alcohol condensation, but if the molecule eliminated is water, then this is referred to as water condensation [103]

A) Alcohol condensation

$$R_3O\text{-Si-OR} + HO\text{-Si}(OR)_3 \rightarrow R_3O\text{-Si-O-Si}(OR)_3 + ROH \qquad (2.2)$$

B) Water condensation

$$R_3O\text{-Si-OH} + HO\text{-Si}(OR)_3 \rightarrow R_3O\text{-Si-O-Si}(OR)_3 + H_2O \qquad (2.3)$$
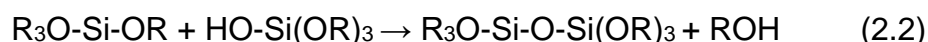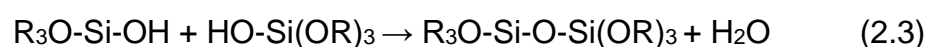
Siloxane bonds are usually the products of condensation reactions involving silanol groups, which usually involves the elimination of water or ethanol. In most cases, condensation is initiated before hydrolysis is complete. Separating the main product of this condensation reaction usually requires a homogenising agent such as ethanol in the case where water is the by-product. This is because alkoxy silanes are immiscible in water. If alcohol is the by-product, then no homogenising agent is required [104]. Based on the pH of the solution, therefore, reaction 2.1 could be promoted in comparison with reactions 2.2 and 2.3, which would favour the formation of silanol and alkoxide.

The condensation reactions are followed by the polymerisation reactions. Polymerisation reactions during gel preparation involve the formation of large molecules from the simpler molecular units called monomers [104]. The reactions can also involve dimers, which are two monomer units or trimers involving three monomer units etc. Structurally, they can be linear or branched chains, as shown below:

$$HO-\underset{\underset{R}{|}}{\overset{\overset{R}{|}}{Si}}-OH \quad + \quad HO-\underset{\underset{R}{|}}{\overset{\overset{R}{|}}{Si}}-OH \quad \longrightarrow \quad HO-\underset{\underset{R}{|}}{\overset{\overset{R}{|}}{Si}}-O-\underset{\underset{R}{|}}{\overset{\overset{R}{|}}{Si}}-OH \quad + \quad H_2O \quad (2.4)$$

Dimmer

$$n \begin{bmatrix} & R & \\ & | & \\ HO - & M & - OH \\ & | & \\ & R & \end{bmatrix} \longrightarrow HO - \begin{bmatrix} R & & R \\ | & & | \\ M & - O - & M \\ | & & | \\ R & & R \end{bmatrix}_{n-1} -OH \; + \; (n-1)\,H_2O \qquad (2.5)$$

Chain
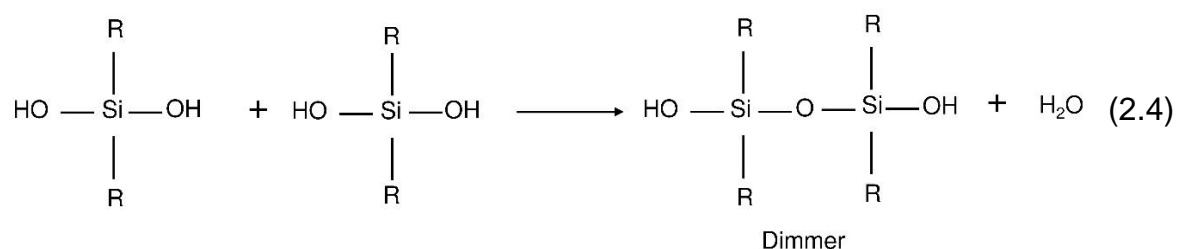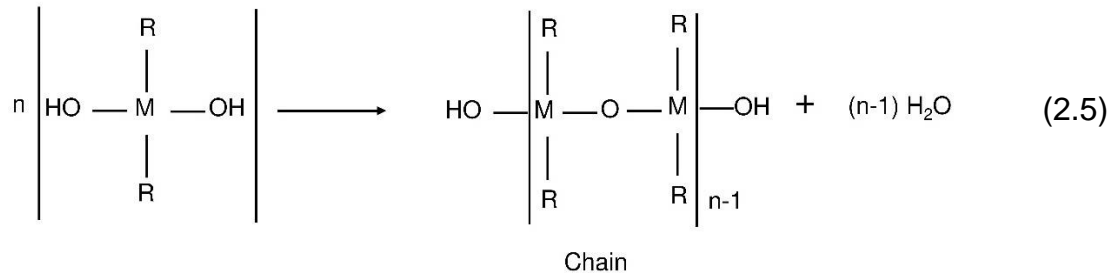
The polymerisation reaction involves three stages, which include: the chemical combination of monomers to form particles, which is followed by particle growth and the linking of particle units to form polymers, thereby thickening the solution to form a gel [97]. Once dimers are able to form, it will preferentially react with monomers to form trimers and other large molecules [103].

The polymerisation mechanism is given below:

$$\equiv Si\text{-}OH + OH^- \rightarrow \equiv Si\text{-}O^- + H_2O \qquad (2.6)$$

$$\equiv Si\text{-}O^- + HO\text{-}Si \rightarrow \equiv Si\text{-}O\text{-}Si \equiv + OH^- \qquad (2.7)$$
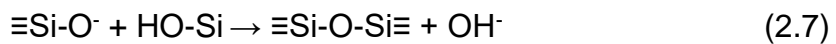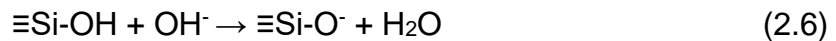
The reaction in a highly acidic medium (< pH 2) favours the formation of a siliconium ion intermediate ($\equiv Si^+$).

$$\equiv Si\text{-}OH + H^+ \rightarrow \equiv Si^+ + H_2O \qquad (2.8)$$

$$\equiv Si^+ + HO\text{-}Si \rightarrow \equiv Si\text{-}O\text{-}Si \equiv + H^+ \qquad (2.9)$$
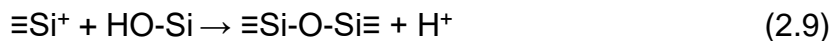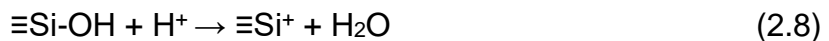
Once the polymerisation begins, gelation can also commence. Gelation involves the formation of a three-dimensional network obtained by means of cross-linked polymers. The rate of gelation can be enhanced if the temperature of the reaction medium is increased [103,104]. The cross-linking of monomer or dimer units will result in an increase in viscosity, leading to the formation of a semi-solid or solid mass. The porosity of the product determines its mechanical strength and behaviour [101,105].

The final stage of coating formation which involves the evaporation of water or alcohol from the matrix [96]. This usually involves a heat treatment process, which is usually carried out between 40 $^\circ$C and 400 $^\circ$C till the gel solidifies [103,106]. The

heating and cooling rates have a significant effect on the mechanical strength of the material [107,108]. Rapid heating and cooling rates can cause fast or slow shrinkage, leading to fracture of the coating (or hardened gel). To avoid this, prolonged and planned thermal treatment, reinforcement of the gel, supercritical drying, or freeze drying has been used to overcome these issues depending on the application [109,110].

2.2 Effect of reaction parameters

In this section, the effect of different reaction parameters, such as the presence of catalyst, pH and temperature on gel formation are discussed in more detail. As mentioned in the previous section, the initial phase during gel formation involves hydrolysis of the precursor, which forms intermediates that contain a network bridge of oxides or alcohols, resulting in a polycondensation reaction with a resulting increase in the solution's viscosity. Subsequently, a solid polymer is formed from the gel during thermal treatment. The presence of a catalyst, pH and different temperatures can influence the rate of these reactions, and it is hereby discussed below [103,111].

2.2.1 Importance of catalysts on gel formation

The catalyst affects the hydrolysis and condensation processes, which control the microstructure of the metal oxide generated from the sol-gel process [103]. Hydrolysis and condensation of TEOS are required to produce tetraethyl orthosilicate (TEOS) gel. In order to produce a gel with consistent properties and homogeneity, a catalyst is required. In this review, the various types of catalysts used in the production of TEOS gel, as well as the influence of these catalysts on the gel's properties are discussed.

Acidic catalysts: Acidic catalysts, such as hydrochloric acid (HCl), sulfuric acid (H_2SO_4), nitric acid (HNO_3), and acetic acid (CH_3COOH), are commonly employed in the synthesis of TEOS gel. These catalysts promote the hydrolysis of TEOS, which generates silanol groups (Si-OH) that can condense with other silanol groups. During the acid catalytic step, the lone pair of electrons on the oxygen atom of the Si-OR group will be attracted to the protons present in the solution, resulting in the formation of an unstable intermediate. Following the impact of the proton, the electronic cloud in the Si–O bond will move towards oxygen. This occurs as a result

of the higher electronegativity of atoms compared to silicon. Consequently, the positive charge on the silicon atom will increase. At this moment, silicon transforms into a substance that is more electrophilic, resulting in the formation of hydronium ion, which detaches from the linkage as small molecules during the condensation step, as shown in the reactions below.

Protonation of ≡Si-OR

$$\equiv Si\text{-}OR + H^+ \leftrightarrow \equiv Si\text{-}\overset{H}{\underset{R}{\overset{|}{O^+}}} \rightarrow \equiv Si\text{-}\overset{H}{\underset{R}{\overset{|}{O^+}}} + HOH \rightarrow \equiv Si\text{-}OH + ROH \quad (2.10)$$

Hydrolysis

Protonation of ≡Si-OH

$$\equiv Si\text{-}\overset{..}{\underset{..}{O}}H + H^+ \leftrightarrow \equiv Si\text{-}\overset{H}{\underset{H}{\overset{|}{O^+}}} \rightarrow \equiv Si\text{-}\overset{H}{\underset{R}{\overset{|}{O^+}}} + Si\text{-}OH \rightarrow \equiv Si\text{-}O\text{-}Si\equiv + ROH \quad (2.11)$$
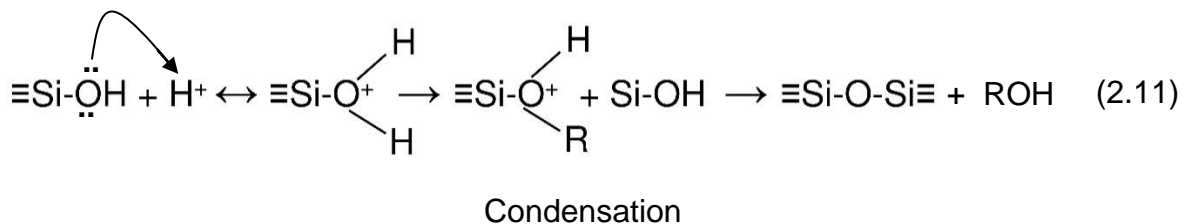
Condensation

Basic catalysts: Ammonia (NH_3) and sodium hydroxide (NaOH) are two examples of basic catalysts that can be used in the production of silica gel. These catalysts facilitate the synthesis of silanol groups and their subsequent condensation into a three-dimensional network. The production of silica gels from TEOS can also involve the use of basic catalysts. In this case, the deprotonation of water molecules following nucleophilic attack by hydroxyl ions on the positively charged silicon ion is the key mechanism that describes the action of basic catalysts during the gelation of silica.

Ammonia (NH_3) or sodium hydroxide (NaOH) are two examples of basic catalysts which can deprotonate water molecules in the reaction mixture. This results in the formation of hydroxyl ions (OH^-) and hydronium ions (H_3O^+). The silicon atoms in the TEOS molecule are susceptible to attack by the hydroxide ions, which ultimately results in the hydrolysis of the TEOS precursor and the formation of silanol (Si-OH) groups. This is followed by the condensation step, where the silanol groups interact

with one another to produce Si-O-Si connections, resulting in the formation of a three-dimensional silica gel network. The presence of a basic catalyst can speed up condensation processes by increasing the concentration of hydroxyl ions in the solution. These hydroxyl ions can serve as nucleophiles that attack silicon atoms, leading to the formation of Si-O-Si bonds, as shown in the reactions below.

Deprotonation of water

$$\equiv Si\text{-}OR + HO^- \leftrightarrow \left[\equiv Si\text{-}OR \overset{OH}{\diagup}\right]^- \leftrightarrow \equiv Si\text{-}OH + RO^- \qquad (2.12)$$

Hydrolysis

Deprotonation of silanols

$$\equiv Si\text{-}OH + \equiv SiO^- \leftrightarrow \left[\equiv Si\text{-}OH \overset{SiO^-}{\diagup}\right]^- \leftrightarrow \equiv Si\text{-}O\text{-}Si \equiv + HO^- \qquad (2.13)$$
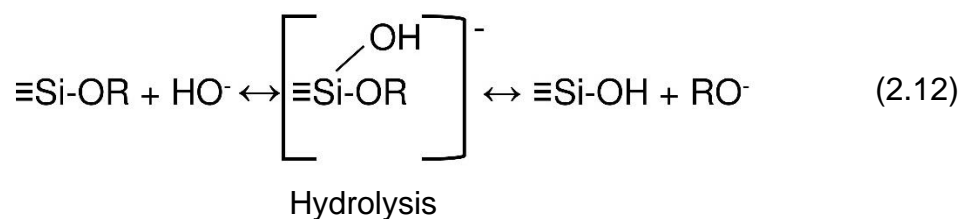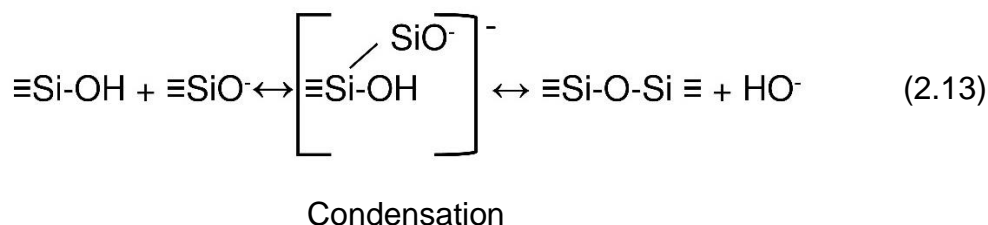
Condensation

The rate of hydrolysis and condensation steps have been reported to be different when basic and acid catalysts are used. The hydrolytic step has been reported to be faster than the condensation step when the acid catalyst is used and vice versa when a basic catalyst is used [103]. This is because in an acidic medium, the presence of protons from reduces the electron cloud around the oxygen atom of the Si-O bond. This decreased nucleophilicity results in enhanced splitting of the resulting intermediate. However, in a basic medium, the hydroxyl ions enhance the condensation step due to its electron-rich state that abstracts protons from the leaving group, resulting in the formation of Si-O-Si linkages in the matrix. In terms of particle sizes, the acid-catalysed reaction yields smaller particle sizes compared to base-catalysed reactions, as shown in Figure 2.1.
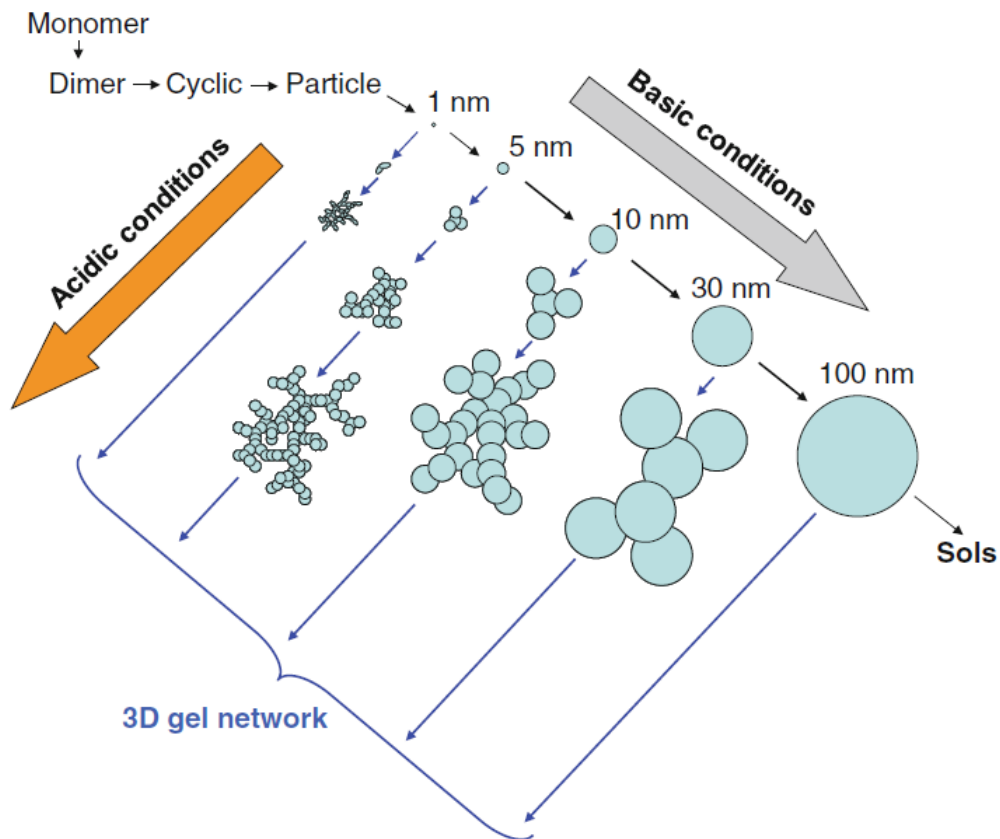
Figure 2.1: Schematic representation of a three-dimensional network showing the effects of acid and basic catalyst on the formation of particles of different sizes in the gel [103].

Pope *et al.* [112] conducted research to investigate the effect of different catalysts on gel formation. In their report, the porosity of silica coating was investigated using an acid and a basic catalyst, including a control reaction where no catalyst was used. The results are presented in Table 2.1. The results indicate that when nitric acid was used as a catalyst, a silica gel with the lowest porosity of about 10% was obtained. However, the use of hydrogen fluoride as a catalyst resulted in a significant increase in porosity up to 67%. According to the authors, this increased porosity was attributed to the fact that HF is a strong acid, which can react with the silica framework that makes up the gel resulting in the cleavage of silicon-oxygen bonds and resulting in the formation of pores within the material [112]. Nitric acid also undergoes a similar reaction with the TEOS precursor to produce silica particles; however, the formation of pores is not as efficient as HF. In addition, 68% porosity was found when ammonium hydroxide was used as the catalyst, despite the fact that

it was anticipated that a basic catalyst would greatly enhance the porosity of the silica gel.

Table 2.1: Porosity of the silica coating using the different catalysts [112]

Catalyst	Porosity (%)
Nitric acid (HNO_3)	10
Hydrogen Fluoride (HF)	67
Ammonium hydroxide (NH_4OH)	68
Without catalyst	43.4

2.2.2 The effect of reaction temperature on gel formation

The control of reaction temperature plays a crucial role in the process of gel formation. The influence of temperature on the kinetics of hydrolysis and condensation reactions is a key factor to consider. Consequently, this determines the composition and properties of the gel. The kinetics of hydrolysis and condensation reactions are influenced by temperature, with higher temperatures promoting faster reaction rates. However, high temperatures can also result in a higher degree of cross-linking, which leads to a gel structure that is dense, more compact, and has fewer pores [109]. On the other hand, lower temperatures may result in a gel structure that is less thick and more porous, but they can also lead to partial gelation, which can lead to a gel structure that is fragile and unstable.

In principle, an increase in temperature enhances the rate at which free primary particles form during the gelation process. According to the reports in the literature, the aggregation of primary particles increases when the reaction temperature is increased compared to room temperature [109,113]. This phenomenon occurs due to the direct relationship between temperature and the kinetic energy of particles. These speed up the movement of the particles, which in turn increases the likelihood that the particles will collide with one another and aggregate. As a result of aggregation, there is an increasing number of secondary particles with time. Therefore, an increase in the reaction temperature reduces the gelation time.

Twej *et al.* [113] also determined the effects of temperature on gel formation. In their report, the change in gelation time when the reaction temperature was set to 30 °C to 60 °C, as shown in Figure 2.2 was investigated. The results indicate that the gelation time was reduced from 144 h to 120 h for pH 4, 35 h to 14 h for pH 7, and 48 h to 19 h for pH 9, which showed the synergistic effects for pH and gelation temperature.
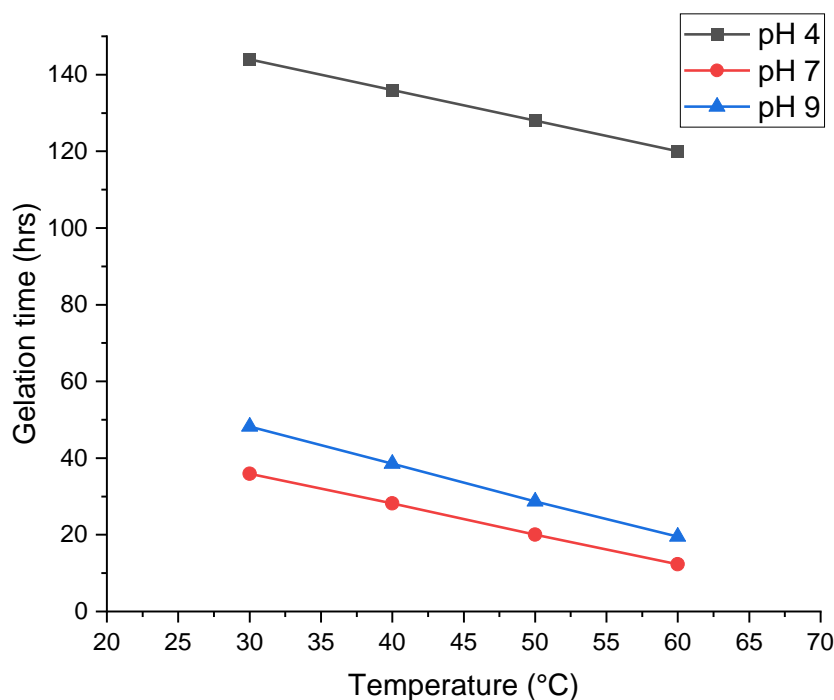
Figure 2.2: Graphical representation of gelation time as a function of temperature at different solution pH [113].

Hegde *et al.* [109] conducted a separate investigation wherein they examined the impact of reaction temperatures on the duration necessary for gelation to take place. In their report, the gelation time was measured from the period that the catalyst was added to the time when the gel started to form. According to the provided definition, the gelation time was observed to be 85 hours while the reaction temperature was maintained at 25 °C. At a temperature of 30 degrees Celsius, a notable decrease in the duration of gelation was seen, with the process taking 30 hours, which is depicted in Figure 2.3. The findings of their study indicated that elevated temperature had a direct correlation with accelerated hydrolysis and condensation reactions, thereby resulting in a speedy process of gelation. However, this caused the gel to shrink because too much solvent was forced out of the gel during the process.

43

Therefore, a moderate temperature not exceeding 50 °C was recommended in order to obtain a good quality silica coating[109].
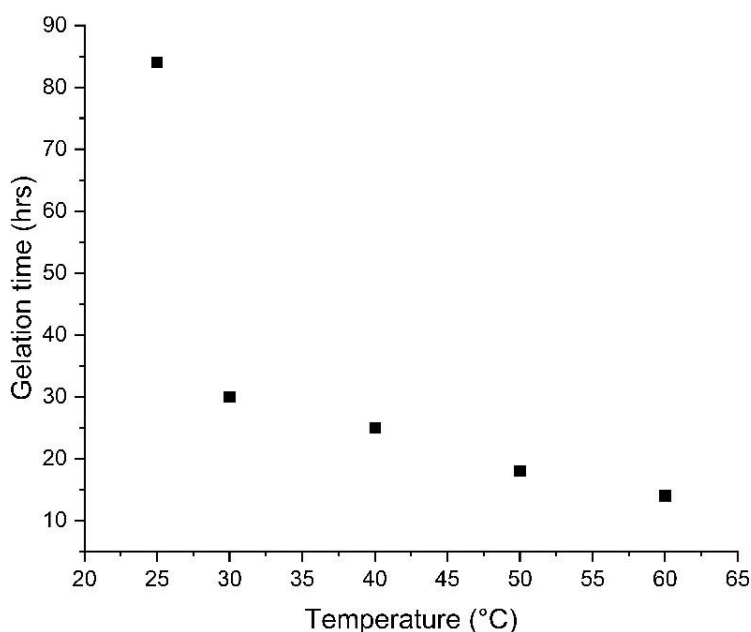
Figure 2.3: Graph showing the effect of the gelation time of silica on temperature. Adopted from Hegde *et al.* [109].

2.2.3 Importance of pH of solution on gel formation

As shown, the pH of the solution involved in the preparation of silica gel is very crucial in the gelation process. This is because it is believed that pH is a determining factor in the rate of hydrolysis and condensation reactions. In this section, the effects of acidic and basic pH on gel formation are assessed. First, the hydrolytic step involved in the gel formation is believed to be favoured at low pH levels [103]. This is because at low pH, the solution contains more protons that facilitate the formation of electrovalent bonds between the electron-rich oxygen atoms of the precursor and protons in the solution. However, when the pH is increased to a basic medium, the number of protons in solution decreases, resulting in a slow hydrolytic step. On the other hand, the condensation step is favoured at high pH levels, this is primarily because at high pH, the solution is rich with hydroxyl ions, which are strong nucleophiles capable of facilitating rapid detachment of the hydronium ions or other leaving groups that are attached to the silica matrix.

Furthermore, pH exhibits a significant influence on various aspects of gel characteristics, including the gelation process, porosity, mechanical properties, and surface morphology. For instance, previous studies have indicated that the pH level could potentially influence the size and distribution of pores within the gel. Specifically, lower pH levels have been observed to lead to the formation of smaller pores that are more evenly dispersed throughout the coating [103]. There are different approaches that may be used in order to regulate pH throughout the silica gel formation steps. The addition of acid or basic solutions to the reaction mixture is a procedure that is often employed in most studies. Experimentally, when Twej *et al.* [113] carried out gelation at pH 4,7 and 9 at 30 °C as shown in Figure 2.4, the duration required for gelation to occur for pH 4, 7, and 9 were 145 h, 48 h, and 28 h respectively. In this report, the gelation time tends to decrease as pH increases from 4 to 7. However, their claims are somewhat premature as very few measurements were carried out in between the two pH values to ascertain the decrease in gelation time, and no other data is provided at pH values lower than 4.
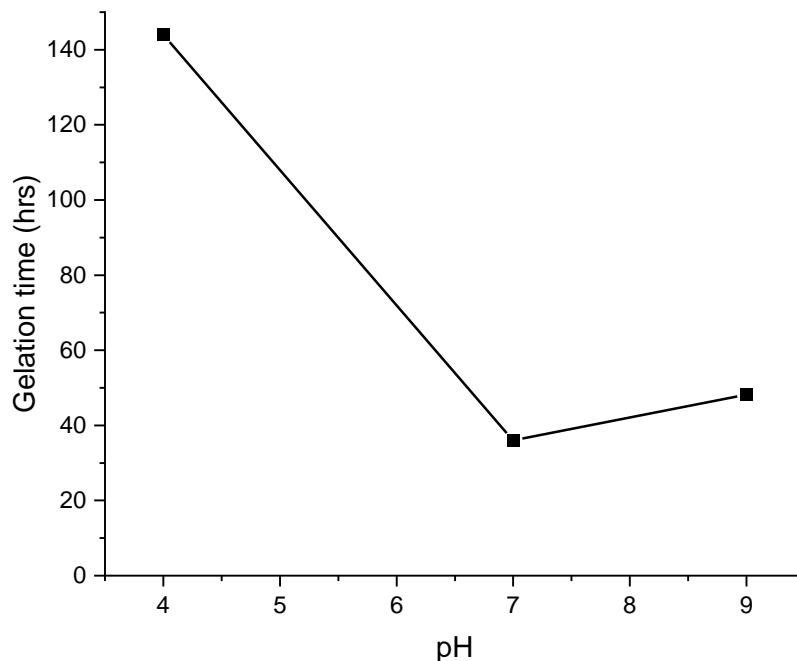
Figure 2.4: Graphical representation of gelation time as a function of different solution pH at a temperature of 30°C [113].

2.2.4 Effect of the presence of metal ion in silica gel

In this section, the effects of incorporating metal ions into the silica framework would be discussed. This is important because the system used in this study will also embed metal nanoparticles in a silica matrix, and metal ions will also be present in the gelation system. Therefore, it is important to assess the effect of dissolved metal ions on gelation. The presence of metal ions in silica gel may have a number of different impacts on the gelation process, and the silica gel's characteristics are produced as a consequence. In the hydrolysis and condensation processes that ultimately result in the production of the silica gel network, the metal ions have the potential to perform the role of catalysts. Consequently, the presence of metal ions may have an effect on the kinetics of the gelation process, which can result in quicker gelation depending on the type and concentration of the metal ions. In addition, the metal ions may interact with the silanol groups located on the silica's surface, which can result in changes to the regional structure of the silica gel. The presence of metal ions, therefore, has the potential to influence the morphology of the silica gel, which may result in differences in the gel's porosity, surface area, and particle size. In general, the influence that metal ions have on the gelation of silica may be rather complicated and is dependent on a wide variety of circumstances. Some of these aspects include the type of metal ion, its concentration, the pH of the system, and the composition of the silica gel.

A typical trend showing the effects of different metal ions on gelation time at different temperatures is shown in Figure 2.5. The figure includes the effect of calcium and magnesium ions on the gelation time, as reported in the literature. Based on the findings of Bansal et al. [114], the rate of formation of silica gel in the presence of effects of metal ions (Mg^{2+} and Ca^{2+}) is shown. The figure indicates that in the absence of metal ions, the gelation time is 156 h when the temperature was 23 °C, and when the temperature was increased to 68 °C, the gelation time was reduced to 7.9 h. When Mg^{2+} was present, the gelation time was 25 hours at 23 °C, and decreased to 1.3 h at 68 °C. When Ca^{2+} was present, the gelation time was 23 h at 23 °C, but decreased to 1.3 h at 68 °C. In summary, the presence of metal ions in the silica matrix results in a reduction in the gelation time, and the combined effect of temperature and metal ions can be used to greatly reduce the gelation time.
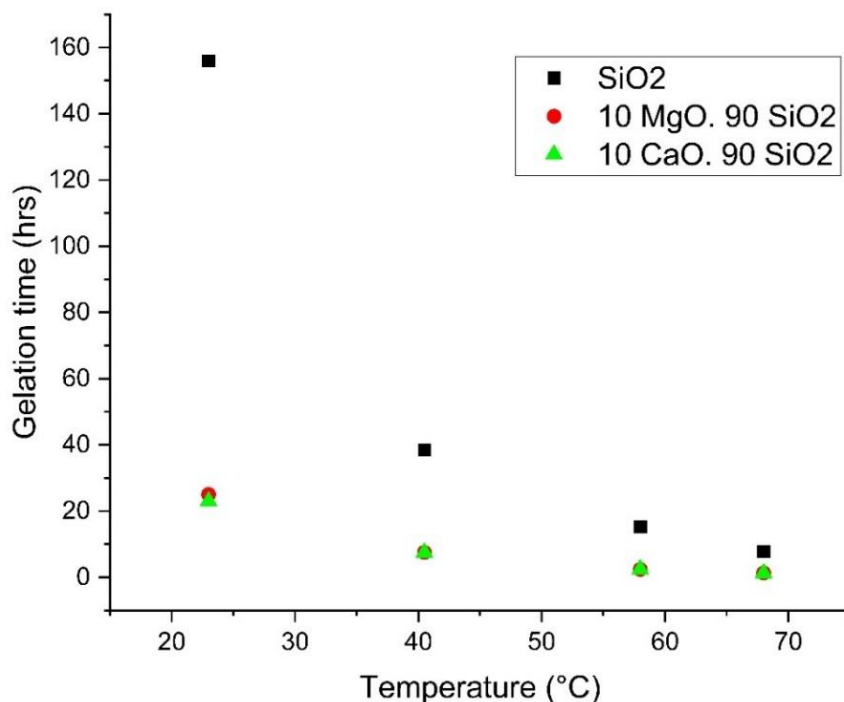
Figure 2.5: Graph showing the effects of gelation time on the temperature in the presence of different metal ions with a solution pH of 4 and 5 [114].

Similar effects were observed in the presence of silver ions in silica, as reported by Li *et al.* [115]. The results presented in this report showed that a gel containing only silica and 0.05% or 0.05% silver ions (Ag^+) required different gelation times as indicated by the change in viscosity as shown in Figure 2.6. In general, gelation is indicated by a sudden increase in viscosity, while the point at which this rapid increase in viscosity is observed in a viscosity-time graph is regarded as the gelation time [103]. In Figure 2.6, a sharp increase in viscosity is set at < 3 cP.

When the criteria for gelation time is used to analyse the data in Figure 2.6, then the increase in the viscosity of the solution can be interpreted as a function of the various silver ion (Ag^+) concentrations and the amount of time. In the absence of silver ions, the gelation time was 145 hours. However, this time significantly decreased to 67 hours and 28 hours when 0.05% and 0.5% silver ions were introduced, respectively.
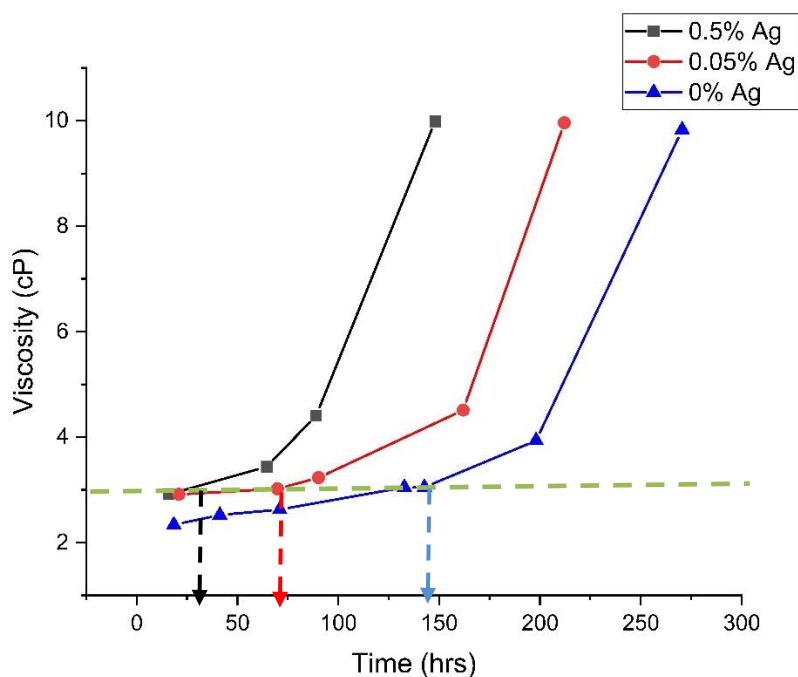
Figure 2.6: Gelation curves for the silica systems with different silver concentrations [115] and this work.

2.3 Synthesis of silver nanoparticle

Since our coating system contains a composite of nanoparticles in silica, since in this section, the methods of preparing colloidal silver nanoparticles, as well as the conditions required to obtain stable nanoparticles are described. This is important because this research involves the incorporation of silver nanoparticles in silica coating for application as a pH sensor. Therefore, here the conditions of synthesizing colloidal silver nanoparticles, including the conditions required to obtain a stable colloidal solution are described. This section covers the available methods that are utilised in the synthesis of silver nanoparticles, including the limitations associated with these techniques. The chemical reduction method, commonly employed in the production of silver nanoparticles, is widely recognised in the literature. This technique entails the reduction of silver ions through the utilisation of a reducing agent. Although many reducing agents have been used in the literature for this purpose, this study will focus on trisodium citrate and sodium borohydride. This is because these are the reducing agents that are also employed in this study.

2.3.1 Employment reducing agents

To synthesise stable silver colloidal silver nanoparticles, the focus has been on two different reducing agents: sodium borohydride and tri-sodium citrate. Here, it will be discussed the reduction process of silver nanoparticles using each reducing agent.

2.3.1.1 Sodium borohydride as a reducing agent

In the synthesis of silver nanoparticles, sodium borohydride ($NaBH_4$) is a strong reducing agent that is frequently used in most studies [116–122]. The solution is usually placed in an ice bath following the addition of $NaBH_4$ to reduce the rate of reduction of silver nitrate [116,117,119,122]. This is important because when sodium borohydride is introduced to the solution, it can quickly react with the silver ions to produce silver nanoparticles by rapidly reducing them. If the reaction takes place too rapidly, it may result in the formation of nanoparticles that are too big or irregular [116–122], which may be unsuitable for many applications. Therefore, it is necessary to regulate the size and shape of the silver nanoparticles during its reaction with the reducing agent by placing the reactants in ice, which helps to slow down the rate of the reaction.

The chemical reaction depicted below illustrates the process of reducing silver nitrate through the utilisation of sodium borohydride:

$$AgNO_3 + NaBH_4 \rightarrow Ag^0 + \tfrac{1}{2}\,H_2 + \tfrac{1}{2}\,B_2H_6 + NaNO_3 \qquad (2.14)$$
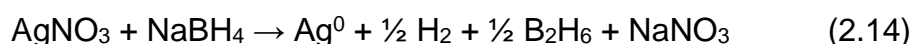
In the literature, it has been reported that reaction time and the concentration of the reducing agent are factors that can influence the stability of silver nanoparticles during its synthesis [89,123,124]. Solomon et al. [89] conducted a study to examine the impact of sodium borohydride concentration on the synthesis of silver nanoparticles through the use of the chemical reduction approach. In their report, silver nitrate ($AgNO_3$) was used as the source of silver. It was reported that the reaction duration and the ratio of the concentration of sodium borohydride to silver nitrate in the solution both affect the stability of silver nanoparticles. It was found a stable colloidal solution could be obtained when the concentration of sodium

borohydride was double that of silver nitrate. Consequently, it was possible to control the size of the silver nanoparticles within the range of 2 nm and 12 nm.

2.3.1.2 Trisodium citrate as reducing agent

Trisodium citrate can also be used during the synthesis of silver nanoparticles. In this case, it serves a dual purpose as a reducing agent and a stabilizer [125,126]. In the literature, trisodium citrate is more active at elevated temperatures due to its thermal decomposition products, such as citric acid, which enhances the reduction of silver nitrate to silver nanoparticles. This also ensures control over the size and homogeneity of the silver nanoparticles that are produced. The heat supplies the activation energy that is essential for the reaction between the citric acid and the silver ions. The chemical reaction employed in the creation of silver nanoparticles utilising trisodium citrate is depicted herein:

$$4Ag^+ + Na_3C_6H_5O_7 + 2H_2O \rightarrow 4Ag^0 + C_6H_8O_7 + 3Na^+ + H^+ + O_2 \qquad (2.15)$$

The synthesis of silver nanoparticles was described by Teruya *et al.* [127], whereby trisodium citrate was employed as the reducing agent. The solution was subjected to heating until it reached its boiling point subsequent to the introduction of the reducing agent, as stated in their report. Consequently, the outcome of this process led to the generation of silver nanoparticles with an average diameter of approximately 100 nm. It was found that the reaction vessel plays a role in the reduction process. A higher particle size (100 nm) was obtained when a beaker was used, but a lower particle size (68 nm) was obtained when a conical flask was used. This is a slightly simplistic explanation, and the most likely difference between the two reaction vessels is the temperature distribution in reaction media. They also reported that the colloidal silver nanoparticle needs to be stored at 4°C in a dark room to prevent from aggregation.

2.3.1.3 Sodium borohydride as a reducing agent and trisodium citrate as a stabilising agent

It is possible to use both sodium borohydride and trisodium citrate during the synthesis of silver nanoparticles. Although this may involve additional cost; however, an improvement in the control over particle size has been reported when both

reducing agent and stabilizer were used in the same system [126,128]. For a solution with sodium borohydride only, the size of the silver nanoparticles was within the range of 2 nm and 12 nm [89]. In contrast, when employing solely trisodium citrate as the reducing agent, the resulting silver nanoparticles exhibited sizes of either 68 nm or 100 nm, dependent upon the specific reaction vessel, as previously described. Therefore, it would be interesting to assess the particle size of silver nanoparticles when both reagents are used in the same system.

Such an approach was taken by Agnihotri *et al.* [126], who assessed the effect of using both sodium borohydride and trisodium citrate during the synthesis of silver nanoparticles. In their report, the precursor was silver nitrate and a particle size ranging within the range of 10 nm and 100 nm was obtained. This result indicates the approach necessary to obtain a particle size between 10 nm and 100 nm, which might be useful for targeted applications.

2.3.2 Preparation of metal nanoparticles using the thermal decomposition method

Thermal decomposition is a chemical technique that involves the breakdown of a chemical compound at high temperatures. This method has been reported in the literature for the synthesis of metal nanoparticles, specifically gold and silver using different corresponding precursors. Despite the relatively less conventional nature of thermal decomposition, its applicability within this context is notable. Notably, investigations into the thermal decomposition of $HAuCl_4 \cdot nH_2O$ and $HAuCl_4 \cdot 3H_2O$ under varying atmospheric conditions, namely air and N_2, have been documented [129,130].

Otto *et al.* [131] conducted an extensive inquiry into the thermal decomposition mechanism of $HAuCl_4 \cdot 3H_2O$ and $AgNO_3$ leading to the formation of Au and Ag respectively. The process was monitored through coupled thermogravimetry differential thermal analysis (TG-DTA), Thermogravimetry/Evolved Gas Analysis-Fourier Transform Infrared (TG/EGA-FTIR), and Evolved Gas Analysis-Mass Spectrometry (EGA-MS) techniques. The characterization of intermediate and final products resulting from thermal decomposition was conducted through ex-situ X-ray diffraction (XRD) and Fourier Transform Infrared (FTIR) methodologies.

For gold nanoparticles, the thermal decomposition of $HAuCl_4 \cdot 3H_2O$ ensued in sequential steps, with $AuCl_3$ emerging as the primary solid product following the initial decomposition at 190 °C. Subsequently, at 240 °C, AuCl which further decomposed to yield the final product Au at 320 °C, as shown in equation 2.16 and 2.17 respectively [131]. Conversely, the thermal decomposition of $AgNO_3$ initiated a melting phase at 360 °C, with the solid intermediate decomposition product containing $AgNO_3$ and trace constituents of an unidentified phase, evident upon heating to 450 °C and subsequent cooling to ambient temperature. While conjecture regarding the presence of an intermediate product persists, proposals within the literature suggest the formation of $(Ag_2O)_3 \cdot AgNO_3$. The ultimate product of thermal decomposition, regardless of atmospheric conditions, is Ag, attained at 600 °C, as shown in equation 2.18 [131].

$$HAuCl_4.3H_2O_{(l)} \rightarrow HAuCl_2(OH)_{2(s)} + 2\ HCl_{(g)} + H_2O(g) \qquad (2.16)$$

$$HAuCl_2(OH)_{2(s)} \rightarrow\ Au_{(s)} + 2\ HCl_{(g)} + \tfrac{1}{2}\ H_2O_{(g)} + \tfrac{3}{4}\ O_{2(g)} \qquad (2.17)$$

$$2AgNO_{3(l)} \rightarrow 2Ag_{(s)} + NO_{2(g)} + NO_{(g)} + 1.5O_{2(g)} \qquad (2.18)$$
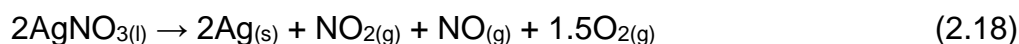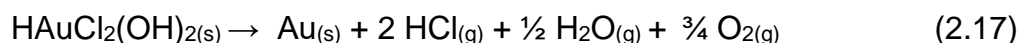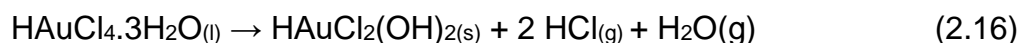
In the existing literature, attention has been given to research supporting the proposed theory. However, Su *et al.* [90] conducted a study wherein metal nanoparticles were synthesized through thermal treatment via chemical decomposition, utilizing Chloroauric acid ($HAuCl_4$) to synthesize gold nanoparticles within a silica matrix. The thermal treatment was conducted at 200 °C, without the inclusion of any reducing agent to facilitate the formation of gold nanoparticles. Notably, the preparation of the silica coating required Tetraethyl orthosilicate (TEOS), ethanol, and water, typically necessitating a heat treatment temperature range of 70 to 100 °C [132–135]. The decision to employ a higher temperature of 200 °C was aimed at facilitating the chemical decomposition of $HAuCl_4$ to form gold (Au) nanoparticles. However, in their research, $HAuCl_4$ was introduced into the solution to achieve the desired Au/silica coating. The presence of gold nanoparticles was confirmed through the analysis of absorption spectra obtained via UV-Vis spectrophotometry. Similarly, palladium nanoparticles were reported to form from Palladium(II) chloride ($PdCl_2$) during heat treatment via chemical decomposition [90].

Furthermore, Li *et al.* [136] presented findings supporting the chemical decomposition theory, demonstrating the formation of silver nanoparticles through the decomposition of silver nitrate ($AgNO_3$) under similar heat treatment conditions for the preparation of Ag/silica coating. In their methodology, $AgNO_3$ was added to the solution containing TEOS, ethanol, and water, followed by heat treatment at 200 °C to facilitate the formation of silver within the silica matrix. Additionally, X-ray photoelectron spectroscopy (XPS) spectra and UV-Vis spectrophotometry absorption spectra were employed in their research to confirm the presence of silver within the silica coating.

2.3.3 Stability of silver nanoparticle

It is also important that the nanoparticles are stable once they are formed, otherwise the properties of the sensor will change with time. Badi'ah et al. [137] used sodium borohydride ($NaBH_4$) as a reducing agent and silver nitrate ($AgNO_3$) as a silver salt in order to synthesise silver nanoparticles. Their study involved the use of different concentrations of $AgNO_3$ for the synthesis of silver nanoparticles. In their report, the stability of the silver nanoparticles was observed for 70 days [137] and the size distribution of the silver nanoparticles changed as a function of time. On the first day, the size of silver nanoparticles was observed to be 36.74 nm, this eventually increased to 162.7 nm after 70 days. These findings are in agreement with the report of Baset et al. [138], who also observed an increase in the size of the silver nanoparticles from 4.1 nm on the first day to 8.1 nm on the tenth day. According to these studies, colloidal silver nanoparticles are stable when maintained at a temperature of 4°C compared to room temperature, where they are more likely to agglomerate. The ability of the particles to aggregate, forming larger particles increases at temperatures greater than room temperature. Therefore, the incorporated metal nanoparticles can aggregate even within a composite which needs to be understood and monitored.

2.4 Optical properties of silver nanoparticle

The pH sensitivity of optical sensors would be derived from the optical properties. This section covers significant discussions relating to the optical characteristics of silver nanoparticles, specifically focusing on its features of localised surface plasmon

resonance (LSPR) and the factors that influence these properties. The optical properties shown by silver nanoparticles are a result of the interaction between light and the valence electrons located on the surface of these nanoparticles [79]. This makes them quite useful for different applications such as: sensors for some applications such as pH measurement and imaging tools. The ability of silver nanoparticles to absorb and scatter light is one of the most important optical features that these particles possess. The optical behaviour of silver nanoparticles is influenced by their size, shape, and chemical composition, which determine their ability to absorb and scatter incident light. These two characteristics become more prominent as the size of the nanoparticle decreases, which ultimately causes a change in the wavelength at which the surface plasmon resonance is observed [77,139]. It has been reported that silver nanoparticles have distinct optical features, such as the ability to absorb and scatter light, as well as the localised surface plasmon resonance (LSPR) property. These properties can be controlled by manipulating the size, shape, and composition of the nanoparticles, which makes it quite suitable for a wide range of sensing and imaging applications.

2.4.1 Localised surface plasmon resonance

Localised Surface plasmon resonance (LSPR) arises from the interaction between metal particles, their surface electrons, and incident light when in proximity to the nanoparticle, as depicted in Figure 2.7. It results from the synchronized oscillation of valence electrons on the metal's surface induced by the interaction with light. As light passes through the nanoparticles, they absorb energy leading to excitation and the generation of an electric field. This phenomenon occurs at a specific wavelength of light, resulting in the absorption of incident photons. Metals such as gold, silver, and palladium have been documented to exhibit LSPR properties [139,140].
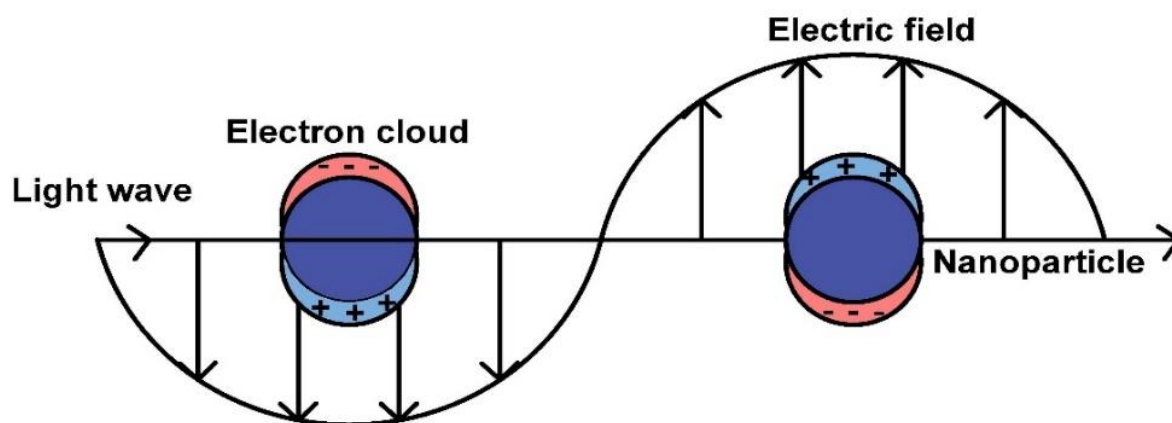
Figure 2.7: Schematic representation of localised surface plasmon resonance property of metal nanoparticle when light is transmitted through it, resulting in an electric field due to excitation of nanoparticle [141].

In addition, when the interaction of metal nanoparticles with light is assessed with a UV-Vis spectrophotometer, the nanoparticles are observed to absorb light of a specific wavelength characteristic of the metal nanoparticle. The extinction coefficient results from the combined coefficient of absorption and scattering coefficient. This results in an extinction peak, which may be attributed to the LSPR property of the nanoparticles in the solution or coating. For instance, gold nanoparticles have been reported to have an extinction peak at a wavelength of 525 nm [82,83,140,142]; however, other studies have reported an extinction band of 400 nm for silver nanoparticles [87,143,144]. In addition, it is also possible that the extinction peak could be shifted to other wavelengths when the particle size and shape change [87,125,145–147]. It has been reported that these changes have a significant effect on the light absorption characteristics of the nanoparticle including the wavelength of extinction [45,46]. The smaller size silver nanoparticles (10–50 nm) have been reported to have an extinction peak at 400 nm, but the larger silver size of nanoparticles (100–220 nm) have also been observed to have a wider peak at longer wavelengths near 500 nm [87,148].

Furthermore, the LSPR band is highly sensitive to the surrounding medium [79,140,149], this is a crucial factor when considering its application as a sensor. At the moment, research is being carried out to assess the sensitivity of different LSPR based sensors such as: pH sensors [81,82,150], temperature sensors [75], pressure

sensors [78], and oxygen sensors [150,151], among others. Although these sensors have been reported to be effective for their respective applications, there has been a dearth of information regarding the reproducibility, durability, and limitations associated with their usage. Therefore, in this research, it would be interesting to explore these properties of silver nanoparticles for potential application as a sensor, which is expected to be used for the measurement of pH at high temperatures and high-pressure conditions usually observed in some oil wells. Therefore, the metal nanoparticles embedded in silica matrix, which is the main strategy employed to achieve this target is hereby described.

2.5 Modification of optical properties of metal nanoparticles in silica

This section assesses the various modifications of metal nanoparticles in silica matrix as a sensor for pH measurement. The two important modifications include the incorporation of metal nanoparticles in the silica matrix and the use of dye-doped silica. The effectiveness of metal nanoparticles embedded in silica for different applications such as measurement of pH, temperature, and oxygen level among others has been studied extensively in different literatures. However, this section will focus on different modifications to silica coating for the purpose of using it as a sensor for pH measurement.

One important factor that has been exploited for such application includes the surface charge of the metal nanoparticles when they are embedded in a silica matrix. The determination of the surface charge of nanoparticles plays a critical role in ensuring the stability of sensors, as it directly influences their unique optical, electrical, and catalytic characteristics. In the literature, there are different studies where metal nanoparticles such as gold [81,82,84,152], silver [153–155] and palladium [81,82] nanoparticles (Np) have been embedded in silica for different applications. In this case, the metal particles serve as nucleation centres for the condensation of silicic acids, which are products of hydrolysis and condensation of tetraethyl orthosilicate (TEOS) in a mixture of an alkaline solution of alcohol and water [156].

Metal nanoparticles are incorporated into silica by the reaction of the metal and silica precursors, which first results in the formation of a gel, which then forms a coating after thermal treatment. A schematic representation of silver nanoparticles embedded in a silica matrix is shown in Figure 2.8, where the silica forms a shell around the metal nanoparticles, forming a core-shell (CS) structure.
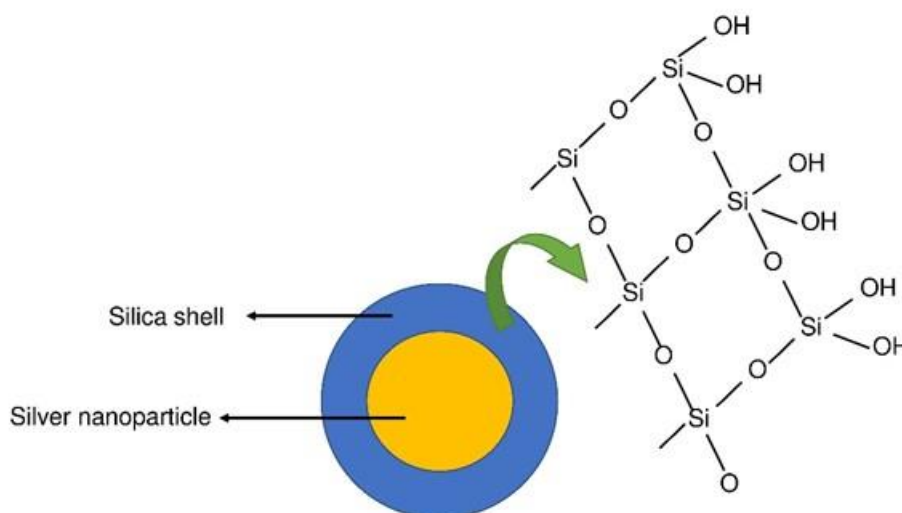
Figure 2.8: Schematic representation of a metal nanoparticle embedded in a silica matrix forming a core-shell structure [156].

Metal nanoparticles embedded in silica offer a higher surface charge compared to a matrix with silica coating only [157,158]. The higher surface charge might enhance the reproducibility of the sensor, which is highly desirable in pH measurement. The increased surface charge is a result of the presence of silanol (-Si-OH) groups on the surface of the silica matrix, which causes the metal nanoparticles to have a negative surface charge. In water, these groups disintegrate into silicate ions (-SiO$_2$), which can adsorb onto the metal nanoparticle's surface and give it a negative charge [60]. The surface charge of metal nanoparticles implanted in silica can also be significantly affected by the pH and ionic strength of the surrounding environment. Deprotonation of surface groups on the nanoparticle can occur at higher pH levels, resulting in a greater negative surface charge [157,159].

Behrens *et al.* [157] analysed the surface charge of silica at different pH using a theoretical model. The results of their findings are shown in Figure 2.9, which indicates that at pH 3 and 9.2, the charge densities were 0 and -55 mC/m^2,

respectively. Also, Wang *et al.* [83] observed that the surface charge densities of gold embedded in silica at pH 2 and 12 were 0 and -300 mC/m^2 respectively. The observed higher charge densities at elevated pH levels have been documented as a direct outcome of heightened protonation/deprotonation processes occurring on the surface of the particles. This leads to the establishment of an electrical double layer influencing the charged particles [159]. On the other hand, Wang *et al.* [158] used a theoretical model to predict the surface charge of gold nanoparticles embedded in silica. At pH 9, the surface charge density of silica is -55 mC/m^2, but the surface charge density of gold-embedded silica is around -150 mC/m^2, which is about three times more than the charge density of just silica coating only, as shown in Figure 2.9. This suggests that the presence of metal nanoparticles embedded in silica forming a core-shell structure type structure, could result in an increase in the surface charge.
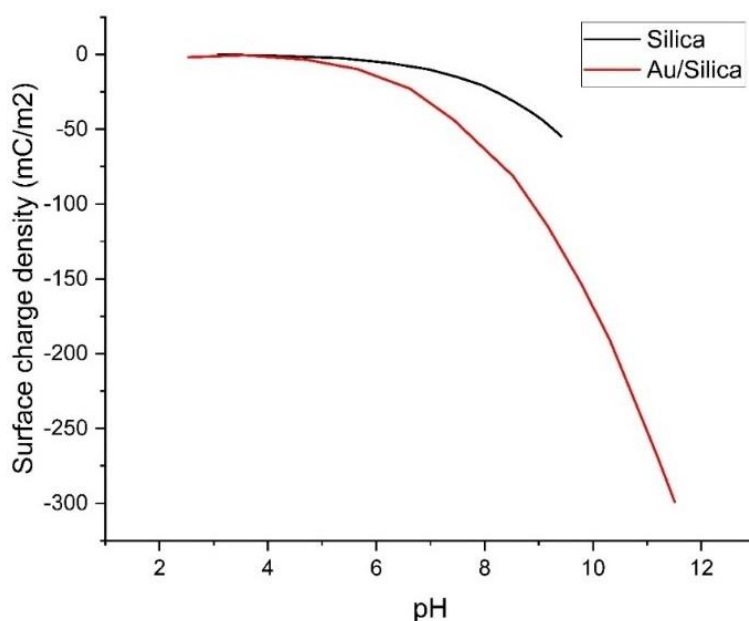
Figure 2.9: Comparison of charge density of silica coating [157] and gold nanoparticle embedded in silica matrix [158].

Changes in the optical properties of some dyes that have been doped in silica for use as a sensor for pH measurement can also provide additional information [82,84,160,161]. For example, Miled *et al.* [160] doped bromothymol blue in silica to form a coating that could be used for pH measurement. Similar work was carried out by Butler *et al.* [161].

Miled *et al.* [160] reported the use of an optical fibre in which the cladding and coating were removed in the middle section of the fibre. They prepared a film of doped bromothymol blue (BTB) in silica on the etched area of the fibre. After coating, the optical fibre was connected to a light source and a detector, and this coated area was immersed in various pH solutions. The films were found to be sensitive to pH changes between pH 2 and 5, leading to alterations in the intensity of light with changes in the pH of the solution. Although the authors reported an optical response with these modified coatings, there is no information on sensitivity in different chemical environments. Moreover, bromothymol blue (BTB) has a working range of pH between 2 and 5; hence, the sensitivity of the measurement may likely be limited to this range. Additionally, David *et al.* [162] described a fluorescence-based pH sensor using α-naphthol phthalein embedded in silica for pH measurement. According to the authors, the sensor could measure the pH of solutions between 4 and 11.

Each sensor was only tested at room temperature and under a single chemical condition, there was no information about the stability or reproducibility of the sensor. In addition, no dye-based silica pH sensor was reported for use under conditions of high temperature and pressures. However, there was some information regarding the stability of metal nanoparticles encapsulated in silica, which will be discussed in the following section.

2.5.1 Stability of metal nanoparticles in silica matrix

In the literature, it has been shown that the stability of silica may be improved by the addition of metal nanoparticles [84,154,163,164]. This is achieved by preventing agglomeration or particle aggregation, which contributes to improvement in the stability of silica. Due to the high surface energy of the silica particles, preventing the development of agglomerates is a typical issue that is usually observed during the synthesis of silica. The process of agglomeration can lead to an enlargement in particle size and a reduction in the specific surface area of the material, which can negatively impact its properties. Metal nanoparticles are utilised as nucleation sites

during the creation of silica. These nanoparticles function as physical barriers between individual silica particles, hence impeding agglomeration.

In a typical study to assess the effect of metal nanoparticles in a silica matrix, the presence of metal nanoparticles may also result in improved resistance to mechanical stress. For example, Bai *et al.* [163] reported that the introduction of zinc doped to silica matrix increased the hardness and strength of the resulting matrix and further boosted the material's stability when subjected to mechanical stress. A similar observation was reported by Aati *et al.* [154], who observed that silver doped in a silica matrix significantly improved the hardness and strength of the matrix. Also, Lu *et al.* [84] reported that the presence of gold nanoparticle in silica improve the stability of coating, which offered a better optical response and is a good choice for pH sensitivity.

The stability of metal nanoparticles embedded in silica has also been experimentally studied. For instance, Masoud *et al.* [165] investigated the thermal stability of gold nanoparticles embedded in silica coating at various temperatures. The results revealed that gold nanoparticle (AuNp) embedded in silica remained stable up to 500 °C, as presented in Table 2.2. The size of the gold nanoparticles was measured using Transmission Electron Microscopes (TEM). Although gold nanoparticles embedded in silica showed minimal particle growth, with an increase of only 2.78% observed at 500 °C, the particle size changed rapidly when the temperature was raised further to 600 °C.

Table 2.2: Particle size of Au on SiO_2 at different temperatures [165]

Condition	Au in SiO_2	AuNp growth (%)
As prepared	3.6 ± 0.9 nm	-
500 °C	3.7 ± 0.9 nm	2.78
600 °C	4.1 ± 1.2 nm	13.89
700 °C	6.5 ± 2.1 nm	80.56

The thermal stability of silver nanoparticles doped in silica was studied by Gould *et al.* [166]. In their report, silver nanoparticles were thermally treated at different temperatures ranging from room temperature to 900 °C and observed in a transmission electron microscope (TEM) to examine the changes in size and shape. Their data show (Figure 2.10 a to d) that morphological changes are usually not expected at temperatures below 800 °C. However, it was shown that if the temperature is increased beyond this threshold, surface indentations occur, and with further heating (T > 900 °C), the size and shape of the embedded nanoparticle can be distorted, as shown in Figure 2.10.
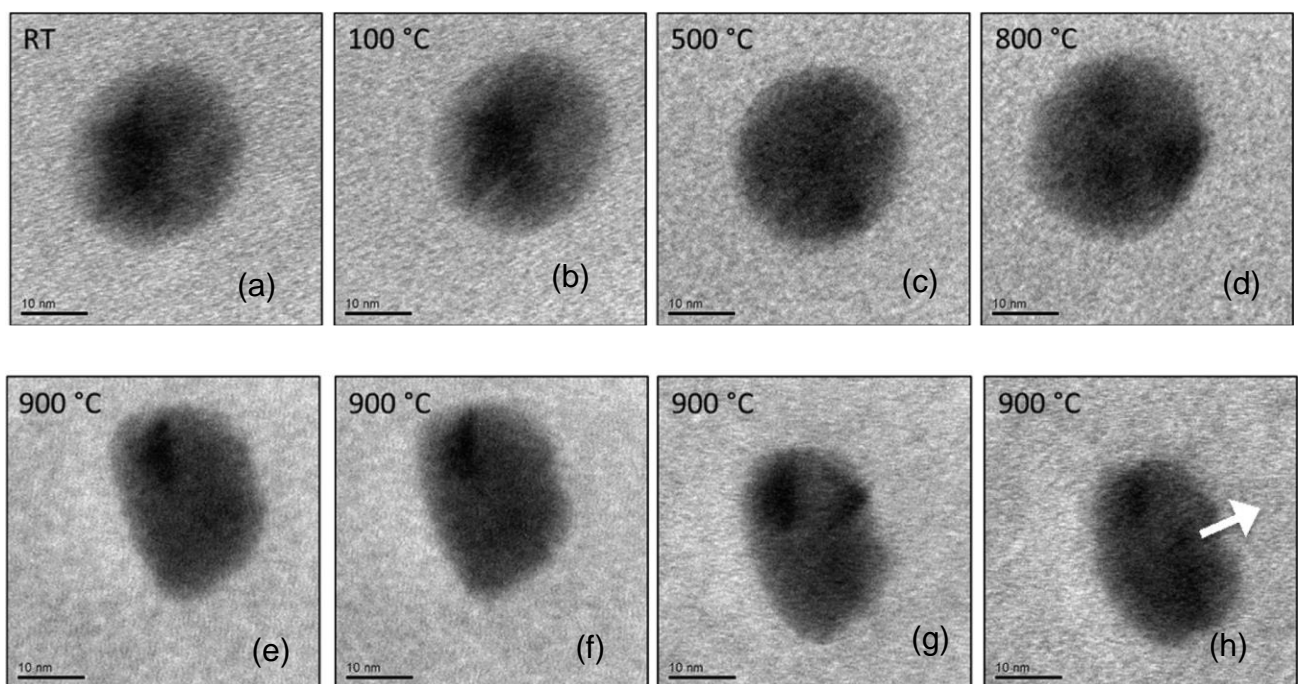
Figure 2.10: TEM images showing the shapes of silver nanoparticles embedded in silica at different temperatures ranging from room temperature up to 800 °C (a-d) and size deformation at 900 °C (e to f) [166].

2.6 Coating methodologies

Since the properties of the metal nanoparticles embedded in silica may also affected by the method of application on the substrate, the different application techniques and the corresponding effects on the properties of the coating are hereby discussed. The deposition of sol-gel films can either be carried out by spraying, dip coating or spinning [35], as shown in Figure 2.11.
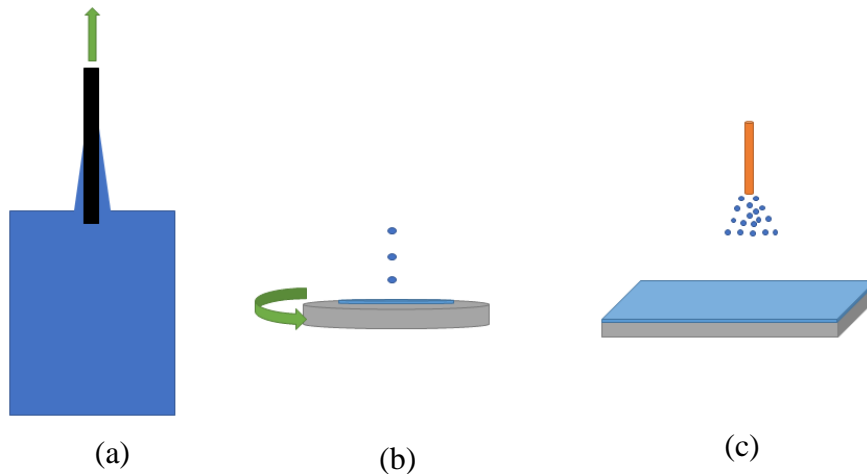
Figure 2.11: Methods of coating deposition on a substrate (a) dip coating (b) spin coating, and (c) spray coating.

Spin coating involves the deposition of thin films of uniform thickness onto a flat surface. In most cases, a minuscule amount of coating material is applied at the centre of the substrate, which is either at rest or spinning at a slow speed. Then, the substrate is spun at rates of up to 10,000 revolutions per minute so that the centrifugal force distributes the coating material over the entire surface. As the substrate rotates, the excess liquid is spun off the edges. This process is continued until the film reaches the required thickness. In most cases, the solvent that is administered is volatile and will concurrently evaporate during the process until a gel is formed. The film may be made thinner by increasing the rotation speed at which it is spun [106,167]. Other properties such as viscosity, concentration, as well as the volatility of the solvent can also influence the thickness of the film. Even though this method has been quite promising in terms of uniformity for flat surfaces, it may not be suitable for substrates that do not have a flat surface, such as optical fibre.

The second method involves dipping the substrate in a solution, followed by a drying process at room temperature. The dip coating technique involves five steps, which includes: immersion, withdrawal, deposition, drainage, and evaporation. Immersion is the first step, where the substrate is submerged at a constant speed in the solution containing the coating. This is followed by withdrawal, where the substrate is removed from the solution. This is accompanied by deposition, where the coating is observed to adhere to the substrate. At this point, the quality of deposits is dependent on the rate of withdrawal. A rapid withdrawal would result in an increased

thickness of the coating on the substrate [168]. The next step is drainage, where the excess liquid on the substrate will flow back into the solution due to gravity. The final step involves evaporation, where a thin layer is formed when the solvent separates from the substrate. The entire steps are shown in Figure 2.12.
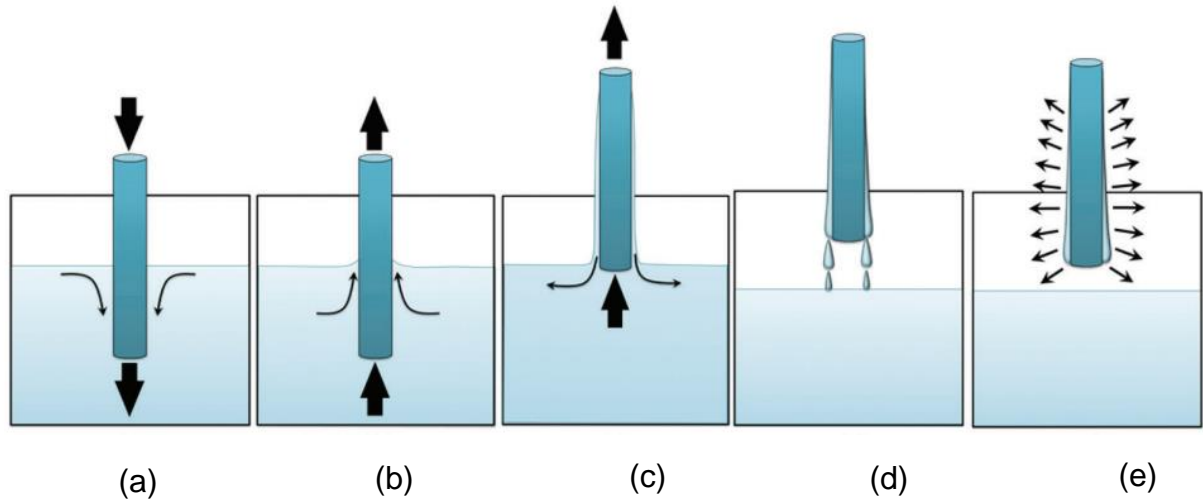
Figure 2.12: The schematic illustration showing the five dip-coating steps: (a) immersion, (b) withdrawal, (c) deposition, (d) drainage, and (e) evaporation [96,169].

In this study, the dip coating method was preferred because it can be easily carried out in the laboratory for both glass slides and optical fibres, and it results in high-quality films compared to the other deposition methods. The speed of deposition plays a crucial role in sol-gel synthesis since it significantly influences the coating's thickness, density, and porosity [167,168,170]. For dip coating, the thickness can also be improved by dipping the substrate multiple times, as shown in Figure 2.13. Therefore, synthesis conditions, withdrawal speed, and the number of dips are key parameters that affect the thickness of the deposits on the substrate. However, the limitation of the dip coating method is that the coating is not always uniform, and it is usually thin [106]. Nevertheless, it is quite suitable for application on optical fibres since it can be used for complex shapes. The effectiveness of this technique on optical fibres are hereby described in the next section.
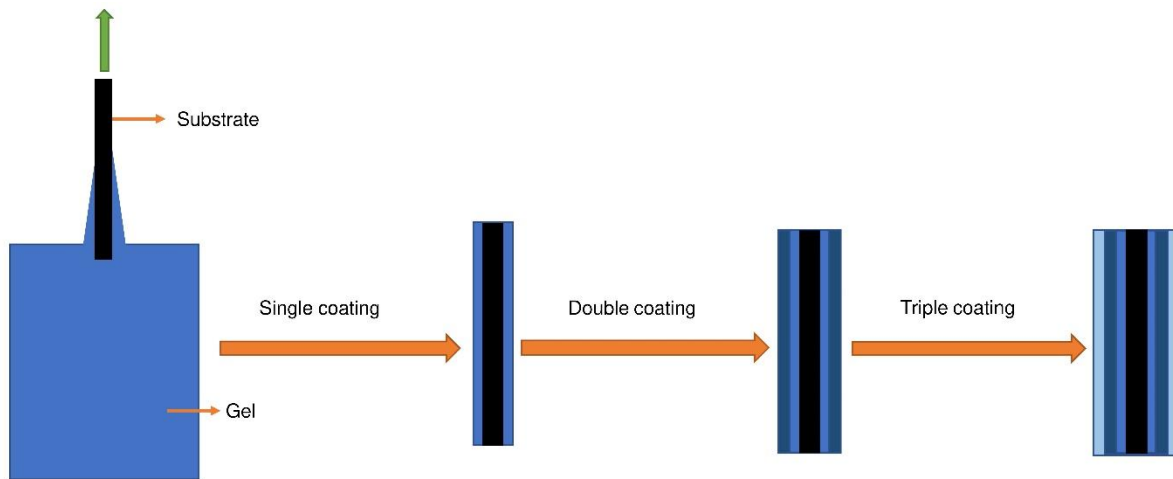
Figure 2.13: Schematic representation of multiple dip-coating method.

2.7 Preparation methods of optical fibres as sensors for pH measurement

Although there are several reports on the fabrication of sensors from optical fibres for various applications, only optical fibre sensors for pH measurement are discussed in this section. This is motivated by the search for a sensor that could measure pH with high precision and accuracy in real-time under high temperature and high-pressure conditions usually encountered in oil wells.

Preliminary measures are necessary prior to the application of the coating onto the optical fibre. Initially, it should be noted that the application of the coating to the core of the optical fibre necessitates the removal of the first two layers, namely the coating and cladding, which collectively constitute the optical fibre. This will facilitate the interaction between light and the coating located in the core of the optical fibre, enabling the evaluation of pH levels in challenging environments characterised by elevated temperature and pressure. The steps involved in the preparation of the optical fibre prior to the application of the coating are shown in Figure 2.14.

Etch the optical fibre of coating and cladding upto the core at the middle part of fibre

Replace the etched area of optical fibre with silica based coating

Using dye or fluorescence doped silica coating

Using metal nanoparticle embedded in silica coating

Connect the coated optical fibre with light source and UV-Vis spectrophotometer

The coated part of optical fibre is dipped in the test solution for the experiement

Record the intensity of light/absorbance/transmitence with change of pH

Figure 2.14: Steps involved in the preparation of silica-based optical fibre as a pH sensor.

The first step involves etching the polymeric coating and cladding to expose the optical fibre's core. This is significant because a small quantity of light may escape from the inner part of the optical fibre, and the resulting effect may determine the efficacy of the intended application. Several methods for etching optical fibre are investigated in the research literature. The majority of researchers [81,82,84,171] employed hydrofluoric acid (HF) for etching optical fibre, which is a highly effective chemical for etching optical fibre quickly. However, HF is a highly toxic and hazardous chemical, and not all laboratories or environments are suitable for its use. Bashir *et al.* [172] reported that it is possible to etch the optical fibre using sodium hydroxide (NaOH) and potassium hydroxide (KOH). The rate of etching was faster when the concentration of the NaOH or KOH, as well as the reaction temperature were increased. After removing the cladding and coating from the core of the optical fibre, the silica-based coating was applied to the core, where the cladding and original polymeric coating were removed.

The development of the replacement coating typically involves the creation of a gel through the sol-gel process. To initiate this process, a solution is initially prepared by mixing the required components, after which a gel forms. Once the gel has been created, the etched optical fibre is dipped into the gel using the dip-coating method. This is followed by a heat treatment process to complete the preparation of silica coating on the optical fibre. The coated optical fibre was consequently connected to the light source and UV-Vis spectrophotometer. After the connection was made, the coated section of the optical fibre was submerged in the test solution, and the pH was adjusted. The experiment measured the pH-dependent variations in light intensity, light absorption, and light transmission. When the light was transmitted through the optical fibre, some light leaked through the etched region of the core. It was found that the intensity of light, properties of silica coating, and the pH of the solution interacted to alter the overall transmitted light, which meant that the system could be used as a sensor.

2.7.1 pH sensing mechanism using optical fibre

The tetrahedral configuration of silica materials is defined by a silicon atom enveloped by four oxygen atoms. Interconnections among silicon atoms are facilitated by oxygen bridges, commonly referred to as siloxane groups or bridges [173]. Regardless of whether silica manifests in a crystalline or amorphous state, its surface comprises silicon and oxygen atoms. Owing to the robust nature of the Si–O bond, silica displays comparatively low reactivity [174,175]. Surface atoms tend to adopt a tetrahedral arrangement due to surplus energy, thereby saturating their free valence with OH groups. The generation of surface silanol groups can occur through two primary mechanisms. In this particular context, the reaction between silica and adsorbed water molecules proceeds gradually, leading to the formation of hydroxide groups on the silica surface. The properties of all silica materials are significantly shaped by the chemistry of silanol groups, their coverage, and the porosity of the silica structure [176,177].

In acidic environments, characterised by a surplus of hydrogen ions (H^+), the surface chemistry of the silica coating undergoes a transformative process known as protonation. This chemical reaction involves the interaction between hydrogen ions

and the Si-OH functional groups present on the silica surface. Specifically, the Si-OH groups gain a proton (H^+), leading to the formation of positively charged species, denoted as $SiOH_2^+$. This phenomenon is encapsulated by the reversible equilibrium reaction [177–179]:

$$SiOH + H^+ \rightleftharpoons SiOH_2^+ \tag{2.19}$$

The acquisition of a positive charge by the silica surface at acidic pH values signifies a shift in its electrostatic properties, thereby influencing its interaction with ions present in the surrounding solution. Conversely, in alkaline conditions characterized by an excess of hydroxide ions (OH^-), the surface chemistry of the silica coating undergoes deprotonation. This process involves the removal of a proton (H^+) from the Si-OH groups, facilitated by the presence of hydroxide ions. The resultant reaction leads to the formation of negatively charged species, represented by SiO^-, accompanied by the liberation of water molecules (H_2O). The chemical equation representing this transformation is given in equation 2.20 [177–179]. The emergence of a negative charge on the silica surface under alkaline conditions signifies a distinct shift in its surface electrochemistry, thereby modulating its interaction with ions in the surrounding environment.

$$SiOH + OH^- \rightleftharpoons SiO^- + H_2O \tag{2.20}$$

The dynamic surface charge behaviour of the silica coating, as modulated by pH-induced chemical reactions, interacts with the presence of silver nanoparticles embedded within the silica matrix. At low pH values, where the silica surface is positively charged due to protonation, the presence of silver nanoparticles accentuates the adsorption of anions from the surrounding solution onto the coating's surface. This phenomenon is attributed to the electrostatic attraction between the positively charged silica surface and the negatively charged ions in the solution. Conversely, under alkaline conditions, the negatively charged silica surface, resulting from deprotonation, exhibits enhanced adsorption of cations from the solution, facilitated by the presence of silver nanoparticles. This adsorption-induced modification in the local refractive index of the coating is instrumental in influencing its optical response, as detected through techniques such as total internal reflection. A schematic representation illustrating the process of ion adsorption onto the optical

67

fibre under varying pH conditions within the solution, as delineated in Figure 2.15, is presented herein.

The reaction in acidic solution : $SiOH + H^+ \leftrightarrow SiOH_2^+$

a)

Light

Core   Cladding   Coating

OH_2^+ OH_2^+
      Si   Si
OH_2^+ Si OH_2^+
      Si
         AgNp   Si—OH_2^+
OH_2^+—Si   Silica   Si—OH_2^+
      Si   Si
OH_2^+ OH_2^+

– Adsorption of negatively charged ion

The reaction in alkaline solution : $SiOH + OH^- \leftrightarrow SiO^- + H_2O$

b)

Light

Core   Cladding   Coating

O^- O^-
      Si   Si
         Si O^-
O^- Si
         AgNp   Si—O^-
O^-—Si   Silica   Si—O^-
      Si   Si
O^- O^-

+ Adsorption of positively charged ion

Figure 2.15: Schematic diagram of surface charge on the optical fibre in (a) acidic solution in the presence of proton (H^+) and (b) alkaline solution in the presence of hydroxyl ions (OH^-).

Moving forward, further exploration into the mechanistic aspects of surface charge dynamics, coupled with advancements in nanomaterial synthesis and characterisation techniques, holds the promise of unlocking novel functionalities and applications for silver nanoparticle-embedded silica coatings. By monitoring the

optical response of the coated optical fibre, which is correlated with the change in refractive index, the pH of the solution can be determined.

2.7.2 State of the art in pH measurement using optical fibres

In 2015, Su and co-researchers [82] were the first to report that optical fibre coated with silica and gold nanoparticles (AuNp) could be used to measure the pH of solutions. In their report, silica and gold nanoparticles were embedded in silica and used to determine the pH of solutions at 80 °C. The initial step in the production of the optical pH sensor involved the formulation of a coating solution using the sol-gel technique. The solution was prepared by mixing the chemicals of chloroauric acid ($HAuCl_4$) as a precursor of gold nanoparticle (Au) and tetraethoxysilane (TEOS) as the precursor of silica, ethanol and deionized water. The mixture was agitated for one hour at 60°C to form the gel. Hydrofluoric acid (HF) solution for 50 minutes for the etching of the optical fibre. Then, the etched optical fibre was dipped into the gel and then heat treated for 45 minutes at the temperature of 200 °C. Subsequently, a light source and detector (UV-visible spectrophotometer) were affixed to the optical fibre coated with silica, as depicted in Figure 2.16. The optical fibre that had been coated was immersed in the test solution, wherein the pH was adjusted as part of the experimental procedure, and the spectra of transmission wavelengths were then documented.
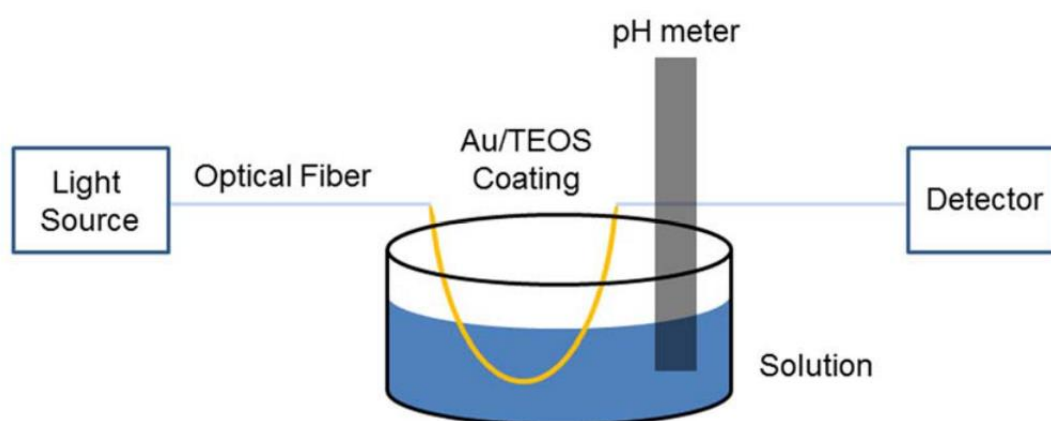
Figure 2.16: Schematic illustration of the experimental setup for pH measurement using gold embedded in silica coating on optical fibre [82].

The results reported by Su *et al.* [82] are reproduced in Figure 2.17. This suggests that the AuNp/silica coating had an absorption band around 525-560 nm. Also, it was observed that the percentage transmittance (%T) decreased as the pH of the solution increased. The experiment was conducted within the pH range of 3 to 11. At the wavelength of 525 nm, the highest transmittance was observed at an acidic pH. Conversely, the transmittance decreased as the pH increased to 11. However, only the change in percentage transmittance (%T) at the wavelength of 525 nm was considered, while the percentage transmittance (%T) at other wavelengths was ignored.
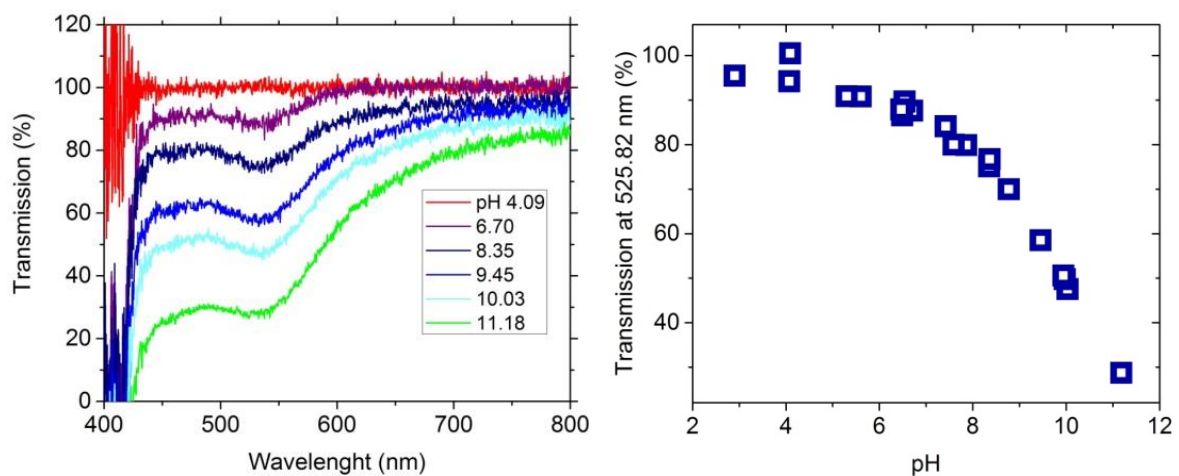
Figure 2.17: (a) Transmission curve at different pH using Au/silica coated optical fibre, (b) The transmittance at the peak plasmon absorption band wavelength as a function of solution pH [82].

In another study carried out by the same research group, Wang *et al.* [158] reported that there was neither an absorption band nor any optical response associated with a change in pH when only silica was used as the coating, as shown in Figure 2.18. Hence, they concluded that the surface plasmon resonance property of gold nanoparticles solely caused the change in absorbance and optical response with a change in pH.
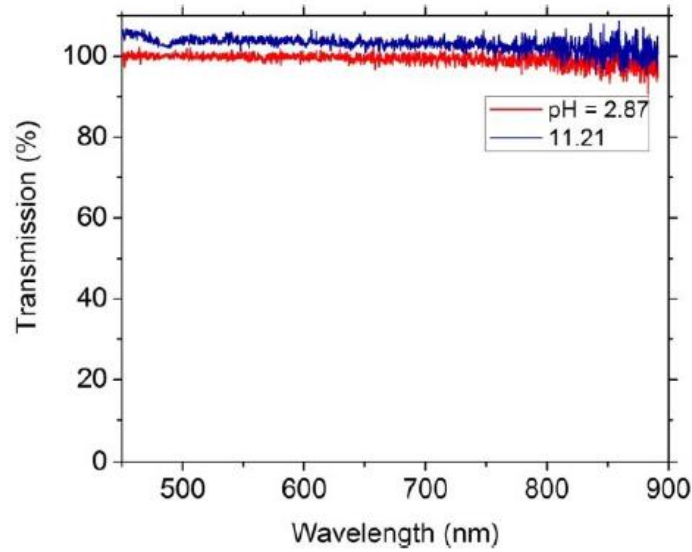
Figure 2.18: Transmission curve at different pH using only silica coated optical fibre [158], showing no change in transmission (%T) of light.

However, this result contradicts the findings of Lu *et al.*[180] , who observed that the LSPR property is not as a result of the metal nanoparticle but silica, as shown in Figure 2.19. Lu *et al.* [180] found that silica coating exhibited an optical response with a change in pH. Lu also tested the response of silica coated optical fibre as well as AuNp-silica coating in their report. The AuNp-silica coated optical fibre showed a greater response with pH compared to the previous result, which only indicated the change in transmittance at different pH. Therefore, it was concluded that the presence of gold nanoparticles improved the stability, sensitivity, and lifetime of the silica coated optical fibre, as shown in Figure 2.19.
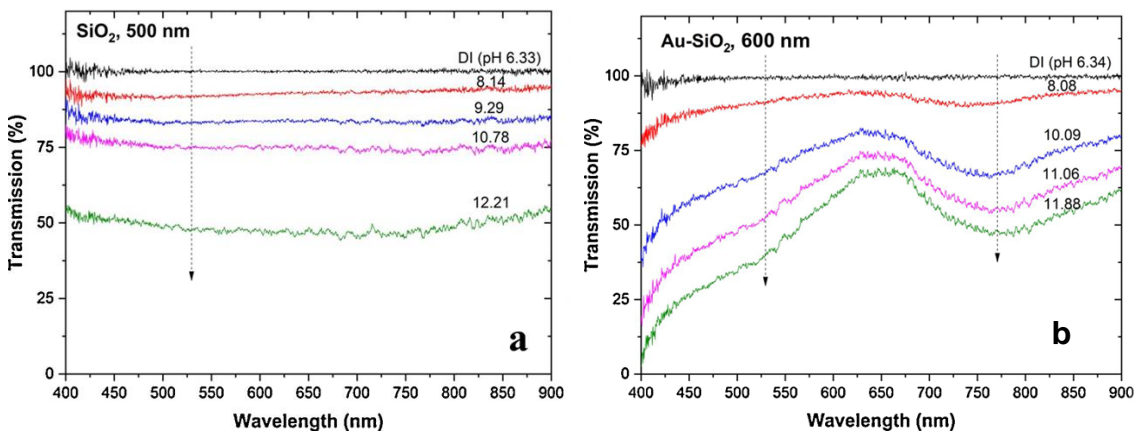
Figure 2.19: Transmission curve with change in pH using (a) silica coating and (b) Au/silica coated optical fibre [180].

Wang *et al.* [158] also reported pH data at 80 °C, there is a shift in the optical response of optical fibre when subjected to a higher temperature. The transmittance was recorded at 550 nm, and the data were normalized between 0 and 1, as shown in Figure 2.20. The experiment was performed with a pH of 2.15 to 7.65. A high transmittance was observed at low pH, and with the increase in pH, the transmittance was observed to decrease. However, as can be seen in the figure, there is a hysteresis in the recorded pH of the sensor.
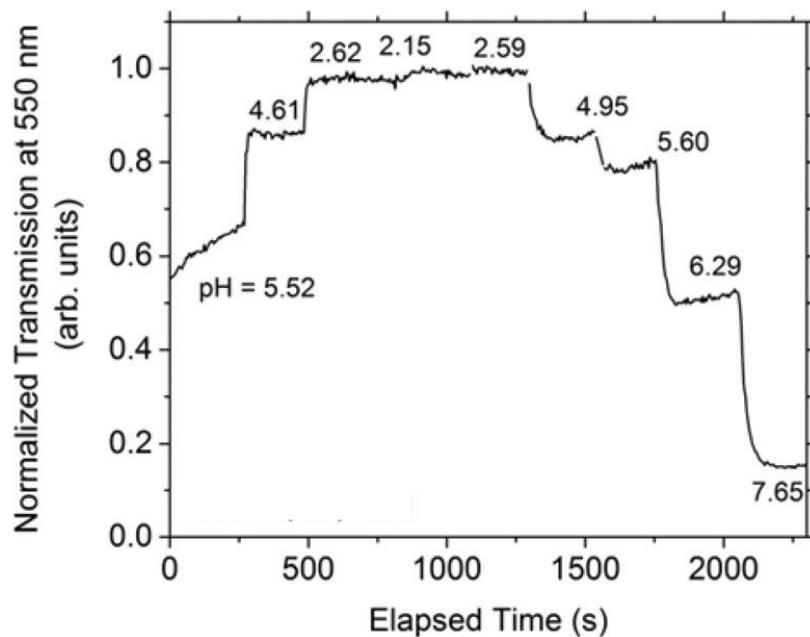
Figure 2.20: Showing the change in transmission at randomly varied pH levels using an Au/silica-coated optical fibre at 80°C [158].

In another report, Wang *et al.* [83] claimed that there was an optical response when an optical fibre was subjected to high pressures of 137.9 bar (2000 psi) [83], as shown in Figure 2.21. A change in transmittance was observed when the pH was changed from 2 to 12 at a high pressure of 137.9 bar. This suggested that gold nanoparticles coated in silica could be potentially used as a pH sensor under high pressure and high-temperature conditions. However, the authors did not reveal the details of the conditions of measurement or the method of preparation. In addition, it has not been revealed how the system was set up or what sort of reaction vessel was used. In this regard, one needs to use their claims continuously.
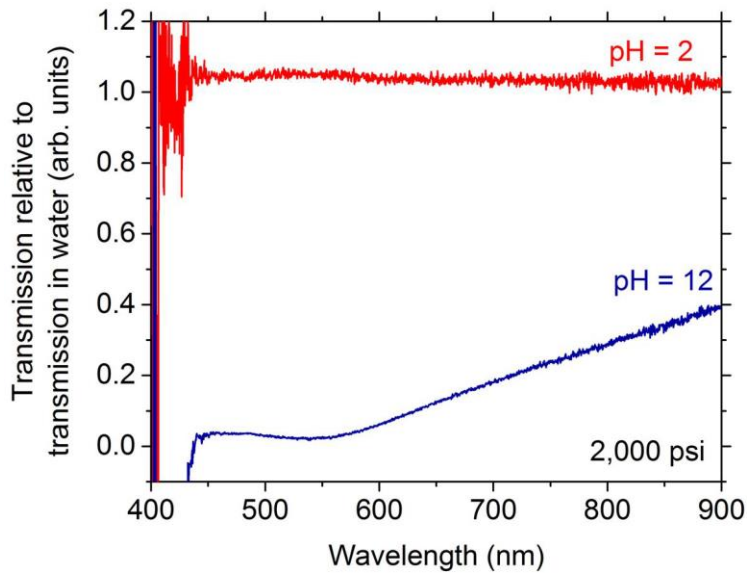
Figure 2.21: Transmission curve at different pH using Au/silica coated optical fibre at high pressure of 2000 psi (137.9 bar) [83].

Furthermore, it would be interesting to assess the optical response of a bare optical fibre, optical fibre coated with silica and metal nanoparticles embedded in silica. This would provide further clarification to the claims reported in the literature discussed above. Moreover, neither of the authors have reported the accuracy and precision of their sensor, nor is there any information on the reproducibility and repeatability of their sensors, which questions the validity of the results provided in these reports. It would be investigated the suitability of silver nanoparticles embedded in silica coating on optical fibre as a pH sensor.

2.8 Summary

The methods involved in the preparation of the silica coating, including the application of the coating on the optical fibre have been discussed in this chapter. In addition, the application of the coating on optical fibres for the measurement of pH at different conditions has been reported. Since, this is an attempt to solve the problems associated with measuring pH under harsh conditions of high temperature and high pressure usually observed in oil wells. This led to the search for new materials that could measure pH at high temperatures and high pressure.

Among the sensing materials, silica coating has been reported to be suitable as a sensing material on optical fibres for this application. However, the effectiveness of

73

the coating for this application is affected by the synthesis conditions, such as reaction temperature, as well as the presence of metal ions in the coating. In addition, metal nanoparticles embedded in silica have also been reported in different studies, which are aimed at assessing its suitability as a sensing material for pH measurements at HTHP conditions. Metal nanoparticles have the potential to boost the stability of silica via a number of different mechanisms. These mechanisms include the avoidance of agglomeration, the formation of chemical bonds with the surface of the silica, and the provision of extra stability to the composite material. For instance, Li *et al.* [115] showed that an increase in the concentration of metal ions reduces the gelation time. Also, increasing the reaction temperature also leads to rapid gelation.

The recent report by Su *et al.* [82] showed that the pH sensitivity of an optical fibre coated with gold nanoparticles embedded in silica was due to the surface plasmon resonance property of gold nanoparticles. However, Lu *et al.* [180] reported that silica coating was the main component responsible for the pH sensitivity, while the presence of gold nanoparticles in the silica merely improves the reproducibility of the sensor. The fact that gold is expensive has necessitated the need for cost-effective materials that could replace gold nanoparticles without compromising its sensitivity for pH measurement.

It is clear from the review of the relevant literature that the silver nanoparticles embedded in silica coating might be an appropriate coating for the application of high temperature and high pressure. This is because the silica matrix would protect the silver nanoparticles from thermal decomposition and might have better stability, which would improve the optical and mechanical stability in performance. Although silver has been reported to have LSPR property; however, to the best of our knowledge, there has been no report assessing the suitability of silver nanoparticles embedded in silica coating as a pH sensor for high-temperature and high-pressure environments, which justifies the need for this study. Also, it would be necessary to investigate the stability of the sensor at temperatures greater than 80 $^\circ$C, including the reproducibility and sensitivity in different chemical conditions, which is lacking in the literature.

CHAPTER 3 : Experimental

CHAPTER 3: Experimental

This chapter describes the fabrication of a fibre optic system, including fibre preparation, coating solution and process, connecting the fibre to the UV-Vis spectrophotometer as a sensor system for the measurement of pH. This begins with the preparation of silica gel and subsequently, the synthesis of colloidal silver nanoparticles (AgNp) using different chemical routes. This is followed by the preparation of silver nanoparticles embedded in silica coating. Then, the etching process to remove the coating and cladding in order to expose the bare optical fibre is described. Thereafter, the process of assembling the exposed fibre optic prior to the application of the coating is discussed. Finally, the application of the bespoke apparatus for measuring the pH of different solutions at temperatures ranging from 25 to 150 °C and gauge pressures of 1 to 5 bar is discussed. The associated challenges during the experiment are also described in detail. This includes a description of the steps involved in preparing the optical fibre prior to coating and addressing the difficulties encountered during this process. A clear explanation of the assembly and coating process would provide an in-depth understanding of the process and challenges involved in applying the coating to the fibre, which is non-trivial.

In summary, this chapter contains a detailed description of the following:

- Methods of gel preparation and conditions affecting gel formation.
- Chemical routes for forming AgNp and a method to produce AgNp/silica composite.
- The etching procedure of optical fibre in order to expose the bare fibre.
- The coating method of the optical fibre.
- The termination of the optical fibre, such as to connect to the detector and light source.
- Assembly of the optical fibre including connections to the light source and spectrophotometer.
- The chemical resistance of the sensor under different experimental conditions including higher temperatures and higher pressures.

3.1 Synthesis of silver nanoparticle embedded in silica

In this section, the primary objective is to provide a detailed method used in this study for the preparation of silver nanoparticles embedded in silica coating. This will be split into three sub-sections. The first part focuses on the preparation of silica gel, including the materials required, techniques, and conditions employed during the synthesis. This is expected to provide the required understanding of the matrix in which the silver nanoparticles would be immersed. The second part explains the preparation of colloidal silver nanoparticles (AgNp) tailored specifically for application as a coating. In this part, different chemical routes including different reducing agents which is aimed at synthesising AgNps with the desired characteristics are provided. The last part focuses on the preparation of an AgNp/silica composite, where silver nanoparticles are embedded within a silica matrix to yield the desired coating. In addition, the degree of uniformity in the coverage of the nanoparticles within the coating structure is explained.

In summary, these three parts are aimed at providing detailed steps involved in the fabrication of a coating based on AgNp/silica composite for application on a fibre optic as a pH sensor, addressing the challenges encountered in the process and presenting strategies employed to overcome these challenges. It is expected that the fabricated pH sensor based on AgNp/silica composite decorated on an optical fibre would exhibit improved properties that could be used as a pH sensor for high-temperature and high-pressure environments.

An overview of the methods used in synthesising AgNp in a silica matrix is shown in Figure 3.1. This involved two different routes carried out to compare the properties, such as stability and adhesion of the resulting composite to a glass substrate. In the first method, the reactants were added to silica one at a time in a sequential order, while the second method involved the addition of all of the starting materials including the precursor of silver nanoparticles along with the other chemicals required for the preparation of silica gel at the same time. Thereafter, the steps in etching the glass slides to improve its adhesive properties and subsequent dip coating are described. This is followed by thermal treatment of the coated glass slides. A detailed explanation of each step is discussed in the next section.

```
                    Sequential method   ┌──────────────┐   Single step method
                                        │ Methods of gel│
                                        │  preparation  │
                                        └──────────────┘
```
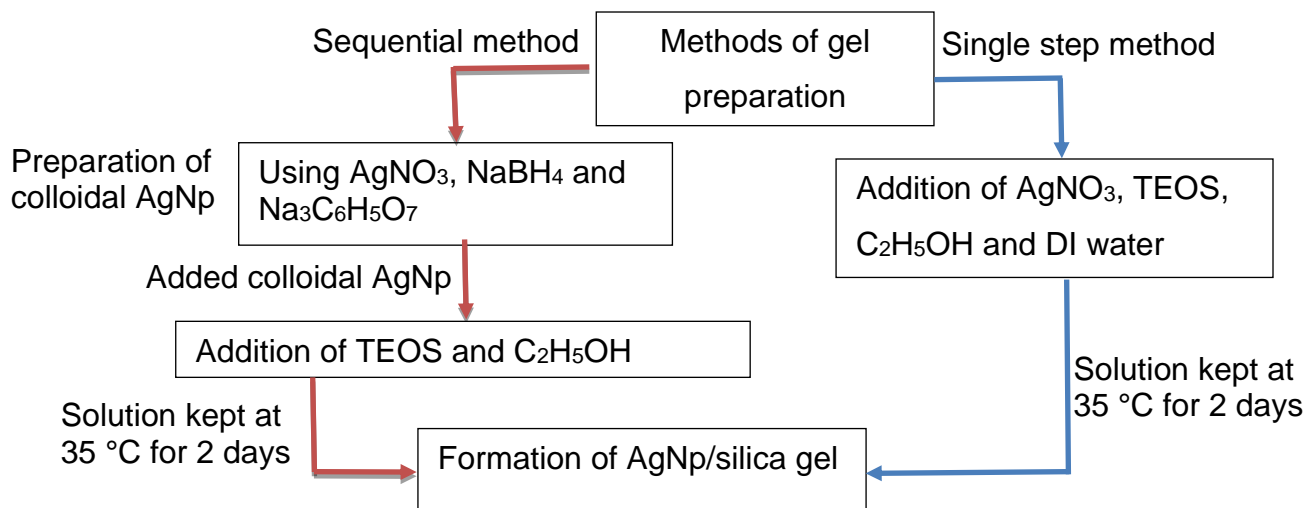
Figure 3.1: The flow diagram showing the synthesis of AgNp/silica gel using two different methods.

3.1.1 Synthesis of silica gel

Silica gel was prepared using tetraethyl orthosilicate (TEOS) as the precursor of silica. This uniform sized was chosen because it has been reported to yield silica particles of with the possibility of controlling the hydrolytic and condensation steps to yield the desired properties [181]. The chemicals used for this process include ethanol (99%), tetraethyl orthosilicate (TEOS) (98%), nitric acid and deionised water. All chemicals were laboratory reagent grade and were purchased from Fischer Scientific. The apparatus needed consists of a 100 ml beaker, a pipette, a magnetic stir bar and some aluminium foil.

In the first method, 8.4 ml of TEOS was added to a 100 ml beaker using a pipette. This was followed by the addition of 8.4 ml of ethanol. Then, 2 ml of the solution adjusted to pH 2 using nitric acid with deionised water was added whilst a magnetic stir bar stirred the solution continuously. The beaker containing the solution was then wrapped with an aluminium foil to prevent the evaporation of volatile chemicals. The solution was then placed on a magnetic stirrer and maintained at a temperature of 35 °C for 4 days, which enhanced gel formation. A representation of this synthetic step is shown in Figure 3.2.

```
┌─────────────────────────────────────────┐
│ Mixing of chemicals including TEOS, ethanol, and │
│ deionized water                          │
└─────────────────────────────────────────┘
                    │
                    │          The solution was kept at
                    │          35 °C for 4 days
                    ▼
        ┌───────────────────────┐
        │ Formation of silica gel │
        └───────────────────────┘
```
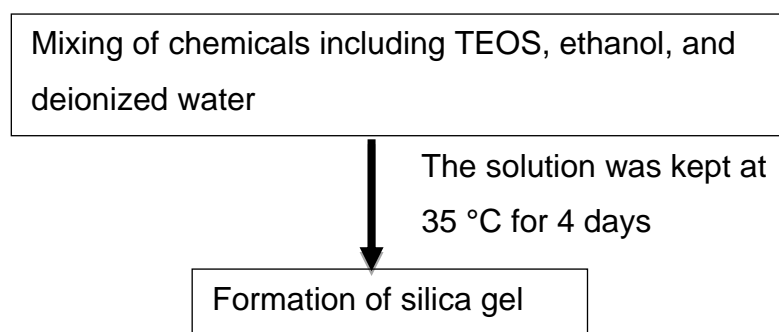
Figure 3.2: Process diagram showing the preparation of silica coating using the sol-gel technique.

3.1.2 Synthesis of colloidal silver nanoparticles (AgNp)

In the synthesis of silver nanoparticles (AgNps), various methods can be employed. In this study, a wet synthetic method was utilised to produce colloidal silver nanoparticles. The procedure required the utilisation of silver nitrate ($AgNO_3$) as the metal precursor and sodium borohydride as the reducing agent. Trisodium citrate, which is believed to serve a dual purpose as a stabilising and reducing agent was also used. The reducing agent facilitated the reduction of silver ions to form nanoparticles in the solution, while the stabilising agent acted as a surfactant to control the surface properties of the silver nanoparticles (AgNp) [126,143,182,183].

To enhance clarity, this section is subdivided into three sections, which cover the use of sodium borohydride as a reducing agent, the use of trisodium citrate as a reducing agent and stabiliser, and the addition of both chemicals in the same system. By exploring these three synthetic routes, further insight who was gained regarding the stability of silver nanoparticles and the role of stabilising agents in their synthesis. The primary objective of this section is to evaluate the effectiveness of these synthetic routes and assess the performance of the synthesised silver nanoparticles when embedded in a silica matrix.

3.1.2.1 Synthesis of silica gel using sodium borohydride as a reducing agent

This section explains the process of synthesising silver nanoparticles by employing sodium borohydride as a reducing agent. The components employed in this synthesis involve silver nitrate ($AgNO_3$) as the primary source of silver nanoparticles, sodium borohydride ($NaBH_4$) as the reducing agent and deionised water. The silver

nitrate (99.8% analytical grade) and sodium borohydride (99% reagent grade) were purchased from Fisher Scientific. The apparatus consists of a 100 ml beaker, 50 ml burette, 500 ml beaker, some aluminium foil, a retort stand with a clamp, magnetic stir bar, and magnetic stirrer. Since silver nitrate ($AgNO_3$) is a light-sensitive chemical that decomposes in the presence of sunlight [184], some precautionary measures to avoid light exposure are required. For instance, the beaker containing the sodium borohydride was covered with aluminium foil to prevent ambient light from entering the system.

First, a 30 ml solution of 2 mM sodium borohydride was prepared and transferred to a 100 ml beaker. An ice bath was made using a 500 ml beaker and the beaker containing the sodium borohydride solution was placed in it. The solution within the ice bath was stirred for 25-30 minutes to control the rate of reduction. Then, 1 mM silver nitrate solution was prepared and 10 ml of the solution was inserted into a burette. With continuous stirring, the silver nitrate solution was added dropwise (1 drop/sec) to the sodium borohydride solution in the beaker. The mixture was continuously stirred to ensure homogeneity of temperature and concentration. The purpose of utilising the ice bath in this procedure is to slow down the rate of reduction kinetics for silver nitrate, since sodium borohydride is a very active reducing agent. This facilitates control over the reaction rate and further reduces the possibility of undesirable side reactions. In the course of preparation, no additional chemicals were introduced with the intent to alter the pH of the solution. Therefore, pH measurements were not conducted during the synthesis of silver nanoparticles.

After adding the silver nitrate to the sodium borohydride, the resulting solution was observed to turn pale yellow. The intensity of the yellow colour was observed to increase with an increase in the reaction time. A small amount of the solution was collected at different reaction times (1-60 minutes) to investigate the light extinction properties using a UV-visible spectrophotometer to confirm the formation of silver nanoparticles. The procedure was carried out, and the maximum reaction time was chosen to be 60 minutes. The solution containing the silver nanoparticles was retained in the ice bath to prevent the aggregation of the formed particles. A schematic of the experimental apparatus and process is summarised in Figure 3.3.
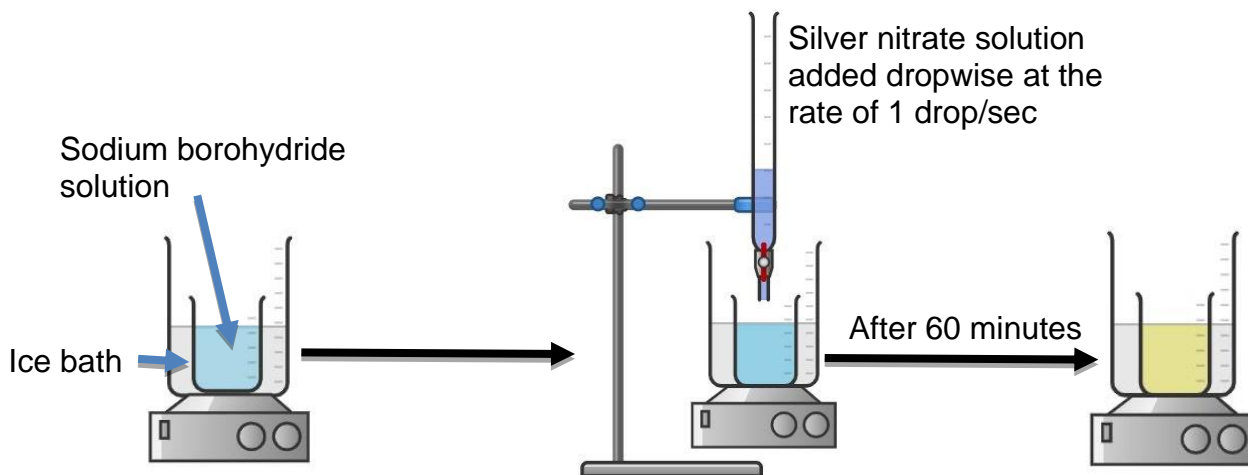
Figure 3.3: Experimental apparatus for the synthesis of colloidal silver nanoparticles using silver nitrate as the precursor of silver nanoparticles and sodium borohydride as the reducing agent.

3.1.2.2 Synthesis of silver nanoparticles using trisodium citrate as a reducing agent

In this section, the synthesis of silver nanoparticles using trisodium citrate as a reducing agent is used. The chemicals used include: silver nitrate ($AgNO_3$) as the precursor of silver nanoparticles, trisodium citrate ($Na_3C_6H_5O_7$) as the reducing agent and deionised water. Trisodium citrate (> 99%, analytical grade) was purchased from Fisher Scientific. The apparatus consists of a 100 ml beaker, 50 ml burette, some aluminium foil, a retort stand with a clamp, a magnetic stir bar, and a heater stirrer (model FB15001 supplied by Fisher Scientific) with a hot plate. The beaker containing the trisodium citrate was wrapped with aluminium foil prior to the addition of silver nitrate to protect it from light, as previously mentioned. A schematic representation of the experimental apparatus for the synthesis of silver nanoparticles using trisodium citrate as a reducing agent is summarised in Figure 3.4.

First, 50 mL of 7 mM sodium citrate was measured into a beaker and placed on the hot plate to raise the temperature to 40 °C. To achieve uniformity in both temperature and concentration, the solution within the beaker was subjected to constant agitation using a magnetic stirrer. This was followed by the addition of 10 ml of 2 mM silver nitrate to the beaker dropwise using a burette, and the solution was stirred for 60 minutes. A second sample was also prepared, where a temperature of

70 °C was maintained to assess the effect of a higher temperature on the formation of silver nanoparticles. The formation of AgNps was checked using a UV-visible spectrophotometer. These experiments were designed to understand the effect of increased reaction temperature (40 °C and 70 °C) on the formation of AgNps as well as the stability of the colloidal solution prepared using both temperature conditions.
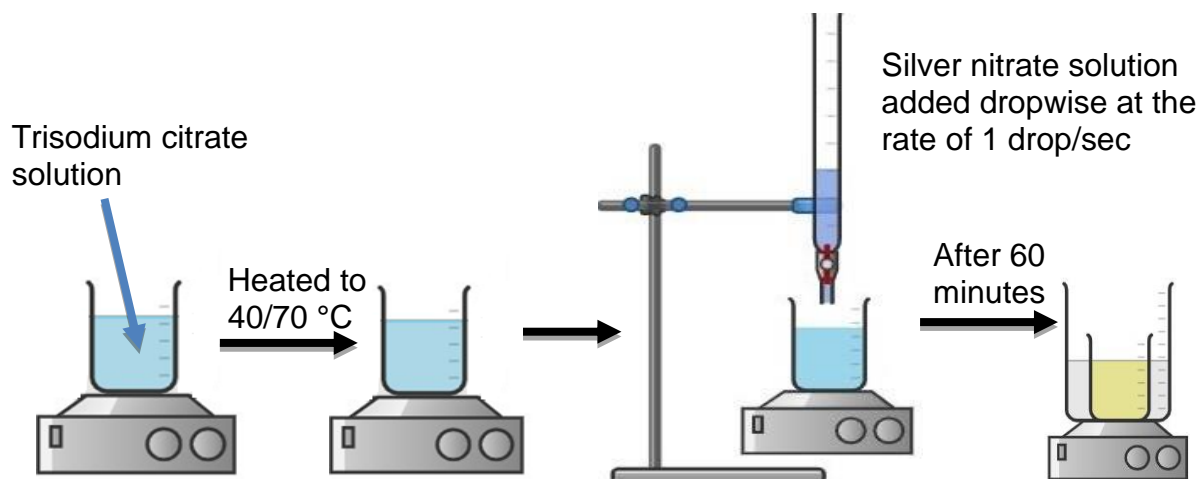
Figure 3.4: Schematic representation of the formation of colloidal silver nanoparticles showing the experimental apparatus and the steps for the synthesis of colloidal silver nanoparticles using silver trisodium citrate as a reducing agent.

3.1.2.3 Sodium borohydride as reducing agent and trisodium citrate as stabilising agent

This section outlines the procedure for synthesising silver nanoparticles by employing sodium borohydride as a reducing agent and trisodium citrate ($Na_3C_6H_5O_7$) as a stabilising agent. The chemicals used include silver nitrate ($AgNO_3$) as the precursor of silver nanoparticles and deionised water. The apparatus consists of a 100 ml beaker, 50 ml burette, 500 ml beaker used for the ice bath, some aluminium foil, pipette, retort stand with a clamp, magnetic stir bar and heater-stirrer. A schematic representation of the experimental apparatus for the synthesis of silver nanoparticles using trisodium citrate as a reducing agent is shown in Figure 3.5.

First, a 38 mL solution of 2 mM sodium borohydride was added to a 100 ml beaker at 4 °C and placed in an ice bath for 30 minutes to attain the temperature of the ice bath. As mentioned, this is required to reduce the reduction kinetics during the nucleation process of silver nanoparticles. Again, the beaker was covered with aluminium foil to prevent the interaction of ambient light with the system. Then, 1 mL of 1 mM silver nitrate was added dropwise into the solution. Following that, a volume of 1 ml of a 1 mM solution of trisodium citrate was introduced dropwise into the same solution. The solution was agitated for a duration of 30 minutes, utilising a magnetic stirrer. Different concentrations (0.5 mM and 1 mM) of the stabiliser (tri-sodium citrate) were prepared, and its effect on the synthesis of colloidal silver nanoparticles was investigated.
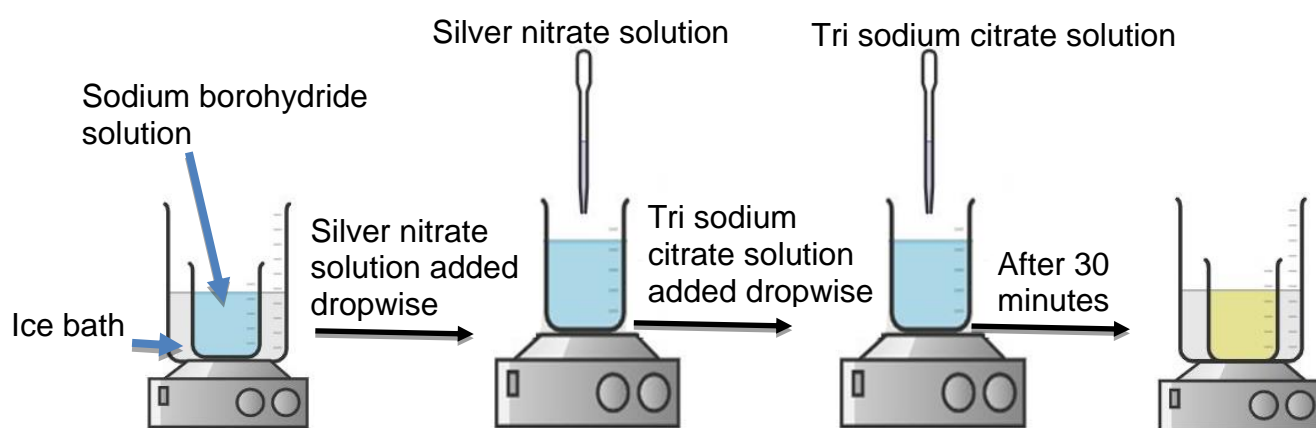
Figure 3.5: Experimental apparatus for the synthesis of silver nanoparticles using sodium borohydride as a reducing agent and trisodium citrate as a stabiliser.

In summary, the preparation of the colloidal AgNps was accomplished using these three distinct methods. All the colloidal AgNp solutions were analysed using a UV-vis spectrophotometer, the method of verifying the presence of silver nanoparticles is discussed next.

3.1.2.4 Detection of AgNps by UV-Vis spectroscopy

Silver nanoparticles are expected to absorb light around 400 nm, as reported in the literature [11-13]. The light extinction around this region would be indicated by the formation of a peak, which could be further analysed to retrieve other useful information, such as particle size and size distribution. The wavelength at which the

peak is observed is characteristic of the metal nanoparticle present in the solution. For silver nanoparticles, a distinct peak is expected around 400 nm. Details on the working principle of a UV-visible spectrophotometer with regard to the measurement of absorbance using a UV-visible spectrophotometer are hereby discussed.

The working mechanism of a UV-visible spectrophotometer depends upon the interplay between light and particles [185]. The instrument quantifies the degree of light absorption or transmission within the ultraviolet (UV) and visible portions of the electromagnetic spectrum. The spectrophotometer consists of a light source that emits a broad spectrum of light, typically including UV and visible wavelengths. The light passes through a collimator, which is an important component of a spectrophotometer that ensures that the collimated light beams are parallel thereby minimising the chance of formation of divergent beams [185]. This is followed by the travelling of the light beam to the diffraction grating, which separates light into its component wavelengths. Its main function is to disperse incident light into a spectrum of colours or wavelengths. Then, the light is passed through a wavelength selector, also called a monochromator to allow light of a specific wavelength to pass through the sample. This light is split into two different parts; the first is made to pass through the reference compartment, while the other is made to pass through the sample compartment. At the end, there is a detector, usually a photodiode or a photomultiplier tube, which converts the light signal into an electrical signal. This signal is then amplified and sent to a display or a computer for data analysis, as shown in Figure 3.6.

The UV-visible spectrophotometer consists of two compartments designed to hold the reference and test samples. The absorbance or transmittance of light in the test solution is usually compared with the reference solution. This setup enables the comparison between the two solutions, facilitating precise analysis and measurements.
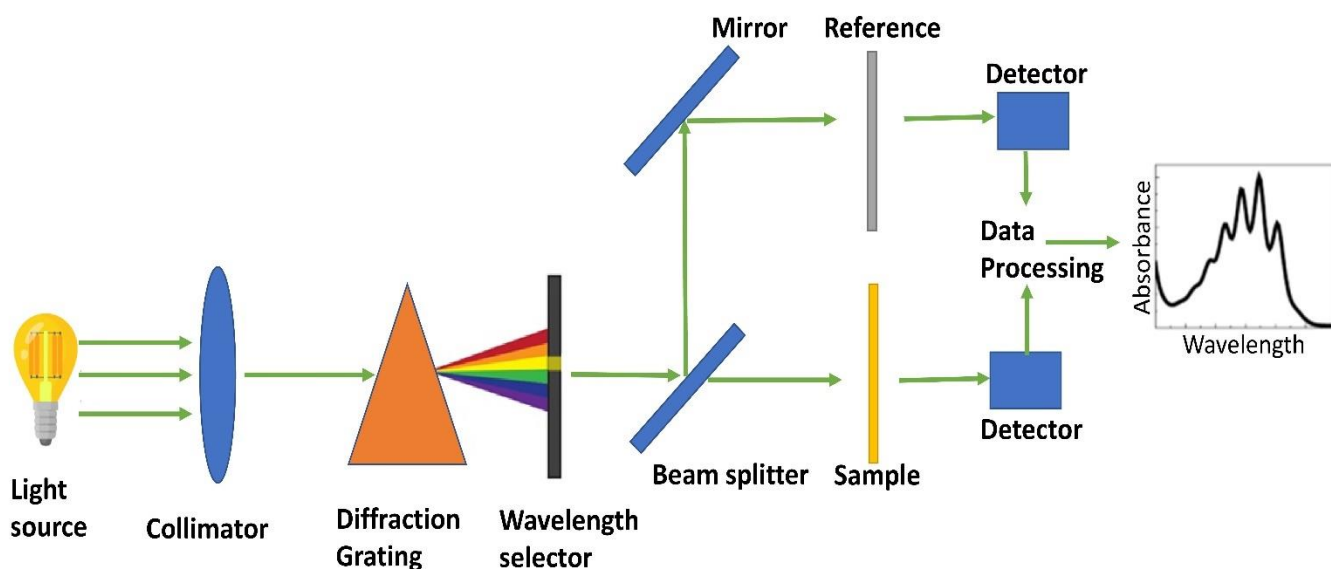
Figure 3.6: Mechanism of light absorption measurements of a colloidal solution using a UV-Visible spectrophotometer.

In practice, the UV-visible spectrophotometer operates by comparing the absorbance or transmittance of light in the test solution with that of the reference solution. As light passes through the test solution, certain wavelengths may be absorbed, leading to a decrease in the intensity of transmitted light or an increase in the intensity of absorbed light. To quantify this interaction, the spectrophotometer measures the ratio of the intensity of transmitted or absorbed light to the intensity of incident light. This ratio is known as the transmittance or absorbance, respectively, and its calculation is based on the fundamental principles of the Beer-Lambert law.

The Beer-Lambert law is a fundamental principle that establishes a relationship between the concentration of the absorbing species in the sample and the absorbance or transmittance of light. According to this law, the greater the concentration of the absorbing species in the solution, the more light it will absorb. Moreover, it also states that the path length of the light through the solution, denoted by the cell length, influences the amount of light absorbed. This implies that longer path lengths result in increased light absorption. The absorption of light by molecules is governed by two fundamental concepts, namely Lambert's law and Beer's law. Lambert's law postulates that the quantity of incident light absorbed exhibits a direct correlation with the optical path length traversed by the light within the medium. Conversely, Beer's law postulates that the degree of light absorption exhibits a direct

correlation with the concentration of the solution. The Beer-Lambert law is a synthesis of the contributions made by Lambert and Beer, which establishes that the absorption of light by a solution is directly proportional to both the concentration of the solution and the distance the light travels through it.
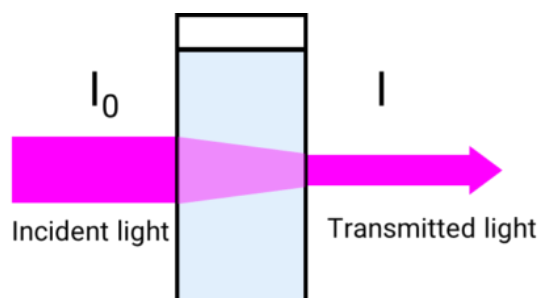
Figure 3.7: Schematic representation showing the relationship between an incident and a transmitted light through a solution.

As shown in Figure 3.7, when an incident light (I_0) traverses through a solution with a concentration (C) and a cell length (ℓ), and the intensity of the transmitted light is represented as I, the Beer-Lambert law can be expressed using equations 3.1-3.5 [186].

$$A \propto l \qquad \text{(From Lambert's law)}$$

$$A \propto c \qquad \text{(From Beer's law)}$$

Therefore, combining Lambert's law and Beer's law

$$A \propto c.l$$

$$A = \varepsilon.c.l \tag{3.1}$$

Where ε is the molar absorptivity coefficient constant.

According to the definition of absorbance (A),

$$A = Log_{10}\frac{I_o}{I} \tag{3.2}$$

Using equation 3.1,

$$Log_{10}\frac{I_o}{I} = \varepsilon.c.l \tag{3.3}$$

Moreover, according to the definition of transmittance (T),

$$T = \frac{I}{I_o}$$ (3.4)

Hence, by multiplying both sides by 100

$$\% \, T = T \times 100 = \frac{I}{I_o} \times 100$$ (3.5)

The spectrum provides information about the extinction characteristics of the sample over a range of wavelengths, which can be used to identify and quantify the presence of specific compounds or analyse the chemical properties of the sample. In summary, a UV-visible spectrophotometer operates by passing light through a sample, measuring the intensity of transmitted or absorbed light, and providing valuable information about the sample's extinction properties at different wavelengths.
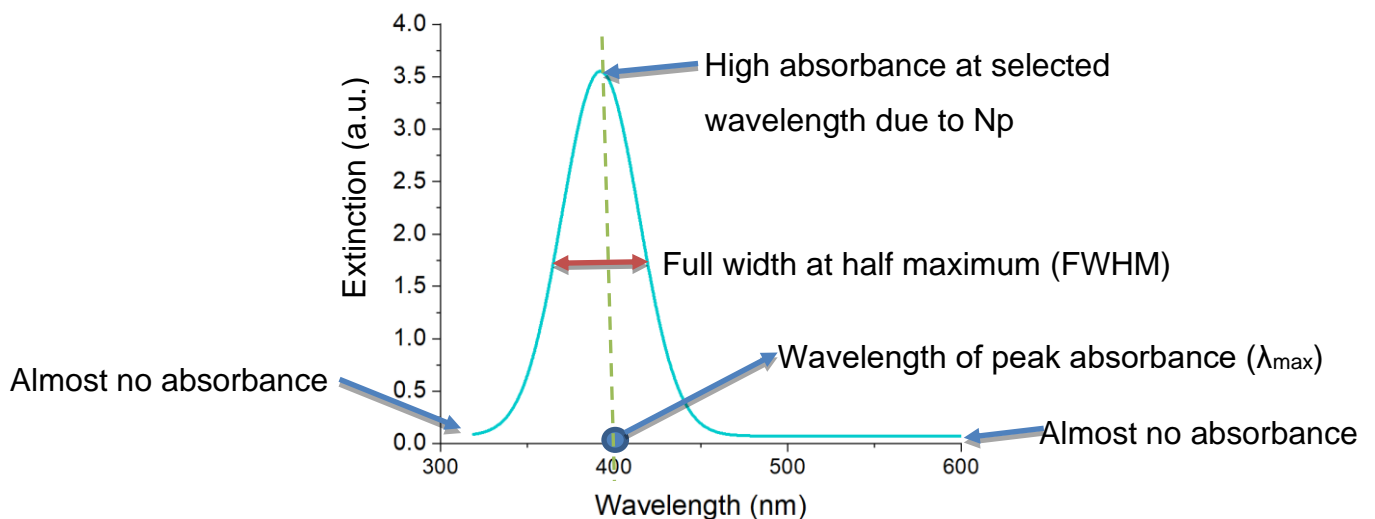
Figure 3.8: The extinction spectra of the colloidal silver nanoparticle showing the wavelength of peak absorbance (λ_{max}) and full width at half maximum (FWHM).

A hypothetical extinction spectra obtained in this study showing the formation of silver nanoparticles is shown in Figure 3.8. Figure 3.8 displays a peak around 400 nm, attributed to the mutual vibration of electrons in silver nanoparticles resonating with light. The occurrence referred to as localised surface plasmon resonance (LSPR) leads to the extinction of light at a particular wavelength. LSPR is a collective oscillation of conduction electrons in response to incident light. The observed

87

absorbance peak indicates the presence of silver nanoparticles in the solution and provides insights into their size distribution. The full wavelength and full width at half maximum (FWHM) are crucial parameters describing both the formation and size distribution of the nanoparticles.

3.1.3 Preparation of AgNp/silica composite

The preparation of AgNp/silica composite can be carried out using two different methods. The first method involves mixing colloidal silver nanoparticles with the silica gel. The second method involves a combination of all the necessary chemicals simultaneously to prepare the AgNp/silica composite. These two methods offer alternative approaches to achieving the desired composite material, which are discussed in forthcoming sections.

3.1.3.1 Method 1: Sequential method

In this section, the method of preparing AgNp-silica composite prior to the decoration on an optical fibre is described. The method involves the use of tetraethyl orthosilicate (TEOS) and ethanol for the preparation of silica gel. The apparatus and procedure for the preparation of colloidal silver nanoparticles was by using sodium borohydride as a reducing agent and trisodium citrate as a stabilising agent are described in section 3.1.2.3. Moreover, in addition with the apparatus required for the preparation of colloidal AgNp, a 50 ml beaker, a pipette, a hot plate and some aluminium foils are also required.

Initially, 8.4 mL of ethanol was measured into a 50 mL beaker using a pipette. 8.4 ml of TEOS was added to the Ethanol using a pipette. Then, 2 ml of a colloidal AgNp solution that had been made up following the process described in section 3.1.2 (c) was added to the beaker containing TEOS and ethanol. The mixture was stirred continuously at a temperature of 35 $^{\circ}$C for two days. An aluminium foil was used to cover the beaker to prevent the loss of volatile compounds. This method is illustrated in the flow chart shown in Figure 3.9.
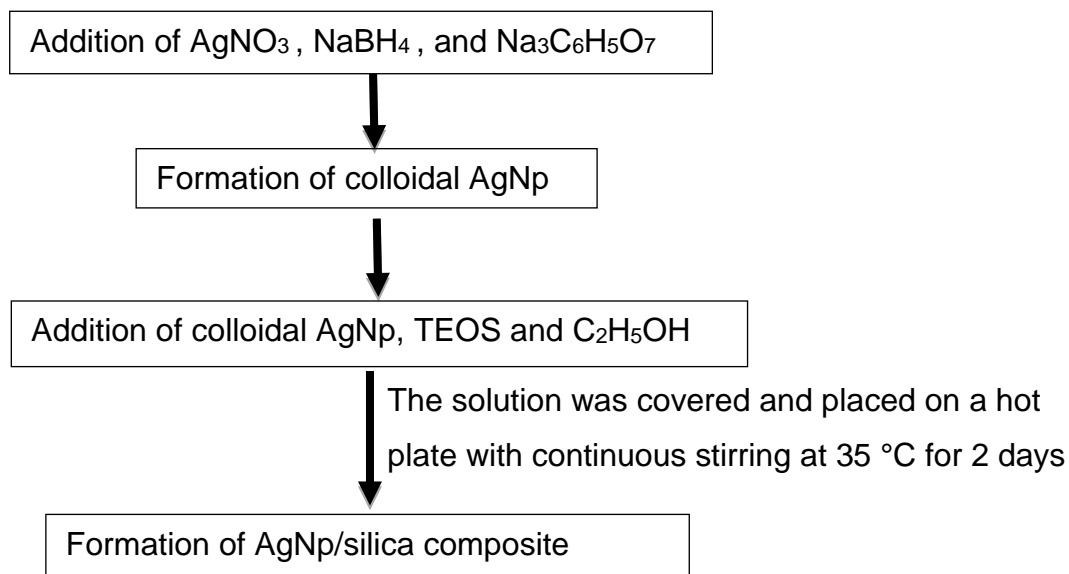
Figure 3.9: Flow chart showing the preparation of AgNp/silica composite where AgNps were prepared separately.

After mixing the colloidal AgNp solution with the TEOS/ethanol solution, the colour of the mixture changed to yellow. However, the colour was observed to change to grey after 24 hours, as shown in Figure 3.10, which was again attributed to the aggregation of the silver nanoparticles. Indeed, it was observed that the grey particles settled to the bottom of the beaker. This meant that the process for forming the composite gel and coating would not be useful for coating optical fibres.
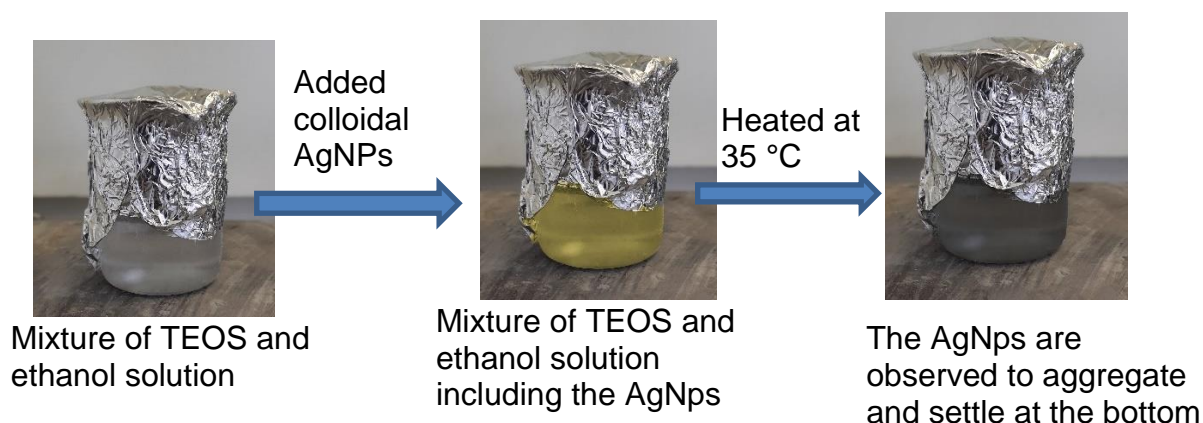
Figure 3.10: Images showing the colour change to yellow and then grey after the addition of the colloidal silver nanoparticles to the mixture of TEOS and ethanol.

Despite the instability of the colloidal solution, the adhesion of the AgNp/silica mixture was tested using glass slides. For the purpose, glass slides made of soda-lime, with dimensions 26 mm × 76 mm × 1.2 mm purchased from Fischer Scientific were used. It is worth noting that although both the glass slide and the optical fibre are silica-based, there is a difference in their material properties; however these experiments were carried out as a first step to determine if the gel mixture would adhere to glass. Glass slides provided a route for the preliminary measurements as it is relatively cheap and easily accessible.

In this study, the glass slides were immersed in the gel and left in contact with the gel for approximately 1 minute, following the dip-coating method. While being withdrawn, a thin layer of the solution remained on the surface of the substrate. Once completely withdrawn, the glass slides were suspended using a clamp to air dry, as depicted in Figure 3.11. The liquid within the film was allowed to evaporate, resulting in a dry film. Subsequently, the glass slides underwent thermal treatment in a furnace at 200 °C for 2.5 hours, with a heating and cooling rate of 2 °C per minute.
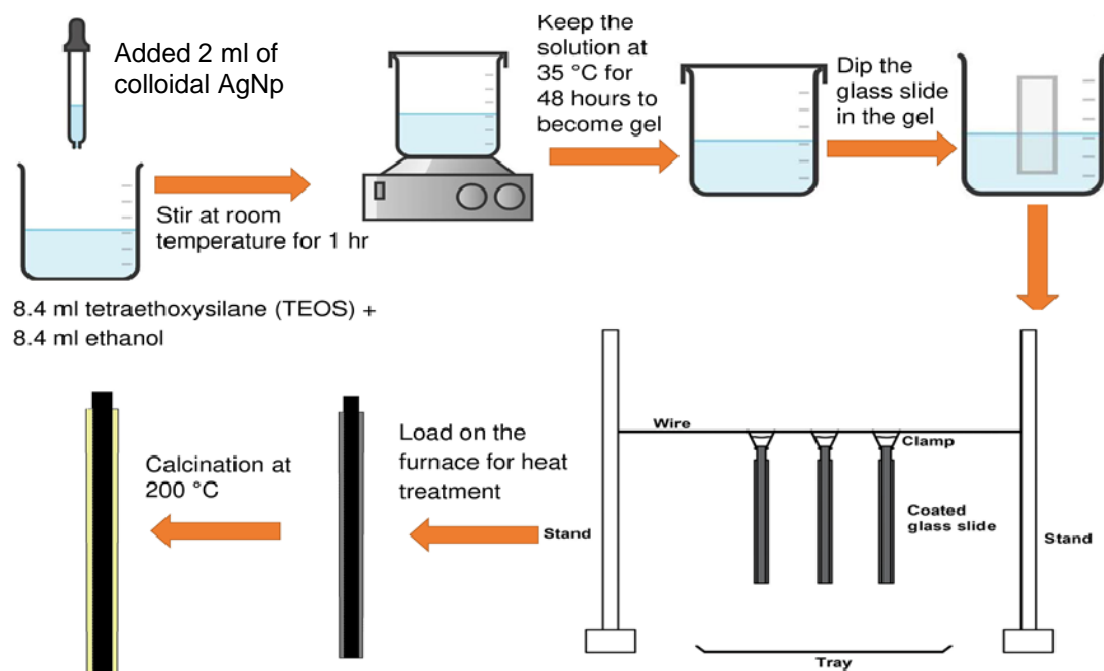
Figure 3.11: Schematic diagram showing the preparation of AgNp/silica composite, a dip-coating procedure using a glass slide and thermal treatment of the coated glass slide at 200 ºC in a furnace for 2.5 h to form a coating.

Therefore, the coating on the glass slides was analysed using the UV-Vis spectrophotometer. The AgNp/silica coating did not only result in poor adhesion with the glass slide, but no visible extinction peak around 400 nm could be formed, as shown in Figure 3.12 (a) and (b), respectively. The absence of a peak suggests that either no silver nanoparticles were formed within the coating, or a negligible amount of the nanoparticles was formed within the coating, which could possibly aggregate and further precipitate within the gel, resulting in the observed grey colour.
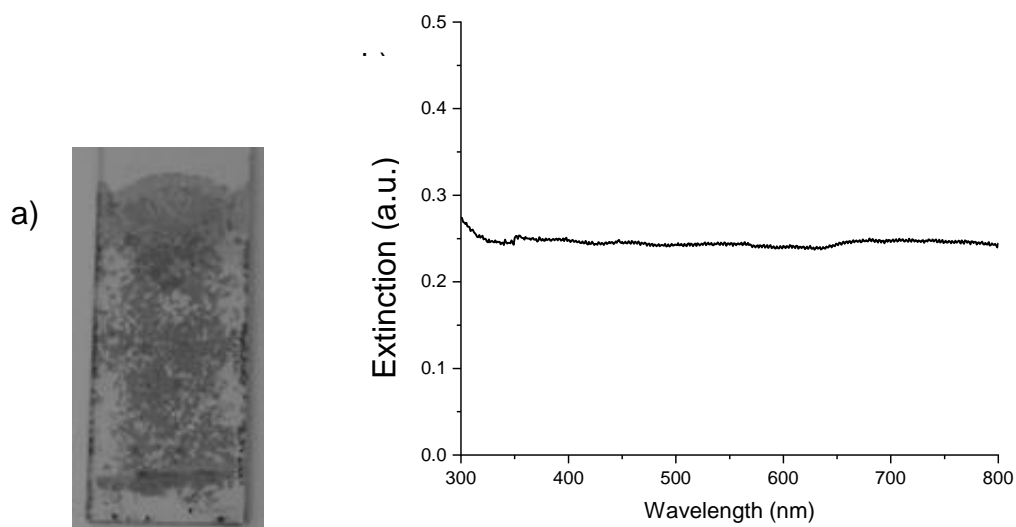
Figure 3.12: (a) Image of AgNp/silica coating on the glass slide showing poor adhesion of the coating with the glass slide, (b) UV-vis spectrum of the coating showing an absence of peak around 400 nm.

This synthesis method indicates that the aggregation of primary particles is a major problem for the formation of AgNp/silica coating. Therefore, to solve this problem, a different method was devised involving combining all starting materials at the same time and adjusting synthesis conditions (such as the use of adjustment of the pH of the solution) so that rapid aggregation of AgNp could be prevented. Details of this new method are described in the next section.

3.1.3.2 Method 2: Single-step method

In this research, therefore a new approach for preparing the AgNp/TEOS composite is presented, which involves the simultaneous addition of all the requisite chemicals, compared to the conventional method of incorporating colloidal AgNp into a silica

precursor, as shown in Figure 3.13. The chemicals used in the synthesis which include tetraethyl orthosilicate (TEOS), ethanol, silver nitrate, nitric acid, deionised water, 50 ml beaker, a pipette, a heated plate, and aluminium foil.

This method used silver nitrate as the metal salt and tetraethoxysilane (TEOS) as the silica precursor within which the synthesised silver nanoparticles are embedded. Specifically, 0.04 g of silver nitrate was added to the container, and 2 mL of nitric acid (HNO_3) was used to adjust the pH to 2. Notably, nitric acid functions as a catalyst in this process, and the acidic pH chosen for the synthesis is expected to produce a coating with fewer pores than an alkaline medium [103,187]. Following this, the entire solution containing TEOS, ethanol, and silver nitrate was stirred at room temperature for 1 h. In order to promote the formation of gel, the temperature was maintained at 35°C within a fume cabinet using a heated plate. The literature recommends a temperature lower than 50°C to prevent shrinkage of the coating [109].

The beaker again had to be covered using aluminium foil to prevent the evaporation of ethanol and TEOS solution. The solution was kept under these conditions for 48 hours to form a gel. Thereafter, the gel was used to coat the glass slide, and the same drying process as previously described was followed. Finally, the coated slides were thermally treated at 200 °C for 2.5 hours with a heating and cooling rate of 2 °C. min^{-1}.
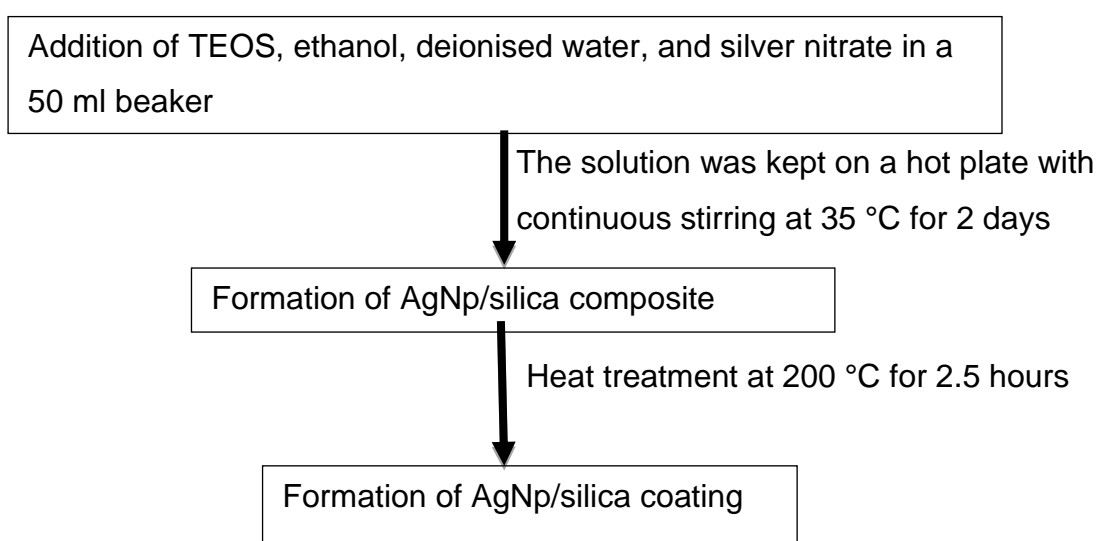
Figure 3.13: Flow chart showing the alternative method of preparing AgNp/silica composite, including thermal treatment at 200 °C for 2.5 h.

The literature has documented the utilization of metal nanoparticles, specifically silver (Ag) or gold (Au), incorporated within silica-based coatings, with a notable emphasis on their performance under heat treatment at 200 °C. This treatment has been noted to facilitate the preparation of Ag or Au embedded within silica-based coatings coating [90,94,95,136,188]. Li *et al.* [136] conducted an investigation into the influence of heat treatment on the fabrication of AgNp/Silica coatings, highlighting the efficacy of the 200 °C temperature regime. Consequently, for the purpose of assessing the adhesive properties of AgNp/silica-based coatings on glass slides as a potential replacement for optical fibre cladding, a range of heat treatment temperatures spanning from 150 to 250 °C for durations of 1 to 3 hours was selected. The ensuing chapter delves into a comprehensive discussion of the results, detailing the optimization process that led to the selection of a heat treatment temperature of 200 °C for a duration of 2.5 hours.

A visual inspection of the coated glass slides indicated the formation of a pale yellow colour with good adhesion with the glass slide. These samples were further inspected using a UV/Visible spectrophotometer to investigate the presence of silver nanoparticles within the coating. The confirmation of the formation of silver nanoparticles was achieved through the observation of an extinction peak within the wavelength range of 400-450 nm, which varied depending on the specific size and shape characteristics of the silver nanoparticles [87,89,144]. An example of such a UV-vis spectrum is shown in Figure 3.14, where an absorbance peak was observed at the wavelength of 430 nm, confirming the formation of AgNps within the coating. Now that a method for obtaining a silica/AgNp coating was established, a second step to improve adhesion to the underlying substrate (glass) was sought. Details of the optimisation process are discussed in the next section.
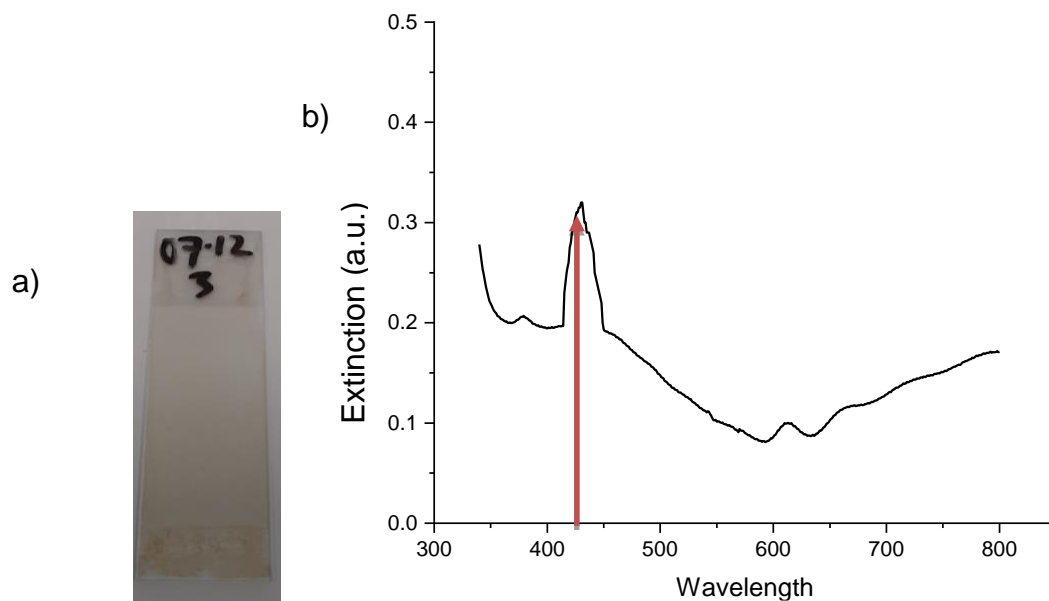
Figure 3.14: A UV-Vis spectrum of AgNp/silica coating on glass slide showing the adhesion of the coating on the glass slide (a) and the corresponding extinction peak observed around 430 nm, which confirms the presence of AgNp in the coating.

The synthesis of a hybrid coating via sol-gel methodology engenders the incorporation of organic constituents, primarily consisting of hydrocarbon-based moieties. Subsequent exposure to thermal treatment at 200 °C introduces the prospect of organic component degradation, albeit with the caveat that the extent of transformation within the silica matrix, specifically SiO_2, may not achieve full completion depending upon the duration and temperature parameters employed [133,135,189]. This observation finds validation in the investigation conducted by Li et al. [190], who subjected silica-based coatings to a range of thermal treatments spanning 200 to 1000 °C, explaining that the eradication of ethoxyl groups reached completion at 500 °C. In light of the current thermal regime of 200 °C, the characterization of the resultant coating warrants classification as silica-based rather than exclusively silica, reflecting the ongoing organic influence despite the likelihood of its partial degradation.

3.1.3.3 Optimisation process of AgNp/silica coating on glass slides

In this section, the techniques that were used to improve the quality of AgNp/silica coating on the glass slide are discussed. The two important factors which were observed to affect the quality of the coating in terms of its adhesion with the glass

slide include the etching conditions of the glass slide as well as the heating and cooling rates used during the thermal treatment step. Details of how these conditions were optimised are discussed in this section.

3.1.3.4 Effect of etching conditions of glass slide on adhesion of the coating

The reason for using glass slides for optimising the coating conditions is mainly due to the fact that the glass surface and coating properties can be investigated using standard materials and analytical methods. Moreover, the use of glass slides is quite economical. However, glass slides have a surface layer which is smooth; it was necessary to etch the glass slides to enhance adhesion by increasing surface roughness. This process involved the use of 50 mL of 7 M sodium hydroxide to etch the glass slides for 1 hour at the temperature of 100 °C. The etching process was carried out to both activate the glass slide as well as increase surface roughness in order to improve the adhesion with the silica coating. This was necessary because the activation process performed on the glass slide could also be applied to the optical fibre since they are made of the same material (silica).

The chemical reaction between sodium hydroxide and glass (silica) is shown below [172].

$$[\text{-Si-O-Si-}] + OH^- \rightarrow [SiO]\text{-} + [\text{-Si-OH}] \tag{3.6}$$

In order to verify the accuracy of the results, the measurement of the thickness of the glass slide was carried out using two different methods, which include a digital micrometre and a high-resolution microscope. When the etched slide was compared against the unetched one, both instruments showed that the thickness of the unetched glass slide, as measured using a digital microscope, was 1.02 mm, while the etched glass slide was 1.01 mm, as shown in Figure 3.15 (a) and (b). The results indicated that the thickness of the glass slide was observed to decrease by 10 microns after etching in 7 M sodium hydroxide for 1 hour at 100 °C. This pretreatment method has been reported as it is safer compared to the conventional method involving the use of hydrofluoric acids, which poses a safety threat [191–193].

95
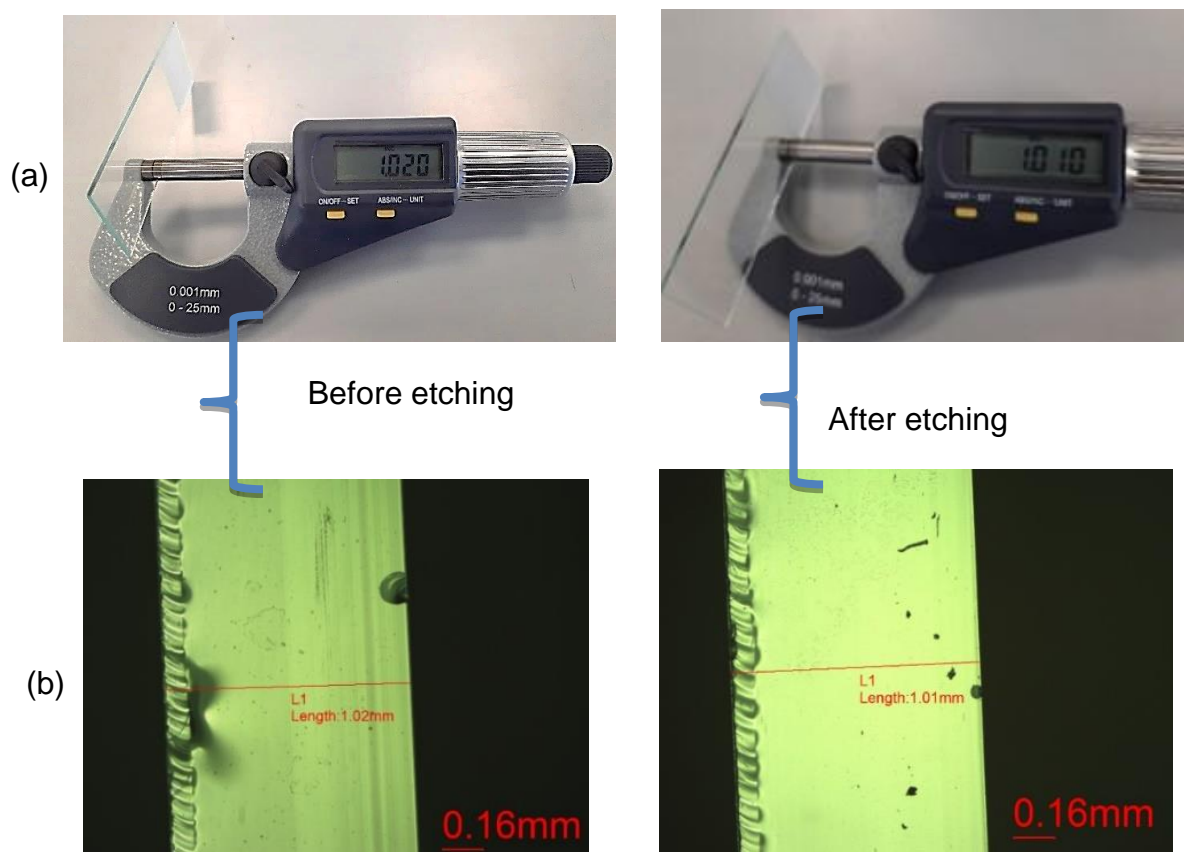
Figure 3.15: Measurement of thickness of glass slide using (a) digital micrometre and (b) a high-resolution microscope before etching in 7 M NaOH for 1 h at 100 °C and after etching in 7 M NaOH for 1 h at 100 °C. The figure shows the thickness of the glass slides before and after the etching.

Dipping the glass slides in the alkaline solution improved coating adhesion, as shown in Figure 3.16. A control experiment where the coating was applied to an unetched glass slide was also investigated. Consequently, the glass slide showed less amount of coating was observed compared to the etched glass slide, as shown in Figure 3.16. The thickness of the AgNp/silica coating on the glass slide was also measured using an optical microscope in order to quantify this. The thickness of the coating was about 1.72-1.95 μm on the unetched glass slide vs. 5.83-6.95 μm on the etched glass slide. It is evident that the etched glass slide using sodium hydroxide improved the hydrophobicity as well as the roughness of the slide, which explains why it could retain more gel on the surface thereby improving the adhesion of the coating as shown in Figure 3.16.
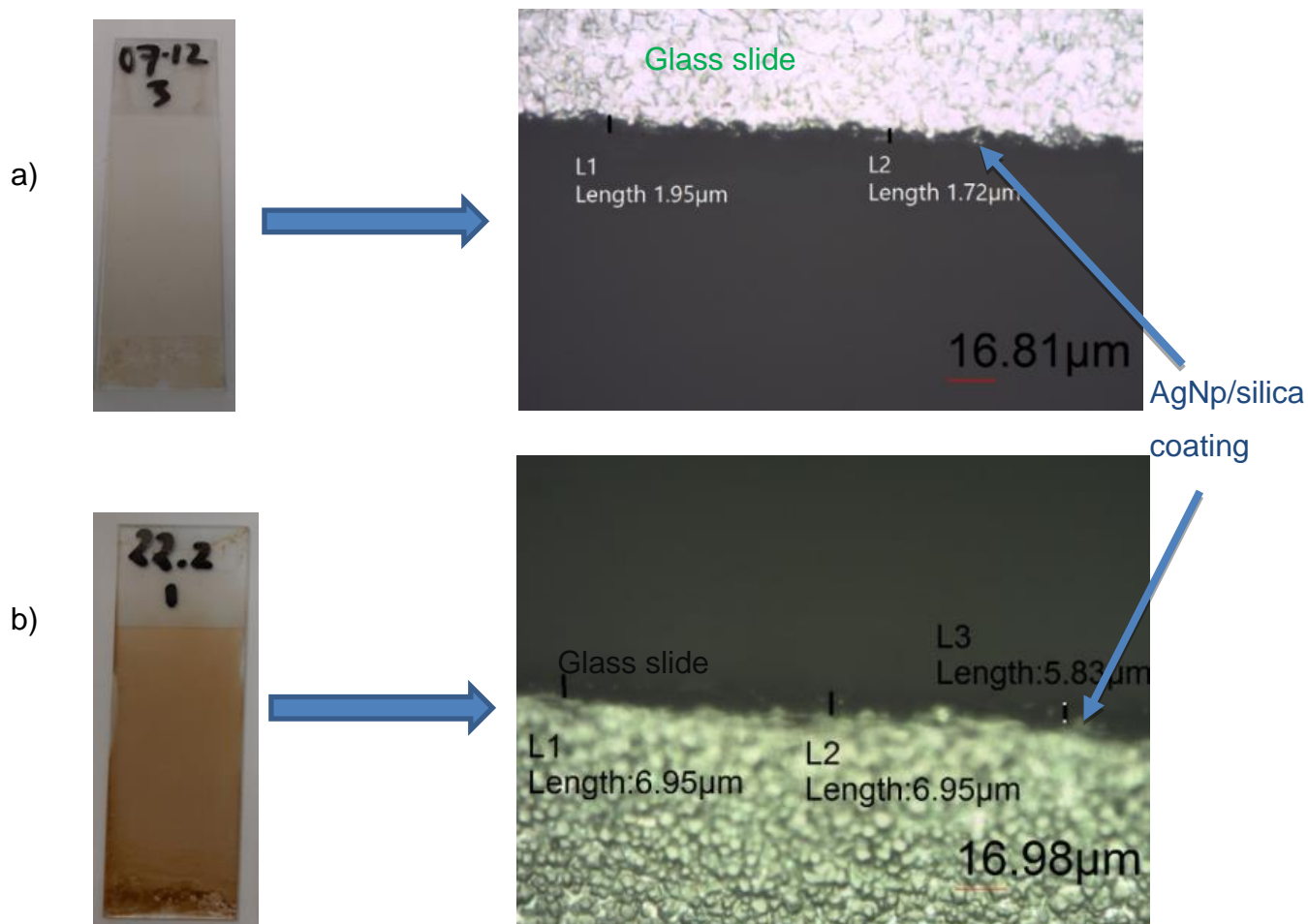
Figure 3.16: Micrographic images of the coated AgNp/silica glass slides with (a) the unetched glass slide and (b) the etched glass slide using 7 M NaOH solution, which resulted in improved adhesion of the coating.

3.1.3.5 Effect of heat treatment

The second factor affecting the adhesion of the coating to the underlying glass was the ability to control the thermal treatment step. A series of experiments was conducted to evaluate the optimal temperature and duration of heat treatment required for the formation of the coating. The heat treatment temperature was chosen to range between 150 to 250 °C for 1 hour to 3 hours. The optimum condition of heat treatment was found to be 200 °C for 2.5 hours.

Slow heating and cooling rates of 2 °C.min^{-1} also contributed to better adhesion properties. This is because it has been reported that a rapid heating and cooling rate

can result in thermal expansion of the coating, culminating in shrinkage of the coating and leading to deadhesion from the glass surface [106,108] as shown in Figure 3.17. This study indicated that a heating rate of 2 $^{\circ}$C.min^{-1} could prevent shrinkage as well as the formation of cracks on the surface of the coating. The quality of the coating improved in terms of adhesion when the heating and cooling rates were as low as 2 $^{\circ}$C.min^{-1} compared to the quality when the heating rates were increased to 4-5 $^{\circ}$C.min$^{-1,}$ as shown in Figure 3.17. This may be attributed to shrinkage arising from thermal shock during the rapid heating and cooling steps.

Figure 3.17: The AgNp/silica coated glass slide after heat treatment (a) with a slow heating and cooling rate of 2 $^{\circ}$Cmin^{-1} showing a good quality of coating with better adhesion with the slow heating and cooling rate. (b) with a fast heating and cooling rate of 5 $^{\circ}$Cmin^{-1}.

The improvement in adhesion of AgNp/silica to the glass substrate during these trials was inferred from an increase in thickness. Moreover, these coatings were observed to show the presence of silver nanoparticles, as indicated by the retention of a yellow colour on the coating, as well as an extinction peak around 400 nm during inspection by UV-Vis spectroscopy. This optimised process of decorating the coating on a glass substrate was then employed to coat the optical fibre, which is discussed in the next section.

3.2 Fabrication of AgNp/silica coated fibre and detection system

In this section, a detailed description of the method to fabricate a coated optical fibre, as well as the steps taken to decorate the AgNp/silica on the optical fibre are presented. The first step involves the selection of optical fibre, this is followed by methods of etching the optical fibre, including the choice of etching solution, which is aimed at removing the coating and cladding from the optical fibre. The effect of different temperatures, which influence the etching rate was also investigated. The efficacy of the etching solution in removing the cladding and the coating was assessed based on the measurement of the thickness of the etched and unetched optical fibre using a high-resolution microscope. This is followed a section by a section on the thermal treatment of the coated optical fibre.

3.2.1 Selection of optical fibre

Optical fibres consist of different types designed for different applications. For a specific application, the choice of optical fibre depends on several factors such as cost, their sensitivity to the target application, and the tolerance to the environmental conditions where it will be used. The optical fibres designed for use as a pH sensor are expected to be sensitive to changes in pH, in addition to being inexpensive and stable to changes in temperature and chemical environment where it will be used [67,68]. For this study, high temperature and high-pressure conditions were also of concern.

Therefore, the fabrication of a pH sensor needed that careful choice of the type of optical fibre is quite important. This is because it is possible for the outer layers of the optical fibre to degrade when exposed to high temperatures and other harsh conditions. Moreover, the functionality as well as durability of the coated optical fibre could be severely compromised under high-temperature and high-pressure conditions. This suggests that the chemical composition of the glass material is quite important when choosing an optical fibre for a specific application.

For high-temperature and high-pressure environments, it is recommended that optical fibres should be made using thermally stable materials such as silica. This is because silica-based optical fibre is thermally stable up to 1100 $^{\circ}$C [194,195]. In

addition, the nature and thickness of the coating are also important to ensure additional protection of the core from damage or degradation during service. In this study, a multimode optical fibre (product model: FG105UCA, Thorlabs), having a glass core was used for the trials. Conventional optical fibres with plastic cores are unsuitable for harsh conditions as the one used in this study. The diameter of the core of the optical fibre used in this study was 105 µm, and the numerical Aperture (NA) is 0.22, which has a bandwidth of 250-1200 nm. This wide bandwidth is highly desirable as it matches the bandwidth expected of silver nanoparticles, which are 400 nm.

A multimode optical fibre (product model: FG105LCA, Thorlabs) with a core diameter of 105 µm and having the same numerical Aperture (NA) of 0.22, decorated with gold nanoparticles embedded in silica has been found to be useful [82,83,158]. A good optical response in terms of sensitivity to pH measurements has been reported for this fibre. The bandwidth of the optical fibre reported in their study is 400-2400 nm, while the LSPR bandwidth of gold nanoparticles is about 525 nm. This suggests that the chosen optical fibre was suitable for gold nanoparticles as its bandwidth falls within the range of the optical fibre. However, it might not be suitable for silver nanoparticles as there might be attenuation due to particle size variation falling below the bandwidth limit of the optical fibre. For this reason, an optical fibre model (FG105UCA), which falls within the bandwidth range of silver nanoparticles was chosen to prevent attenuation.

Furthermore, the performance of an optical fibre in high-temperature and high-pressure environments can also be affected by the type of optical fibre considering the composition and mode of operation of the optical fibre. The single mode which allows only one wavelength of light to pass through can have a higher sensitivity. However, the restriction of operation within a single wavelength poses limitations for sensor applications. On the other hand, multimode optical fibres allow multiple wavelengths of light to pass through which is ideal for use as a pH sensor. Therefore, in this study, a multimode optical fibre was used in all the trials, this is due to the fact the intended application requires a specific wavelength range of 400 to 800 nm rather than a single-mode optical fibre.

3.2.2 Connection of optical fibre to light source and detectors

In this section, the materials used for the connection of the optical fibre, as well as the detailed description of the various parts involved, are discussed. The entire optical fibre connection consists of a detector (USB 4000, ocean optics), light source (halogen lamp), straight tip (ST) terminator, adaptors (ST-ST), and optical fibres (FG105UCA, Thorlabs). In industry, different types of terminators are used to modify the ends of the optical fibre. These include: straight tip (ST), subscriber connector (SC), lucent connector (LC), ferrule connector (FC) and sub-miniature version A (SMA).

The choice of terminator depends on the intended application and instrumental requirements. To connect the optical fibre, it is essential to fix the terminator at both ends of the optical fibre, which allows the connection of one optical fibre to another. For this project, an ST terminator was used due to its availability, cost effectiveness and ease of installation. Although a ready-made ST-ST (both ended ST) terminated optical fibre is available, but it was quite expensive, at about £95 for 1 m length. Therefore, a bare optical fibre (Model FG105UCA, cost only £2 per meter) was purchased, and the terminators were purchased separately and the system was built from basic parts. The steps involved in preparing the ST-ST terminated optical fibres are discussed below.

3.2.3 Preparation of ST-ST terminated optical fibre in the laboratory

In order to terminate the optical fibre, two essential tools were used, which included: a mechanical stripper and a fibre cleaver (model FC-6S), as shown in Figure 3.18. A couple of unique ST terminators (Model: B10127C) and optical fibre clamps (Model: BFT1) were also purchased from Thorlabs, an optical fibre supplier company. A mechanical stripper is a tool used to remove the coating made of polymer from the optical fibre, while the fibre clever is used to cut the optical fibre and straighten the ends, as shown in Figure 3.18 (b).
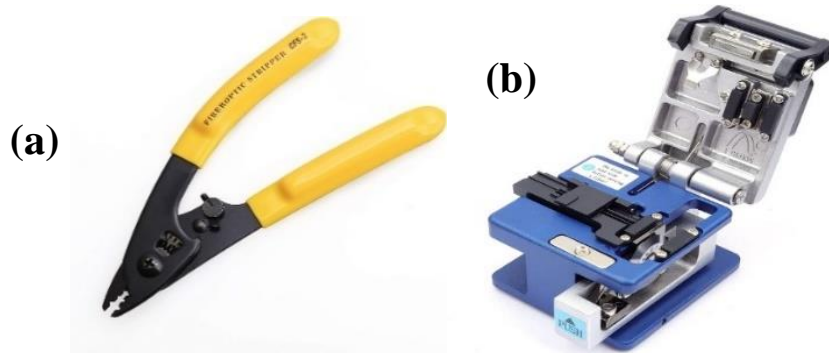
Figure 3.18: The optical fibre termination tool (a) mechanical stripper (b) fibre cleaver.

In order to assemble the ST terminator at the end, the mechanical stripper was used to remove the cladding of 15 mm at both ends, after which the fibre cleaver was used to cleave the end into a flat shape, as shown in Figure 3.19. A flat ending of the fibre is essential if it must be connected to another optical fibre without loss of light. Moreover, a flat end provides minimal connection loss, as has been found by other researchers [196,197]. After the cleavage of the optical fibre, the ends were cleaned using lint-free wipes to remove dust. At this point, the optical fibre is ready to be assembled with other parts. This is the final step for the termination process in order to assemble the fibre and connect it with the ST terminator.
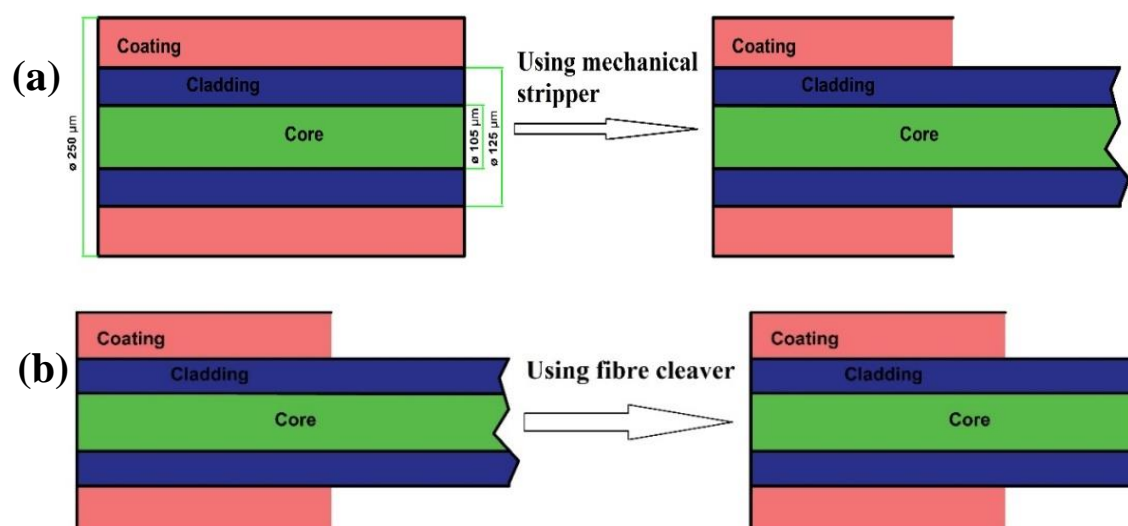
Figure 3.19: A schematic diagram showing the termination process of the optical fibre. (a) Fibre end after coating removal using a mechanical stripper, (b) Fibre end after straightening the ends using a fibre cleaver.

A fibre clamp is designed to join the bare optical fibre with the ST terminator. The terminator interface is equipped with a magnet and alignment key to attach and align compatible terminators quickly and could be locked into place. The clamp was equipped with rubber grips to minimise stress on the fibre and hold the fibre in a fixed position. Once the ST terminator was placed on the clamp, the stripped fibre was fed through the clamp and ST terminator until the core of the fibre reached the end of the terminator, as shown in Figure 3.20. Then, the clamp was released to hold the optical fibre at a fixed position. The ST termination process was carried out in this manner for both ends of the optical fibre. An advantage of this method is that the terminator can be reused, which is quite economical. The final step involved the connection of the ST-ST terminators to the light source at one end of the optical fibre and the UV-visible spectrophotometer at another end, which is discussed in detail in the next section.
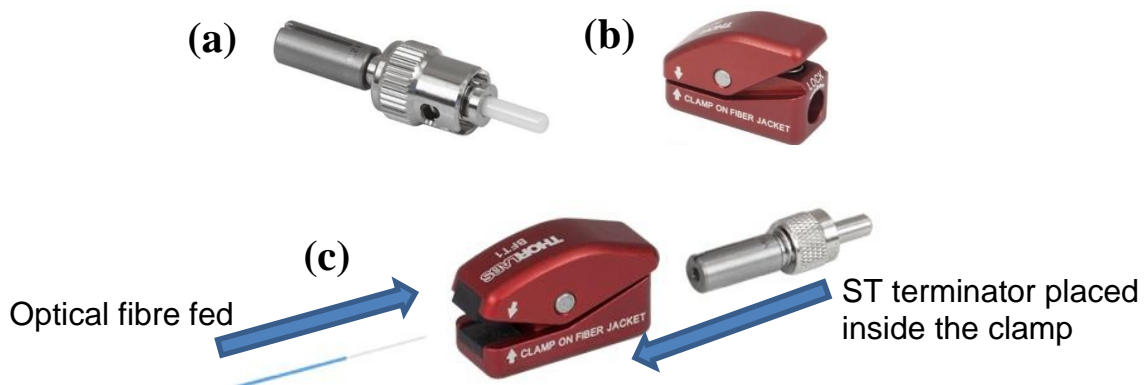
Figure 3.20: Pictures showing the instrument required for the termination process (a) ST terminator (Model: B10127C), (b) optical fibre clamp (Model: BFT1), and (c) assembly of the optical fibre and the clamp [198]

3.2.4 Connection of ST-ST terminated optical fibre with a light source and detector

The key components that constitute the sensor system used in this study include: a light source, detector, and optical fibre. A comprehensive description of each component including its role and functionality is hereby described.

3.2.4.1 Light source

The light source comprises of a 400 W halogen lamp, which is housed within a modified lamp enclosure (LSH-T100, supplied by Horiba Jobin-Yvon). A metal case was used to protect it against exposure to ambient light. The halogen lamp is encased in a metal case, as illustrated in Figure 3.21 (a). This serves as a protective barrier which protects against direct contact of the emitted light with the eye. It also includes a tube that connects the optical fibre to the light source. When the lamp was in operation, it was observed that the metal case heated up. To mitigate this issue, a USB fan was strategically positioned at the base of the lamp to enhance heat dissipation and prevent overheating. Additionally, a shutter mechanism was incorporated within the metal case to regulate the light entering the tube. This feature was instrumental in selectively permitting or obstructing the passage of light into the fibre, ensuring desired light transmission efficiency.

To secure the optical fibre in place, Ø10 mm ferrules were used, as illustrated in Figure 3.21 (c). These ferrules served as connectors, ensuring a secure and reliable connection between the optical fibre and the surrounding components. In order to exercise control over the power output, the light source was connected to a direct current (DC) power supply. This connection allows for the manipulation of both voltage and current while effectively regulating the power of emitted light. The power supply employed in this setup operates within a voltage range of 0 V to 30 V. This provides a suitable range to adjust the light intensity to suit experimental requirements. The light source used for the experiments was controlled by a power supply, which allowed one to dial in the current or voltage manually as per experimental needs.
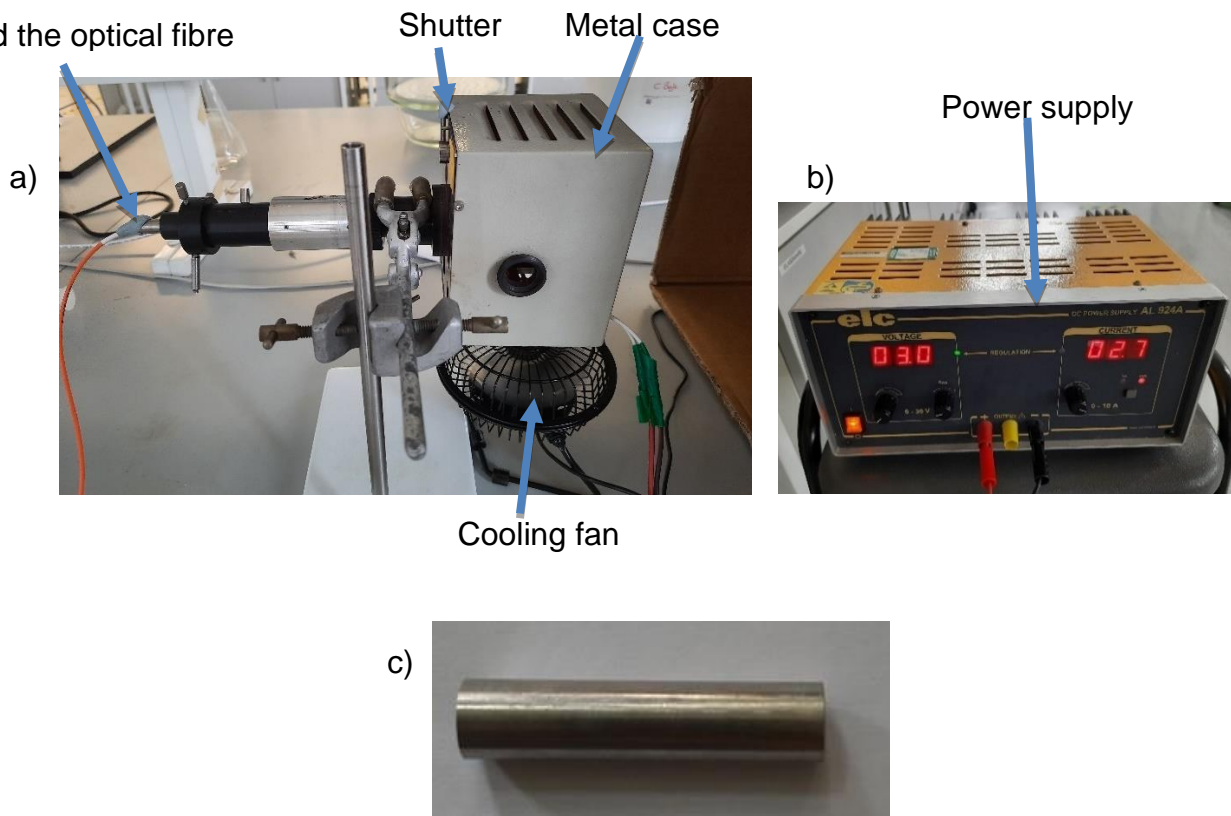
Figure 3.21: The image of the light source showing: (a) light source, (b) power supply, (c) Ø10 mm ferrule incorporated into the tube holding the optical fibre.

3.2.4.2 Detector

A UV-visible spectrophotometer, specifically the USB 4000 model manufactured by Ocean Optics, was employed as the detector in this study. Ocean Optics is recognised as a prominent provider of spectroscopy solutions. The USB 4000 spectrometer (as shown in Figure 3.22) is specifically tailored for applications involving optical fibres. It encompasses the fundamental operational principles and mechanisms of a UV-visible spectrophotometer, as explained in the preceding section (3.1.2.4). Notably, the key distinction lies in its design with respect to optical fibre usage in the absence of an integrated light source. UV-visible spectrophotometers play a crucial role in the quantitative analysis of light absorption, transmission, and reflection within the ultraviolet (UV) and visible (Vis) sections of the electromagnetic spectrum. These instruments employ an assembly of optical components and detectors to collect and analyse light. The portable and easily

installable nature of this UV-Vis spectrophotometer facilitates its versatility. It is proficient in detecting optical signals within a wavelength range of 200 to 1100 nm. Furthermore, the integration time can be tailored within the range of 3.8 ms to 10 seconds. Integration time represents the duration in which the UV-visible spectrophotometer's detector accumulates photons in a singular measurement. The utilisation of an SMA 905 connector is necessary to interface the optical fibre with this instrument [199].

Figure 3.22: A Picture showing the detector used in this study (Model: USB 4000, Ocean Optics).

To capture the intensity of light and its corresponding wavelengths, the detector (USB 4000 model by Ocean Optics) was connected to a computer running the "Spectrasuit" software. This software facilitated the recording of spectral data and allowed for the configuration of measurement parameters, instrument calibration, and visualisation and manipulation of spectral data. Notably, the software enables the specification of integration time for each measurement. It is important to note that the spectrophotometer possessed a maximum intensity detection limit of 65,000 arbitrary units (a.u.).

3.2.4.3 Assembling and completion of the connection

The process of establishing a connection between the optical fibre and the light source, as well as the detector, involves the integration of three distinct sections, as depicted in Figure 3.23. Section 1 comprises the detector and a fixed optical fibre, while section 3 includes the light source and another fixed optical fibre. The intermediate section, denoted as section 2, pertains to the coated optical fibre. The following sections provide a detailed description of each section separately.
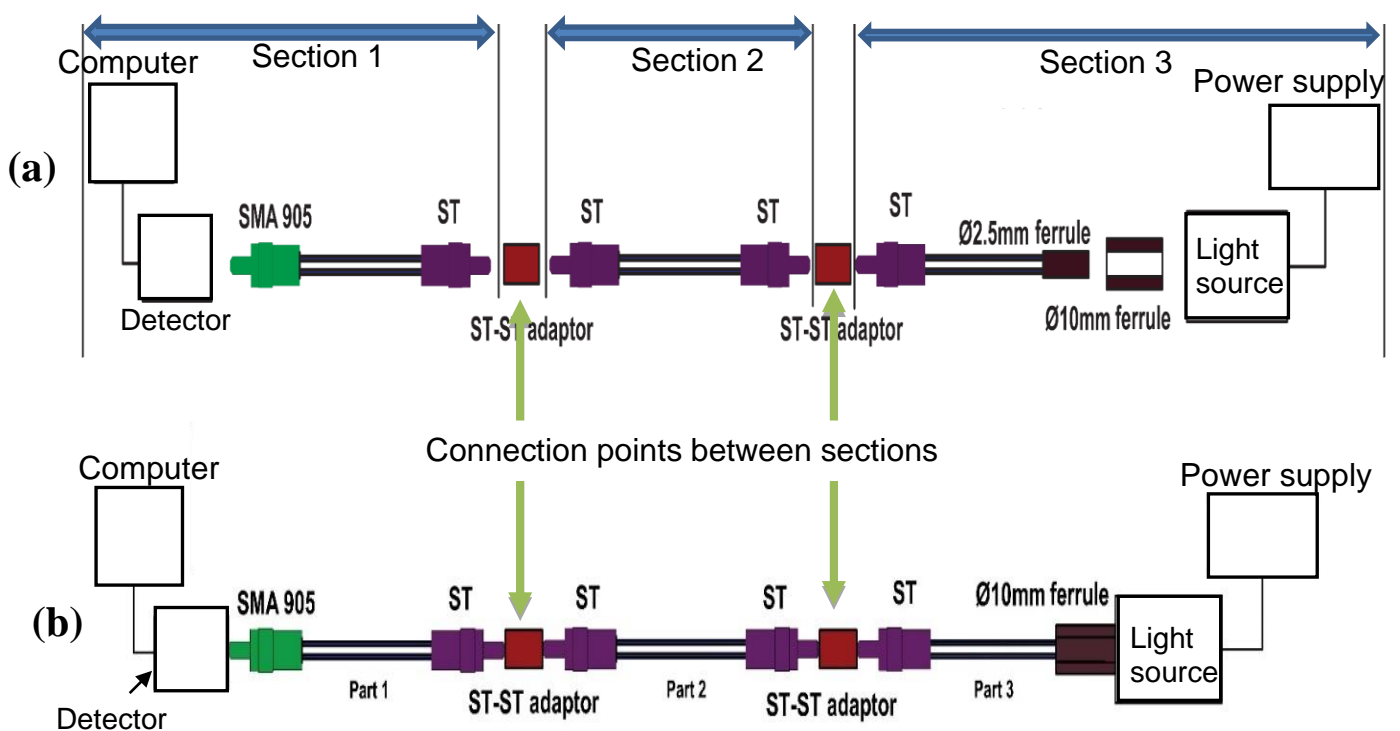
Figure 3.23: Schematic diagram showing the connection of optical fibres (a) Composition of each part of the optical fibres including terminators (b) Complete connection of all parts.

The first section, denoted as Section 1, involves the integration of a detector. As mentioned, the detector (model USB 4000 manufactured by Ocean Optics) was connected to a computer with a specialised software (Spectra Suite). This software facilitated the recording of light intensity readings across different wavelengths within the range of 100 to 1100 nm. To ensure seamless connectivity, all optical fibres were fitted with ST terminators. Considering the fact that the detector of the USB 4000 model is equipped with an SMA 905 terminator, it was imperative to employ an

optical fibre terminating in an SMA 905 connector at one end and an ST connector at the other. In this study, an optical fibre meeting these specifications was procured from Thorlabs and employed to establish the desired connection. One end of the SMA 905 terminator was connected to the detector, while the ST-terminated end was coupled to the subsequent optical fibre, constituting the second part of the connection.

The mid-section of the second part consisted of a bare optical fibre. This represents the most important part, where the AgNp/silica coating would be decorated following the aforementioned steps and further tested as a pH sensor. This section consisted of the ST-ST terminated optical fibre the construction of which was described in the previous section. Both ends of the optical fibre were connected to another optical fibre using an ST-ST adaptor.

Section 3 involved the use of a light source with a fixed optical fibre, with one end connected to the light source and the other end linked to section 2. One end of the optical fibre was coupled with a Ø10mm ferrule and connected to the light source, while the opposite end required an ST terminator, in line with the connections in section 2. The primary challenge encountered was the unavailability of a Ø10mm ferrule for purchase. Although Thorlabs offered a Ø2.5mm ferrule, procuring a Ø10mm ferrule would require a specialised custom order, which was deemed prohibitively expensive.

To overcome this challenge, an optical fibre was purchased from Thorlabs, and an optical fibre was procured from Thorlabs, featuring an ST terminator termination on one end and a Ø2.5mm ferrule termination on the other end. To facilitate the required coupling, a Ø10mm ferrule with a Ø2.5mm bore, measuring 50mm in length, was machined in the Chemical and Process Engineering workshop. The purchased Ø2.5mm ferrule from Thorlabs was procured and inserted into the prepared Ø10mm ferrule. Subsequently, the entire Ø10mm ferrule assembly was inserted into the light source, as depicted in Figure 3.23. The other end consisting of the ST terminator, was connected to another optical fibre terminated with an ST terminator using an ST-ST adapter.

3.2.4.4 Data capture and analysis

To assess light intensity and associated wavelengths, this study utilised the 'Spectrasuit' computer program in conjunction with the Ocean Optics USB 4000 model detector. This software facilitated the acquisition of spectral data, offering features for adjusting measurement parameters, instrument calibration, and visualisation and manipulation of spectral data. Notably, it allowed the customisation of integration time for individual measurements. It is important to highlight that the spectrophotometer had a detection limit for maximum intensity set at 65,000 arbitrary units (a.u.). Following the assembly of all three sections of the optical fibre, the objective was to achieve a light intensity of at least 60,000 a.u., as depicted in Figure 3.24. This target aligns with the detector's maximum detection limit of 65,000 a.u., ensuring optimal sensor sensitivity during the experimental trials, particularly in the context of its use as a pH sensor.
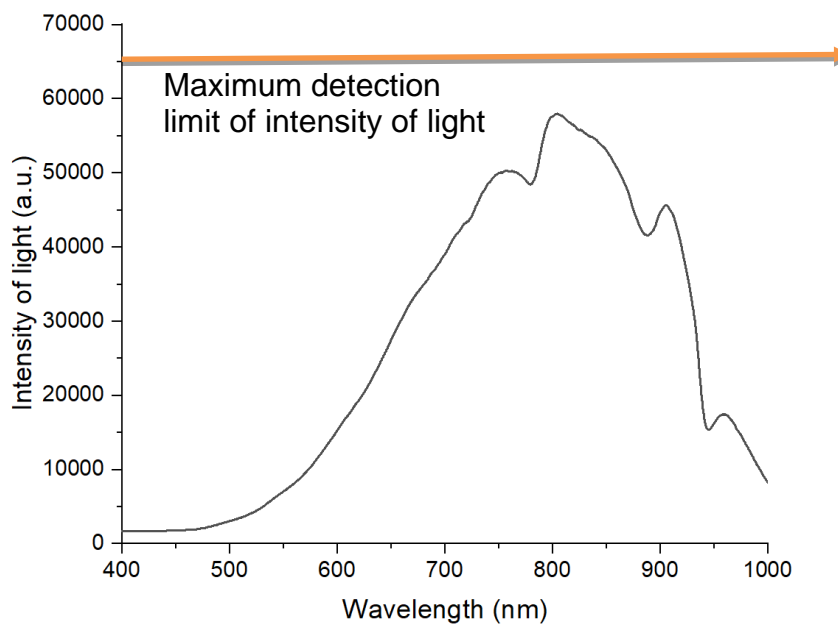
Figure 3.24: Intensity of light using the coated optical fibre as measured using a UV-visible spectrophotometer.

To achieve a targeted maximum light intensity of at least 60,000 arbitrary units (a.u.), the voltage of the light source was increased while simultaneously decreasing the integration time. After careful consideration, a voltage of 6.5 V was selected for the light source, and the corresponding integration time of 5 ms was set on the detector.

These experimental configurations were chosen to attain the highest achievable sensitivity. Several optimisation experiments were conducted, varying the voltage of the light source from 2 V to 6.5 V, in order to determine the optimal conditions. The results revealed that a voltage of 6.5 V provided the most favourable outcomes in terms of sensitivity. A comprehensive discussion of these optimisation experiments can be found in the forthcoming results chapter. Thereafter, the second part of the optical fibre design was coated with an AgNp/silica coating, as discussed in the following section.

3.2.5 Decoration of the optical fibre with the AgNp/silica coating

A multimode optical fibre (FG105UCA, Thorlabs) consisting of three layers: outer layer, cladding, and core was used for this study. The central region of the structure is referred to as the core, which consists solely of silica and possesses a diameter measuring 105 microns. The subsequent layer comprises the cladding, composed of fluorine-doped silica, with a thickness of 10 microns surrounding the core. The outer layer of the optical fibre is coated with a thickness of 62.5 microns coating composed of an acrylate polymer. The layout of the optical fibre describing all three layers is shown in Figure 3.25. In this study, the top two layers were removed to expose the core of the optical fibre so that it could be decorated with the AgNp/silica coating. The process of removal of the outer layer and the cladding is discussed below.
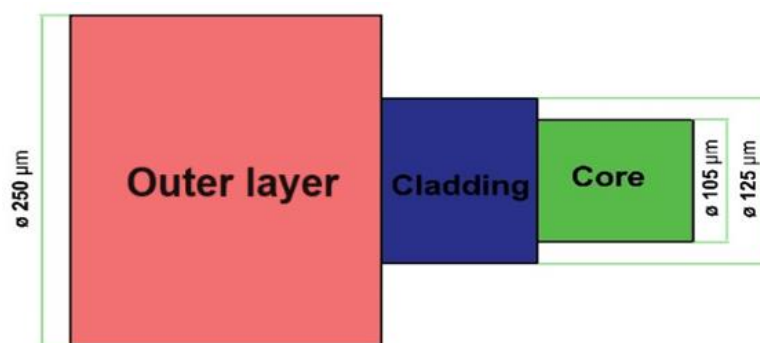
Figure 3.25: Schematic diagram of an optical fibre showing the three layers.

3.2.5.1 Etching of optical fibre

The main objective of the etching of the optical fibre is to remove the first two layers (outer layer and cladding). In the literature, concentrated hydrofluoric acid (HF) has been used to achieve this task [83,171,200]. However, hydrofluoric acid was avoided in this work due to its toxicity. Hydrofluoric acid was replaced by a less hazardous chemicals, such as 7 M NaOH that could etch the optical fibre more safely. Other researchers have used different concentrations of sodium hydroxide (NaOH) or potassium hydroxide (KOH) for similar purposes [172,201]. The etching process is a significant step required to replace the cladding with the Ag/silica coating on the core of the optical fibre so that light could interact with the coating to serve as a pH sensor.

However, the etching rate of sodium hydroxide or potassium hydroxide is slower than hydrofluoric acid. The etching rate of HF was reported to be 20 microns per hour, while 3 mol/L KOH could only etch 1.5 microns per hour at 95 °C and 3 mol/L NaOH could only etch 2.5 microns per hour at 95 °C [172].

This study employed a 7 M NaOH solution as the etching solution in order to remove the coating and cladding from the optical fibre. The selection of a concentrated NaOH solution was motivated by safety considerations in the context of removing the coating and cladding from the optical fibre. The complete removal of the coating and cladding was an essential objective of the etching process. The achievement of this objective was determined by the reduction in the optical fibre's diameter from 250 microns to 105 microns, which corresponds to the diameter of the core.

The experiment began by preparing a 50 ml solution of 7 M NaOH. The etching solution was then poured onto a petri dish and placed on a hotplate, maintaining a constant temperature of 70 °C for the etchant. Once the desired temperature was reached, a section of approximately 10 cm from the middle of the optical fibre was immersed in the etching solution. The etching process lasted for 12 hours at the same temperature, resulting in an average etching rate of approximately 12 μmh^{-1}.

Following the etching process, the fibre was taken out and washed with deionised water before being air-dried. The outer layer material used was a polymeric substance, while the cladding was made of silica. Since the etching rates of the two layers might differ, it was challenging to determine individual rates. As a result, an average etching rate was calculated for both layers. To improve the etching rate, additional optimisation procedures were implemented, which will be detailed in the subsequent sections. The next section also discusses various strategies to optimise the etching conditions.

3.2.5.1.1 Optimisation of the etching process

In this section, the different conditions employed to improve the etching rate using 7 M NaOH solution are reported. During the etching process, the optical fibre was etched, which resulted in a decrease in diameter. When the coating was removed, the fibre became fragile as the coating which protected the optical fibre was removed, and the optical fibre fractured at the slightest stress, as shown in Figure 3.26.
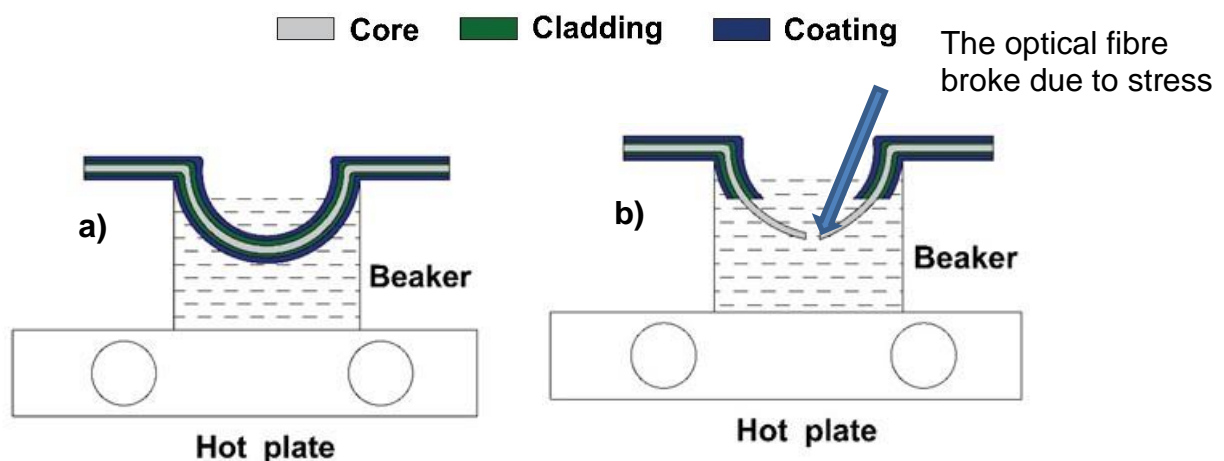
Figure 3.26: A schematic diagram showing the etching process of optical fibre in a beaker (a) before etching, (b) after etching, where the optical fibre was observed to break within the region where the etching was carried out, which may be attributed to excessive stress in an attempt to remove the etched optical fibre from the beaker.

To solve this problem, the beaker was replaced with a petri dish (which provided a gentle curved surface to rest) containing 50 ml of the etching solution, as shown in Figure 3.27. The dish was placed on a hotplate to heat the solution to 70 °C. The optical fibre was gently placed on the petri dish to avoid breakage, and the petri dish helped to reduce the stress during the etching process. The temperature was continuously monitored using an infrared temperature gun with an accuracy of ±1.5 °C during this process. As the solution was heated to 70 ± 1 °C, the solution evaporated continuously. To counteract the loss of liquid, the etching solution (7 M NaOH) was replenished dropwise every 15 minutes. The dropwise addition prevented a change in the reaction temperature and allowed the etching process was carried out for 12 hours.
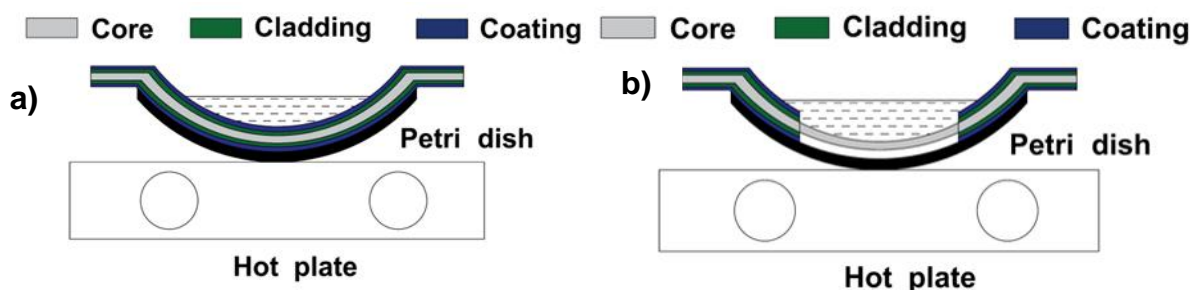
Figure 3.27: A schematic diagram showing the etching process of optical fibre using a petri dish (a) before etching, (b) after etching, where the optical fibre was etched without breakage.

3.2.5.1.2 Influence of etchant temperature on etching rate

The effect of different etchant temperatures ranging from 70 to 125 °C on the etching rate of optical fibre was systematically investigated in order to develop an efficient protocol for fibre etching. Optical fibres with an initial diameter of 250 μm were subjected to etching processes, reducing their diameter to nearly 105 μm. The experimental protocol involved conducting three replicates at each etchant temperature to ensure the reproducibility of the results. Average etching times, accompanied by their standard deviation (SD), were calculated and presented in Table 3.1.

Table 3.1: Effect of etchant temperature (70 to 125 °C) on etching rate of optical fibre using the etching solution of 7 M NaOH

Etchant temperature	Etching time (Average ± SD.)	Average etching rate
70 °C	720 ± 60 min	12.08 μmh^{-1}
80 °C	580 ± 50 min	15.00 μmh^{-1}
100 °C	270 ± 30 min	32.22 μmh^{-1}
125 °C	60 ± 5 min	145.00 μmh^{-1}

The effect of temperature on the etching rate clearly indicates a significant decrease in the diameter of the optical fibre as the etchant temperature increases. Notably, at 125 °C, the etching process achieved complete etching of the core within an average time of approximately 60 minutes. In contrast, etching at 100 °C required an average time of 270 minutes, while at 80 °C and 70 °C, the etching durations extended to 580 and 720 minutes, respectively. The data highlights the enhanced effectiveness of the etching solution with increasing temperature, leading to an accelerated etching rate. Remarkably, the temperature of 125 °C demonstrated a drastic reduction in etching time to 60 minutes. Notably, by increasing the etchant temperature to 125 °C, it was possible to increase the average etching rate to 145.00 μmh$^{-1,}$ and the etching time was reduced to 60 mins. It is important to note that the hotplate utilised in this study had a maximum temperature limit of 125 °C, and thus all etching experiments were limited to that temperature and required an etching time of 60 minutes.

3.2.5.2 Verification of coating and cladding removal

An optical microscope was employed to measure the diameter of the optical fibre before and after the etching process. Prior to conducting the experiment, the optical fibre was connected to both the light source and detector to establish the necessary optical pathway. This connection allowed the recording of the light intensity passing through the optical fibre. Subsequently, after the completion of the etching process, the etched optical fibre was connected to the light source and detector to record and compare the intensity of light with that of the unetched and etched optical fibre

samples. It is important to note that the cladding and outer layers serve the purpose of confining light within the core of the optical fibre. Therefore, the removal of these layers during the etching process implies that light would likely escape from the optical fibre. Therefore, by quantifying the intensity of light exiting the optical fibre, it becomes possible to verify the effectiveness of the etching process.

The spectra depicting the intensity of light versus wavelength, collected by a detector throughout the etching process, are presented in Figure 3.28. Initially, when the unetched optical fibre with a thickness of 250 µm was connected, the spectra displayed 100% light transmission, which is represented by the black line in Figure 3.28. Subsequently, the etched optical fibre was connected, and a similar recording of exiting light intensity was repeated. Notably, as the optical fibre was etched and its diameter reduced to 106 µm, a substantial reduction in light intensity was observed, as depicted by the red line in Figure 3.28. It became apparent that a significant portion of the transmitted light began to leak through the etched region of the optical fibre. Furthermore, as the etching time was increased and the diameter of the optical fibre continued to decrease, the spectra in Figure 3.28 demonstrated a further reduction in light intensity. Ultimately, when the core diameter reached 100 µm, the spectra indicated a complete leakage of light, depicted by the bottom line in Figure 3.28.

This analytical technique enabled the identification of light leakage upon transmission through the etched optical fibre, serving as empirical evidence of successful etching. The diameter of both the etched and unetched optical fibres was also measured using a high-resolution (HR) optical microscope, yielding precise measurements which corresponded to the fibre diameter before and after etching. Further elaboration on methodologies employed for these measurements is provided in the subsequent section.
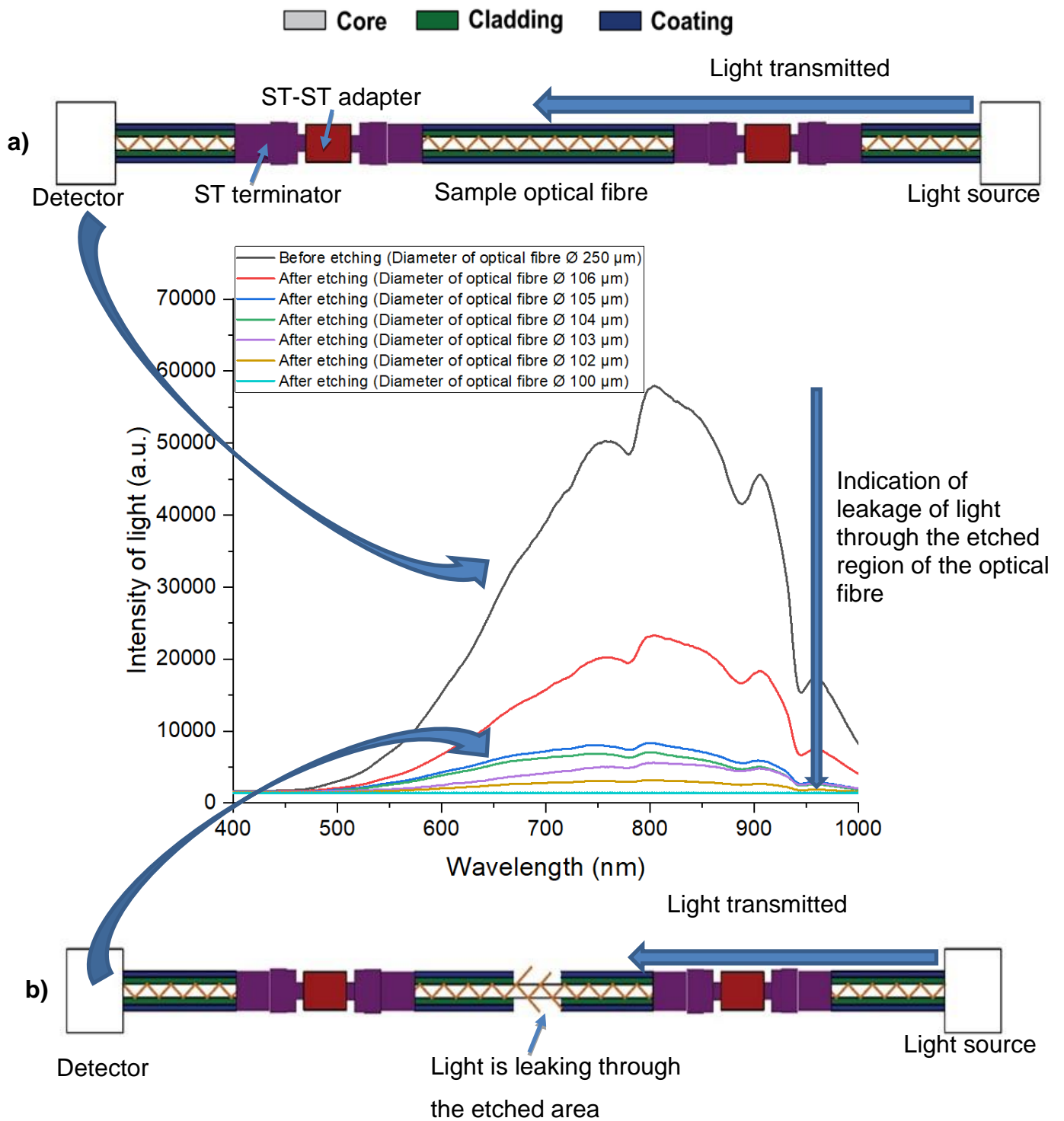
Figure 3.28: A schematic diagram showing the optical fibre with the corresponding UV-Vis spectrum (a) before etching and (b) after etching, showing the intensity of light when the optical fibre was etched to different thickness levels.

The diameters of the optical fibres after etching were determined using an optical microscope, and corresponding images are shown in Figure 3.29 (a)-(f). Specifically, Figure 3.29 (a) represents the unetched optical fibre with a diameter of 250 µm, as indicated by the black line in Figure 3.28. The diameters obtained from the measurements, denoted as (b) to (e), are shown in Figure 3.29 alongside the corresponding core diameters of 105 µm, 104 µm, 103 µm, and 102 µm. These measurements signify the gradual reduction in diameter brought about by the etching procedure. Notably, when the diameter reached 100 µm, as depicted in Figure 3.29 (f), complete leakage of light was observed, as indicated by the bottom line in Figure 3.28.

It is important to stress that attaining an optimal diameter is critical for ensuring adequate light transmission and to preserve the sensitivity of the optical fibre. If the core diameter is more than 105 µm or less than 103 µm, the system would have excessive light or insufficient light, potentially compromising the sensitivity of the optical measurements and its function as a sensor. The procedure described here was employed for batch etching of optical fibres with the objective of etching their core diameter to 104 µm. Each batch consisted of the simultaneous preparation of three optical fibres. Next, the procedure for decorating the AgNp/silica coating on the etched optical fibre is discussed.
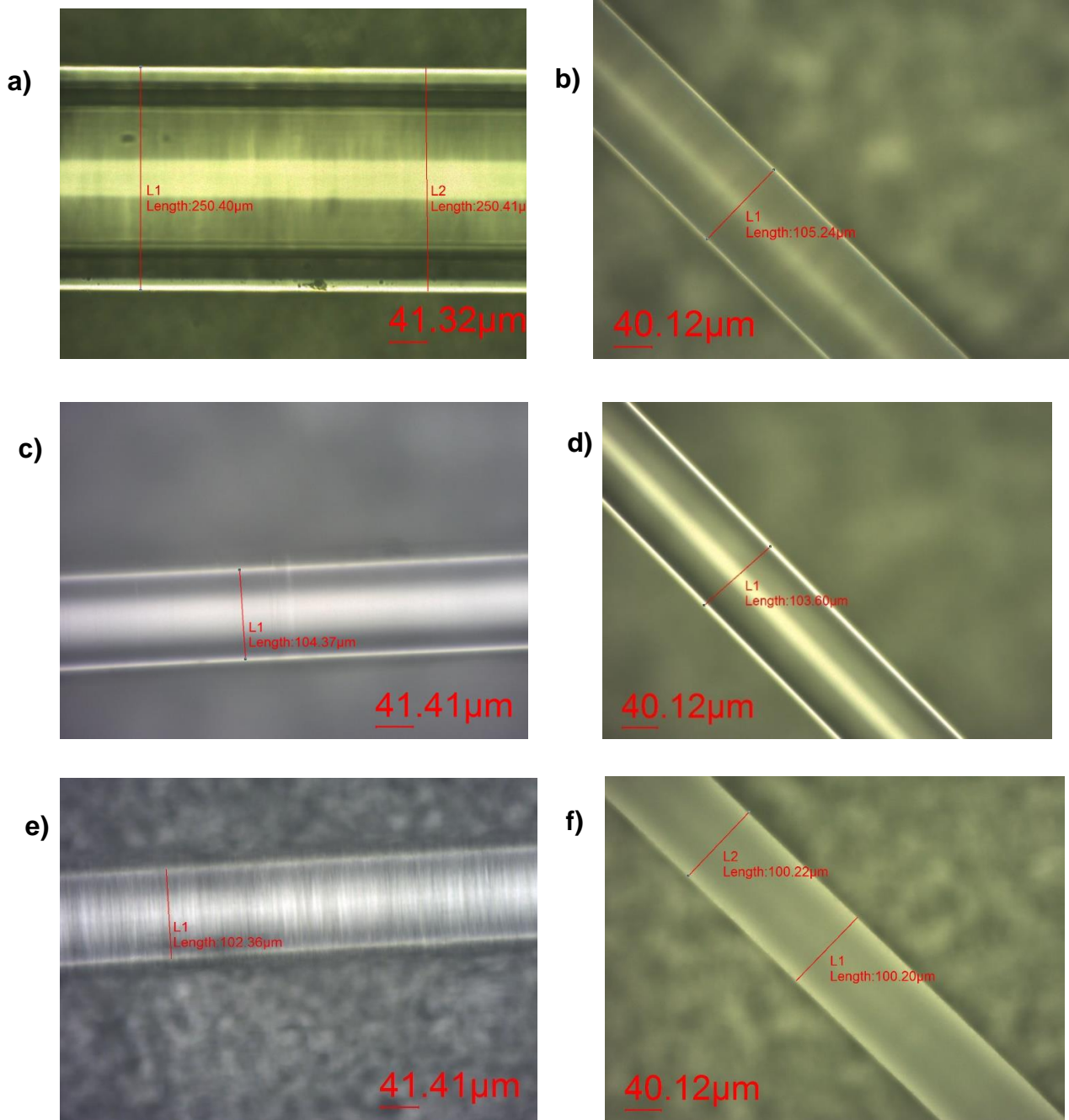
Figure 3.29: Micrographic images of the etched optical fibre showing different diameters before and after the etching, (a) 250 µm, (b) 105 µm, (c) 104 µm, (d) 103 µm, (e) 102 µm and (f) 100 µm.

3.2.6 Decoration of the etched optical fibre with AgNp/silica

The final stage involved in the fabrication of AgNp/silica coated optical fibres involves the dip coating of the etched region of the optical fibre with an AgNp/silica gel solution. A petri dish, as described in section 3.2.5.1, was utilised to place the etched portion of the optical fibre in an AgNp/silica gel and allowed to remain in contact for one minute. This was to ensure adequate adhesion between the gel and the core of the optical fibre. Thereafter, the optical fibre was gently lifted from the gel, permitting any excess solution to evaporate, as illustrated in Figure 3.30. This process was repeated thrice, involving the immersion of the optical fibre in the gel solution followed by removal in order to incrementally augment the coating thickness, thereby constituting a tri-dip coating process. Each experimental trial employed three distinct etched optical fibres to ensure the repeatability and reproducibility of the coating process.
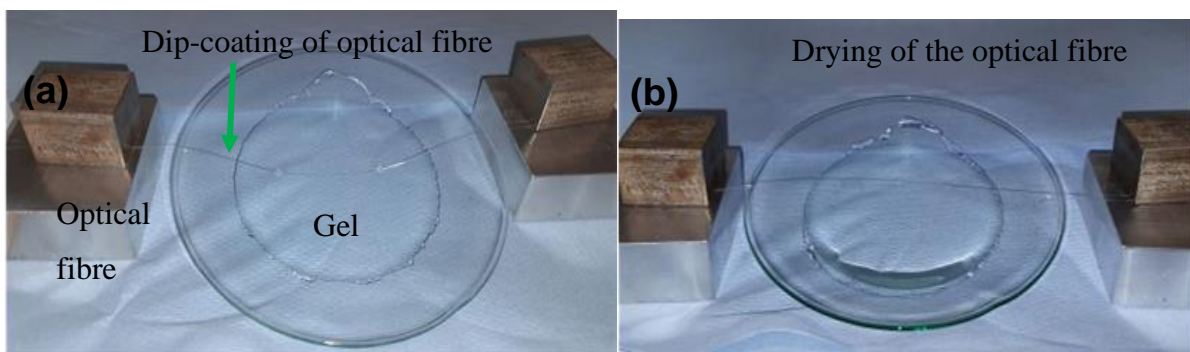
Figure 3.30:Dip coating and drying of coated optical fibre (a) Optical fibre was dip-coated in the gel, b) Optical fibre was dried after dip-coating.

Following the dip coating process, the optical fibre was subjected to heat treatment by placing it inside an oven. The heat treatment was performed at a temperature of 200 °C for a duration of 2.5 hours. To minimise thermal stress on the optical fibre, both the heating and cooling rates were carefully maintained at 2 °C per minute throughout the heat treatment process. The temperature was gradually increased from room temperature (20 °C) to 200 °C, with a heating rate of 2 °C/min. The temperature was then held steady at 200 °C for the aforementioned duration of 2.5 hours. Subsequently, a controlled cooling rate of 2 °C/min was employed to cool the

optical fibre to room temperature. The entire heat treatment procedure typically took approximately 5.5 hours to complete.

Following the completion of the heat treatment, the optical fibre was delicately removed from the oven, and the length of the coated region was measured using a measuring tape. The measured length was found to be 11 cm. Furthermore, the thickness of the coated area was quantified using optical microscopy, resulting in an example for which is illustrated in Figure 3.31. Although there was a variability of ±1 μm in the dipping process. The thickness after coating with AgNp/silica was always observed to be greater than the pre-coating thickness of 104 microns. The quantification allowed one to measure the AgNp/silica coating thickness on the optical fibre, which was determined to be approximately 5.5 microns.
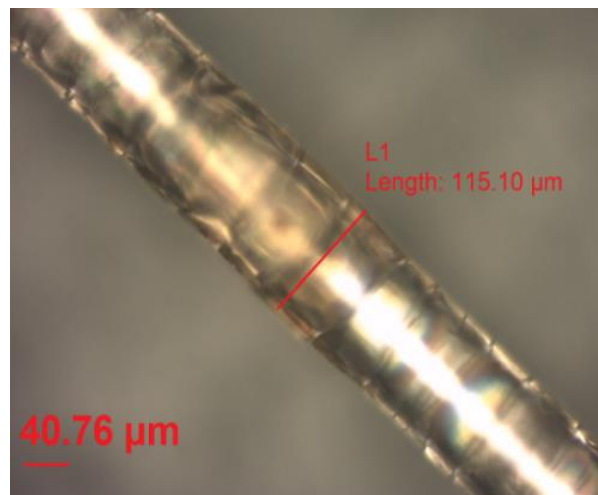
Figure 3.31: Micrographic image showing the following: (a) The length of the coated part of the optical fibre measured after thermal treatment, (b) A micrographic image showing the adherence of the coating to the optical fibre.

Therefore, these experiments indicated that the coating and cladding were successfully removed from the optical fibre, and the AgNp/silica coating was applied to the etched area of the optical fibre. The experiments also proved that the coating process produced AgNp/silica coatings of reproducible thickness. Prior to commencing the preparation process for the coated optical fibre, a microscopic examination of the optical fibre's diameter was conducted at three key stages: before etching, following etching, and ultimately after the application of the AgNp/silica

coating onto the core. The optical fibres with significantly different thicknesses were excluded from the trials. These flawed fibres were discarded appropriately in a dedicated bin.

3.3 Development of a pH sensor using an AgNp/silica coated fibre

This section aims to describe the fabrication and assembly of AgNp/silica coated optical fibres for optical pH measurement. Two distinct sets of experimental apparatus were developed and employed for these experiments. One is designed for conducting experiments at room temperature, and the other specifically tailored for high-temperature and high-pressure conditions. An in-depth analysis for the assessment of sensor performance through the evaluation of sensitivity, reproducibility, and repeatability is also provided.

3.3.1 System for room temperature

The experimental setup employed in this study is shown in Figure 3.32, representing the connections and components involved in the experiments. The configuration consists of the interconnection of three sections of optical fibres, one with the light source, and another with the detector, while the middle section of the optical fibre was designated as the sensor, as mentioned earlier (section 3.2.4.3). The equipment used consisted of a detector, specifically the USB 4000 model from Ocean Optics, which facilitated the recording of light intensity. The light source operated at a voltage of 6.5 V, and an integration time of 5 ms was determined to be the optimal setting for conducting the experiments. Spectrasuit software was utilised to record light intensity across different wavelengths, while Logger lite software was used to record the pH of the solution using a potentiometric pH probe.

Prior to commencing the experiment, a bare optical fibre was employed as the reference, enabling the recording of the signal transmitted when 100% light was incident on the system. For comparison, a potentiometric pH meter was included in the setup to monitor and record the pH of the solution. This step was taken to verify and compare the optical pH measurement with the potentiometric pH measurement method.
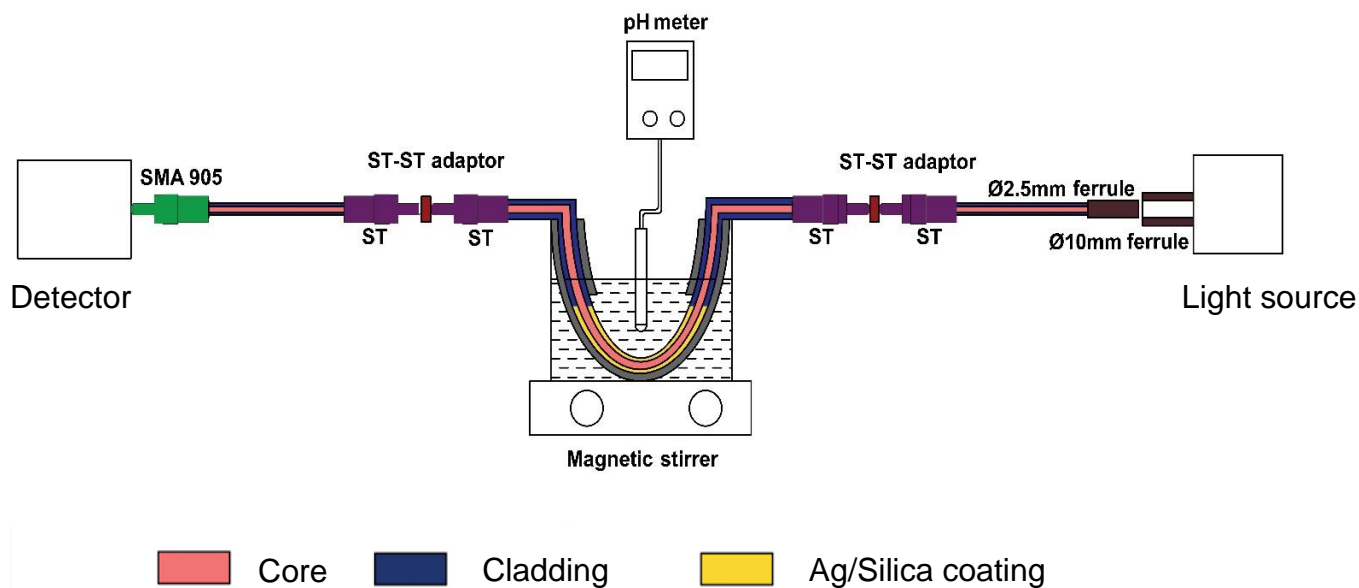
Figure 3.32: The schematic diagram showing all the connections and parts of the coated optical fibre.

The apparatus constructed to measure the pH of different solutions using the coated optical fibre was set up as shown in Figure 3.33. Due to the fragility of the optical fibre, it was placed within a plastic tube, which protected it from shock. The plastic tube was obtained by slicing the tubing into two halves at the middle. The optical fibre was then inserted in the tube such that the coated region of the fibre was exposed to the solution, which enabled it to remain in direct contact with the test solution. The arrangement of the coated optical fibre together with the plastic tube is shown in Figure 3.33 (a).

Then the coated optical fibre was placed in a liquid reservoir with a magnetic stirrer, which provided agitation to ensure a homogeneous solution. The connection between the AgNp/silica coated optical fibre, the detector, and the light source was established, with the coated optical fibre positioned in the middle section, as earlier described in section 3.2.4.3. A potentiometric pH probe was also placed within the solution to monitor and record the pH of the solution using the conventional method for reference and also to determine the corresponding light attenuation and pH changes, as shown in Figure 3.33 (b). The AgNp/silica coated optical fibre and the glass container were covered using a box to protect the entire apparatus from ambient light. This experimental procedure involved changing the pH gradually by the addition of either an acid or an alkali to deionised water (pH 6.3) via a dropper,

122

thereby enabling the alteration of the solution's pH within the range of 3 to 11 and recording the measurement by the potentiometric and optical methods.
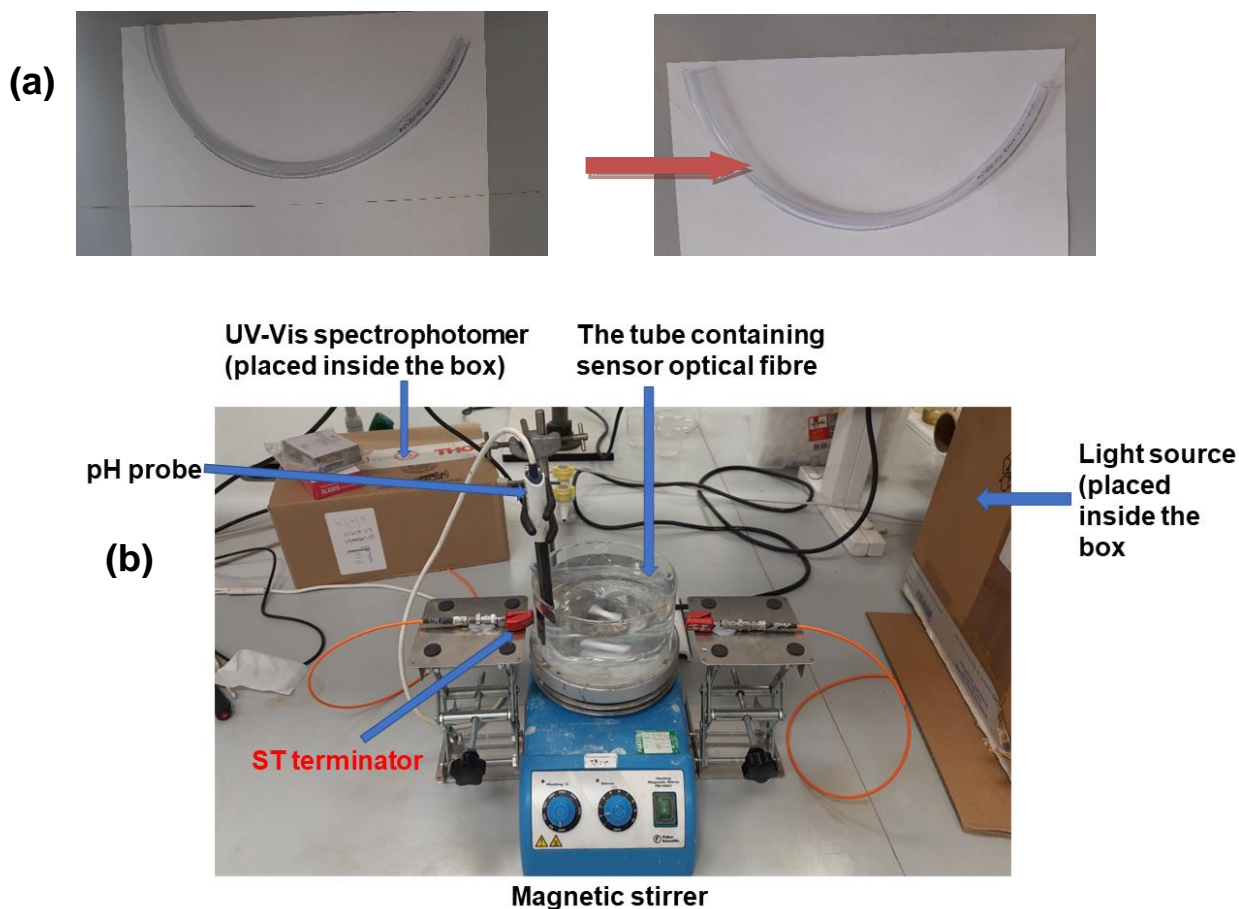
Figure 3.33: Images showing connections of the coated optical fibre (a) The coated optical fibre placed inside the plastic tube (b) The coated optical fibre with the tube was connected with the UV-Vis spectrophotometer and a light source in a liquid reservoir.

3.3.1.1 Procedure for the experiment

In order to provide a comprehensive overview of the processes involved in this study, it is essential to begin with the establishment of a clear day-counting system. Day 1 marks the initiation of the procedures, followed by a sequential count of subsequent days. On the first day, the preparation of the AgNp/silica composite solution commenced, taking into consideration that the gel would be ready after 2 days, necessitating lab access on day 3 and 4. The solution was prepared and then placed on a hot plate to maintain a temperature of 35°C for 2 days, with detailed procedures outlined in section 3.1.3.2.

Moving to day 2, the process of optical fibre preparation was initiated. Three optical fibres were extracted from the optical fibre bundle, prepared for connection, and underwent the termination process, as elaborated in section 3.2.3. After successfully completing the termination process, the optical fibres were connected to a light source and detector to ensure their readiness for use. Subsequently, the diameter of the optical fibre was measured using an optical microscope. This was followed by the commencement of the optical fibre etching process, aiming to remove the outer layer and cladding until reaching a diameter of 104 ± 1 μm, with detailed procedures provided in section 3.2.5.1. The diameter of the core was also measured using the optical microscope.

The morning of day 3 marked the readiness of both the AgNp/silica composite gel and the etched optical fibre. The etched optical fibres were then coated using the dip coating method, followed by a heat treatment process as described in section 3.2.6. The heat treatment was initiated on the morning of day 3 and concluded in the afternoon. In the afternoon, stock solutions required for the experiment were prepared in preparation for the following day's experimentation.

On day 4, it was removed of the AgNp/silica-coated optical fibres from the oven, followed by the measurement of their coated diameters using the optical microscope. These coated optical fibres were connected to the light source and detector, as outlined in section 3.3.1. The optical fibres were securely placed inside a glass container, which was then partially filled with deionised water. This container was positioned on a magnetic stirrer to ensure a homogeneous solution while adjusting the solution's pH. Subsequently, the recording of light intensity commenced, and experimentation with varying solution pH levels was initiated, with corresponding light intensity readings documented. For every pH value within the solution, it was recorded the intensity of light for three times, and the average intensity of light was calculated. Initially, a pH sensor calibration was performed by recording light intensity values for solutions with pH levels of 3, 5, 7, 9, and 11. Subsequently, following the calibration curve establishment, the acquired light intensity data from the experimental measurements could be translated into pH values within the solution.

3.3.2 System and apparatus for higher temperatures and pressures

The evaluation of the stability of the coated optical fibre under conditions of high pressure and high temperature lacks an established standard apparatus. To address this, a pressure vessel with model number XX6700P01 (depicted in Figure 3.34) was selected for use in the experiment. The pressure vessel is manufactured by Millipore Corporation. The details of this pressure vessel's specification can be found in Appendix C. It has a capacity of 3.8 litres (1 gallon), and it is specifically designed for high-temperature and high-pressure tests. This pressure vessel is mainly used to dispense fluids under pressure and is capable of maintaining high pressure within the reservoir. Constructed from 316 stainless steel, the pressure vessel demonstrates compatibility with both acidic and basic substances. The vessel's maximum gauge pressure capacity is 6.9 bar; however, in consideration of safety precautions, the experiments were limited to a maximum gauge pressure of 5 bar.

Figure 3.34: The image of the pressure vessel (model number XX6700P01, capacity of 3.8 lit, manufactured by Millipore Corporation).

The pressure vessel required several modifications to facilitate high-temperature and high-pressure experiments. The vessel had a limited number of ports, as depicted in Figure 3.34, necessitating customisation for the experimental requirements. A safety valve was incorporated to ensure maintenance of the maximum gauge pressure. Port 1 and Port 2 were the adapted to serve as the inlet and outlet for the optical fibre, respectively, as illustrated in Figure 3.35 (a). Union fittings were employed to replace the original fittings on both ports (Port 1 and Port 2) of the pressure vessel. At the lower section of the union fitting, a push-in fitting was added, as depicted in Figure 3.35 (a), to securely hold the tube where the middle section of the optical fibre

would be positioned. To ensure a reliable seal for the pressure vessel, a piece of polytetrafluoroethylene (PTFE) material was precisely machined to fit with the union fitting. Subsequently, a bore with a diameter of Ø250 µm was created at the centre of the PTFE component, serving as an aperture for inserting the optical fibre. Finally, a nut fitting was employed to establish a secure connection, completing the configuration, as depicted in Figure 3.35 (a).
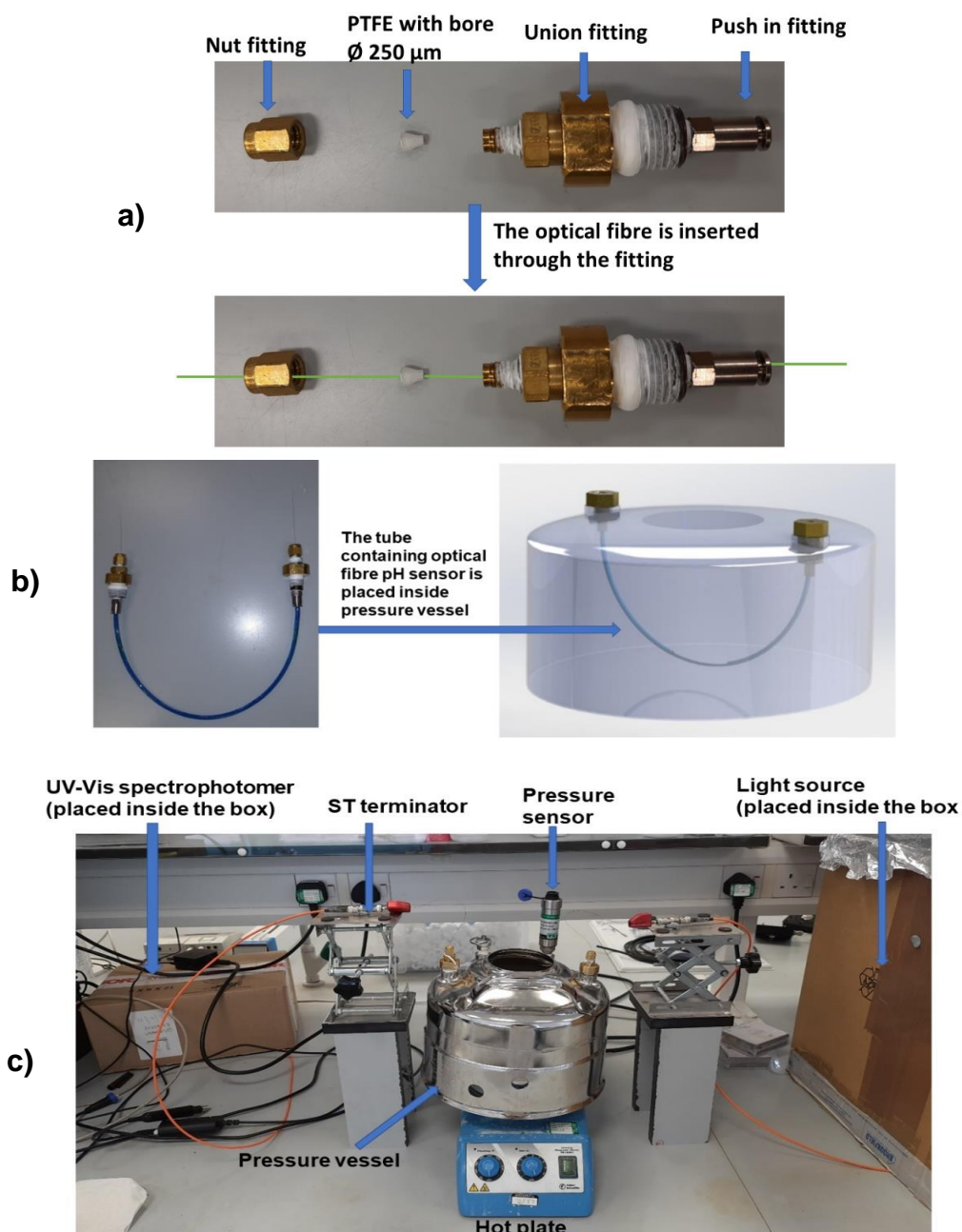
Figure 3.35: Images showing the connections for measurement of pH at high pressure and high temperature (a) Using different fittings of the pressure vessel (b) using a plastic tube and fittings (c) The complete setup.

The assembly involved the utilisation of a sliced tube (similar to that described in section 3.3.1) composed of polytetrafluoroethylene (PTFE). Considering the delicate nature of the optical fibre, it was initially enclosed within a protective tube to safeguard it against stress and shocks in high-pressure experiments. As mentioned, the optical fibre was inserted into the tube, ensuring that the AgNp/silica coated section remained exposed to the solution, thereby enabling direct contact between the optical fibre and the test solution.

Next, one end of the coated optical fibre was carefully threaded through the union fitting in conjunction with the push-in fitting, as depicted in Figure 3.35 (b), subsequently passing through the PTFE component and ultimately securing it within the nut fitting. The same procedure was followed for the other end of the AgNp/silica coated optical fibre, ensuring insertion into all the fittings of the other port, as illustrated in Figure 3.35 (b). The assembled optical fibre system was then cautiously positioned within the pressure vessel, with port 1 and port 2 designated for the insertion of the optical fibre. To prevent any potential leakage, all threaded areas were tightly sealed using PTFE tape.

The utilisation of Port 3 was reserved for the connection of a pressure sensor, serving the crucial purpose of gauge pressure measurement within the pressure vessel. A pressure sensor of model GS4200-USB, manufactured by ESI Technologies, was procured for this specific measurement task. Notably, this pressure sensor is engineered to operate within the pressure range of 0 to 16 bar (with an accuracy of ≤0.15%), encompassing the desired experimental conditions. In order to establish the necessary data acquisition setup, the pressure sensor was connected to a computer through a dedicated sensor interface ESI-USB©, as provided by the manufacturer. This interface facilitated seamless communication between the pressure sensor and the computer, enabling the acquisition and subsequent analysis of gauge pressure measurements.

After securely tightening the union fittings, ST terminators were affixed to both ends of the coated optical fibre. These terminators served the purpose of connecting the optical fibre to the light source and detector, as described in the earlier section dedicated for the completion of the connection (Section 3.2.4.3). Subsequently, a

total of 2.5 litres of the designated test solution was carefully introduced into the pressure vessel. Following this, the lid of the vessel was securely closed, ensuring a sealed environment for the experiment. The experimental setup for high-pressure and high-temperature measurements can be observed in Figure 3.36, depicting a schematic diagram illustrating the configuration of the apparatus.
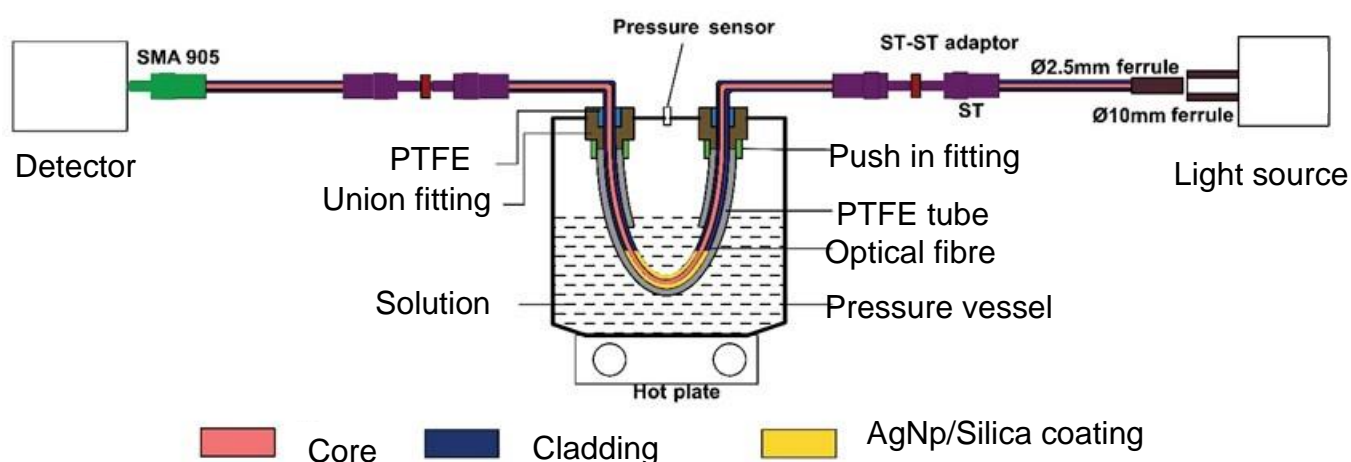
Figure 3.36: The schematic diagram of the experimental setup for the measurement of pH at high temperature and high pressure.

The pressure vessel was heated using a hot plate. When the solution was heated, the pressure inside the vessel was measured using a pressure sensor. The pressure sensor measures the pressure inside the vessel. Prior to heating, the pressure sensor was reset to zero, corresponding to gauge pressure. The pressure sensor was reset to 0 bar under ambient conditions, characterized by a room temperature of 25 °C or 298 K. Throughout all experimental procedures, a consistent reference point for pressure measurement was maintained, with 0 gauge pressure established as the baseline, reflective of the ambient pressure at 25 °C. Subsequent computations and data analyses were based exclusively on gauge pressure considerations. Thus, the reported pressure values herein specifically pertain to the gauge pressure within the vessel under investigation. However, a hotplate was utilized to heat the pressure vessel, which was challenging to maintain a uniform heating rate across all trials. A specific temperature setting was employed on the hotplate to raise the pressure vessel temperature to achieve a desired target gauge pressure (such as 1 bar, 2 bar, or 5 bar, among others). Once the target pressure

was attained, it was sustained for a duration of 30 minutes to ensure stability, after which natural cooling was allowed to return the system to ambient temperature.

In the realm of thermodynamics, the phase rule expresses a pivotal principle governing the equilibrium states within systems characterized by pressure (P), volume (V), and temperature (T), commonly referred to as "PVT" systems. Understanding the foundational principles of steam tables is crucial for comprehending their utility. The term "steam tables" denotes compilations detailing the properties of saturated steam, including vital information such as temperature-pressure correlations. An illustrative excerpt from these tables is presented below [202–204]:

Table 3.2: Pressure-Temperature data for saturated steam [202–204]

Temperature (°C)	Pressure (Bar)
20	0.02337
50	0.1233
100	1.01325
120.2	2.0
151.8	5.0
179.9	10.0

Saturated steam delineates a phase equilibrium scenario wherein equilibrium occurs within the process as shown in equation 3.7:

$$H_2O \text{ (liquid)} \rightleftharpoons H_2O \text{ (steam)} \tag{3.7}$$

During saturation, the aforementioned forward and reverse processes occur at equal rates [204,205]. Each temperature-pressure pair denoted above serves as a specification of saturated steam with respect to intensive variables. This inference derives from the Gibbs Phase Rule, a comprehensive exposition of which is available elsewhere. In the context of a generic system potentially comprising multiple chemical species across various phases, the count of independent variables may deviate from two [203–205]. For a system constituted of C components (distinct

129

chemical entities) and P phases, the number of independent variables denoted as F, is explicated by the Gibbs Phase Rule [204,205] as shown in equation 3.8:

$$F = C - P + 2 \tag{3.8}$$

Here, F signifies the number of degrees of freedom, i.e., the count of intensive variables that can be altered independently without affecting the phase count; P represents the number of phases; C conveys the count of components, synonymous with the number of unique chemical constituents.

The derivation of the Gibbs Phase Rule proceeds from the phenomenon of thermodynamic equilibrium among distinct phases, resulting in a reduction in the count of independent variables under such conditions. To elaborate, the equivalence of chemical potentials between two phases in equilibrium diminishes the count of independent variables by one for each equivalence. For instance, the chemical potentials of liquid and vapour are contingent upon both temperature (T) and pressure (P). However, when these phases attain equilibrium, their chemical potentials equate. If either pressure or temperature remains fixed, the other variable is unequivocally determined by this equivalence. When a liquid coexists in equilibrium with its vapour at a designated pressure, the temperature is stated by the equated chemical potentials and is denoted as the temperature. Similarly, at a given temperature, the vapour pressure is uniquely ascertained by the same equivalence relation.

In the context of the steam/water equilibrium system, C=1 (solely comprising H_2O) and P=2 (liquid and vapour phases). Consequently, applying the equation 3.8:

$$F = 1-2+2 = 1$$

Evidently, a solitary degree of freedom ensues, thereby signifying that upon specifying one intensive factor, all others are inherently predetermined. Thus, in referencing saturated steam at 179.9 °C, the temperature is fixed, thereby consuming the sole degree of freedom, and the pressure is inherently fixed at 10 bar.

Therefore, the acquisition of temperature data during High-Temperature High-Pressure (HTHP) experiments utilizing optical fibre proved unfeasible, while recording pressure remained possible using the pressure sensor. In accordance with the Gibbs Phase Rule, the singular recording of pressure suffices, given the existence of established correlations between pressure and temperature derived from standard steam tables. Additionally, a distinct series of experiments was conducted with the specific objective of calibrating both pressure and temperature measurements within the experimental vessel. This is similar to the concept of generating a "steam table", which in case would be a variety of chemicals dissolved in water. The vessel was set up as shown in Figure 3.37. All the fittings were prepared using the PTFE material in the CPE workshop to fit the thermocouple inside the pressure vessel. The thermocouple was connected to the computer through a Pico logger to record the inside temperature of the pressure vessel during the experiments. A calibration curve was constructed to convert the gauge pressure up to 5 bar to the corresponding temperature. The calibration curve was plotted for DI water, pH 5 using phosphoric acid and pH 9 using sodium hydroxide.

Several experiments were performed, which involved recording the intensity of light at the gauge pressure of 1 bar, 2 bar and 5 bar to observe the stability of the coating during the heating cycle. For each experiment, at first the hot plate temperature was increased. The gauge pressure of the vessel was increased when the temperature of the hot plate was increased due to the vaporisation of some of the fluid. The pressure and intensity of light were then recorded. After each experiment, the hot plate was turned off and allowed to cool. The intensity of light during the cooling cycle was also recorded. In addition, an optical microscope was used to measure the diameter of the optical fibre before and after the experiments to assess any dissolution of the coating due to the HTHP environment.
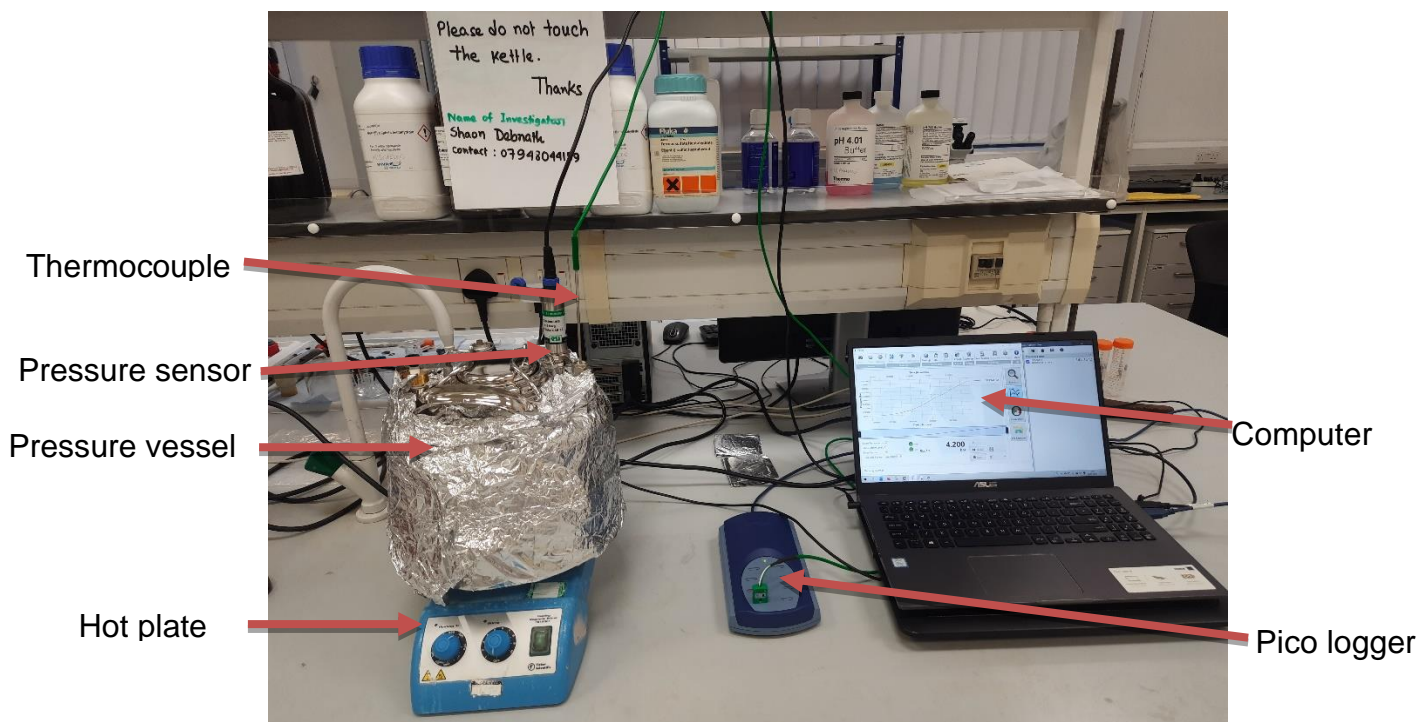
Figure 3.37: Images showing the connections for the calibration of pressure and temperature.

3.3.2.1 Procedure for the experiment

The preparation procedure for the AgNp/silica-coated optical fibre up to day 3 closely follows the description provided in section 3.3.1.1. However, on day 4, the experimental setup differed as it involved specialised apparatus for high-temperature and high-pressure (HTHP) environments. On this day, the AgNp/silica-coated optical fibres were removed from the oven, and their coated diameters were measured using an optical microscope. Subsequently, these coated optical fibres were connected to the light source and detector, as previously outlined.

To create the HTHP environment, the optical fibres were securely placed inside a pressure vessel, which was then filled with the test solution necessary for the experiment. The connection and fittings of the pressure vessel, including the optical fibre, were completed. The pressure vessel was positioned on a hot plate, and a pressure sensor was attached, initially reset to zero under ambient conditions. The intensity of light was recorded at a gauge pressure of 0. Notably, the intensity of light

was recorded three times for each data point, and the average intensity of light was used for subsequent calculations.

Following this initial recording, the pressure vessel was sealed with a lid. The hot plate was then turned on to raise the temperature within the vessel, and the intensity of light was continuously monitored and recorded as the gauge pressure increased. Once the desired gauge pressure was reached, it was maintained for half an hour to ensure stability. The hot plate was then turned off to allow the vessel to cool, and the intensity of light during the cooling cycle was recorded. This process involved multiple cycles of heating and cooling without opening the lid or disconnecting the optical fibres, demonstrating its reproducibility and repeatability. Furthermore, the entire experiment was repeated to confirm the consistency of the results.

3.3.3 Durability of the pH sensor

The durability and stability of the sensor in acidic and basic conditions are presented here. These experiments are grouped into two sections: the first involves measurements at room temperature, while the other section involves measurements at higher temperatures and pressures. These measurements are aimed at providing a comprehensive understanding of the sensor's chemical stability under varying conditions and environmental factors. The results obtained will provide valuable insights into the sensor's performance and reliability when exposed to different chemical substances.

3.3.3.1 Sensor at room temperature

It is essential to check the stability and performance of the optical fibre pH sensor in different chemical conditions. The experiments were conducted using 3 different acids and with sodium hydroxide solution as an alkali, as shown in Table 3.3. Firstly, fresh solutions of 500 ml of 0.01 M acid and the base were prepared separately. The acid and base were added using a pipette to control the pH of the solution for each experiment.

Table 3.3: Chemical solutions used for pH measurement using the coated optical fibre

Experiment no	Acid	Base
1	Phosphoric acid (H_3PO_4)	Sodium hydroxide (NaOH)
2	Sulfuric acid (H_2SO_4)	Sodium hydroxide (NaOH)
3	Hydrochloric acid (HCl)	Sodium hydroxide (NaOH)

For each experiment, the intensity of light at the wavelength of 300-1000 nm at different pH of 3,5,7,9 was recorded. Afterwards, the intensity of light at the wavelength of 800 nm for pH 3,5,7,9,11 respectively was extracted and plotted as a best fitted curve to obtain the optical pH calibration curve.

3.3.3.2 Sensor at higher temperatures and higher pressures

The stability of the coated sensor was also assessed at higher temperatures and higher pressure in different chemical conditions, as presented in Table 3.4. The first experiment was carried out in deionised water at different gauge pressures up to 5 bar to assess if there was any coating dissolution. Then, it was explored in an acidic solution of pH 5 prepared using phosphoric acid and then in an alkaline solution of pH 9 prepared using sodium hydroxide. Finally, the AgNp/silica coated optical fibre was checked in artificial seawater. The preparation of artificial seawater was carried out using ASTM standard (ASTM D 1141-98). This involved 0.613 M of NaCl, 54.65 mM of $MgCl_2.6H_2O$, and 28.82 mM of Na_2SO_4 were added to deionised water to prepare the artificial seawater.

Table 3.4: List of chemicals for the experiments at high pressure and high temperatures

Experiment number	Solution
1	Using deionised water (pH 5.8)
2	pH 5 using phosphoric acid (H_3PO_4)
3	pH 9 using sodium hydroxide (NaOH)
4	Using artificial seawater

3.4 Challenges associated with experimental arrangement

This study encountered certain challenges that are imperative for discussion in order to provide guidance for future designs of coated optical fibres intended for similar applications. Several difficulties were encountered during the experiments, which, if not adequately addressed, could have a substantial adverse impact on the sensitivity of the optical response of the AgNp/silica coated optical fibre. The two primary challenges identified include the ingress of ambient light through the light source and the presence of dust particles on the optical fibre. These challenges are discussed in detail below, outlining their potential implications and the importance of mitigation strategies for reliable experimental outcomes.

3.4.1 Interaction of ambient light with the system

The light source used in this experiment had built-in perforations (presumably for colling), as illustrated in Figure 3.38, which allowed ambient light to infiltrate the system. To ensure the integrity of the experimental setup and enhance the sensitivity of the sensor, a protective enclosure in the form of a box was employed. This enclosure served a dual purpose: shielding the light source from any potential influence of ambient light and creating a darkened environment conducive to optimal sensor sensitivity. This precautionary measure was deemed necessary due to the presence of ambient light, which comprises a range of wavelengths that could introduce interference and compromise the experimental outcomes.
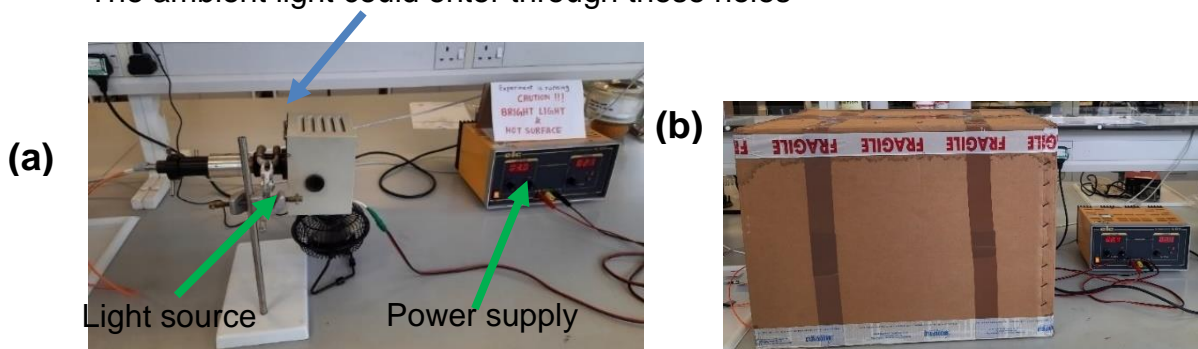
Figure 3.38: Images showing the connection of the coated optical fibre to the light source (a) The light source is connected to the power supply (b) A box used to protect the light source from ambient light.

To provide empirical evidence of the presence of ambient light passing through the light source, an experimental procedure was conducted following the completion of the three sections of the optical fibre, as outlined in section 3.2.4.3. The objective was to record the intensity of light detected when no light was transmitted to the system (0% light transmission). Spectral measurements were captured both before and after covering the light source with a box. The obtained spectra depicted variations in the intensity of light, with the uncovered light source revealing the presence of four distinct peaks, as illustrated in Figure 3.39. Conversely, when the light source was covered, all the observed peaks were no longer observed. This experimental evidence underscores the necessity of addressing the ingress of ambient light to ensure accurate and reliable measurements within the system.
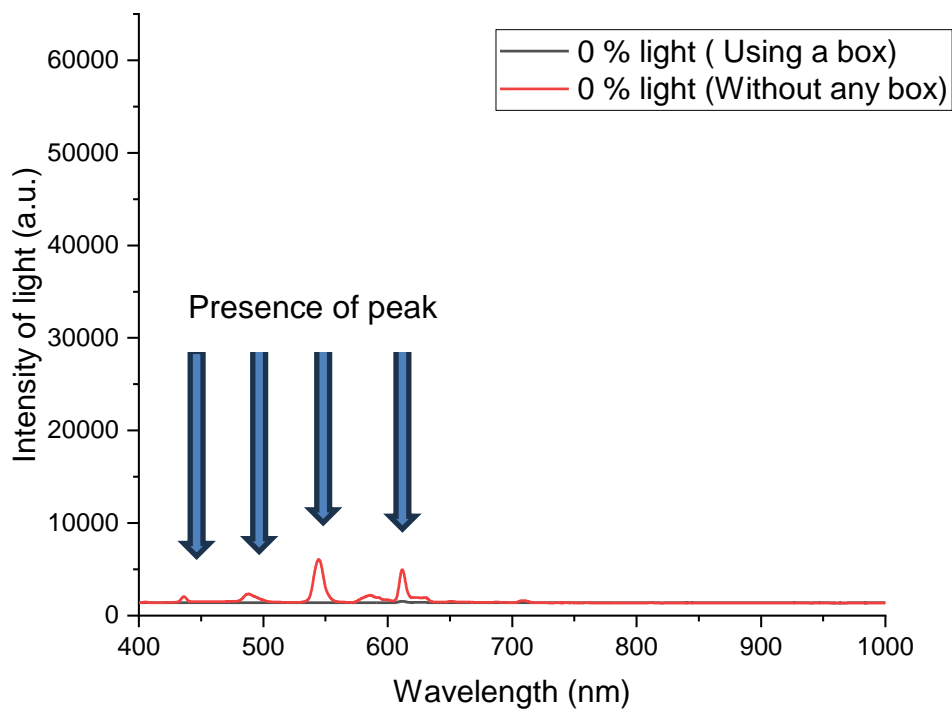
Figure 3.39: The spectra showing peaks indicating the presence of ambient light that entered through the light source.

3.4.2 Dust in the optical fibre

The connections of the optical fibre were divided into three sections, with interconnection facilitated through an ST-ST adapter. During the experimental procedures, it became apparent that the presence of dust within the optical fibre

connection could lead to fluctuating signals. The presence of dust particles on the optical fibre surface partially obstructed the passage of light, resulting in a reduction in signal intensity, as illustrated in Figure 3.40 (a).

a)

b)
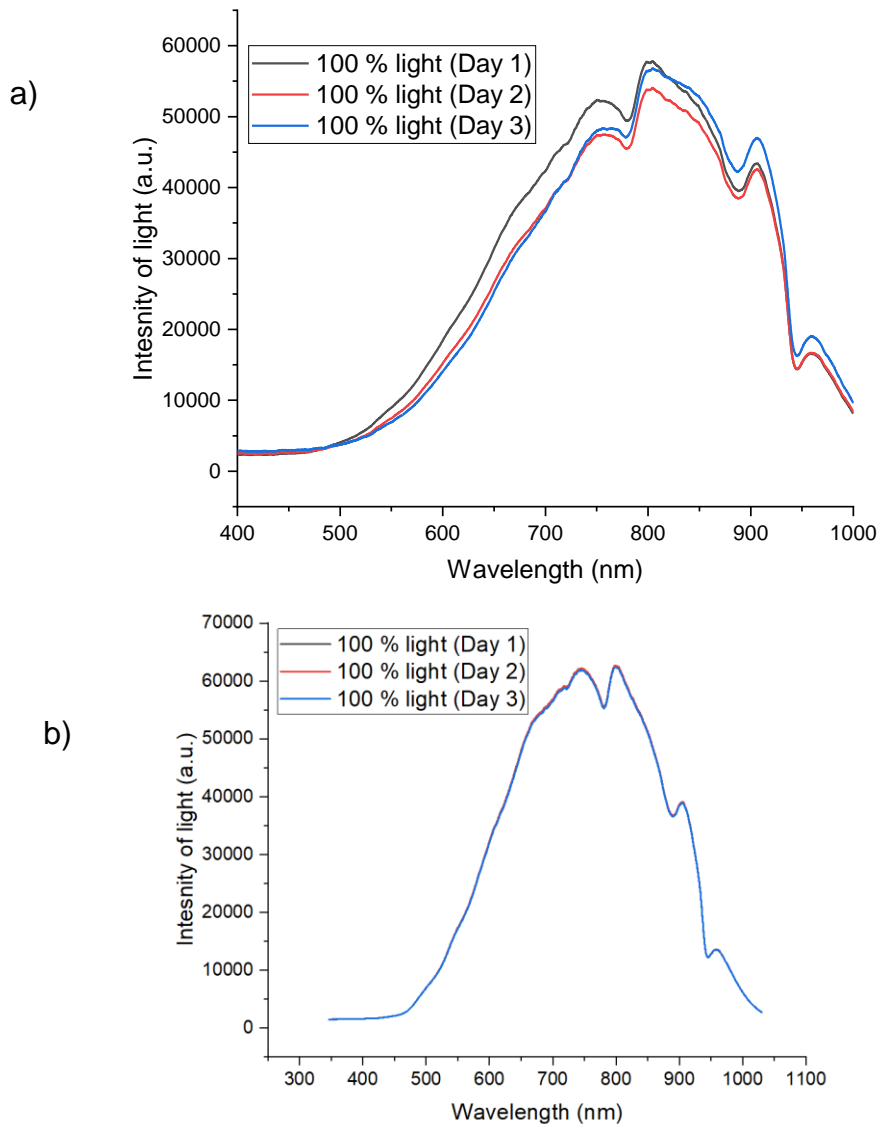
Figure 3.40: The spectra showing 100 % light transmitted through the system under different sanitary conditions (a) the presence of dust on the optical fibre causing the variation in signal that causes the error, (b) after cleaning the optical fibre showing a reproducible signal.

Notably, it was observed that even when employing the same experimental settings and optical fibre, signal variations were observed from day to day due to the presence of dust particles on the optical fibre. However, it was discovered that prior cleaning of the ends of optical fibres using the acetone before each experiment

significantly improved the signal quality, rendering it more reproducible on a day-to-day basis, as depicted in Figure 3.40 (b). This finding emphasises the importance of mitigating the impact of dust particles by implementing regular cleaning procedures for the optical fibres, thereby ensuring consistent and reliable signal measurements.

In order to mitigate the aforementioned issue, it was important to adopt certain measures. For example, prior to the onset of experiments, it was necessary to disassemble both the adaptor and terminator components, followed by thorough cleaning using lint-free wipes. This cleaning process ensured the removal of any dust or contaminants that could compromise the integrity of the optical fibre connection. Furthermore, upon completing the experiment, it was crucial to protect the terminator by securely covering it with the provided cap, as depicted in Figure 3.41. This preventive measure effectively shielded the terminator from the accumulation of dust particles, thereby maintaining the cleanliness of the optical fibre assembly. By adhering to these practices, the adverse impact of dust contamination on the experimental setup was effectively minimised.
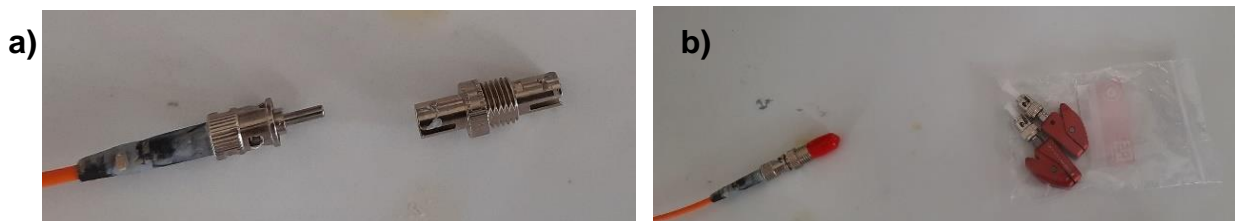
Figure 3.41: a) The ST terminators and adapters without cover, and (b) The ST terminators and adapters with cover.

3.5 Summary of experimental protocol

In this section, a brief recap is provided for the experimental protocol conducted at both room temperature and under high temperature and high pressure (HTHP) conditions. While the optical pH sensor successfully measured pH at room temperature, it encountered stability issues preventing pH measurement in HTHP environments.

3.5.1 Summary of pH Measurement at room temperature

The procedures for measuring pH at room temperature using the AgNp/Silica coated optical fibre are outlined below.

- Preparation of an AgNp/silica coated optical fibre.
- Preparation of the test solution for adjusting the solution's pH.
- Take a plastic tube and cut it into half at the midpoint of the coated optical fibre section, thereby exposing the coating.
- Gently place the plastic tube containing the AgNp/silica coated optical fibre onto a glass container where the experiments will be conducted. This glass container should be equipped with a magnetic stirrer, ensuring the mixing of the solution.
- Switch on the detector and light source. Establish a connection with a standard optical fibre (an optical fibre with cladding and coating) used as a reference. Record the I_{100} (with the shutter in the open position, allowing full light transmission through the system, considered as the full beam) and I_0 (with the shutter in the closed position, preventing light transmission through the system, considered as system noise).
- Replace the AgNp/silica coated optical fibre with the reference optical fibre and establish connections with the light source and detector.
- Carefully fill the glass container halfway, ensuring that the coated optical fibre is submerged in the water.
- Introduce a calibrated potentiometric pH probe into the solution to validate the optical pH measurements against potentiometric pH measurements.

- Cover both the light source and the glass container, along with the coated optical fibre, using two separate boxes to minimise the presence of ambient light in the system.

- Use a pipette to add acid or base solution drop by drop to alter the solution's pH. After each addition, wait for 30 to 60 seconds to stabilise the pH readings and light intensity. Record the light intensity corresponding to each pH value of the solution.

- Record the light intensity for pH values of 3, 5, 7, 9, and 11, subtracting I0 from each recorded intensity.

- Initiate the experiment by recording the light intensity three times for a specific solution.

- Lastly, construct a calibration curve to determine the optical pH for various chemical conditions. With this experimental setup, it is possible to measure the light intensity for an unknown pH solution and calculate its pH using the calibration curve.

- In order to ensure experimental reliability, each experiment was conducted thrice for any experiment, and the average value is presented in the results section. This provided the basis of variation for any measurement.

- Additionally, three optical fibres were prepared concurrently to assess the reproducibility within a batch. Sensitivity analysis was further conducted to evaluate variations across batch production.

3.5.2 Summary of stability test of the coating at higher temperature and higher pressure

The experimental procedure for the HTHP experimental apparatus involved several steps. First, pressure readings of the vessel were recorded using the HTHP apparatus. Subsequently, separate experiments were conducted to establish a correlation between pressure and temperature, which resulted in the creation of a calibration curve. This curve allowed for the conversion of gauge pressure to temperature.

Here's a refined version of the procedure:

- Prepare the AgNp/silica coated optical fibre.

- Prepare test solutions to adjust the pH of the solution.

- Insert the coated optical fibre into a plastic tube, cutting the tube in half in the middle section to expose the coating.

- Carefully place the plastic tube containing the AgNp/silica coated optical fibre inside the pressure vessel where experiments will be conducted.

- Switch on the detector and light source. Establish connections with a bare optical fibre (with cladding and coating) as the reference optical fibre. Record the intensity with the shutter on (I_{100}, representing full beam) and with the shutter off (I_0, indicating system noise).

- Replace the AgNp/silica coated optical fibre with the reference optical fibre, ensuring proper connections with the light source and detector.

- Carefully fill the pressure vessel with the solution, ensuring that the coated optical fibre is immersed in the water.

- Reset the pressure sensor to zero before commencing the experiments; all pressure readings are recorded as gauge pressure.

- Position the pressure vessel on the hot plate, but do not initiate heating yet.

- Complete the high-pressure fittings to secure the optical fibre in place, and then close the lid of the pressure vessel.

- Cover the light source with a box to minimise ambient light interference in the system.

- Begin the experiment by recording the intensity of light three times for each data point.

- Start heating on the hotplate and record the intensity of light corresponding to the gauge pressure. Subtract $I0$ from all recorded light intensities.

- Maintain the system at the desired gauge pressure for 30 minutes to stabilise the system; this constitutes the heating cycle.

- The heating and cooling cycle should be repeated more than once as it necessitates multiple cycles.

- At the end of the experiment, turn off the hot plate to allow the pressure vessel to cool down. Record the intensity of light and the corresponding pressure of the vessel. This cooling cycle concludes the experiments in the high-pressure and high-temperature system.

CHAPTER 4 Results: Optical Properties of Materials and Sensor Systems

CHAPTER 4

Results: Optical Properties of Materials and Sensor Systems

This chapter presents the results of the colloidal silver nanoparticles (AgNp), including the effects of various parameters such as the type of reducing agent, reaction time, and temperature. While some of the rationales for carrying out these experiments are presented in Chapter 3, the results needed much more detailed discussion to clarify the optimised methods and the behaviour of the optical sensor in the forthcoming chapters. Also, the stability of colloidal silver nanoparticles obtained from different synthetic routes is assessed and discussed. The chapter covers the outcome of embedding silver nanoparticles in silica and the application of the composite gel on a glass slide and optical fibre to form a coating. In addition, the chapter also addresses the effect of key parameters such as gelation time, reaction temperature, and the number of dip coatings, which significantly impact the quality of the fabricated coating for the optical fibre sensor.

Furthermore, the stability of colloidal silver nanoparticles obtained via different synthetic pathways is assessed and subsequently discussed. This assessment involves a thorough investigation into the outcome of embedding silver nanoparticles within a silica matrix. The application of this composite gel onto a glass slide and optical fibre is also developed upon, as it forms the basis for creating a protective coating. The chapter will also address the influence of critical parameters, such as gelation time, reaction temperature, and the number of dip coatings, all of which significantly affect the quality and performance of the fabricated coating tailored for the optical fibre sensor.

A pivotal feature explored within this chapter pertains to the durability of the coating, specifically its adhesion to the glass slide. This adhesion process is a crucial step in the fabrication of the optical sensor, and thus, its thorough analysis and discussion are paramount. Subsequently, the chapter proceeds to analyse the resulting coating through advanced characterisation techniques, including scanning electron microscopy (SEM), energy dispersive X-ray analysis (EDX), and optical microscopy. These findings are then compared against the results obtained in this study with

relevant literature, allowing for a comprehensive assessment of coating characteristics and performance.

These in-depth analyses and characterisations play a pivotal role in offering solutions to the challenges associated with the sensor's functionality and stability, particularly when subjected to the harsh conditions of elevated temperatures and pressures commonly encountered within the confines of oil wells. Consequently, the findings within this chapter lay the foundation for addressing critical issues and optimizing the performance of the optical sensor, ensuring its reliability in demanding operational environments.

4.1 Optical properties of colloidal silver nanoparticles and their stability

This section presents the full set of results showing the formation of colloidal silver nanoparticles using different reducing agents, such as sodium borohydride and trisodium citrate. Also, the effect of various parameters, such as temperature and reaction time, which influence the formation of silver nanoparticles and the estimated particle size and the stability of silver nanoparticles in solution are discussed. To ensure clarity, the results are organised into three sections based on the chemicals employed. The first section presents the results obtained when sodium borohydride was used as the reducing agent. The second section presents the findings when trisodium citrate was used as the reducing agent. The third section covers the results obtained when sodium borohydride and trisodium citrate were used in the same solution. In this case, sodium borohydride functions as the reducing agent, while trisodium citrate serves as the stabiliser.

The primary objective of this set of experiments was to synthesise stable silver nanoparticles since colloidal silver nanoparticles have been reported to be quite unstable due to enhanced aggregation during synthesis [93,122,206]. This was a challenging issue, especially when it involved embedding metal nanoparticles within a silica matrix whilst maintaining their functionality and structure. Nevertheless, various strategies were explored to enhance stability, including an assessment of the effect of temperature on gelation time and the effect of different reducing agents.

4.1.1 Optical properties of colloidal silver nanoparticles using sodium borohydride as the reducing agent

The formation of AgNp, as represented by the chemical equation 4.1, while the images of the synthesised colloidal solutions at different reaction times are shown in Figure 4.1.

$$AgNO_3 + NaBH_4 \rightarrow Ag + \tfrac{1}{2} H_2 + \tfrac{1}{2} B_2H_6 + NaNO_3 \qquad (4.1)$$
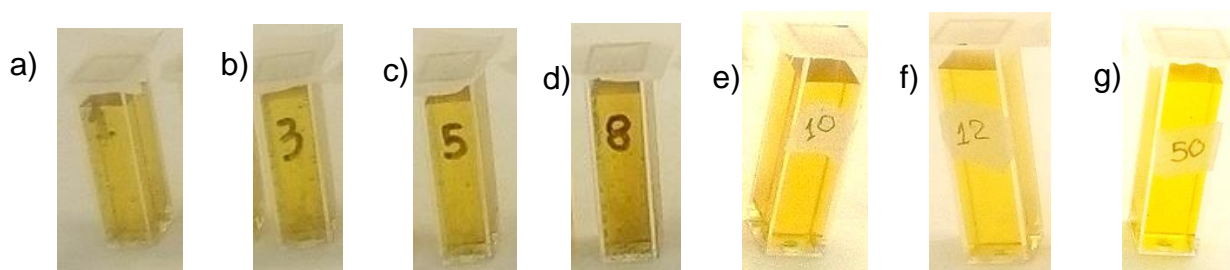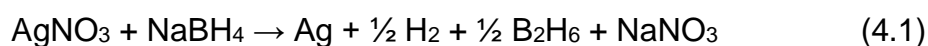
Figure 4.1: Image showing the formation of the colour of different intensities indicating the formation of colloidal silver nanoparticles at different reaction times for 1 mM $AgNO_3$: 2 mM $NaBH_4$: a) 1 min, b) 3 mins, c) 5 mins, d) 8 mins, e) 10 mins, f) 12 mins, g) 50 mins.

The results shown in Figure 4.1 indicate an increase in the intensity of the yellow colour as the reaction time increased. The formation of a yellow colour is an indication of the presence of silver nanoparticles in the solution [122,206–208]. In this study, the increase in the intensity of the yellow colour with reaction time could be attributed to the increased amount of silver nanoparticles with time. From the result, it suffices to assume that the efficacy of the reduction of silver nitrate using sodium borohydride is enhanced when sufficient time is allowed for the complete conversion of the starting material (silver nitrate) to silver nanoparticles.

The presence of silver nanoparticles in the solution was confirmed by the characteristic extinction of light around 400 nm, as has been stated in the literature [91,120–122,209,210]. The intensity of the yellow colour becomes more pronounced as the reaction time increases due to the increase in their concentration. As shown in Figure 4.1, cuvettes subjected to a reaction time of at least 10 minutes exhibited a more distinct yellow colouration compared to those with reaction times below this threshold. Furthermore, an extension of the reaction time to 50 minutes was

examined to study the stability of the colloidal solution. It was found that even after 50 minutes, the yellow colour remained unchanged, which was characterised by UV-Vis extinction spectra. This suggests that the colloidal solution of silver nanoparticles was stable.

The UV-Vis extinction characteristics of the colloidal silver nanoparticles are shown in Figure 4.2. An extinction peak is observed around 400 nm for all reaction times ranging from 1 min to 50 mins [91,211,212]. This is caused by the electrons of metal nanoparticles moving in sync with the light wave, which explains the observed extinction peak around 400 nm [122,206–208]. Figure 4.2 shows a Gaussian line fitting of the extinction curve, which was carried out to obtain more insight into the extinction characteristics. The extinction spectra showed an extinction peak of around 400 nm for all the samples recorded from 1 to 50 minutes, which is characteristic of the presence of silver nanoparticles [122,207,208,212]. The absorbance is observed to increase with reaction time, which indicates the increased amount of silver nanoparticles in the solution.
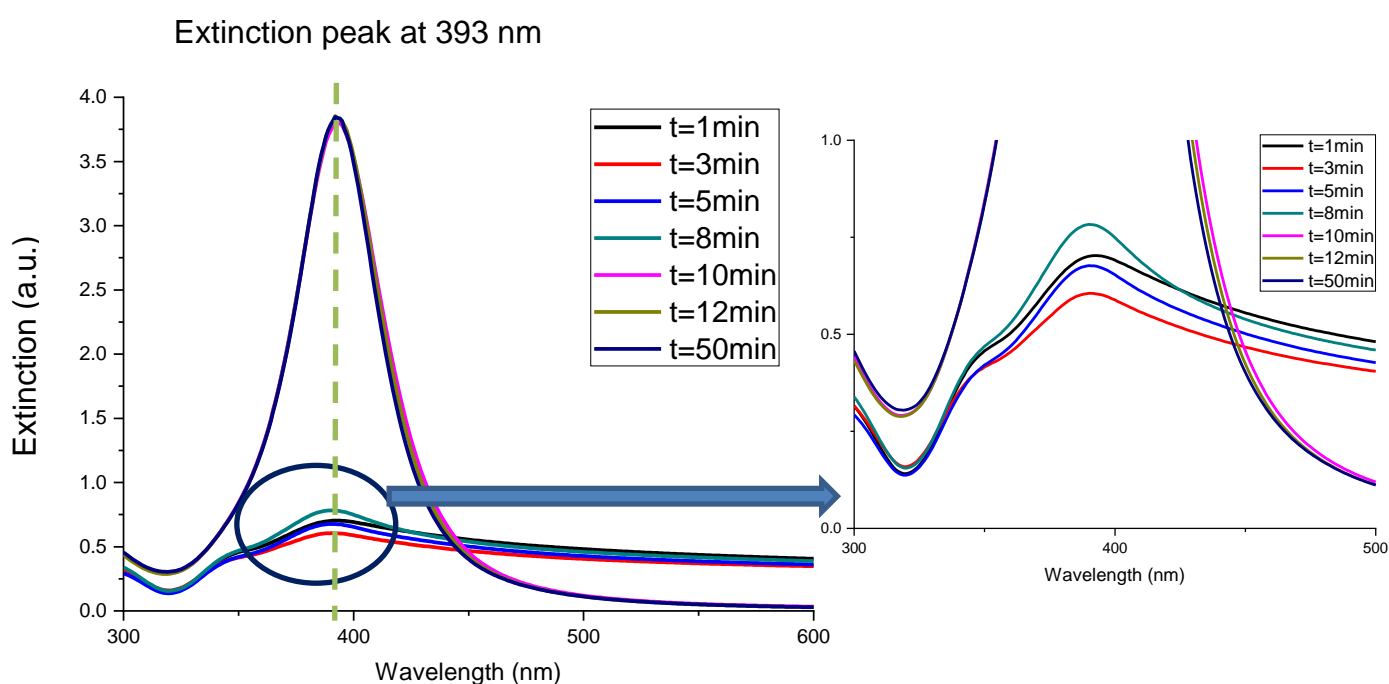
Figure 4.2: UV-Vis extinction spectra with Gaussian line fitting at different reaction times for the solution of 1mM AgNO$_3$: 2mM NaBH$_4$.

Silver nanoparticles exhibit localised surface plasmon resonance (LSPR) properties, characterised by their ability to absorb energy at a specific wavelength of light, resulting in an extinction peak. Ideally, silver nanoparticles are known to exhibit an extinction peak at approximately 400 nm [91,120–122,209,210,213,214]. However, it's important to note that the exact wavelength of this extinction peak can vary depending on the size and shape of the nanoparticles [122,207]. In a study by Solomon *et al.* [122], silver nanoparticles were synthesized using a chemical reduction pathway that employed sodium borohydride as the reducing agent, a method similar to the one used in our current study. Their findings indicated that the absorbance peak should occur around 400 nm, with the full width at half maximum (FWHM) ranging from 50 nm to 70 nm after a reaction time of 3 minutes. In this present study, a similar extinction peak position was observed, further supporting the consistent behaviour of silver nanoparticles in terms of their LSPR properties.

The full width at half maximum (FWHM) is the width of a spectrum at half of its maximum amplitude [215,216]. This is an important parameter that gives an idea of the size distribution of nanoparticles present in the solution. A narrow value of FWHM implies a narrow size distribution of nanoparticles in solution [207,208]. Higher values of FWHM reflect an increase in the polydispersity of AgNps [207,217,218]. This could be caused by variations in the nucleation process and the nanoparticles' growth rate during synthesis. Initially, the FWHM value of 99 nm was observed after just a minute of reaction time, as shown in Table 4.1. The FWHM value was observed to be 99 nm after 1 min of reaction time, this was observed to reduce to 80 nm after 8 minutes. This decrease in FWHM value is observed to continue for 10 minutes when a relatively stable value of 55 to 52 nm was observed from 10 to 50 minutes of reaction time. This decrease in the value of FWHM as the reaction time increased is indicative of the narrower size distribution. On the other hand, a decrease in FWHM with respect to reaction time indicates a decrease in the size distribution of silver nanoparticles in the solution. Solomon *et al.* [122] reported that a slightly greater FWHM was noted at the 3-minute mark. Notably, the FWHM values within the range of 50 to 70 nm were achieved after 10 minutes of reaction time, which is slightly longer than the duration reported in the literature. Our results are in qualitative agreement with those reported in the literature [122].

Table 4.1: Peak wavelength and absorbance values of colloidal silver nanoparticles formed from 1mM AgNO$_3$: 2mM NaBH$_4$ for different reaction times (1-50 minutes)

Reaction time (mins)	Peak Wavelength λ_{max} (nm)	Extinction (a.u.)	Full width at half maximum, FWHM (nm)
1	393	0.70	99
3	391	0.61	96
5	390	0.68	90
8	390	0.78	80
10	392	1.90	55
12	392	1.93	53
50	392	1.92	52

Agnihotri *et al.* [207] reported the relationship between the wavelength of maximum extinction (λ_{max}) and the size of the silver nanoparticles. As they have used the same conditions as ours, a relationship is derived and plotted as a line fitting from their data as shown in the below equation. The extraction procedure is shown in Appendix D.

$$Particle\ size = \frac{\lambda_{max} - 389.77}{0.69} \tag{4.2}$$

The present concept of particle size prediction represents an approximate value which may not necessarily be the actual particle size. This could partly be attributed to the different methods of preparing standard particle size which has been reported to vary depending on the method [120–122,210,213,214,219,220]. Using the equation 4.2, it is possible to predict the size of silver nanoparticles using the wavelength of the maximum extinction (λ_{max}) obtained from the UV-Vis spectrophotometer. In this study, the wavelength of maximum extinction (λ_{max}) is observed to lie between 390 nm and 393 nm. Using equation 4.2, when λ_{max} is 393 nm, the expected particle size is 4.68 nm. Therefore, the size of silver nanoparticles in this study is approximately 5 nm.

In the literature, similar results showing the size of silver nanoparticles within the range of 5 nm and 30 nm have been reported when sodium borohydride was used as the reducing agent [122,207,208,221]. Interestingly, Badiah *et al.* [208] reported the maximum extinction (λ_{max}) of 399 nm using the same chemical system as reported in this study. Similarly, Banne *et al.* [222] *and* Solomon *et al.* [122] also reported the maximum extinction (λ_{max}) of 395 nm and 400 nm respectively, when sodium borohydride was used as the reducing agent. The difference between the reported particle size in these two studies could be attributed to either the differences in the method of measuring the size of nanoparticles such as Transmission Electron Microscopy (TEM), dynamic light scattering (DLS) or differences in the synthetic methods. Since the potential application of the AgNp/silica coating as an optical pH sensor has not yet been thoroughly investigated, and therefore the effective particle size for this particular application has not yet been established, the main objective of our study focused on obtaining a stable silver nanoparticle within the coating.

As a next step, therefore, the stability of the colloidal silver nanoparticles was observed for 24 hours. A colour change occurred from yellow to grey after 6 hours, and thereafter a dark grey colouration was observed after 24 hours, as shown in Figure 4.3. The corresponding change in the light extinction properties, as measured using a UV-Vis spectrophotometer, is shown in Figure 4.3. The results indicate a shift in the peak of maximum extinction (λ_{max}), which would correspond to larger particles indicative of the growth in the size of silver nanoparticles with time. In addition, the FWHM becomes wider, indicating an increase in polydispersity.

Furthermore, absorbance at the wavelength shifted towards of 500 nm for the solutions after 6 and 24 hours (illustrated by the red and blue curves in Figure 4.3). This suggests the potential formation of transitional chemical species over time, contributing to absorption characteristics not seen in the UV-Vis spectrum of the fresh solution (depicted by the black line in Figure 4.3). Silver nitrate ($AgNO_3$) possesses light-sensitive properties, rendering it susceptible to photochemical reactions upon exposure to light [214,223]. This phenomenon induces the decomposition of the compound. The presence of ambient light may also facilitate the transition of silver nitrate into other chemical states. Such observations indicate

the instability of colloidal silver nanoparticles in solution, potentially attributable to alterations in coloration and UV-Vis spectral features.
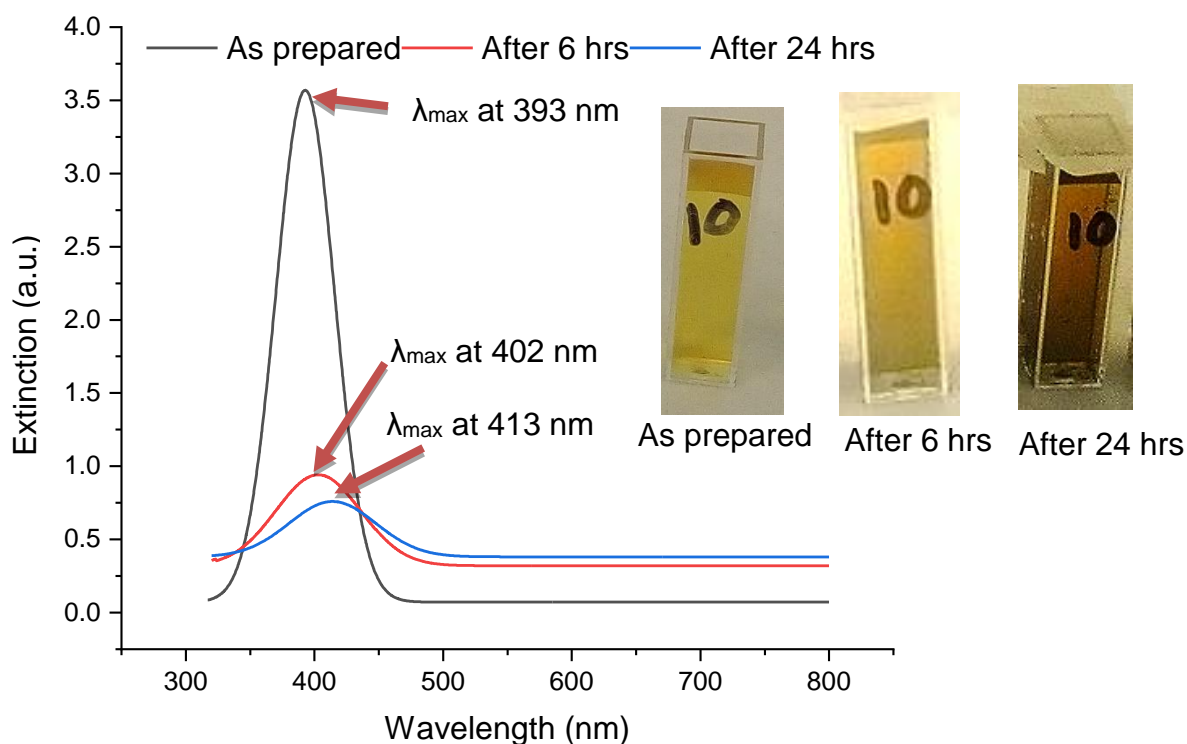
Figure 4.3: UV-Vis extinction spectra and images of colloidal silver nanoparticles demonstrating stability over a 24-hour period.

In the literature, a similar investigation conducted by Badiah *et al.* [208] has been reported. In their research, they synthesized silver nanoparticles employing the same chemicals, using silver nitrate as the precursor for AgNp and sodium borohydride as the reducing agent, reflecting the approach employed in this experiment. They measured the absorbance and monitored the evolving colour of colloidal silver nanoparticles over a duration of 70 days. In their report, the yellow colour of the solution was observed to gradually change to grey after 12 hours. This shift in the peak of maximum extinction (λ_{max}) to higher values could be attributed to the aggregation of silver nanoparticles, which increased the particle and polydispersity in the solution. Overall, this set of experiments shows that AgNps of low polydispersity and 393 nm can only be stable after 50 mins, and the solution degrades thereafter. Therefore, this AgNp fabrication method may be difficult to use manufacturing optical sensors.

4.1.2 Optical properties of colloidal silver nanoparticles using trisodium citrate as the reducing agent

Trisodium citrate is frequently used as a stabiliser as well as a reducing agent. The reducing ability of trisodium citrate was assessed independently to evaluate its potential in reducing silver nitrate to silver nanoparticles. Therefore, it would be interesting to compare the performance of trisodium citrate, which has a dual function of reducing the metal precursor and stabilising the nanoparticles formed. The reduction of silver nanoparticles using silver nitrate ($AgNO_3$) as the source of silver ions and trisodium citrate ($Na_3C_6H_5O_7$) as the reducing agent can be represented by the chemical equation below [16].

$$4AgNO_3 + Na_3C_6H_5O_7 + 2H_2O \rightarrow 4Ag^0 + C_6H_8O_7 + 3NaNO_3 + H^+ + O_2 \quad (4.3)$$
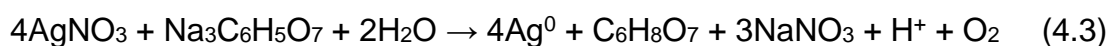
Similar to sodium borohydride, the formation of silver nanoparticles using trisodium citrate as the reducing agent was observed to be influenced by temperature and reaction time. The effects of different factors, such as temperature and reaction time, that influence the formation of silver nanoparticles using trisodium citrate are discussed here.

4.1.2.1 Effect of temperature

The synthesis of silver nanoparticles was explored by utilizing trisodium citrate as a reducing agent under two different temperatures, specifically at 40°C and 70°C, with a reaction time of 30 minutes for each condition. The aim of using the two different temperatures was to determine the effect of this reaction parameter. Further increase in temperature up to 100 °C has been reported to result in rapid aggregation due to faster reaction kinetics [224], which makes it quite challenging to control the growth of the nanoparticles and therefore was not attempted. The colour change of the solution at the two temperatures is shown in Figure 4.4, while the extinction spectra are shown in Figure 4.5.
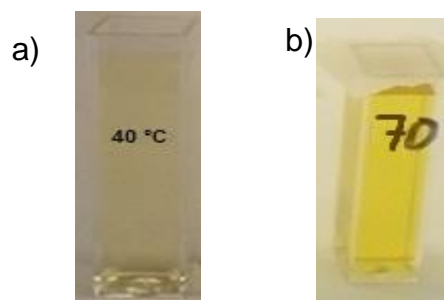
Figure 4.4: Image showing the colour of silver nanoparticle using trisodium citrate as a reducing agent at different reaction temperatures (a) 40 °C and (b) 70 °C.

A significant change in the intensity of the yellow colour of the two solutions was observed with increasing the reaction temperature. When the reaction temperature was 40 °C, the colour of the solution was observed to be pale yellow. When the temperature was increased to 70 °C, the colour of the solution increased to bright yellow, which was indicative that more silver nanoparticles were formed as the temperature was increased. Other studies have also noted a significant increase in the yield of silver nanoparticles as the reaction temperature was increased, particularly in cases where tri-sodium citrate was employed as the reducing agent [225]. This may be attributed to faster reaction kinetics associated with increased temperature, leading to a high yield of the silver nanoparticles in solution. It has been reported that at room temperature, there is no formation of silver nanoparticles when trisodium citrate is used as a reducing agent, and the reducing potential seems to be suppressed at lower temperatures [224,226].

Characterisation of the samples carried out at 40 °C, and 70 °C using a UV-Vis spectrophotometer showed a higher absorbance of around 400 nm for the sample carried out at 70 °C compared to the sample carried out at 40 °C as shown in Figure 4.5. This confirms that a higher number of silver nanoparticles is obtained as the temperature is increased up to 70 °C. The wavelength of maximum extinction peak (λ_{max}) was observed at 417 nm and 425 nm, respectively for the reaction temperatures of 40 °C and 70 °C, showing that the particle sizes at the two temperatures do not differ considerably.
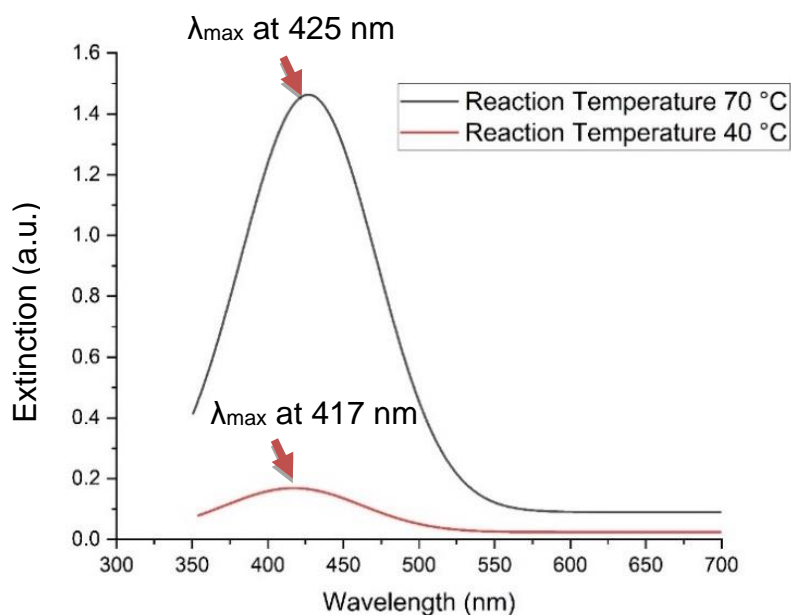
Figure 4.5: UV-Vis extinction spectra at different reaction temperatures (40 °C and 70 °C)

Table 4.2: The peak wavelength and absorbance values obtained from the UV-Vis extinction spectra at different reaction temperatures when tri-sodium citrate was used as the reducing agent for 30 minutes of reaction time.

Reaction temperature (°C)	Peak Wavelength λ_{max} (nm)	Extinction (a.u.)	Full width at half maximum, FWHM (nm)	Calculated AgNp diameter (nm)
40	417	0.16	106	39.4
70	425	1.46	105	51.1

Details of the extinction characteristics of the two samples are presented in Table 4.2. When the λ_{max} was at 417 nm, the approximate particle size derived from equation 4.2 was 39.4 nm. Similarly, when the λ_{max} was 425 nm, the approximate particle size was 51.1 nm using the same equation. It means that the reaction temperature at 40 °C yielded a particle size of 39.4 nm, which increased to 51.1 nm when the temperature was increased to 70 ºC. At the reaction temperature of 70 °C, more silver nanoparticles were formed in the solution as more extinction values were recorded.

It was observed that there was no significant change in the FWHM values for samples carried out at 40 °C and 70 °C, which suggests that there is no significant change in the size distribution of the nanoparticles. It is likely that high reaction temperatures greater than 70 °C may promote faster reaction, resulting in a rapid reduction of silver ions and nanoparticle formation compared to lower temperatures. For instance, Chaudhary *et al*. [210] reported that the reduction of silver ions to silver nanoparticles using trisodium citrate as the reducing agent at room temperature took 14 days to form the silver nanoparticles with a size of 44.0 nm. Also, Mazzonello *et al.* [121] reported that when the reaction temperature was increased to 60 °C, the particle size was 27 nm, which was further increased to 63 nm when the reaction temperature was increased to 100 °C. In this study, a similar trend to that observed previously is also noted. The particle size of the silver nanoparticles was found to increase with the increase in the reaction temperature, which is indicative of accelerated particle agglomeration leading to the formation of larger particles.

4.1.2.2 Effect of reaction time

In the previous section, we have reported the effect of temperature for a single reaction time of 30 minutes. It would also be interesting to observe how reaction time impacts the process at a reaction temperature of 70 °C, especially when tri-sodium citrate is employed as the reducing agent. Therefore, the effect of different reaction times ranging from 30 to 60 minutes on the property of colloidal silver nanoparticles using trisodium citrate as a reducing agent was carried out at that temperature. The colour change and the extinction spectra of the samples investigated at different reaction times are shown in Figure 4.6. and Figure 4.7, respectively.

(a)   (b)   (c)
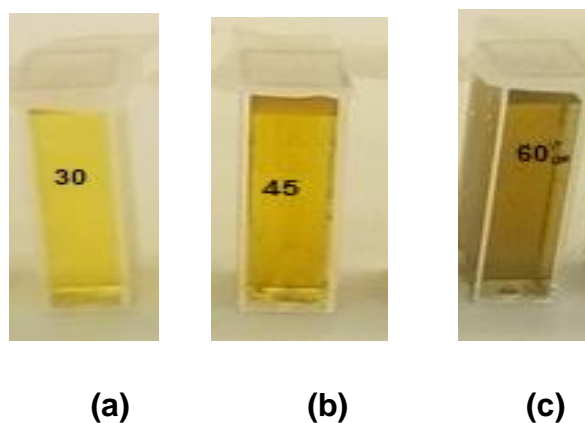
Figure 4.6: Image showing the colour of silver nanoparticle using trisodium citrate as a reducing agent at different reaction times (a) 30 min, (b) 45 min, and (c) 60 min.

After 30 minutes, the colour of the solution was observed to change to bright yellow, at 45 minutes the colour of the solution decreased in intensity and turned greyish. This was clearly visible after 60 minutes, as illustrated in Figure 4.6. One possible explanation for this is that the silver nanoparticles in the solution are aggregating, which would mean that the nanoparticles are becoming less stable as the reaction time was extended since the gradual transformation into a grey colour is an indication of enhanced aggregation.
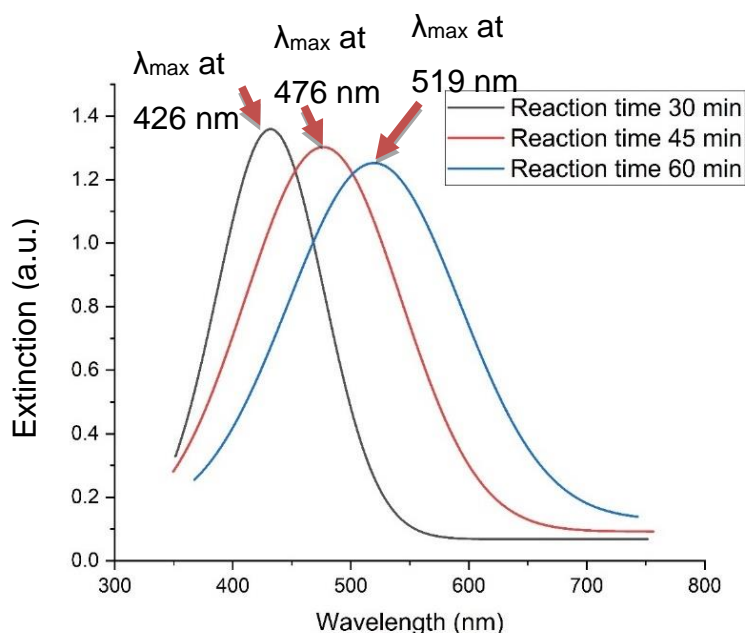
Figure 4.7: UV-Vis extinction spectra of colloidal silver nanoparticle when trisodium citrate was used as a reducing agent at different reaction times (30 min, 45 min, and 60 min).

An analysis of the UV-Vis spectra for the solutions, as shown in Table 4.3, indicates that indeed the peak shifted towards higher wavelengths and the FWHM widened when reaction time increased. This indicates an increase in particle size as well as polydispersity as the reaction time is increased. The wavelength of maximum extinction (λ_{max}) was observed at 426 nm, 476 nm, and 519 nm, respectively for the reaction time of 30 mins, 45 mins and 60 mins, which was carried out at 70 °C. When λ_{max} was 426 nm, the approximate particle size was 52.5 nm, as computed using equation 4.3. Similarly, when λ_{max} was 476 nm and 519 nm, the estimated particle size was observed to be 125 nm and 187 nm, respectively. Clearly, the prolonged reaction time promoted nanoparticle growth, which resulted in an increase in the particle size, which explains why λ_{max} shifted to a higher value. Furthermore, the increase in FWHM value shows that the prolonged reaction time is encouraging nanoparticle aggregation, resulting in larger clusters or agglomerates, leading to greater polydispersity. It is noteworthy that the heating entailed in the synthesis process is contributory, as elevated temperatures readily exacerbate the agglomeration phenomenon, thereby potentially precipitating alterations in particle sizes.

Table 4.3: Peak wavelength and absorbance values of UV-Vis extinction spectra at different reaction times carried out at 70 °C using trisodium citrate.

Reaction time (min)	Peak Wavelength λ_{max} (nm)	Extinction (a.u.)	Full width at half maximum, FWHM (nm)	Calculated AgNp diameter (nm)
30	426	1.35	106	52.5
45	476	1.30	155	125
60	519	1.25	171	187

Our results are in agreement with the work of Bastús *et al.* [227], who showed that the prolonged reaction time affects the particle size and size distribution, which reflects on the results of the UV-Vis extinction spectra with evidence of a shift to higher values. Using a reaction temperature of 70°C for the synthesis of silver

nanoparticles poses a challenge, as higher temperatures tend to increase the likelihood of particle aggregation. Consequently, achieving stable colloidal silver nanoparticles with tri-sodium citrate as the reducing agent may prove to be challenging.

4.1.3 Optical properties of colloidal silver nanoparticles using sodium borohydride as the reducing agent and trisodium citrate as a stabiliser

The preceding sections explored the stability of sodium borohydride and trisodium citrate, where aggregation posed an issue, which meant that these procedures could not be used for coating optical fibres. For this reason, one used sodium borohydride was used as a reducing agent, followed by the addition of trisodium citrate to improve the stability of the silver nanoparticles.

(a)   **(b)**
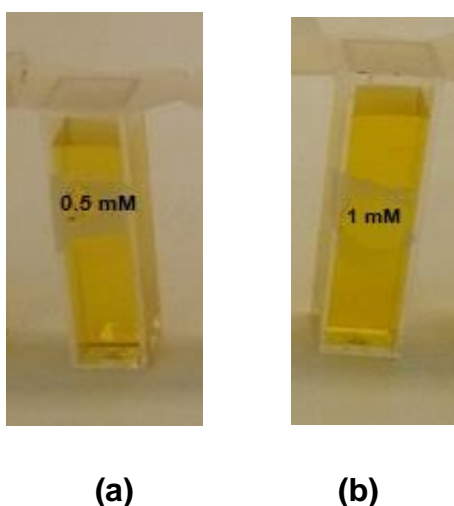
Figure 4.8: Image showing the colour of colloidal silver nanoparticle using a fixed concentration of sodium borohydride as a reducing agent (2 mM sodium borohydride) and different concentrations of trisodium citrate as stabilising agent at 30 mins reaction time (a) 0.5 mM concentration of trisodium citrate (b) 1 mM concentration of trisodium citrate.

The result showing the change in intensity of the yellow colour of the colloidal solution of silver nanoparticles using sodium borohydride as a reducing agent and trisodium citrate as a stabiliser is presented in Figure 4.8, and the corresponding extinction spectra in Figure 4.9. The intense yellow colouration indicates the formation of a stable silver nanoparticle colloidal solution, which is observed to be similar for both 0.5 mM as well as 1 mM trisodium citrate. This could be due to the

stabilising effect of trisodium citrate, which prevents aggregation of the silver nanoparticles. The results indicate no visible differences in the colour of the colloidal silver nanoparticles prepared from different concentrations of stabilising agents of 0.5 mM and 1 mM trisodium citrate.
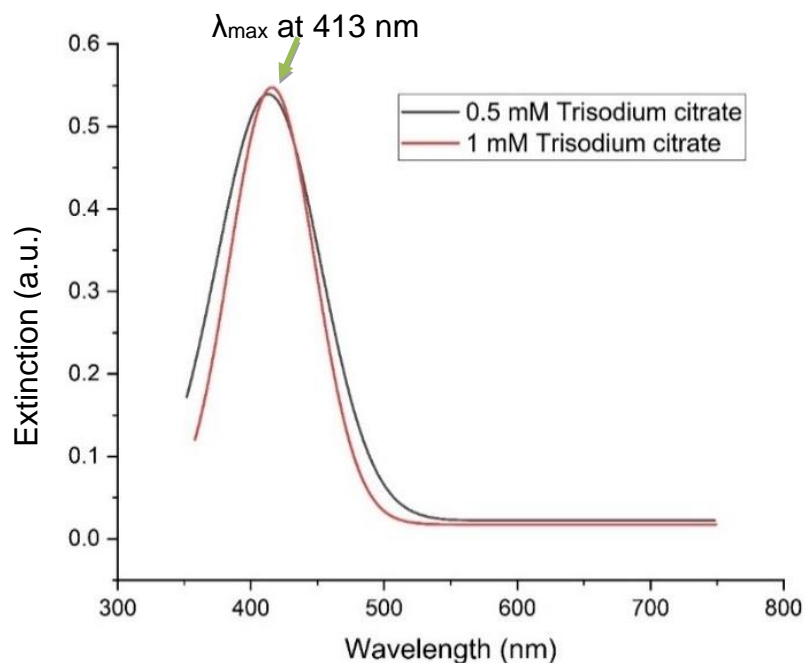
Figure 4.9: The UV-Vis spectra of silver nanoparticles obtained using a fixed concentration of sodium borohydride as a reducing agent and different concentrations of trisodium citrate as stabilising agent at 30 mins reaction time (a) 0.5 mM concentration of trisodium citrate (b) 1 mM concentration of trisodium citrate.

The UV-Vis extinction spectra for both concentrations of trisodium citrate (0.5 mM and 1 mM) are shown in Figure 4.9. The absorbance of the two sample solutions is nearly the same 0.54 to 0.55, respectively. The wavelength of maximum extinction (λ_{max}) was observed at 413 nm and 414 nm for the concentration of 0.5 mM and 1 mM trisodium citrate, respectively. The light extinction characteristics of the colloidal solution prepared from different concentrations of trisodium citrate, as summarised in Table 4.4, show that the of silver nanoparticles were approximately 33 to 35 nm. The FWHM values were observed to decrease from 91 to 75 nm with increasing concentration of trisodium citrate from 0.5 mM to 1 mM, suggesting that polydispersity decreased for the higher concentration. Therefore, adding trisodium citrate to the solution helps improve the stability of the colloidal solution. It is likely

that an increased amount of citrate ions tends to offer more protection to the silver nanoparticles and prevent them from aggregation [207,212]. This might be useful in obtaining a more uniform size distribution of silver nanoparticles.

Table 4.4: Peak wavelength and absorbance values of UV-Vis extinction spectra at different concentrations of trisodium citrate.

The concentration of trisodium citrate	Peak Wavelength λ_{max} (nm)	Extinction (a.u.)	Full width at half maximum, FWHM (nm)	Calculated AgNp diameter (nm)
0.5 mM	413	0.54	91	33
1 mM	414	0.55	75	35

There are several studies on the synthesis of silver nanoparticles using sodium borohydride and trisodium citrate. Agnihotri *et al.* [207] reported the synthesis of different sizes of silver nanoparticles ranging from 10 nm to 100 nm, where the concentration of silver nitrate, sodium borohydride and trisodium citrate were altered. The incorporation of NaBH4 in the reduction process led to the generation of a substantial amount of silver nanoparticles. During this particular stage, the primary mechanism involved the reduction of silver cations, resulting in the formation of new silver nuclei. The secondary process, known as Ostwald ripening, also played a role. The formation of silver nanoparticles occurred initially, followed by their further

Trisodium citrate fulfils an indispensable role as a stabilizing agent during the synthesis of silver nanoparticles utilizing sodium borohydride, owing to its multifaceted properties. Primarily, trisodium citrate serves as a co-reducing agent alongside sodium borohydride, facilitating the reduction of silver ions (Ag$^+$) to yield silver nanoparticles. This dual reduction capability ensures a controlled and efficient reduction process, thereby mitigating the risk of excessive nanoparticle aggregation or growth [118,210,228]. Additionally, trisodium citrate assumes a pivotal function as a stabilizing agent by inducing electrostatic and steric repulsion between the nanoparticles, thereby preventing their agglomeration and ensuring colloidal stability. Its capacity to form a protective sheath around the nanoparticles impedes their growth and agglomeration by inhibiting direct particle-particle interactions. Furthermore, trisodium citrate exhibits versatility in modulating the size and

morphology of the resultant silver nanoparticles, thereby enhancing the reproducibility and tunability of the synthesis process.

Agnihotri *et al.* [207] conducted a comprehensive review on the synthesis of silver nanoparticles across diverse size ranges, employing sodium borohydride as the reducing agent and trisodium citrate as the stabilizing agent. Their inquiry underscored the pivotal role of trisodium citrate in stabilizing silver nanoparticles. The controlled synthesis protocol adopted a co-reduction strategy executed in two stages, as shown in Figure 4.10. Initially, the reduction process was initiated utilizing $NaBH_4$, leading to the generation of a substantial quantity of silver nanoparticles. Concurrently, this phase instigated the formation of new silver nuclei by reducing silver cations, accompanied by Ostwald ripening as a secondary process. Following the initial stage, the silver nanoparticles formed therein actively engaged in the growth phase, wherein trisodium citrate-mediated reduction of residual Ag ions predominated. Notably, trisodium citrate was introduced simultaneously with $NaBH_4$ during the primary stage, primarily serving to passivate the nanoparticles and hinder their agglomeration. The maintenance of an optimal $NaBH_4$ to trisodium citrate ratio emerged as a critical factor governing the modulation of nucleation and growth processes within the two-stage co-reduction model.
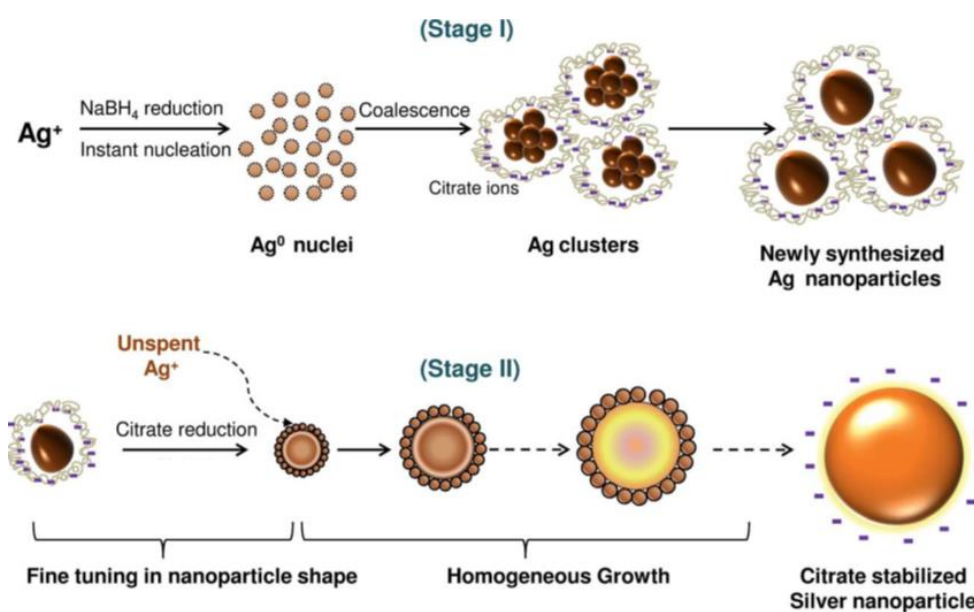
Figure 4.10 : Schematic illustration of the synthesis of silver nanoparticles (AgNPs) with controlled size through the utilization of a co-reduction strategy [207].

160

4.2 Optical properties of AgNp/silica coating

This section presents the results obtained when AgNp/silica was coated on the glass slide. First, the results showing the reduction in thickness of the etched glass slides prior to the application of the coating on the glass slide are discussed. In addition, the effects of different factors, such as temperature and gelation time, that affect the adhesion of the coating on the glass slides are also covered. Preliminary assessments of the adhesion of the AgNp/silica coating on glass slides are hereby presented. This is followed by the results of using these optimised protocols for the application and manufacturing of a coated optical fibre.

4.2.1 Effect of reaction temperature and gelation time

In this section, the results showing the effects of reaction temperature on the gelation time will be discussed. The gelation temperature, at which the reactants, including tetraethyl orthosilicate (TEOS), ethanol, silver nitrate, and deionized water, undergo a transition from a liquid or gel state to form a gel. Gelation temperature played an important role in forming a composite AgNp/silica coating. An increase in gelation temperature decreases the time for gelation to occur. However, this must not be too fast, as rapid gelation could also weaken the bond between particles. A series of experiments were carried out to gather information on the conditions required for gelation while retaining an optically active coating. Figure 4.11 shows samples of AgNp/silica coatings on the glass slide. The gel used for the samples was prepared under ambient conditions (22 °C) and allowed to undergo a maturation period of 24 hours, as illustrated in Figure 4.11 (a). In order to ameliorate the coating properties, a series of experiments were then conducted in which the AgNp/silica coating was applied on the glass slide and subjected to a temperature of 35 °C for varying durations of 24 hours, 48 hours, and 72 hours, which are shown in Figure 4.11 (b), (c), and (d) respectively.

The resulting images indicate that increasing the reaction temperature to 35 °C resulted in an intense yellow colouration, indicating an increased formation of silver nanoparticles in comparison to the samples prepared under room temperature (22

°C). For the case of sample (c), not only the intensity of the yellow colour of the coating increased, but adhesion also improved. However, the coating became powdery when the gelation time was increased to 72 hours whilst a short gelation time might provide insufficient bond in the gel to form, a high gelation time may cause shrinkage of the coating resulting in powders. Therefore, a suitable gelation time is needed, which balances the desired formation of silver nanoparticles and adhesion. These results indicate that the coating obtained at 35 °C for 48 hours showed the best quality, probably as a result of the formation of strong bonds between particles, matrix and the glass surface.
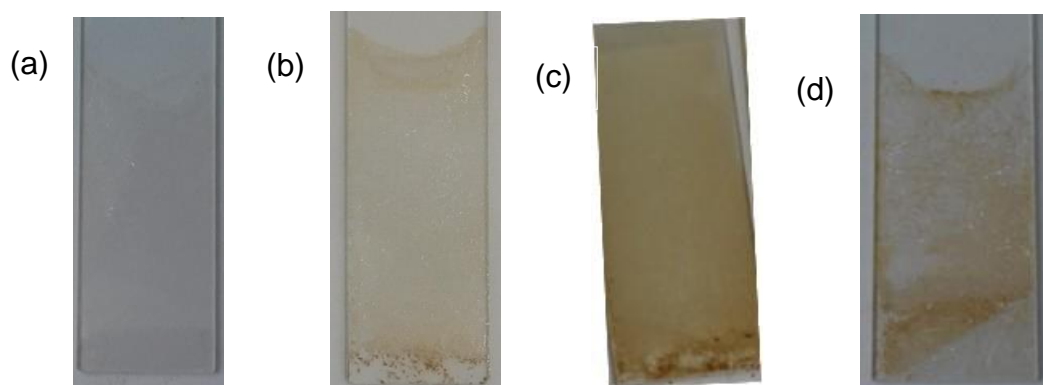
Figure 4.11: Pictures of AgNp/silica coating on glass slides (a) coating obtained from gel prepared at room temperature (22 °C) and kept for 24 hrs (b) coating prepared from gel at 35 °C and kept for 24 hrs, (c) coating prepared from gel at 35 °C and kept for 48 hrs, (d) coating prepared from gel at 35 °C and kept for 72 hrs.

The extinction spectra of the four samples after heat treatment at 200 °C for 2.5 hours are shown in Figure 4.12. An extinction peak is observed at around 428 nm for all samples. Although the peak of the sample prepared at 22 °C for 24 hours (black line) was only slightly visible, the peak of the sample prepared at 35 °C for 24 hours (red line) shows better absorbance, indicative of the presence of silver nanoparticles. The peak became more distinct for sample (c). The absorbance peak decreases for sample (d). This could be attributed to the powdery nature of the coating, which may have led to a loss of AgNps.
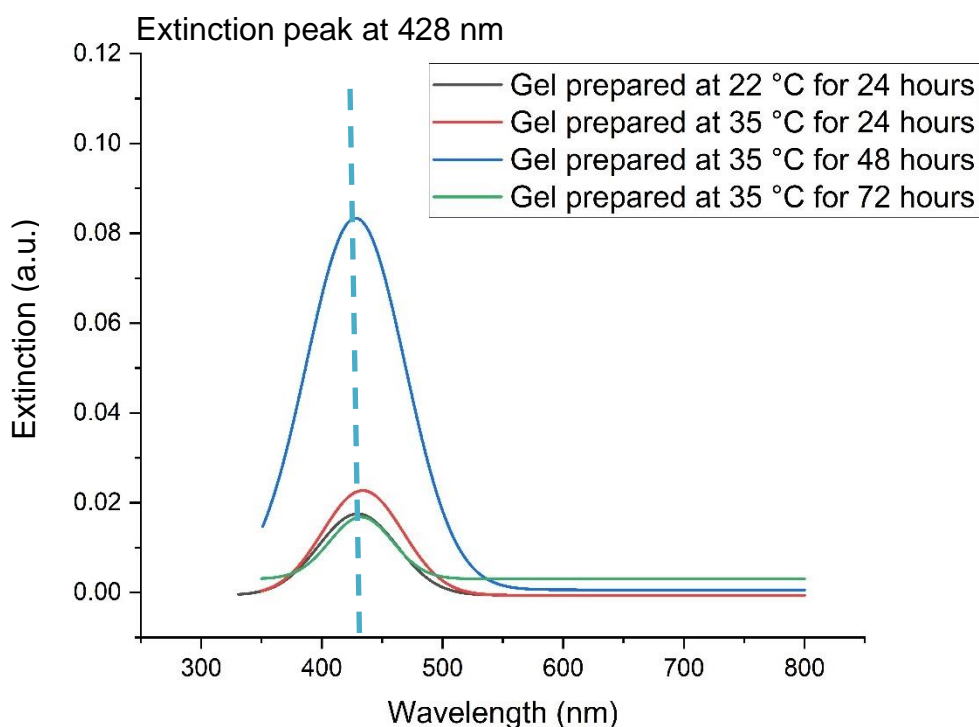
Figure 4.12: The UV-Vis spectra of the AgNp/silica coating prepared in different gelation temperatures and times, where it is shown that the best absorbance peak were appeared with the sample while the gel was prepared at 35 °C for 48 hours (blue line).

Overall, it can be summarised that achieving good adhesion of a coating to a substrate necessitates providing adequate time and optimal conditions during the gel formation process, thereby fostering strong bonds between the particles. Consequently, this approach may lead to the attainment of both satisfactory coating adhesion and high coating quality. These observations not only led to the understanding that gelation temperature was important but that the heat treatment of the gel to convert it to a composite may also be important, which is described in the next section.

4.2.2 Effects of heat treatment temperature

The AgNp/silica coating on the glass slide was subjected to different heat treatment temperatures (150-250 °C) and for different holding times (1-3 hours). Samples obtained by subjecting them to the heat treatment conditions stated in the figure caption are typical, as shown in Figure 4.12.
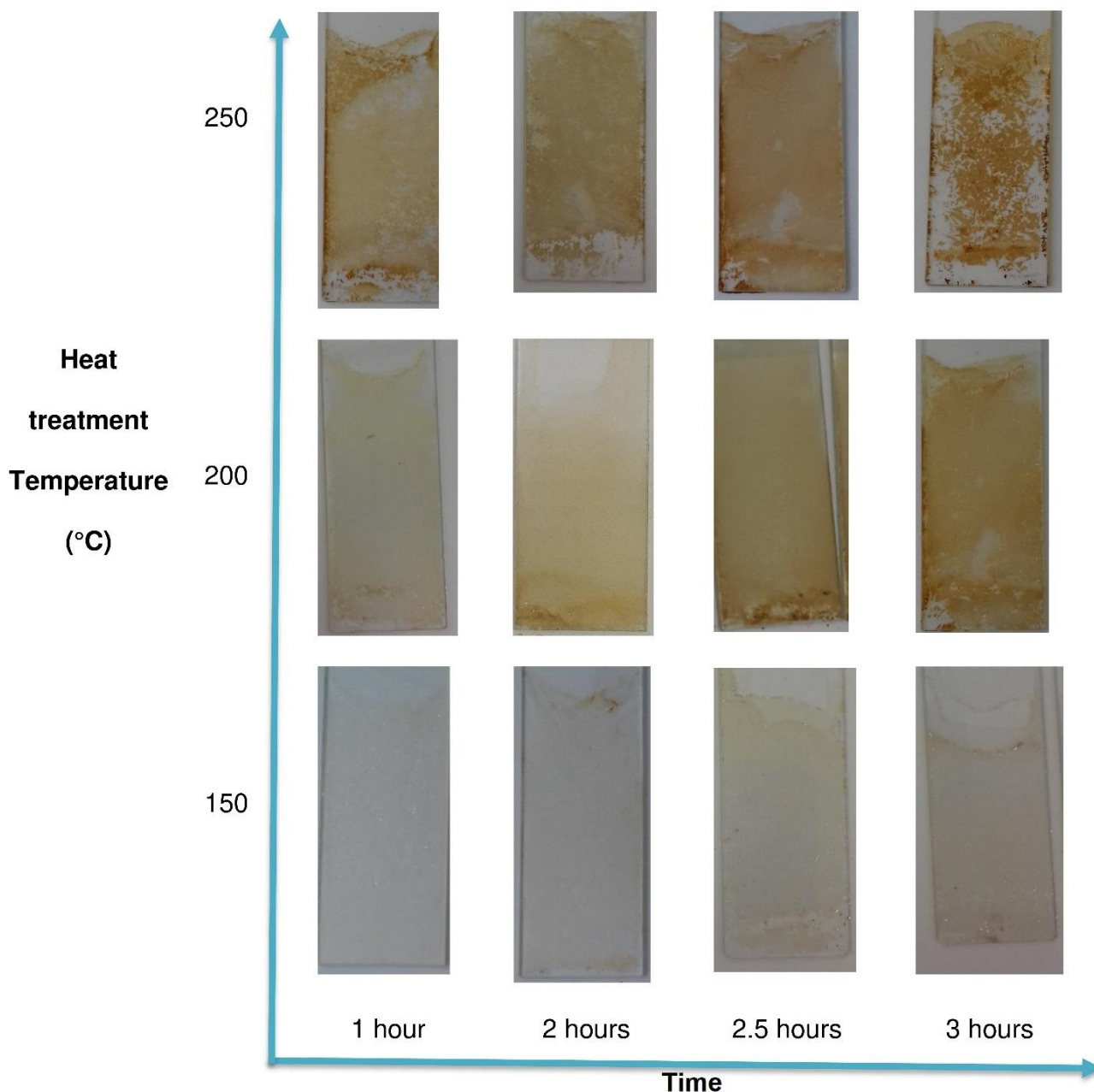
Figure 4.13: Silica coating prepared at different heat treatment temperatures (150-250 °C) for different holding times (1-3 hours).

Results shown in Figure 4.13 indicate an increase in the intensity of the yellow colour as the heat treatment temperature increases from 150 °C to 250 °C, indicating the presence of optically active silver nanoparticles. At 150 °C, for example the coating was observed to adhere to the glass, and only a pale-yellow colour was obtained. The intensity of the colour was remarked to improve when the temperature was raised to 250 °C. The brightness of the colour was observed to increase with the holding time. This suggests that increasing the holding time will result in more

164

formation of silver nanoparticles. Although the coating heat treated at 250 °C had a higher intensity of the yellow colour, indicating the presence of more silver nanoparticles compared to other temperatures, coating adhesion to the glass slide was poor. Besides, cracks in the coating were observed, possibly due to stress at the high temperature. Indeed, when the coating was heat treated at 200 °C for 2 hours or 2.5 hours, the samples retained a brighter colour as well as good adhesion with the glass slide.

The UV-Vis spectra displayed in Figure 4.14 depict the absorbance of samples prepared at 200°C for 1 hour, 2 hours, 2.5 hours, and 3 hours. The absorbance peak of the sample treated for 1 hour (black line) is relatively small, suggesting that there might not have been enough time for a significant amount of silver nanoparticles to form on the coating. As the holding time increased to 2.5 hours (blue line), the extinction intensity at the wavelength of 425 nm noticeably increased, indicating a gradual increase of optically active silver nanoparticles on the silica coating, and decreased for the sample treated for 3 hours (green line), as demonstrated in Figure 4.14. This observation corresponds to the visual observations in Figure 4.13.
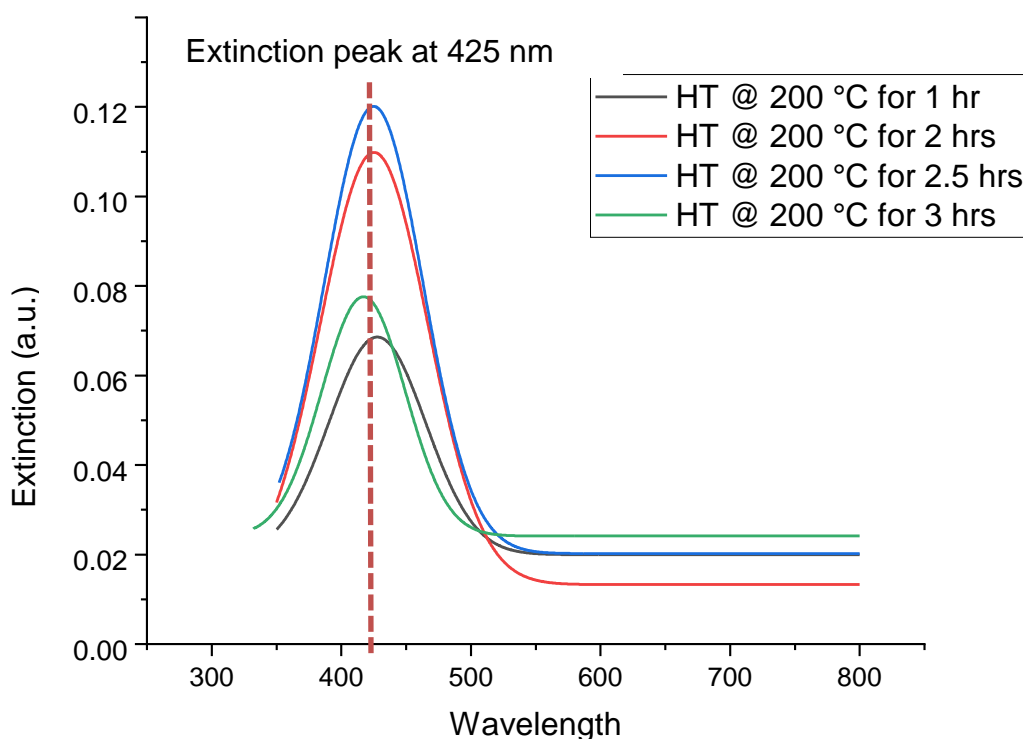
Figure 4.14: The UV-Vis extinction spectra of the coating heat treated at 200°C for different holding times (1, 2, 2.5 and 3 hours).

The absorbance of samples prepared at different temperatures of 150°C, 200°C and 250°C, with a holding time of 2.5 hours, reveal that the sample treated at 150°C for 2.5 hours (indicated by the black line) shows a relatively small absorbance peak, suggesting there is insufficient time for a significant amount of silver nanoparticles to form. Upon increasing the temperature to 200°C for the same holding time (shown by the red line), the extinction intensity at the wavelength of 425 nm increases notably. Interestingly, when the temperature was raised to 250°C (indicated by the blue line), the extinction intensity decreased, similar to the case in Figure 4.14. This reduction in extinction intensity could not only be due to the loss of AgNps due to a cracked/powdery deposit but could also be attributed to the oxidation of silver particles at 250°C [136]. As a result, the heat treatment temperature of 200°C for 2.5 hours yielded the most favourable optically active and adherent composite coating, which could be transferred to fabricate coated optical fibre.
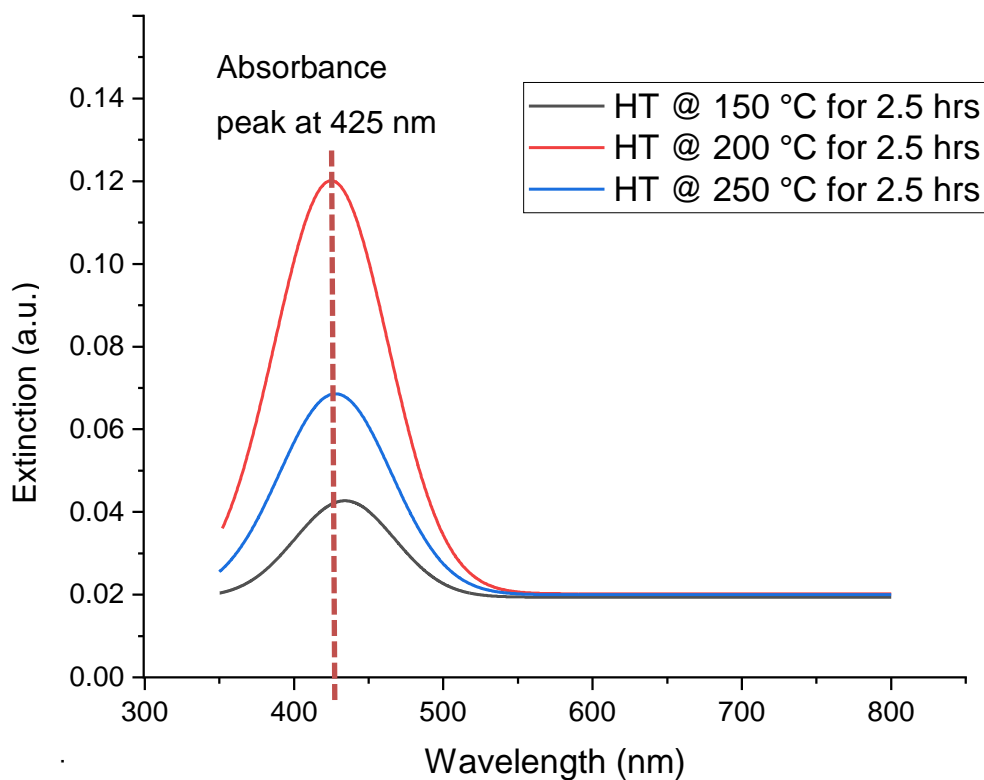
Figure 4.15 : The UV-Vis extinction spectra of the coating heat treated at 150 °C, 200°C and 250°C for 2.5 hours of holding times.

The UV-Vis spectra depicted in Figure 4.15 demonstrate that the extinction peaks were seen at a nearly identical wavelength of 425 nm. This observation suggests that the coating may not result in an increase in the size of silver nanoparticles. The presence of a silica matrix in conjunction with silver nanoparticles may potentially impede the growth of the nanoparticles.

The results obtained in this research show several similarities with those reported in the existing literature. Li *et al.* [136] conducted an investigation on the coating of silver nanoparticles embedded in silica, applied on a glass slide with various heat treatment temperatures ranging from 200 °C to 400 °C. The extinction spectra are reproduced in Figure 4.16. Based on the findings presented in their study, it was observed that the extinction peak exhibited a drop in magnitude with the progressive increase in heat treatment temperature beyond the threshold of 200 °C. The observed phenomenon was attributed to the process of oxidation occurring in the silver particles. Moreover, it was observed that when the temperature surpassed 200 °C, there was an occurrence of inter-diffusion between the silver within the coating and the sodium that was present in the substrate [136].
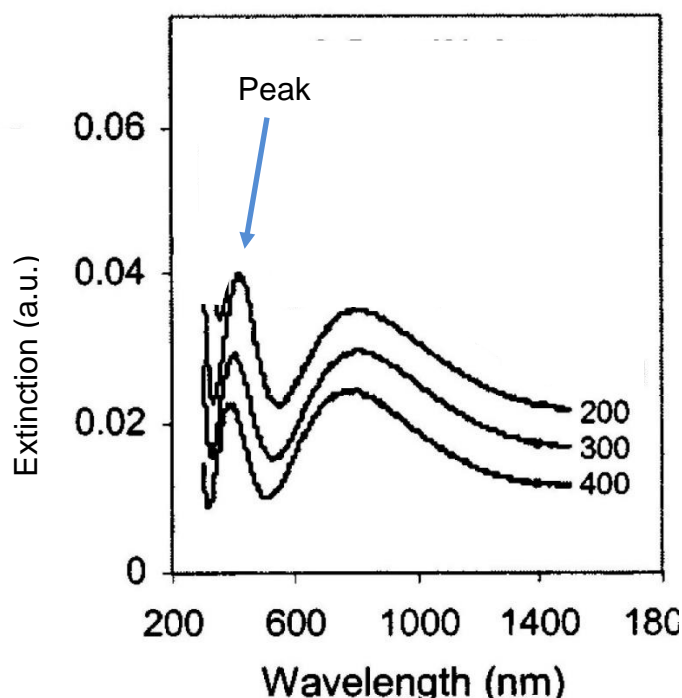
Figure 4.16: The UV-Vis extinction spectra of the AgNp/silica coating heat treated at 200 °C, 300°C and 400°C for 2 hours of holding time reported in the literature (Reprinted with permission from [136]).

4.2.3 Effect of number dips

The results showing the effects of multiple dip coating on the glass slides for different times such as single, double, and triple coating as obtained using a high-resolution microscope, are shown in Figure 4.17. Results shown in Figure 4.17 indicate that the thickness of the coating increased gradually with an increase in the number of dips. However, it was observed that the coating was not uniform in thickness throughout the surface of the glass slide. The thickness of the coating on the glass slide was measured at five distinct locations. The accuracy of the optical microscope is within a range of ±1 micron (μm). Other researchers have also reported non-uniform coating on glass slides using such an approach [229,230]. Therefore, it was necessary to make measurements at different points on the surface of the glass slide and then calculate the average thickness for each sample. With a single dip, an increased average thickness of 6 to 8 microns was observed. This increased to 8 to 10 microns with double coating and a further 12 to 16 microns for triple coating.
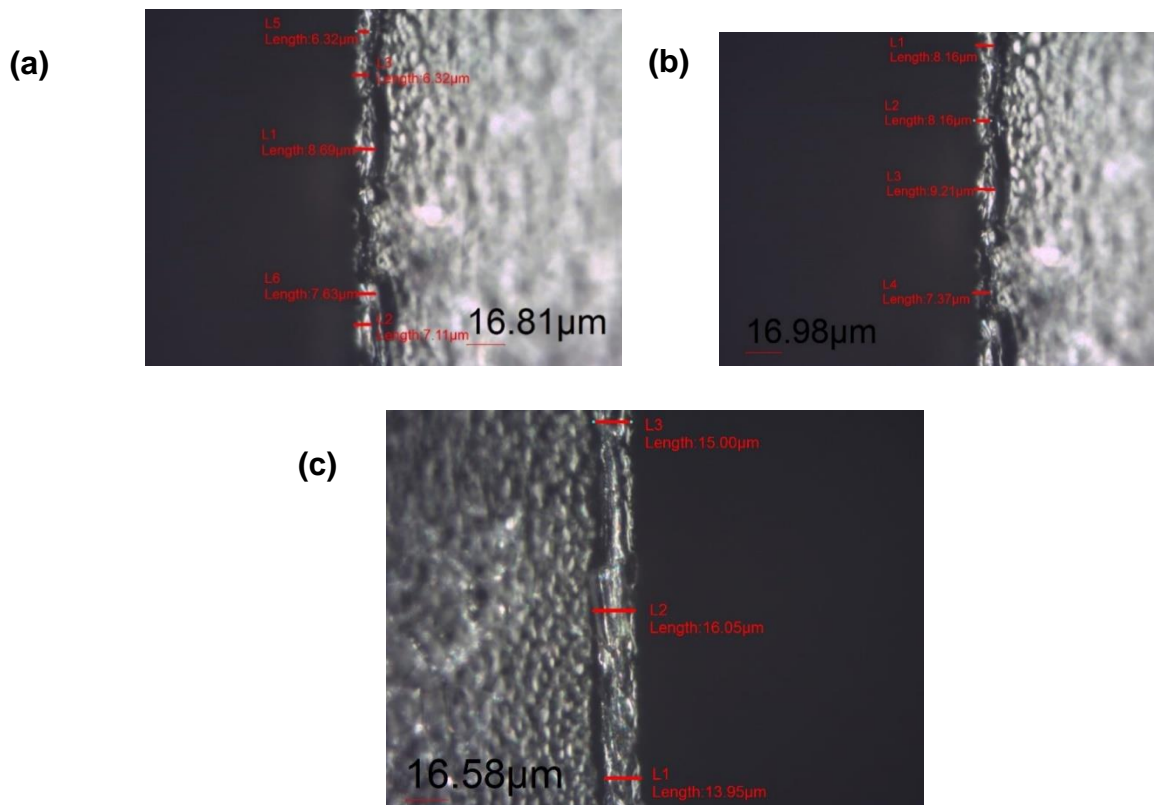
Figure 4.17: The micrographic image of AgNp/silica coating showing the thickness for different dip-coatings: (a) single dip-coating, (b) double dip-coating, (c) triple dip-coating.

The process of applying the coating to the glass slide was carried out in a manner similar to that used for coating the core of the optical fibre with the gel. This involved following a consistent set of conditions to assess the optimal number of dip coatings of AgNp/silica gel onto the optical fibre. The aim of this procedure was to determine the most favourable conditions for achieving strong adhesion between the coating and the optical fibre.

The outcomes of the thickness of AgNp/silica coated optical fibre coating, as observed through a microscope, are illustrated in Figure 4.18. These micrographic images provide insights into the diameters of both the coated and uncoated optical fibres, which will be elaborated upon in the subsequent paragraphs. As shown in Figure 4.18, it was noted that the AgNp/silica coating adhered remarkably well to the optical fibre, effectively covering the entire surface of the fibre. This adherence resulted in a noticeable increase in the core diameter, transitioning from 105.66 microns for the uncoated sample to 107.94 microns for a single coating, 110.76 microns for a double coating, and 115.10 microns for a triple coating. Additionally, it was evident that the thickness of the coating exhibited a gradual increment corresponding to the number of dip coatings applied.

There are no reported findings for comparison with these results. However, it is a well-established concept in literature that an increase in the number of dip coatings can lead to a corresponding increase in the thickness of the coating [229]. This research aligns with existing knowledge, demonstrating that the coating thickness indeed increased as the number of dips increased. These findings highlight the effectiveness of the coating process in enhancing the diameter and thickness of the optical fibre, with the number of dip coatings having a direct impact on these dimensions. The improved adhesion achieved through this method shows considerable promise for its potential use as a sensor.

(a)   **(b)**

(c)   **(d)**
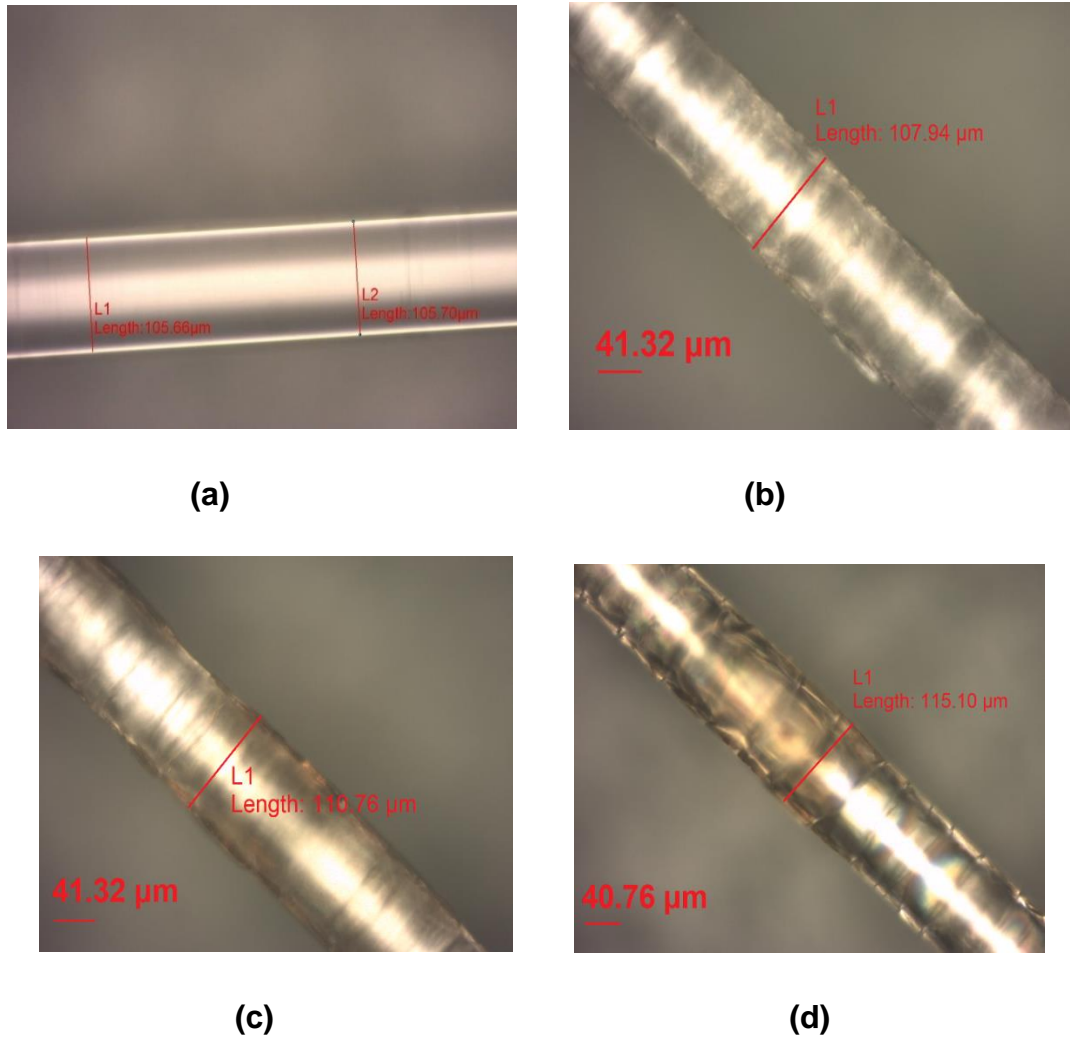
Figure 4.18: Micrographic image of optical fibre (a) before coating, (b) after single coating, (c) after double coating, and (d) after triple coating.

4.2.4 Characterisation of AgNp/silica coating

In this section, the results showing the characterisation of the AgNp/silica coated optical fibre including the durability test, Scanning Electron Microscope (SEM) and Energy Dispersive X-ray analysis (EDX), are presented and discussed. These were carried out to understand the morphology, composition as well as durability of the coated optical fibre. The durability of the AgNp/silica coating was carried out in different chemical environments. A micrographic examination was carried out using an SEM to observe the morphology of the AgNp/silica coating. This was followed by an investigation of the chemical composition using EDX Analysis.
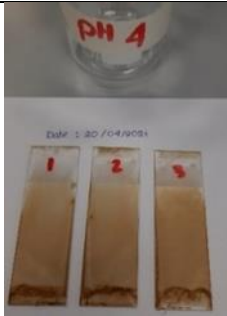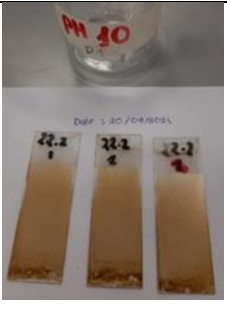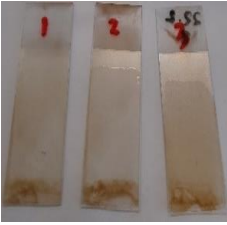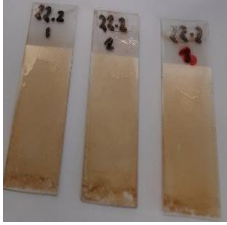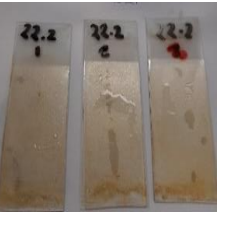
4.2.4.1 Durability test of coating

This section consists of the results of a durability test on AgNp/silica, including its adherence to a glass slide under varying pH conditions (pH 4, 6, 8, and 10) over a period of seven days. The acidic solutions having pH values of 4 and 6 were prepared using phosphoric acid, while the alkaline solutions with pH values of 8 and 10 were prepared using sodium hydroxide.

Table 4.5 summarises the results obtained from the durability test. The data demonstrates that the AgNp/silica coated glass slide immersed in the solution with pH 4 exhibited poor adhesion, as the coating dissolved into the solution after only three days. Hence, no trace of the coating was observable after the seven-day duration. Similarly, the samples submerged in solutions with pH 6 and 8 also experienced dissolution after three days. The dissolution process increased with contact time up to seven days, leading to the removal of a greater amount of the coating from the surface of the glass slide.

Conversely, the AgNp/silica coating on the glass slide immersed in the solution with pH 10 showed significant resistance to dissolution throughout the seven-day period. Even after being exposed to the solution for the full duration, minimal loss of the coating from the glass slide's surface was observed. This finding suggests that the AgNp/silica coating is less stable in acidic conditions but displays improved stability in alkaline environments. It can be therefore inferred that the rate of loss of the AgNp/silica coating is higher in acidic solutions compared to alkaline solution. This behaviour is unexpected because a TEOS (or silica) matrix should be more stable in acids [231–235], and further investigation is required, which will discussed later.

Table 4.5: Durability test of AgNp/silica coating on the glass slide dipped in the solution prepared using phosphoric acid and sodium hydroxide at pH 4, 6, 8, and 10.

	pH 4	pH 6	pH 8	pH 10
Day 0				
Day 3				
Day 7				

The loss rate of AgNp/silica coating on the optical fibre is presented and discussed in this section. The AgNp/silica coated optical fibre was dipped in an acidic solution (pH 3), deionised water (pH 5.9) and an alkaline solution (pH 10), as shown in Figure 4.19. The acidic solution was prepared using phosphoric acid, while the alkaline solution was prepared using sodium hydroxide solution. The optical fibre was kept for 7 days at room temperature (22°C).
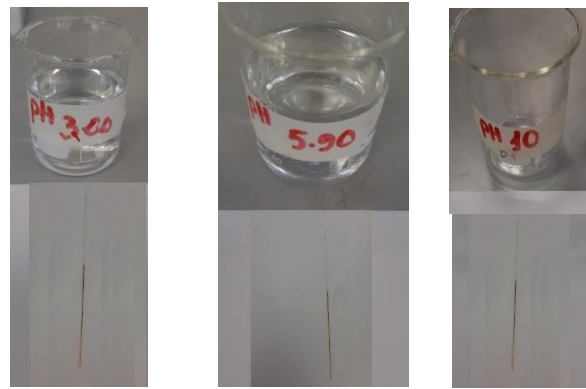
Figure 4.19 : Images showing the results of the durability test of AgNp/silica coating on the optical fibre dipped in the solution prepared using phosphoric acid (pH 3), deionised water (pH 5.9) and sodium hydroxide (pH 10).

In this study, a high-resolution microscope was employed to accurately measure the thickness of an optical fibre. Initially, the thickness of the coating was measured prior to immersion in the solution, which serves as the baseline measurement (referred to as day 0). Subsequently, measurements were taken at two-day intervals for a total duration of six days. To ensure reliability, the thickness was measured at different locations along the optical fibre, resulting in five independent measurements. The average thickness, along with the corresponding standard deviation, is presented in Figure 4.20.

Prior to commencing the experiments, the average thickness of the AgNp/silica coating was observed to be 5.2 µm, as shown in Figure 4.20. However, a rapid dissolution rate of the coating was observed when exposed to an acidic solution. After four days, complete loss of the coating was observed, indicating its susceptibility to acid attack. Conversely, when the optical fibre was immersed in deionised water, a slower loss rate was observed. Furthermore, the loss rate in an alkaline solution was found to be lower compared to acidic environment. The micrographic images showing the diameter of the optical fibre at different times of day 0, day 2, day 4, and day 6 for all the solutions, can be found in Appendix E. This suggests that the AgNp/silica coating is vulnerable to acid-induced loss, leading to a higher loss rate in acidic solutions at room temperature.
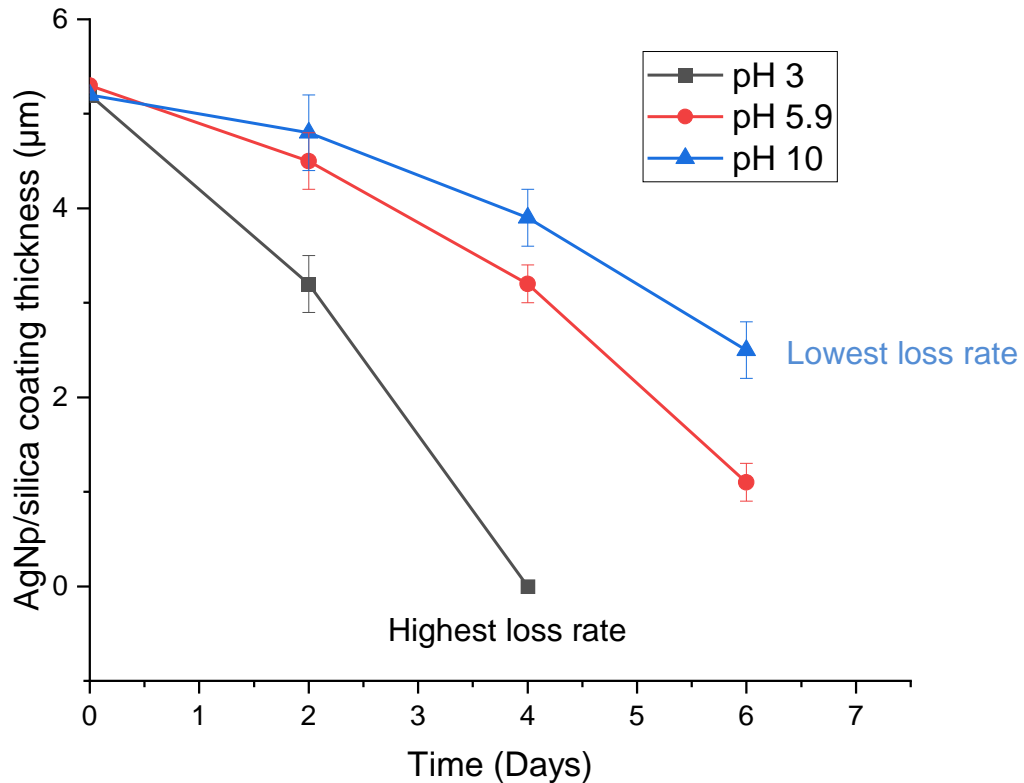
Figure 4.20: The results of durability test of AgNp/silica coating on the optical fibre dipped in the solution prepared using phosphoric acid (pH 3), deionised water (pH 5.9) and sodium hydroxide (pH 10) showing the dissolution of coating with time.

Numerous studies have been conducted to investigate the loss behaviour of silica, yielding a range of findings. Loss rates under ambient temperatures have been observed to be slow [231,234,235]. However, as the temperature increases, solubilities and loss rates exhibit marked escalation. It has been documented that pH marginally impacts solubility within the pH range of 3 to 7. Yet, dissolution experiences a slight augmentation until pH 10. Beyond pH 10, silica loss accelerates swiftly. Some studies indicate a slightly elevated dissolution rate in basic solutions compared to acidic solutions [231,234–236]. The theory of dissolution of silica is discussed below for a better understanding.

Silica (SiO_2) comprises silicon and oxygen atoms, and when subjected to water or aqueous solutions, water molecules interact with the silicon-oxygen bonds on the silica's surface. This interaction disrupts the bonds, resulting in the formation of silicic acid, as demonstrated by the below equation [237–239].

$$SiO_2 + 2H_2O \rightarrow H_4SiO_4 \qquad (4.7)$$

174

At higher pH levels, the solution turns more alkaline due to hydroxide ions (OH-) originating from compounds such as sodium hydroxide (NaOH) or other bases. This augmentation of hydroxide ions raises their concentration within the solution. This concentration shift significantly influences the equilibrium reactions involving silicic acid:

$$H_4SiO_4 \rightleftharpoons H_3SiO_4^- + H^+ \tag{4.8}$$

$$H_3SiO_4^- \rightleftharpoons H_2SiO_4^{2-} + H^+ \tag{4.9}$$

$$H_2SiO_4^{2-} \rightleftharpoons HSiO_4^{3-} + H^+ \tag{4.10}$$

An increase in OH^- ions prompts the equilibrium shift to the right in reaction 4.8, favouring silicic acid formation. In reactions 4.8 to 4.10, H^+ ions can act as bases, counteracting the hydroxyl ions (OH^-) produced during silicic acid dissociation. This shift encourages the rightward movement of the equilibrium in reactions 4.8 to 4.10, yielding greater concentrations of negatively charged $H_3SiO_4^-$, $H_2SiO_4^{2-}$, and $HSiO_4^{3-}$ ions. Essentially, higher alkalinity in the solution steers the equilibrium reactions towards generating various ionised forms of silicic acid. These ionised forms possess greater solubility in water, prompting an accelerated silica dissolution rate.

Nevertheless, this system also entails the presence of silver nanoparticles embedded within silica. The literature contains numerous studies detailing the dissolution of silver nanoparticles within acidic environments [220,240,241], attributed to the oxidative dissolution reaction whereby silver atoms undergo oxidation to form Ag^+ ions [240]:

$$Ag(s) \rightarrow Ag^+ + e^- \tag{4.11}$$

Dissolution rates are contingent on several factors, including solution pH, nanoparticle size and surface area. Notably, concentrated acids enhance the dissolution process.

Within this particular context, the phenomenon of silver nanoparticles (AgNp) dissolution ensconced within a silica coating under acidic conditions is anticipated to be primarily instigated by AgNp oxidation, consequently influencing the overall stability of the coating. Conversely, the dissolution of silica is expected in alkaline solutions owing to its inherent solubility in such environments. As a result, dissolution

processes manifest under both acidic and alkaline conditions, potentially leading to the delamination of the coating. The coating fabrication involved a three times dip coating procedure, wherein the dissolution of silica or oxidation of silver nanoparticles could contribute to delamination. This delamination was observed as a diminution in coating thickness, likely attributable to inadequate bonding within the coating structure. Notably, the challenge posed by the oxidation of silver nanoparticles in acidic media exacerbates the loss of AgNp/silica within acidic environments relative to alkaline ones.

4.2.4.2 Results of Micrographic examination

In order to examine the surface of the AgNp/silica coated optical fibre, a micrographic examination was conducted using a Scanning Electron Microscope (SEM), as shown in Figure 4.21. This examination focused on the morphology of the coating, specifically at the core of the optical fibre.

The SEM analysis enabled the determination of the diameter of the coated optical fibre. Measurements taken at different locations on the fibre revealed variations in diameter, ranging from 111 to 117 microns. Moreover, during the examination, the presence of cracks on the surface of the coated optical fibre was observed. These cracks signify the existence of weak bonds between particles on the surface of the coating, which ultimately leads to rapid break down of coating. It is worth noting that the occurrence of cracks on the surface of the coating has been previously reported in literature, where they have been associated with the porosity of silica coating [230,242,243]. This further supports the notion that the observed cracks are a result of inadequate bonding between the particles, which can negatively impact the stability and durability of the coating.
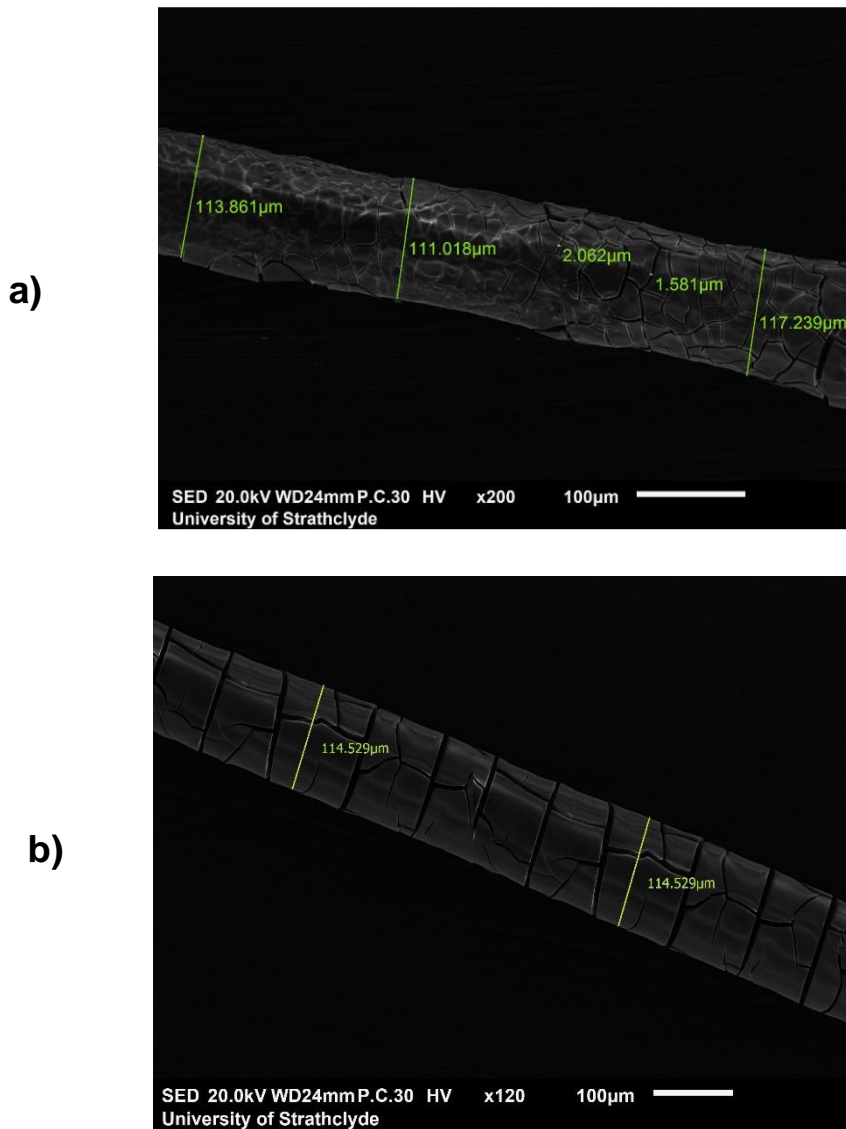
Figure 4.21: SEM image on the surface of AgNp/silica coating of optical fibre on two different samples (a) and (b).

According to the literature, it was reported the presence of microcracks on the surface of silica coatings using the SEM [244,245]. As silica is a porous material, there might be shrinkage due to the loss of organic part in solvent during the heat treatment. As a result, these microcracks tend to propagate along the surface. It might be minimised by the implementation of a slower rate for both heating and cooling rate during the heat treatment [36]. However, Twej et al. [246] asserted that they derived benefits from employing a chemical additive, N,N-dimethylformamide, on the silica to mitigate cracking [246].

4.2.4.3 Energy Dispersive X-ray analysis (EDX) analysis of coating

The elemental characterisation of AgNp/silica coated optical fibre samples was conducted using Energy-Dispersive X-ray (EDX) spectroscopy, and the results are presented in Table 4.6. In order to investigate the effects of different pH environments on the composition of the samples, a total of five samples were prepared, with four of them being immersed in specific solutions for a duration of 24 hours. The solutions employed for immersion included H_2SO_4 (pH 3), H_3PO_4 (pH 3), HCl (pH 3), and NaOH (pH 10), while the remaining samples served as the reference and were not subjected to any immersion. This analysis aimed to assess the changes in the composition of the samples following exposure to varying pH conditions.

The initial sample, which did not undergo any immersion, exhibited a composition containing 46.09% silicon (Si), 4.81% silver (Ag) and 49.07 % oxygen (O). However, upon immersion in acidic or alkaline solutions, a reduction in the levels of both silicon and silver was observed. Notably, the reduction was more pronounced when the samples were subjected to immersion in acidic solutions. On the other hand, the alkaline solution with a pH of 11 showed relatively less reduction in the silicon and silver content compared to the acidic solutions, as evidenced by the data presented in Table 4.6.

The levels of oxygen also differ among various sample conditions. Prior to immersion in a solution, the sample contained approximately 59.07% oxygen. Subsequent to immersion in different solutions, there are observable changes in the oxygen content. The samples underwent immersion in distinct solutions with varying pH levels (H_2SO_4 pH 3, H_3PO_4 pH 3, HCl pH 3, NaOH pH 10). It is evident that the pH of the solution exerts an influence on the distribution of elements in the sample, particularly with regard to the oxygen content. On the whole, the oxygen content appears to increase when the sample is immersed in acidic solutions (H_2SO_4, H_3PO_4, HCl) in comparison to the initial state. In summary, the results from EDX indicate a greater oxidation of silver in acidic solutions as opposed to alkaline solutions. These findings support the results obtained for glass slides, which focused on the durability test conducted at room temperature. It was noted that higher levels of dissolution occurred in acidic solutions compared to alkaline solutions. The

substantial decrease in the silicon and silver content following immersion in acidic solutions provides further confirmation of the dissolution earlier discussed.

Table 4.6: Chemical analysis on the surface of AgNp/silica coated optical fibre using EDX.

Sample condition	Si (%)	O (%)	Ag (%)	Others (P-C-Al-Na-S)
Sample before dipping in solution	46.09 ± 8.61	49.07 ± 4.16	4.81 ± 1.34	The other elements could be traced from impurities of chemicals/ sample plate in SEM
Sample dipped in H_2SO_4 (pH 3)	17.26 ± 3.35	81.49 ± 5.44	0.55 ± 0.19	
Sample dipped in H_3PO_4(pH 3)	20.03 ± 4.42	79.47 ± 5.84	0.27 ± 0.05	
Sample dipped in HCl (pH 3)	18.43 ± 5.30	79.82 ± 2.55	1.37 ± 0.59	
Sample dipped in NaOH (pH 10)	37.96 ± 4.20	59.52 ± 5.56	2.13 ± 0.44	

Upon reviewing the available literature, it was found that no similar study could be identified for the purpose of direct comparison. This can be attributed to the innovative nature of the current research. However, a comprehensive study conducted using EDX revealed that the silica sample had a silicon (Si) content of 64.2% and an oxygen (O) content of 35.8% [247]. The values examined in this analysis exhibit a strong correlation with the outcomes observed. It is important to highlight that this study also includes the element silver (Ag). The EDX results obtained exhibit modifications in composition, indicating variations in the chemical composition following the incorporation of silver nanoparticles into the silica matrix after being immersed in both acidic and basic solutions.

4.3 Proposed model of dissolution of AgNp/silica coating

The dissolution of the AgNp/silica coating was observed to result in the loss of material in both acidic and basic solutions, as discussed in the previous section. Moreover, cracks were spotted on the coating when examining the surface using SEM. When the coating is immersed in any solution, whether it is basic or acidic, the dissolution of the coating is initiated. The presence of proton (H^+) or hydroxide ion (OH^-) could easily penetrate through the crack and weaken the bonds at the surface structure. A model illustrating the dissolution of the coating is shown in Figure 4.22. As discussed in the previous section, although silica is reported to be more stable in acid than in alkaline solutions, the silver nanoparticles could still oxidise, resulting in an overall breakdown of the AgNp/silica coating. On the other hand, the silica coating itself is susceptible to dissolution in alkaline solutions, which also leads to the breakdown of the AgNp/silica coating. Overall, the AgNp/silica coating may be susceptible to attack by both protons (H+) and hydroxide ions (OH-), resulting in the complete breakdown or dissolution of the coating.
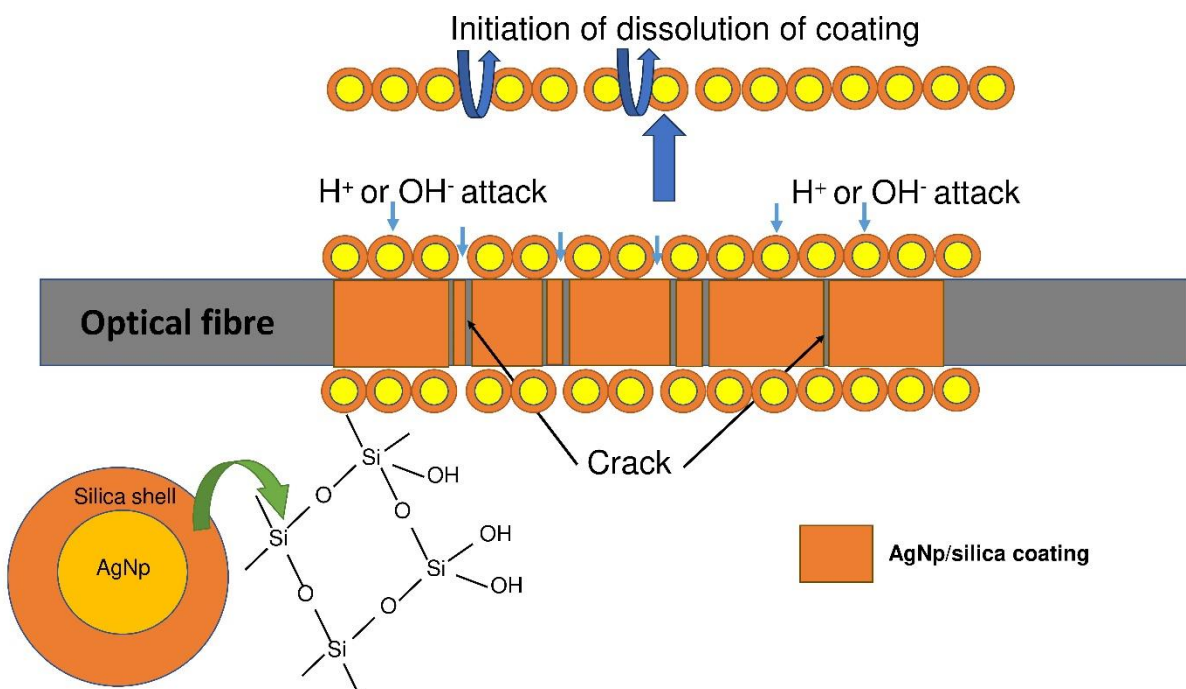
Figure 4.22 : Proposed mechanism showing the dissolution of AgNp/silica coating.

4.4 Summary

This study primarily focused on the synthesis and characterisation of colloidal silver nanoparticles using various chemical routes. It was observed that different sizes of silver nanoparticles could be synthesised by employing different chemical routes and reducing agents. However, to ensure the stability of the colloidal silver nanoparticles, the use of a stabiliser was found to be necessary. This stabiliser played a crucial role in maintaining the stability of the nanoparticles by preventing their aggregation, which could lead to the formation of larger particles. It was possible to achieve stable colloidal silver nanoparticles using a stronger reducing agent as sodium borohydride and then using a stabiliser as trisodium citrate.

In addition to the synthesis of colloidal silver nanoparticles, the study also explored the preparation of an AgNp/silica-coated optical fibre. To achieve this, all the required chemicals were mixed simultaneously. After conducting several trials under different conditions, a gelation temperature of 35 °C for 48 hours was identified as the most suitable condition. Subsequently, the gel was applied to a glass slide and subjected to heat treatment. The optimal condition for heat treatment was found to be 200 °C for 2.5 hours, as it showed the best adhesion of the coating to the glass slide. To further enhance the adhesion of the AgNp/silica coating on the glass slide, optimisation experiments were performed. It was observed that multiple dip coating increased the thickness of the coating on the optical fibre as expected.

An etching process using 7 M NaOH was used to selectively remove the cladding and coating layers of the optical fibre, exposing the core where the AgNp/silica coating was applied. During the etching process, it was determined that an optimum core diameter ranging from 103 to 105 microns was necessary to achieve the desired pH sensitivity. Furthermore, a series of optimisation experiments were carried out to determine the best combination of parameters between the light source and detector to attain the best sensitivity of the sensor. It was observed that as the voltage of the light source increased, the integration time of the detector needed to be reduced to adjust the light intensity and ensure the maximum intensity within the system. After several iterations, a configuration with a light source voltage of 6.5 V and an integration time of 5 ms was identified as the most suitable for achieving optimal sensitivity in optical pH measurements.

Lastly, durability tests were conducted on the AgNp/silica coating, revealing its dissolution under varied acidic and basic conditions. Enhanced susceptibility in acidic environments, compared to basic, was observed at room temperature, corroborated by energy-dispersive X-ray spectroscopy (EDX) analyses that demonstrated notable compositional changes in silicon (Si), silver (Ag) and oxygen (O). There was a significant reduction in the content of silicon and silver and an increased amount of oxygen, which indicated the oxidation of silver when the coating was dipped in the acidic solution.

The durability test and EDX analysis helped to understand about the stability of AgNp/silica coating and that the silver nanoparticle suffered from oxidation problems in acidic conditions (less than pH 3), which caused dissolution of coating. On the other hand, there are less dissolution in the alkaline solution (up to pH 10), which could be attributed to silica itself due to loss of silica. Concurrent scanning electron microscopy (SEM) analysis showed the presence of cracks, which might cause a faster breakdown of coating.

CHAPTER 5 Results: Optical pH measurement by AgNp/Silica Coated Optical Fibres at Room Temperature

CHAPTER 5

Results: Optical pH Measurement by AgNp/Silica Coated Optical Fibres at Room Temperature

This section discusses the results obtained from the pH measurement using optical fibre at room temperature. As mentioned, following the etching of the optical fibre using 7 M of NaOH, the etched section was coated with silver nanoparticles that had been incorporated in a silica coating. This was followed by the connection of the coated optical fibre to a detector and a light source. Then, the coated optical fibre was immersed in solutions of different pH that had been prepared using acids and bases. The intensity of the transmitted light was measured and compared with solutions of different pH. A change in intensity is expected at different pH levels because the silica coating possesses a surface charge that may undergo protonation and deprotonation depending on the acidity or basicity of the solution. This would result in a change in the refractive index, which would change depending on the pH of the solution. This is the reason why the intensity of the transmitted light was measured as a function of different solution pH and enables the system to work as a sensor.

This thesis chapter embarks upon an incremental exploration, commencing with the optimisation of the optical measurement technique. The objective is to attain the outmost optical sensitivity in pH measurement. Following this optimisation, the subsequent experiments are undertaken in triplicate, ensuring a robust assessment of the sensor's repeatability and reproducibility. Each repetition consisted of etching the optical fibre in 7 M NaOH, dipping it in the AgNp/silica gel, and finally carrying out the heat treatment to obtain a coated optical fibre. The optical response of the coated optical fibre at different pH was investigated. The results obtained for each of the optical fibres prepared in the same batch were compared with each other as well as with other relevant studies in the literature. This allows one to compare the reproducibility within a single batch (intra batch) and between each batch (extra batch). The outcome of these results was to determine the usefulness of the optical fibre based pH system for room temperature applications. The experimental procedures detailed within this chapter were conducted under conditions of standard room temperature and ambient pressure.

In summary, this chapter will cover the following:

- Identification of the optimal arrangement of the light source and detector to yield the maximum sensitivity for optical pH measurement.
- Determination of the most suitable diameter of the etched optical fibre which is necessary to assess the optimal optical sensitivity at different pH.
- Calibration of the optical pH measurement.
- Optical pH measurement in different chemical conditions like acids: phosphoric acid, sulfuric acid and hydrochloric acid and base: sodium hydroxide
- Reproducibility of the sensor prepared in the same batch as well as in different batches.
- As a control of the experiment, the optical response of the optical fibre was etched and coated with only silica to determine the effectiveness of AgNp/silica coating.
- Random optical pH measurement, including the comparison of the accuracy of the optical method of measuring pH with the potentiometric pH method.

5.1 Optical properties of fibre and sensor system

In this section, the key parameters requiring optimisation, including the choice of optical parameters associated with the light source and detector, such as the intensity of light entering the system, the current and voltage passing through the optical fibre, the integration time, as well as finding the right diameter at the core of the optical fibre which is to be etched is described. This is important because these parameters directly influence the performance and accuracy of the optical system. By optimising these parameters, one can enhance the signal-to-noise ratio, improve sensitivity, and increase the overall efficiency of the system.

The intensity of light entering the system is a crucial parameter as it determines the amount of signal that can be detected. Finding the optimal intensity ensures that the signal is strong enough to be measured accurately without causing saturation or excessive noise. Similarly, adjusting the current and voltage passing through the optical fibre helps in controlling the transmission characteristics and maximising the signal strength. Integration time is another parameter that requires optimisation. It

determines the duration over which the light signal is integrated, affecting the sensitivity of the system. Longer integration times allow for better detection of weak signals but can result in slower response times. Therefore, finding the right balance between integration time and signal strength is crucial to achieve optimal performance.

Moreover, finding the right core diameter for the optical fibre to be etched is crucial. The core diameter affects the propagation of light within the fibre and transmission characteristics. By carefully selecting the appropriate core diameter, we can optimise the coupling efficiency and improve the overall performance of the optical system. Additionally, the core diameter also influences the interaction between light and the surrounding environment, such as the sensing materials or analytes. Thus, selecting the right core diameter is essential for achieving optimal sensitivity and accuracy.

5.1.1 Baseline conditions of the light source and detector

This section covers the results of the application of the AgNp/silica coated optical fibre as a pH sensor. The main objective was to achieve reproducible and repeatable optical data for use as an optical pH sensor. It was important to ensure that optimum sensitivity and the best detector signal were obtained.

By gradually increasing the voltage of the light source from 2.0 V to 6.5 V, a significant decrease in the integration time from 3000 ms to 5 ms was obtained. The result presented in Table 5.1 indicates that increasing the voltage of the light source resulted in a corresponding increase in the current, leading to a decrease in the integration time. The data presented in this study demonstrates the integration times required for achieving a light intensity of 60,000 arbitrary units (a.u.) using different currents. It should be noted that the detector utilised in this experiment has a maximum capacity of 65,000 a.u.

Table 5.1: Parameters of the light source and detector utilising an unetched optical fibre as the reference.

Light source		Detector
Voltage (V)	Current (A)	Integration time (ms)
2.0	2.2	3000
2.5	2.5	700
3.0	2.7	250
3.5	2.9	85
4.0	3.2	40
4.5	3.4	25
5.0	3.6	15
5.5	3.8	10
6.0	4.0	7
6.5	4.2	5

An unetched optical fibre served as the reference fibre to collect "baseline" performance. It was employed to capture spectra corresponding to both 100% (full light beam) and 0% (shutter closed) light transmissions from the light source, denoted as I_{100} and I_0, respectively. For each voltage setting, as outlined in Table 5.1, measurements of I_{100} and I_0 were taken. Subsequently, the optical fibre was connected to the AgNp/silica coated optical fibre while concurrently measuring the light intensity (I). A separate set of measurements for I_{100}, I_0, and I was recorded for each voltage level. To mitigate system noise, a baseline correction procedure was implemented. In this context, I_0 was treated as the system noise, captured during the 0% light transmission phase, and was employed for noise elimination.

For the baseline correction, the intensity of light transmitted through the reference optical fibre after the baseline correction is given as follows:

$$I_B = I_{100} - I_0 \tag{5.1}$$

Similarly, the intensity of light transmitted through the coated optical fibre after the baseline correction is given in the equation below.

$$I_S = I - I_0 \qquad\qquad (5.2)$$

Also, the intensity of light passing through the coated optical fibre (I_S) and the incident light transmitted through the reference optical fibre (I_B) was used to calculate the absorbance (A) using the formula below:

$$A = log_{10}\frac{I_B}{I_S} \qquad\qquad (5.3)$$

After carrying out the baseline correction using equation 5.2, I_S for each voltage of experiments was plotted as shown in Appendix F.

The signal obtained using two different voltages (3.5 V and 6.5 V) for both the reference and coated optical fibres were further examined to display their intensities over a range of wavelengths. The results are shown in Figure 5.1 and Figure 5.2, respectively.
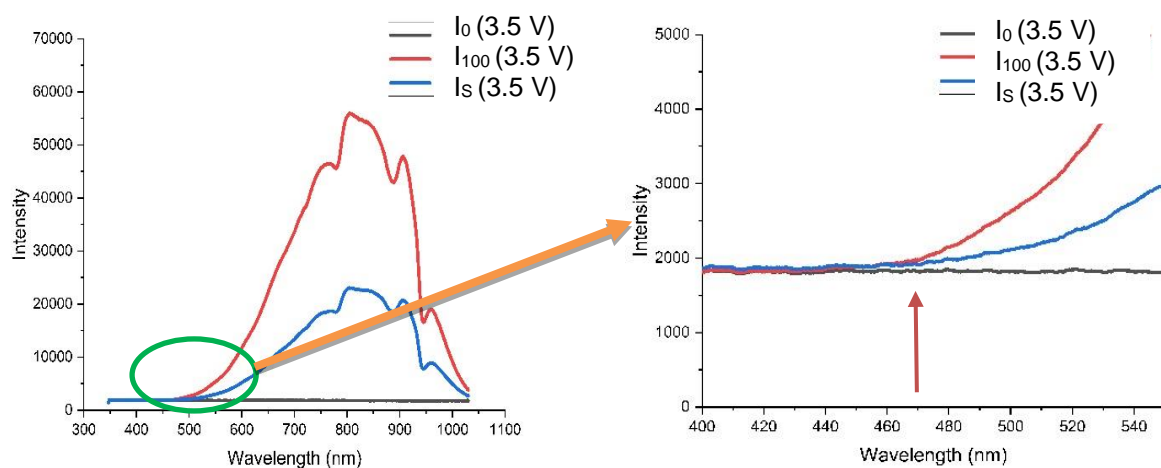
Figure 5.1: The UV-visible spectra showing the intensity of light using the reference (I_0 and I_{100}) and coated optical fibre (I_S) at 3.5 V of light and 85 ms of integration time.
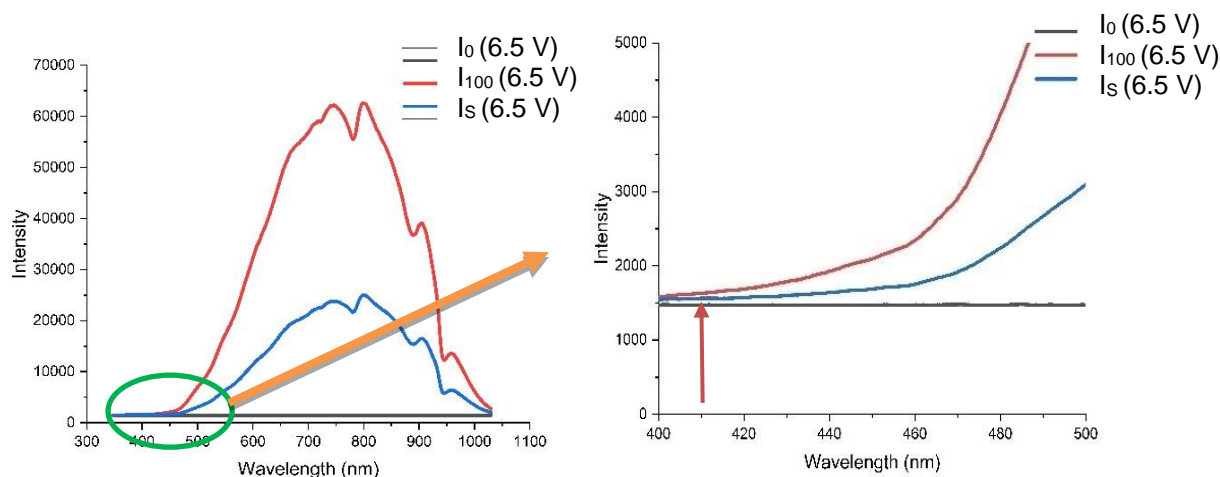
Figure 5.2: The UV-visible spectra of the intensity of light using the reference (I_0 and I_{100}) and coated optical fibre (I_S) at 6.5 V of light and 5 ms of integration time.

The data shown in Figure 5.1 indicates that the intensity of light using 3.5 V of light for I_{100} and I_S was almost the same up to the wavelength of 470 nm. This was also observed to show an increasing trend with a further increase in wavelength beyond 470 nm. On the other hand, the intensity of light at 6.5 V was almost the same for I_{100} and I_S up to 410 nm. Similarly, this was observed to also increase with wavelength beyond 410 nm, as shown in Figure 5.2. Thus, a shift in wavelength to a lower value was observed at the 6.5 V of light. Therefore, the use of a lower voltage was avoided in order to obtain a reasonable change in intensity.

Consequently, within the framework of this investigation, a voltage of approximately 6.5 V was deemed optimal for achieving heightened sensitivity. This determination was informed by the operational constraints of the UV-Vis spectrophotometer, which imposed a maximum integration time of 4 ms. Consequently, the exploration of more intense light intensities exceeding 6.5 V was precluded, as doing so would have necessitated a reduction in the integration time below the minimum threshold of 5 ms. Furthermore, it is noteworthy that no polishing methodology was applied to the terminated optical fibre throughout the course of this study, a factor that could potentially influence the attenuation of light intensity. Thus, the adoption of a 6.5 V voltage setting from the light source, in conjunction with a 5 ms integration time at the detector, is deemed the best configuration for the experimental setup, considering the limitations imposed by the available apparatus and instrumentation.

5.1.2 Conditions of etched optical fibre for pH measurements

The purpose of optical fibre etching was to decrease the outer diameter from 250 microns to 105 microns. This section is focused on discussing the results of the pH sensitivity at different diameters of the core of the optical fibre. This was aimed at finding the best option with the highest sensitivity to changes in pH. Figure 5.3 illustrates the pH sensitivity of the optical fibre utilising core diameters of 106 microns, 104 microns, and 102 microns. Solutions of different pH ranging from 3, 7, and 11 were investigated. In this study, the same conditions were used for a reference optical fibre to compare the sensitivity just to ensure that the observed result is strictly due to the etched optical fibre coated with AgNp/silica.

The findings depicted in Figure 5.3 (a) pertain to pH sensitivity when the optical fibre's core was etched to 106 microns. Notably, this configuration demonstrated markedly low sensitivity, which could be attributed to minimal light leakage, leading to reduced sensitivity. Similarly, Figure 5.3 (c) illustrates the diminished sensitivity observed when the core diameter was reduced to 102 microns. In this case, excessive light leakage from the system became apparent due to the over etched core diameter. Conversely, promising sensitivity results were evident when the optical fibre's core was etched to 104 microns, as depicted in Figure 5.3 (b). A critical prerequisite for optical pH sensitivity is maintaining adequate light within the system. This experiment underscores the pH sensor's enhanced sensitivity within the core diameter range of 103 to 105 microns. This range signifies the limits within which an appropriate amount of light is retained in the system. Beyond the lower limit, excessive light leakage occurs, while surpassing the upper limit leads to an abundance of light within the system. Both scenarios impede the sensitivity of pH measurement in aqueous solutions.

The configuration of the coating is undoubtedly a critical factor influencing the sensitivity of the sensor. Within the framework of this study, an exhaustive examination was conducted utilizing a singular coating structure, as delineated in the methodology chapter. Nevertheless, an intriguing avenue for further investigation lies in the comparative analysis of sensor sensitivity across varied coating structures. Such an endeavour holds promise for elucidating additional insights into optimizing the pH sensitivity of optical fibre-based sensors in future.
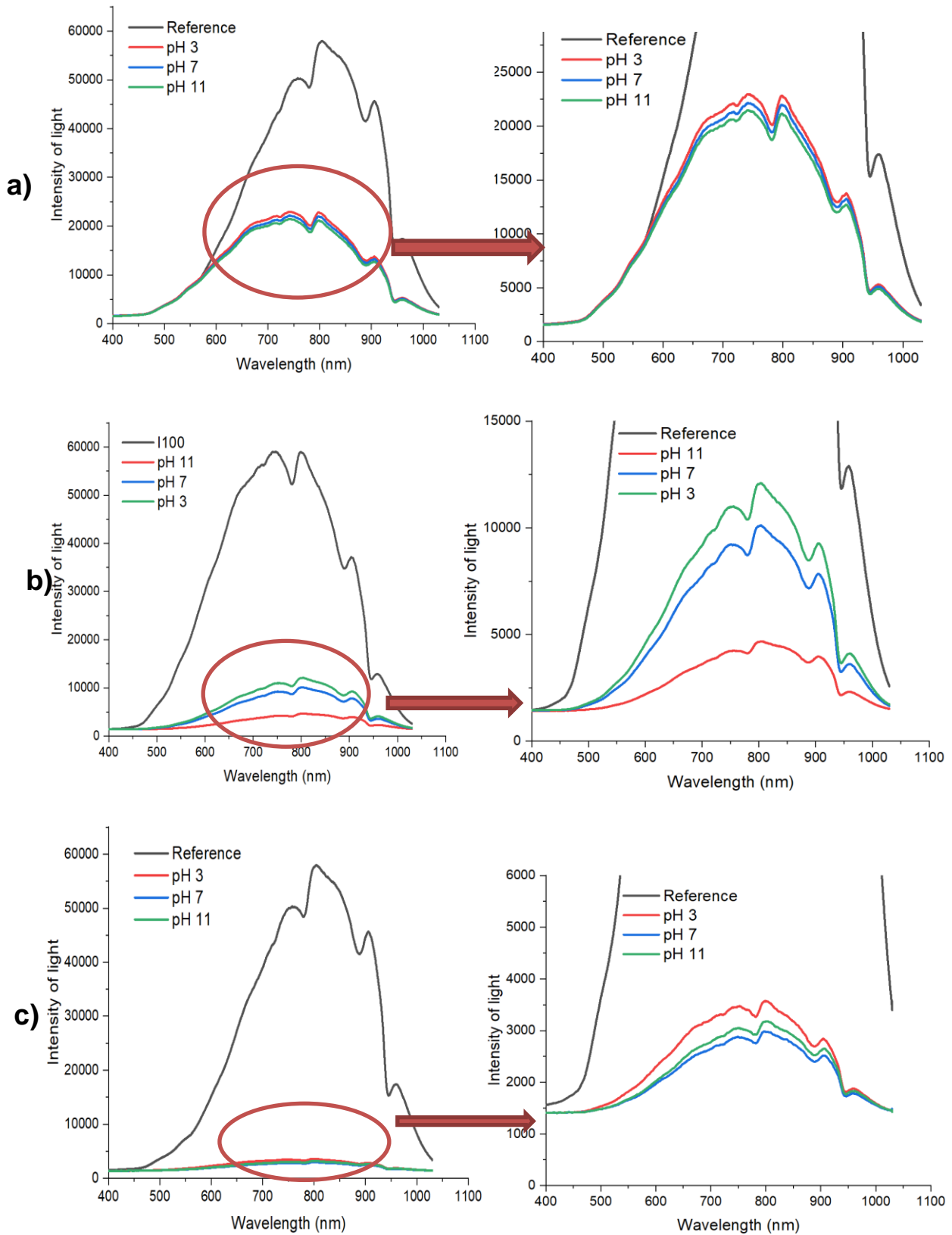
Figure 5.3: The pH sensitivity at different core diameters of the optical fibre (a) 106 microns, (b) 104 microns, (c) 102 microns.

To the best of our knowledge, there has been a scarcity of studies investigating the effect of a coated optical fibre on optical sensitivity, which could be utilised as a pH sensor for comparison. Nevertheless, the absence of such findings emphasised the fundamental significance of such outcomes within the scope of this research. These results were deemed imperative to lay the foundation for an effective optical measurement system capable of assessing the pH change within the solution. In the following section, the performance of the AgNp/silica-coated optical fibre as a pH sensor will be assessed by employing these optimisations under various chemical conditions.

5.2 Measurement of pH in different solutions using AgNp/silica coated optical fibre

These experiments were carried out to evaluate the response of the pH sensor that has been coated with AgNp/silica in different acids such as phosphoric acid, sulphuric acid and hydrochloric acid, among others. The anions in these solutions can alter the surface charge due to the interaction of the ions produced by the acid and the base with the silica layer. This study will assess how hydronium ions from acids and their basic counterions interact with the coating to provide a pH response. The concentration of the solution, expressed as a pH value, should have a direct and proportionate influence on the number of hydronium ions that are present in the solution for the coated fibre to function as a pH sensor, but their conjugate bases (derived from the anions) can also influence surface charge.

Therefore, in order to verify that the sensor is operating optimally, the sensitivity of the sensor has to be studied. It is also essential to assess the reproducibility and repeatability of the sensor in these measurements in order to ensure that the developed sensor is reliable for real-life applications. This section contains the results of three separate measurements. A comparison of the pH response of coated optical fibres prepared in the same and different batches, as well as a comparative assessment of the pH response of the coated optical fibre prepared in this study with other optical fibres reported in the literature as well as potentiometric method of measuring pH of different solutions, are reported. This provides a comprehensive assessment of this type of sensor against other available techniques.

5.2.1 Optical pH measurement solution in phosphate media

In the oil and gas industry, various chemicals are present, including phosphate ions [41,248–250]. Therefore, the experimental solution conditions were selected to represent the presence of these chemicals in oil and gas. To facilitate this assessment, an optical fibre coated with AgNp/silica was connected to a light source and a detector attached to it. In the context of the oil and gas industry and downhole conditions, the anticipated pH range typically falls within 4 to 8 [65]. However, for the experiment, a broader pH range of 3 to 11 was selected. The pH alteration involved the addition of 0.1 M of sodium hydroxide and 0.1 M of phosphoric acid to the solution in order to obtain a solution with a pH range of 3 to 11. This would allow extensive evaluation of the sensor performance across different pH levels. In order to ascertain the effectiveness of the sensor, different tests were conducted to assess its repeatability, reproducibility, stability, and sensitivity.

In this study, a titrimetric technique involving phosphoric acid and sodium hydroxide was employed to adjust the pH of experimental solution, as has been suggested by previous researchers [90,94,95,188]. The AgNp/silica coated optical fibre was immersed in the solution, and the pH was adjusted from 3 to 11 and connected to a detector and a light source. Prior to commencing the experiment, a reference optical fibre (unetched optical fibre) was employed to establish the baseline value for light intensity. This baseline values were recorded as I_{100} (with 100% light intensity) and I_0 (with a closed shutter), as depicted in Figure 5.4 across a variety of wavelengths. After adding the AgNp/silica coated optical fibre into the system, the intensities of light corresponding to each pH level were measured and recorded. A potentiometric pH meter was dipped in the solution to record the pH of the solution for comparison. The pH of the solution was adjusted within the range of pH 3 to pH 11 with an interval step of 1, using either acid or base. The results of the intensity of light were plotted as a function of pH (Figure 5.4). Then, the baseline correction was carried out by subtracting the value of I_0 from all the intensities obtained for the pH.
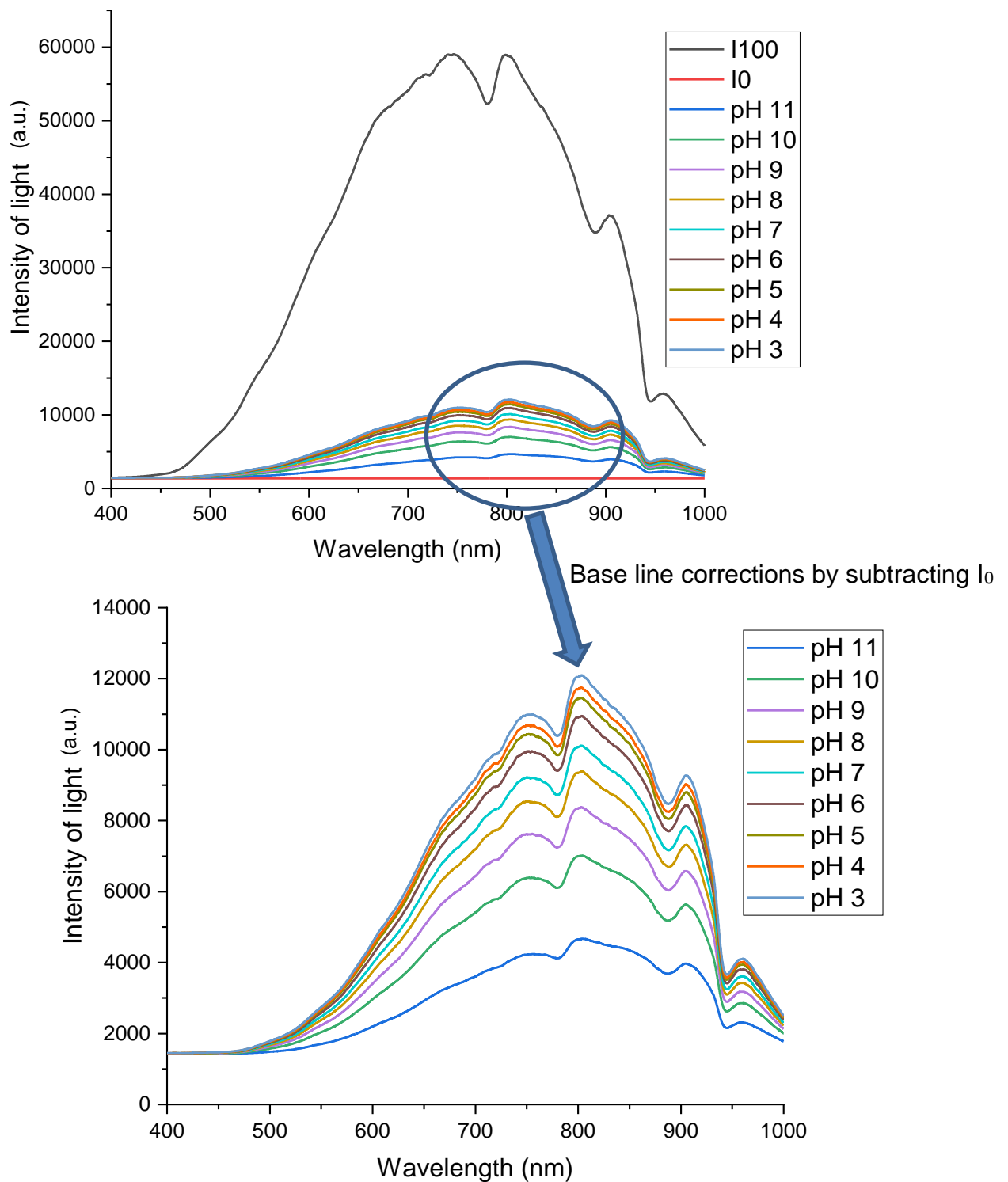
Figure 5.4: The change in intensity of light at a different wavelength of light in different pH solutions using H_3PO_4 and NaOH.

The results shown in Figure 5.4 indicate that the intensity of light increased as the pH of the solution decreased, showing that the AgNp/silica optical fibre was pH-responsive. The observations made in the experiment indicated that the lowest

intensity of light, represented by the blue line in the graph, was observed in the solution with the highest pH (pH 11). As the pH of the solution gradually decreased towards pH 3, the intensity of light was observed to increase accordingly. These findings provide the basic concept that the system responded to pH changes.

Among all the pH solutions tested, it was observed that the solution with a pH of 3 exhibited the highest intensity of light, surpassing the intensities observed in the other pH solutions. This finding suggests that the solution with a pH of 3 had higher transmittance compared to the solutions at different pH levels. To further analyse and compare the intensities of light at different pH levels, the recorded values were converted to the percentage of transmission (%T) relative to the intensity of light at pH 3, which served as the reference point for comparison. Figure 5.5 illustrates the transmittance of light for all the pH solutions. Notably, a distinct peak in transmittance was observed at a wavelength of 530 nm. This peak indicates that at 530 nm, the light had the highest level of transmission through the solutions. However, it is important to note that the change in transmission was visible across a broad range of wavelengths, spanning from 500 nm to 1000 nm, for all the pH solutions. This broad response indicates that the coating of AgNp/silica on the optical fibre contributed to the overall transmittance observed.

The presence of the AgNp/silica coating on the optical fibre played a crucial role in achieving the observed response and influencing light transmission across different wavelengths. In addition, the transmittance for all the pH solutions was observed to show a peak at a wavelength of 530 nm, with visible changes in transmission observed across a wide range of wavelengths (500 nm to 1000 nm). The observed change in transmittance could be attributed to the presence of the AgNp/silica coating on the optical fibre, which affected the transmission of light and corresponding changes in pH across the test solutions. The following section will discuss the potential reasons and mechanisms associated with the change in light intensity as the pH of the solution changes.
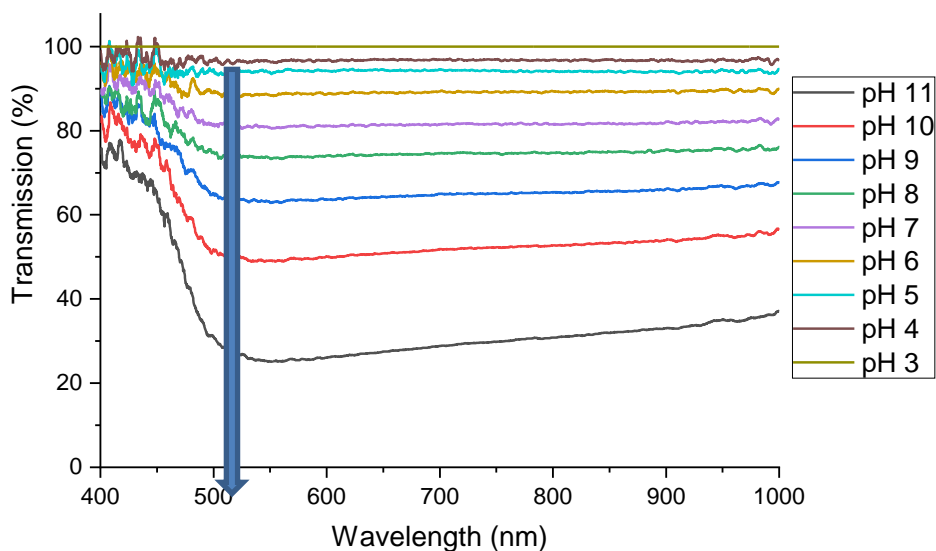
Figure 5.5: The percentage of transmission of light at a different wavelength of light in different pH solutions using H_3PO_4 and NaOH

This section aims to provide an in-depth explanation of the mechanism of pH measurement using a coated optical fibre. The foundation of this technique lies in the theory of total internal reflection, which shows a change in the refractive index between the core and cladding of the fibre. It is believed that total internal reflection is a major factor that is responsible for the observed effect even when the cladding was substituted with an AgNp/silica coating. This is because the optical response observed is a direct consequence of the change in refractive index resulting from changes in the pH of the solution [90,188].

This could be further explained by the change in surface charge density facilitated by the incorporation of silver nanoparticles within the silica matrix. Notably, the surface charge of the silica layer can be manipulated by altering the pH of the test solution, as reported in the literature. Previous studies have reported an increase in the charge density of the coating due to the presence of metal nanoparticles within the silica matrix [95,251].

The silica surface consists of Si-OH active bonding, which undergoes various reactions depending on the pH of the solution. The following reactions demonstrate the potential reactions that are likely to occur at the surface at different pH levels [178,179]:

$$\text{In acidic solution: } SiOH + H^+ \leftrightarrow SiOH_2^+ \qquad (5.4)$$

$$\text{In alkaline solution: } SiOH + OH^- \leftrightarrow SiO^- + H_2O \qquad (5.5)$$
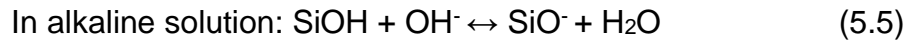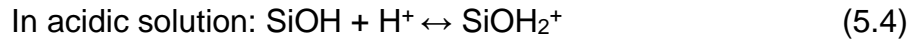
These reactions indicate the change in the surface chemistry of the silica coating due to changes in the pH of the solution. By monitoring the optical response of the coated optical fibre, which is correlated with the change in refractive index, the pH of the solution can be determined. This innovative approach enables precise pH measurements by leveraging the principles of total internal reflection and surface chemistry induced by the presence of silver nanoparticles within the silica coating. When the pH of the test solution was modified from pH 3 to 11, it was observed that the surface of the silver nanoparticle embedded in the silica coating has the potential to adsorb ions present in the solution. The extent of ion adsorption on the surface of the coating is directly linked to the pH of the solution. This localised modification in the effective refractive index can be influenced by the pH of the solution, primarily due to surface charge effects and the formation of a corresponding depletion layer at the interface between the matrix and the solution [175,176].

This phenomenon can be further explained by considering the behaviour of silver nanoparticles within the silica matrix when exposed to varying pH conditions. At low pH values (acidic conditions), an increased concentration of H^+ ions in the solution promotes the protonation of the Si-OH groups on the surface of the coating, resulting in a positively charged surface. Consequently, this positive charge attracts anions from the solution, leading to their adsorption on the coating's surface. The presence of these adsorbed ions creates an altered local refractive index, affecting the overall optical response [188,252]. Conversely, at high pH values (alkaline conditions), increased concentration of OH^- ions in the solution leads to deprotonation of the Si-OH groups on the coating's surface, rendering it negatively charged. This negative charge then attracts cations from the solution, causing their adsorption onto the surface. Once again, this adsorption of ions induces changes in the local refractive index, thereby influencing the optical properties of the coating.

In this study, phosphoric acid (H_3PO_4) and sodium hydroxide (NaOH) were used to adjust the pH of the solution. The chemical reaction that illustrates the interactions between phosphoric acid and silica is shown in equations 5.6 and 5.7 [253]:

$$H_3PO_4 \rightarrow H^+ + H_2PO_4^- \qquad\qquad (5.6)$$

$$Si-OH + H_3PO_4 \rightarrow Si-OH_2^+ + H_2PO_4^- \qquad\qquad (5.7)$$
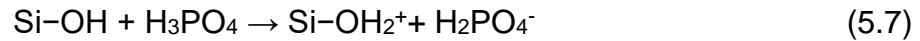
Phosphoric acid provides protons used to protonate the silanol groups on the silica surface, forming positively charged sites ($Si\text{-}OH_2^+$) and dihydrogen phosphate anions ($H_2PO_4^-$). Phosphoric acid can protonate the silanol groups, leading to an increase in the positive surface charge density. The extent of protonation depends on the acid concentration and pH of the solution. In aqueous solutions, phosphoric acid can exist in different forms of ions ($H_2PO_4^-$, HPO_4^{2-}, PO_4^{3-}), and these ions could participate with silica for the adsorption of ions on the surface [253]. The formation of the associated adsorption of ions at the coated matrix–solution interface further contributes to the changes in the effective refractive index. By considering these surface charge effects, it becomes evident that the hydronium anions and cations of the solution play a crucial role in modifying the optical response of the coated optical fibre. This interplay between pH, surface charge, ion adsorption, and local refractive index provides the foundation for pH measurement using coated optical fibre, a complex process.

In a study conducted by Wang *et al.* [95], the researchers investigated the use of gold nanoparticles in a silica matrix (Figure 5.6a) and palladium nanoparticles in a silica matrix (Figure 5.6b) and decoration on an optical fibre for pH measurement. The results indicated distinct optical responses for these different nanoparticles. For instance, gold nanoparticles exhibited a peak in their spectrum at a wavelength of 525 nm, indicating strong interaction with light. On the other hand, palladium nanoparticles displayed a broad response across a wide range of wavelengths from 400 nm to 900 nm, without a peak, as shown in Figure 5.6 (b). The response observed with palladium nanoparticles is somewhat similar to silver nanoparticles. Moreover, in the spectrum of silver nanoparticles, a vague peak was observed at the wavelength of 530 nm and a broad response from 400 to 900 nm, as shown in Figure 5.5. This peak can be attributed to the localised surface plasmon resonance (LSPR) property of nanoparticles. The AgNp/silica coating does not show a clear peak, as that observed for AuNp/silica in Figure 5.6. However, the palladium nanoparticles, being a weaker plasmonic metal, did not exhibit any peak in their spectrum at all.
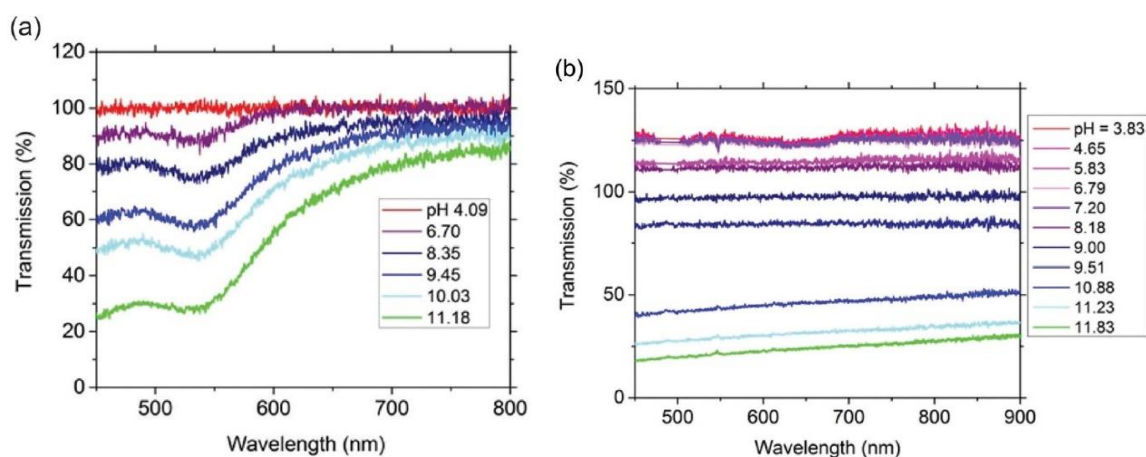
Figure 5.6: The percentage transmission of light at different wavelengths in different pH solutions using (a) AuNP/silica and (b) PdNP/silica [95].

In the realm of localized surface plasmon characteristics, palladium nanoparticles typically demonstrate a diminished resonance in contrast to their gold and silver counterparts [254,255]. The wavelength at which localized surface plasmon resonance peaks occur spans from 200 to 2000 nm, contingent upon the specific sizes and geometries of the nanoparticles (AuNp, AgNp or PdNp) [255,256]. The presented curves for AuNp, AgNp, or PdNp collectively exhibit monotonic behaviour, wherein alterations in directionality coincide consistently with variations in pH levels. It was observed that the highest degree of light transmission occurred within solutions characterized by lower pH values, with a subsequent decline in transmission noted as pH levels were raised within the solution. Notably, the determination of particle sizes and shapes in previously reported studies has been challenging, hindering direct comparisons of their surface plasmon properties within a consistent framework. It is observed that palladium nanoparticles embedded in silica exhibit a subdued LSPR response compared to gold and silver counterparts, potentially accounting for the absence of discernible peaks across the entire wavelength spectrum. Conversely, gold nanoparticles incorporated within silica matrices manifest stronger resonance peaks, whereas silver nanoparticles within silica exhibit weaker peaks, reflecting the varying strengths of their LSPR characteristics.

Numerous studies have demonstrated that optical properties are related to the scattering behaviour of silica particles, which relies on the alteration of an effective refractive index within their immediate vicinity [95,257]. Moreover, the pH level of the solution phase could potentially influence this alteration due to surface charge effects and the formation of a corresponding layer at the interface between the matrix and solution [188,251]. These observations show the significance of the presence of metal nanoparticles in the silica matrix to the optical response of the sensor. The study also revealed that gold nanoparticles demonstrated a clear peak, whereas silver nanoparticles exhibited a vague peak due to their distinct plasmonic properties. On the other hand, palladium nanoparticles, which possess a lower plasmonic behaviour, did not display any peak. Nevertheless, the presence or absence of peaks did not affect the optical pH measurement significantly, as optical responses were observed across various wavelengths for AgNp/silica, AuNP/silica, and PdNp/silica coatings. The extinction of light by Au nanoparticles is attributed to plasmon resonance due to the inherent dissimilarity in the light extinction properties of the two materials [258–260]. The consistent response observed regardless of the specific optically active material embedded in the silica matrix, strongly implies that the dominating factor is the presence of silica itself. It is important to note that the silica coating, which was common across all coatings, likely played a substantial role in influencing the optical response in different pH solutions. Further discussion regarding the results of the optical response in the presence of just the silica coating will be discussed later in this chapter.

5.2.1.1 Analysis of optical properties

As mentioned above, when there is no distinct (sensitive) peak, then need to choose the wavelengths for pH measurement. In this section, there are further discussions and analyses of the results of the optical properties of AgNp/silica coating as a pH sensor, such as shown in Figure 5.4 are discussed. The wavelengths of 550 nm and 800 nm were selected to investigate the changes in light intensity. The reason for choosing 550 nm and 800 nm was to assess and compare the light intensity change at lower and higher wavelengths. These results are shown In Figure 5.7 (a), which suggests that the intensity of light at 550 nm was observed to be 1612 for the solution with a pH of 11. As the pH of the solution decreased, the intensity of light

increased. At pH 3, the intensity of light reached 2365 at the wavelength of 550 nm. Similarly, in Figure 5.7 (b), the intensity of light at 800 nm was observed to be 4652 for the solution with a pH of 11. As the pH of the solution decreased, the intensity of the light increased, following the same trend observed at the wavelength of 550 nm. At pH 3, the intensity of light reached 12054 at the wavelength of 800 nm.
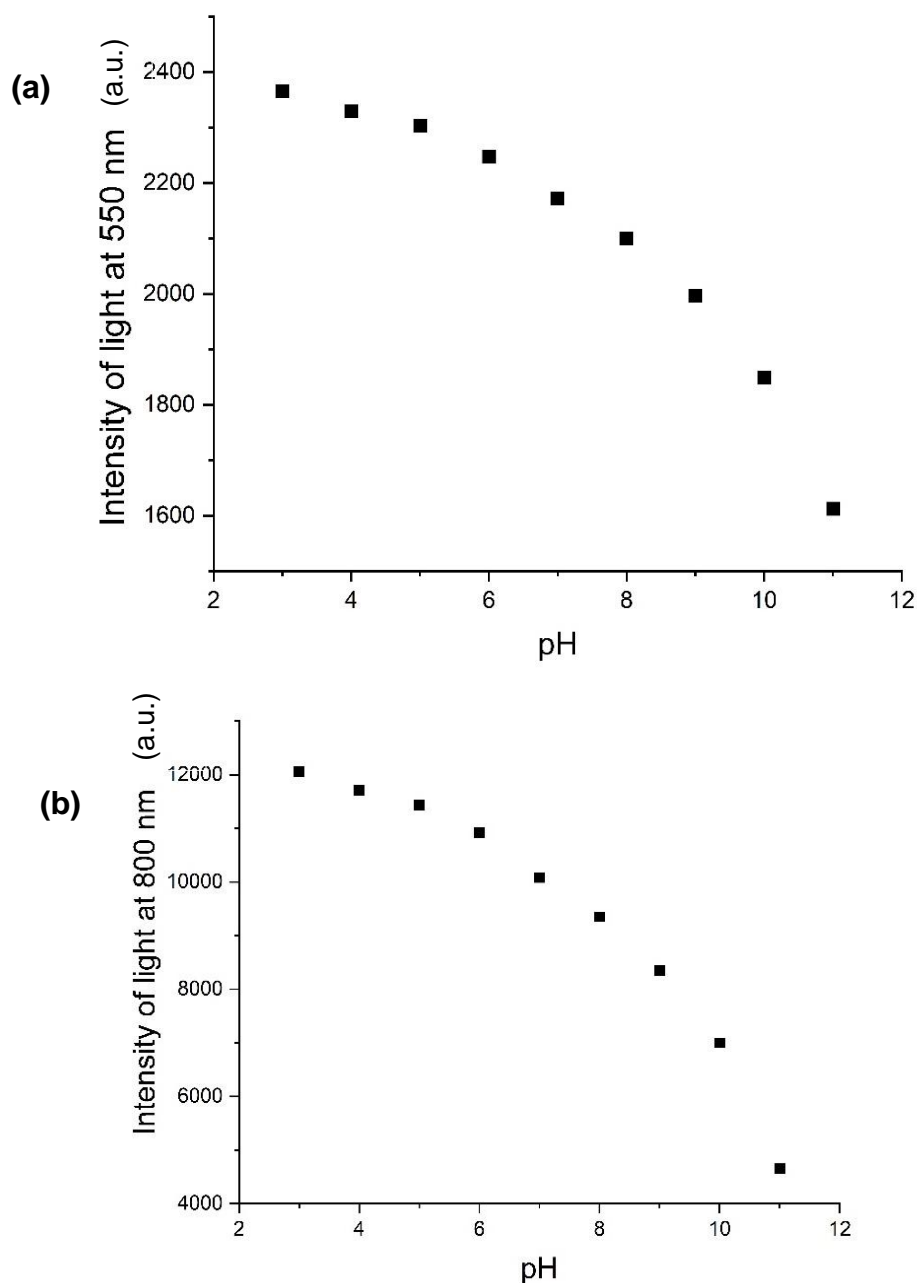
Figure 5.7 : (a) The change in intensity of light at the wavelengths of (a) 550 nm and (b) 800 nm using H_3PO_4 and NaOH.

In order to compare the changes in intensity at the wavelengths of 550 nm and 800 nm, the data was further normalised to a scale of 0 to 100, as shown in Figure 5.8. This normalisation allows for a more straightforward assessment of intensity variations between the two wavelengths. Analysing the normalised data, the change in intensity at the wavelength of 550 nm was observed as follows: from pH 11 to pH 10, the change was 31; from pH 10 to pH 9, the change was 20; from pH 9 to pH 8, the change was 13; from pH 8 to pH 7, the change was 10; from pH 7 to pH 6, the change was 10; from pH 6 to pH 5, the change was 7; from pH 5 to pH 4, the change was 4; and from pH 4 to pH 3, the change was 4.
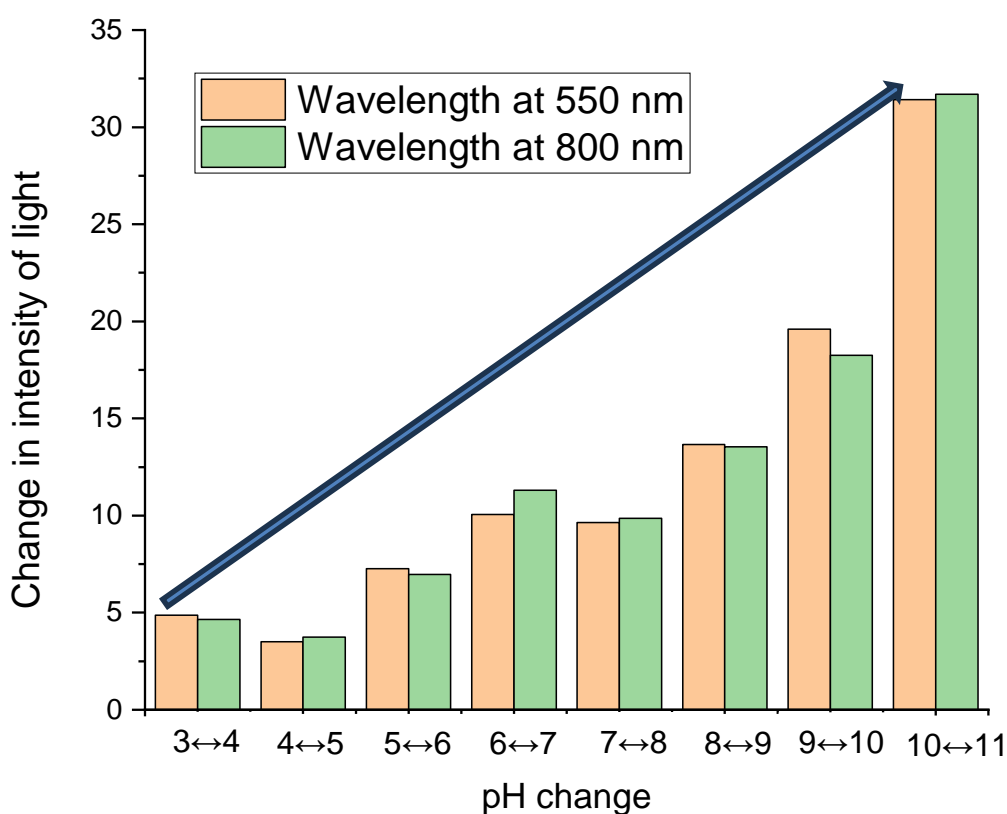
Figure 5.8 : (a) The change in intensity of light at the wavelength (a) 550 nm (b) 800 nm using H_3PO_4 and NaOH.

These results indicate that the change in intensity was lower in acidic solutions (lower pH values), with a gradual increase observed as the pH of the solution was increased. Notably, the rate of change in intensity was similar between the two wavelengths, indicating a consistent response to pH variations. These findings demonstrate that the intensity of light at both 550 nm and 800 nm as pH-dependent. In addition, as the pH of the solution decreases, indicating increased acidity, the

intensity of light also increases. This correlation suggests that the sensor's response to changes in pH levels is consistent across different wavelengths. The substantial increase in light intensity as the pH decreases from 11 to 3 underscores the sensor's sensitivity and ability to accurately detect and quantify pH variations. The measured intensities at these specific wavelengths provide valuable information for analysing the sensor's response to pH changes. These observations contribute to the understanding of the sensor's performance characteristics and aid in the optimisation of the sensor's design for pH measurement applications.

In a study conducted by Su *et al.* [82] to assess the sensitivity of an optical fibre pH sensor utilising AuNp/silica coated optical fibre, the pH of the solution was adjusted using phosphoric acid and sodium hydroxide as depicted in Figure 5.9 (black data points). It was reported that a higher change in transmission at higher pH values, with a comparatively lower change in transmission observed in acidic conditions. This response closely resembles the results obtained in the current research involving AgNp/silica (red data points). There are similar trends found in this research as AuNp/silica were reported. A common factor shared by both the AuNP/silica and AgNp/silica coatings is the presence of a silica coating. The key difference lies in the incorporation of different metal nanoparticles within the coating. This indicates that the silica coating itself plays a significant role in the sensitivity or that AgNp and AuNp behave similarly to the sensor with respect to pH changes in the solution. The optical response was analysed at a wavelength of 525 nm, but it can be analyzed at any other wavelength.
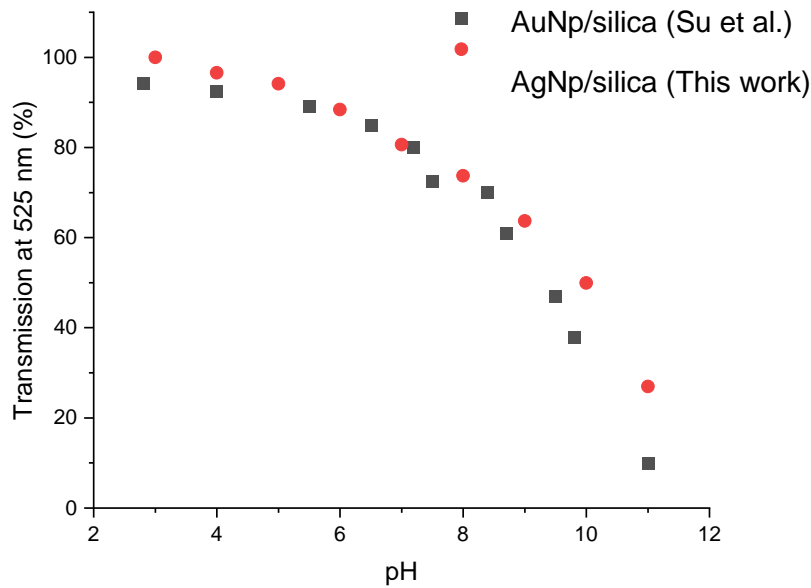
Figure 5.9: Comparison of normalised transmission of light at the wavelength of 525 nm using AuNP/silica coating [82] and AgNp/silica on optical fibre as a pH sensor.

5.2.1.2 Repeatability and reproducibility analysis

To assess the performance and reproducibility of the sensor, a thorough investigation was conducted using three different optical fibres prepared simultaneously, ensuring they were from the same batch. The optical fibres were etched using the same etching solution, coated with the same AgNp/silica gel, and subjected to heat treatment in the same batch. The purpose of analysing optical fibres prepared from the same batch was to evaluate the variation in performance among the three samples as pH sensors. By examining the change in intensity of light for different pH levels using these three optical fibres, it would be possible to understand the consistency and reproducibility of the sensor's response.

Figure 5.10 (a) presents the change in intensity for various pH levels using the three different optical fibres. It is observed that the intensity of light was quite reproducible across the three samples. This implies that, despite being distinct fibres, they displayed reproducible responses to changes in pH. This consistent behaviour is an essential characteristic of a reliable pH-sensing method. Furthermore, Figure 5.10 (b) shows the error bars associated with the response of the three samples. The error bars represent the variability in the measured intensities among the optical fibres. Notably, the error bars appear to be relatively lower (with around ± 146 nm),

suggesting a reasonable level of consistency and agreement among the samples' responses. This lower variability reinforces the reproducibility of the sensor and provides confidence in the accuracy and reliability of the obtained results. These findings verify the reliability and suitability of the sensor for pH measurement applications, as they demonstrate the ability to consistently produce accurate and reproducible results across multiple samples fabricated using a single batch.
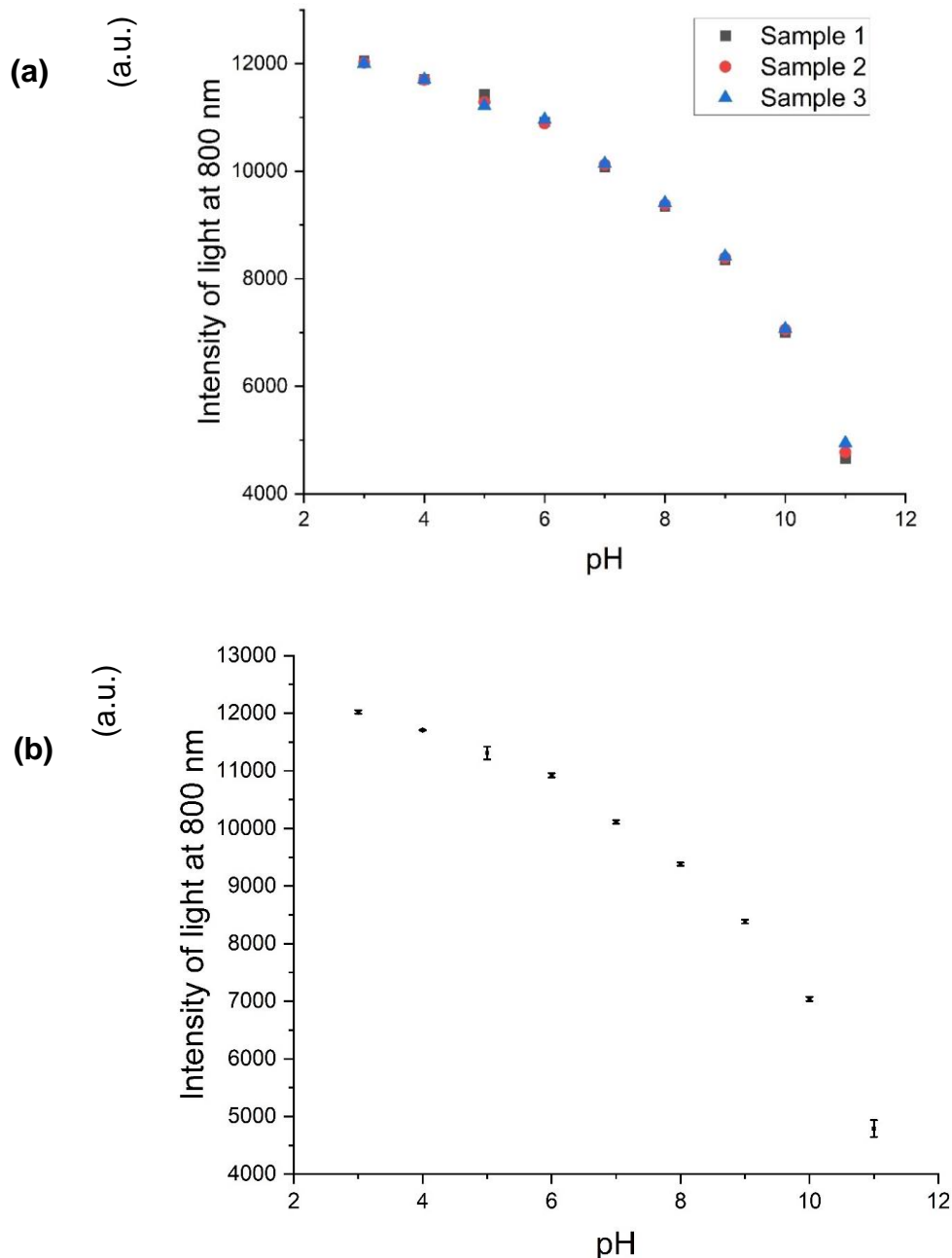
Figure 5.10: The change of intensity in different pH solutions using three different optical fibres prepared using H_3PO_4 and NaOH (a) in the same batch, (b) showing the error bar.

In second phase of experimentation, the pH sensors were prepared using from different batches to assess the impact of batch variations on its performance. It was observed that samples from the same batch exhibited a high degree of similarity, suggesting consistent characteristics and responses. However, when comparing optical fibres prepared in different batches, the same differences in response were observed, which are illustrated in Figure 5.11.

During the preparation of the optical fibres, one factor that could contribute to batch variations is the etching rate of the optical fibre. This rate may differ on a day-to-day basis due to slight fluctuations in the concentration (7 M) of the etching solution NaOH or variations in the heating temperature of the etching solution (125 °C). These variations can influence the etching rate and, consequently, impact the final diameter of the core of the optical fibre. The targeted diameter was set at 104 µm, but in practice, the actual core diameter in day-to-day etching processes showed slight deviations, resulting in a final core diameter of 104 ± 1 µm. Even this slight change in diameter can significantly affect the optical fibre's response.

However, the consistency of the light intensity trend remained uniform across all batches, suggesting a stable correlation with pH levels. Nevertheless, variations in intensity were noted at the same pH values between different batches. For instance, at pH 11, the intensities at 800 nm for batches 1, 2, and 3 were recorded as 4790, 6227, and 6885, respectively. As the solution's pH decreased to 3, the intensities increased for batches 1, 2, and 3, measuring 12023, 13058, and 13539, respectively. On average, the change in intensity per unit pH for batches 1, 2, and 3 was 904/pH, 853/pH, and 831/pH, respectively. These inequalities in intensity among the batches can be ascribed to uncertainties in the etching process, encompassing variations in the etching rate and minor disparities in the composition of AgNp/silica gel between batches. These factors collectively contribute to the observed variability in the production of optical fibre pH sensors across batches.
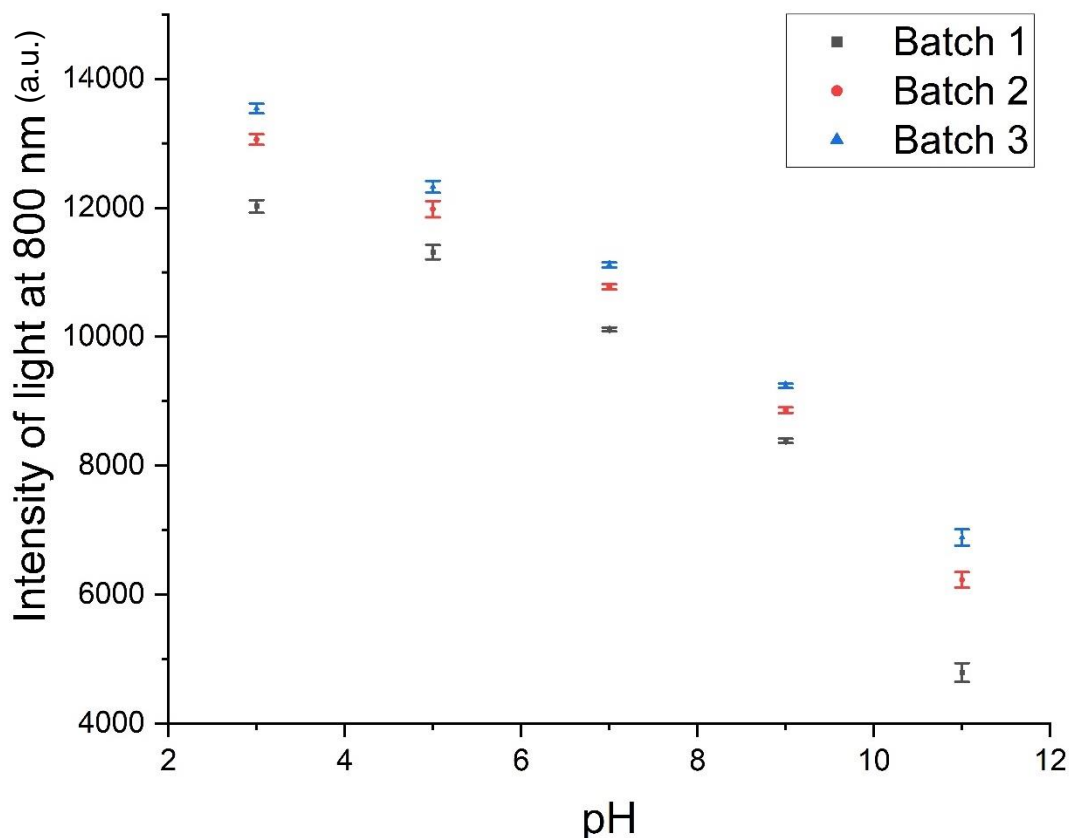
Figure 5.11: The change of intensity in different pH solutions using three different optical fibres prepared in 3 different batches using H_3PO_4 and NaOH.

5.2.1.3 Calibration of sensor in phosphate and hydroxide media

From the aforementioned experiment, it was observed that the intensity of light varied among different optical fibres prepared in different batches. However, a consistent signal was obtained among the optical fibres within the same batch. So, the calibration of pH measurement using the optical method is necessary for batch production. To perform the calibration for pH measurement, the intensity of light at a specific wavelength of 800 nm was recorded for solutions with pH values of 11, 9, 7, 5, and 3, as shown in Figure 5.12. Unlike the previous graphs, which plotted pH against the intensity of light, this calibration plot displayed the intensity of light against pH. The rationale behind this reversal is that the fitting line or curve, denoted as y, is a function of the independent variable x, which in this case, is the intensity of light. Consequently, the light intensity was plotted on the x-axis, allowing the fitted line or curve to be used for direct optical pH measurement without further conversion. This approach minimises potential calculation errors.

As a result, a line fitting was drawn, and the corresponding equation is displayed in Figure 5.12 (a). The coefficient of determination (R^2), which measures the goodness of fit, was found to be 0.90 for the line fitting. Additionally, a polynomial fitting indicated an improved coefficient of determination (R^2) of 0.99, as shown in Figure 5.12 (b). The polynomial fitting was carried out to determine the optimal method for optical pH measurement, and it demonstrated that the second-order polynomial fitting produced a better fitting compared to linear fitting, as evidenced by a higher coefficient of determination (R^2). The procedure for deriving the fitting equations for linear and second-order polynomial regression is explained in Appendix G, elucidating the manner in which these equations are derived from experimental raw data.

The calibration equation using the linear fitting is shown in below Equation 5.8:

$$y = -0.001 * x + 16.743 \tag{5.8}$$

Also, the calibration equation for the polynomial fitting is shown in the below Equation 5.9:

$$y = -1.57836E - 07 * x^2 + 0.00159 * x + 6.9904 \tag{5.9}$$

In the subsequent section, the equations derived from the calibration curve will be used to convert the recorded intensity of light into corresponding optical pH values. This process of conversion will enable direct and accurate measurement of optical pH without the need for additional calculations, thereby reducing the likelihood of errors.
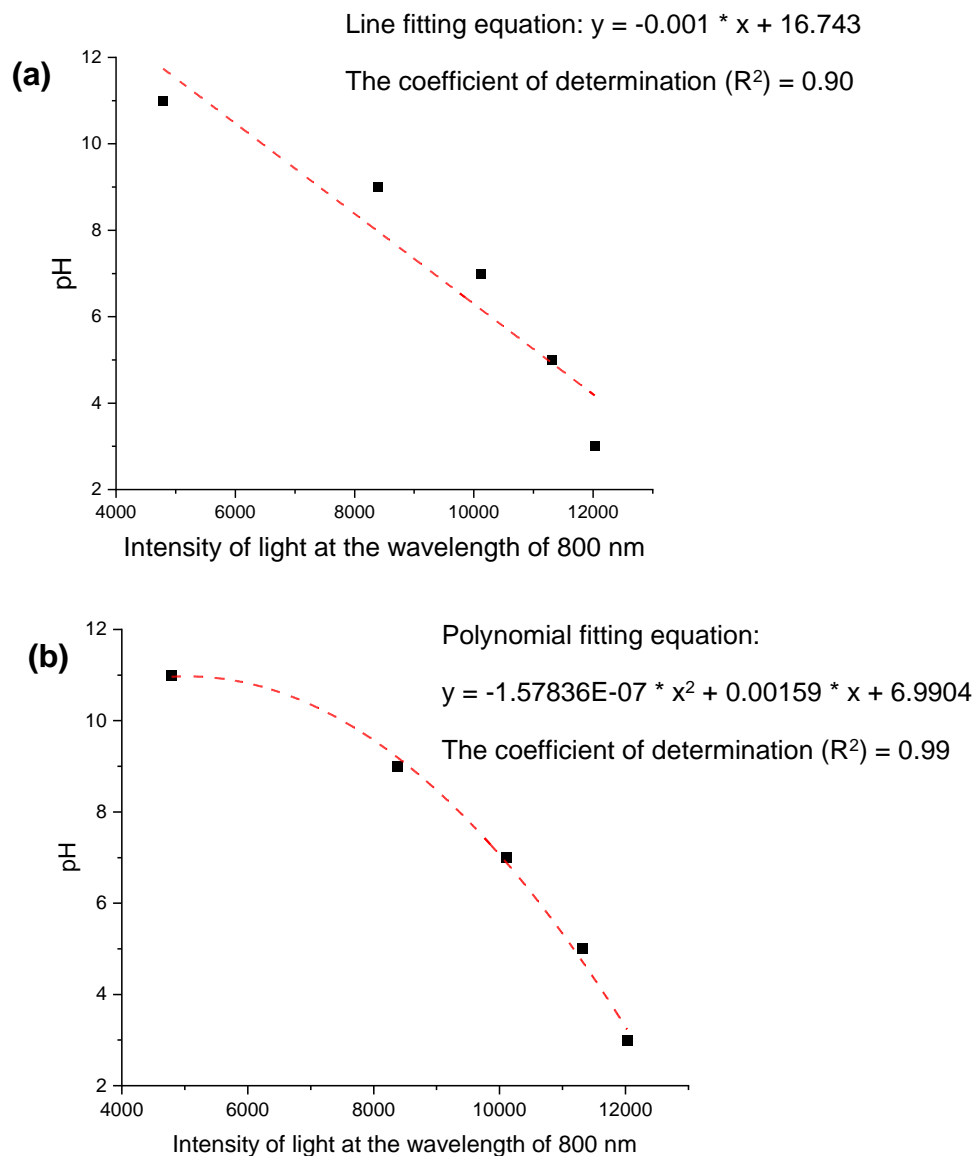
Figure 5.12: The pH calibration curve using H_3PO_4 and NaOH with 5 data points: (a) linear fitting, (b) polynomial fitting.

Additionally, a second-order polynomial calibration curve fitting was performed using nine data points ranging from pH 3 to 11, as depicted in Figure 5.13. The same chemicals, H_3PO_4 and NaOH, were utilised as in the previous analysis with five data points. The objective of this analysis is to compare the calibration curve generated from five data points with that of nine data points. Following the analysis of the nine data points, the second-order polynomial fitting equation is provided below, and the coefficient of determination (R^2) remains at 0.99, consistent with the calibration using five data points.

$$y = -1.52655E - 07 * x^2 + 0.00153 * x + 7.0204 \qquad (5.10)$$
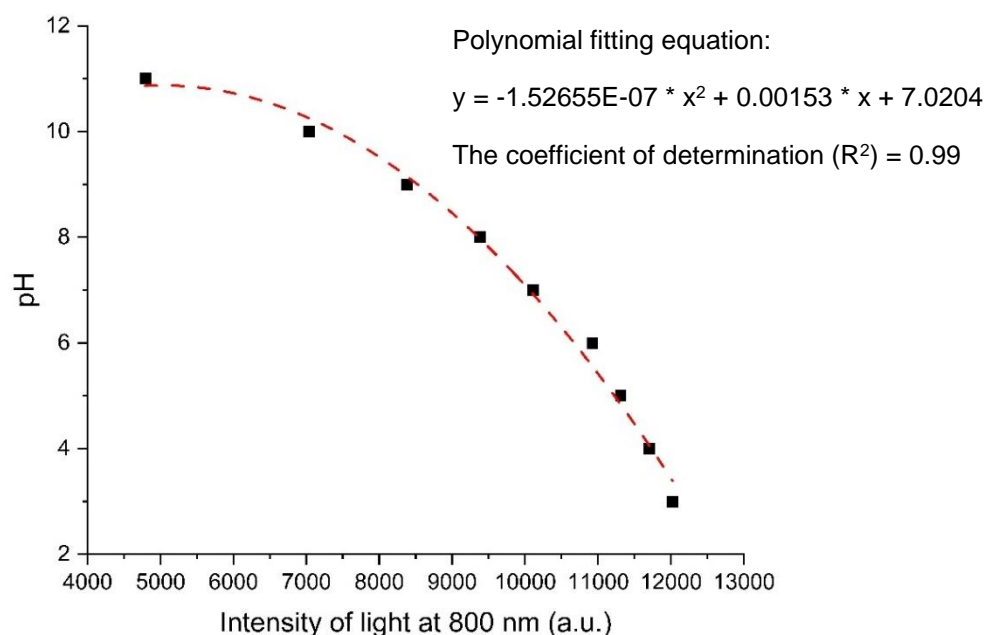
Figure 5.13: The pH calibration curve using H_3PO_4 and NaOH with 9 data points: (a) linear fitting, (b) polynomial fitting.

As a result, the intensity of light at 800 nm obtained during calibration for pH levels of 3, 7, and 11 was converted to optical pH using calibration equations derived from 5 data points (equation 5.9) and 9 data points (equation 5.10), as indicated in Table 5.2. It was observed that the optical pH values obtained from the 5 data points calibration curve exhibited less deviation from the potentiometric pH compared to the 9 data points calibration curve, as illustrated in Table 5.2. Consequently, the 5 data points calibration curve offered a closer approximation to potentiometric pH. Furthermore, utilising 5 data points was more convenient, as each data point represented the average of 3 measurements. Consequently, employing 5 data points was a more convenient approach for constructing a calibration curve. Therefore, for subsequent calibrations, the 5 data points method would be preferred.

Table 5.2: Comparison of optical pH measurements using the 5 and 9 data points calibrations.

pH (Potentiometric)	Intensity of light at 800 nm (a.u.)	Using 5 data points calibration: Equation 5.9)		Optical pH (using 9 data points calibration: Equation 5.10)	
		Optical pH	pH deviation from potentiometric pH	Optical pH	pH deviation from potentiometric pH
3	12023	3.29	0.29	3.35	0.35
7	10112	6.93	0.07	6.88	0.12
11	4790	10.99	0.01	10.85	0.15

The equation presented in Equation 5.9 was formulated using data obtained from optical fibres prepared in the same batch as Batch 1. The aim is to assess the similarity or dissimilarity of Equation 5.9 fitting across different batches, comparing the results. Table 5.3 displays the calculated optical pH values derived from the calibration fitting equation established for Batch 1, utilising the recorded light intensity during experiments in Batches 1, 2, and 3. Since the fitting equation was derived from Batch 1 data, it was observed a closer alignment between the optical pH and potentiometric pH measurements for Batch 1. However, in Batches 2 and 3, it was noticed slightly larger deviations in alkaline solutions with pH levels of 9 and 11. The errors become more pronounced in acidic conditions, specifically at pH 3 and 5. This discrepancy could be attributed to the fact that changes in intensity relative to pH alterations are more significant in acidic environments compared to alkaline solutions. Hence, when variations in intensity occur due to differences between batches, the associated errors become more pronounced. This analysis emphasises the significance of calibrating the batch production process to enhance the reproducibility of pH measurements.

Table 5.3: Comparison of the optical pH measurements within different batches.

	pH (Potentiometric)	Intensity of light at 800 nm (a.u.)	Optical pH (Using polynomial fitting Equation 5.9)
Batch 1	11	4790	10.99
	9	8384	9.23
	7	10112	6.93
	5	11310	4.78
	3	12023	3.29
Batch 2	11	6227	10.77
	9	8859	8.69
	7	10775	5.80
	5	11978	3.39
	3	13058	0.84
Batch 3	11	6885	10.46
	9	9236	8.21
	7	11112	5.17
	5	12326	2.61
	3	13539	-0.42

5.2.1.4 Verification of optical pH measurement

A series of random pH measurements were then conducted to determine if the optical fibre, along with the calibration data provided reliable pH values. This process involved the pH of the solution being randomly adjusted between pH 3 and 11 using a phosphate-based medium, with the pH being altered randomly 50 times. During the pH adjustment process, the intensity of light at a wavelength of 800 nm was recorded using the fabricated pH sensor. For verification, the pH of the solution was measured using a potentiometric pH meter, this would be referred to as the potentiometric pH. The recorded intensities of light at 800 nm were subsequently converted to pH values and would be termed optical pH. Both Equations 5.8 and 5.9, respectively, were utilised to convert the intensity of light to optical pH. All the recorded data and calculations for converting optical pH using these equations are provided in Appendix H.

The results of the random experiment were plotted using both the line fitting (represented by black data points) and the polynomial fitting calibration equations (represented by red data points), as shown in Figure 5.14. Additionally, an ideal line (blue line) is also included, which represents the curve where the optical pH is equal to the potentiometric pH value. By examining the position of the data points relative to the ideal line, it can be determined if the optical pH values are higher or lower than the potentiometric pH values. If the data point falls below the ideal line, then this suggests that the optical pH values obtained are lower than the corresponding potentiometric pH value. On the other hand, if the data point is above the ideal line, then the optical pH values obtained are higher than the corresponding potentiometric pH value. This would reveal if there was a systematic bias for over or under prediction.

In Figure 5.14, a visual analysis reveals distinct patterns in the representation of data points derived from two distinct calibration methods for optical pH measurement. Specifically, it was observed that the black data points, generated through linear fitting, exhibit a notable dispersion from the ideal line (blue line). This noticeable difference, where data points are diverging significantly from the ideal line, strongly suggests a lower degree of accuracy in the optical pH measurements when utilising the linear fitting calibration against the potentiometric pH values. In contrast, the red data points, which are the product of the polynomial fitting method, cluster closely around the ideal line in Figure 5.14. This pronounced clustering of data points in proximity to the ideal line serves as a compelling indicator of heightened accuracy in the optical pH measurements when compared to the potentiometric pH values. The alignment of these data points with the ideal line underscores the minimal deviation exhibited by the optical pH values obtained through polynomial fitting in relation to the reference potentiometric pH values.
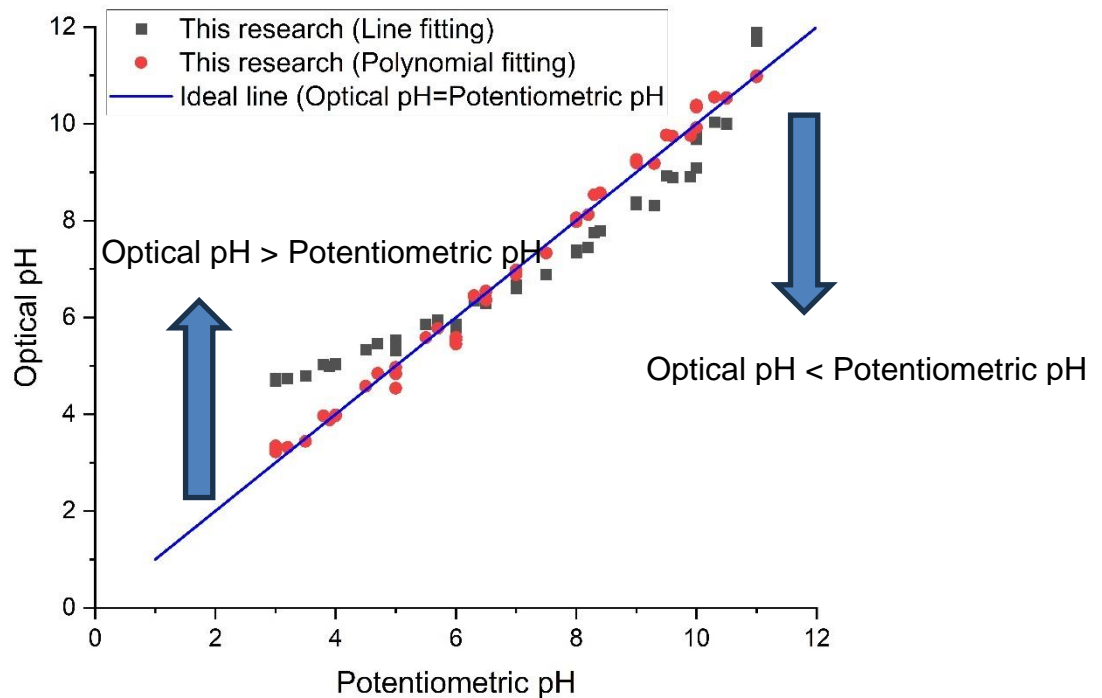
Figure 5.14: Comparison of calculation of optical pH measurement (using H_3PO_4 and NaOH) between using the line fitting and polynomial fitting with the ideal line where optical pH = potentiometric pH.

To assess the agreement of optical pH measurements with potentiometric methods, both sets of data were plotted and shown in Figure 5.15. Figure 5.15 (a) presents the relationship between potentiometric pH and optical pH using the calibrated linear fitting, while Figure 5.15 (b) shows the relationship between both methods using the calibrated polynomial fitting. In both graphs, two lines, which were offset by ±0.5, were added from the potentiometric pH. This offset range of ±0.5 represents the tolerance for the accuracy of optical pH measurement, indicating that values falling within this range could be considered as "tolerance" of measurements. The results indicated that the data points obtained using the linear fitting deviate from the actual values, as they are scattered outside the area of potentiometric pH ±0.50, as shown in Figure 5.15 (a). On the other hand, the polynomial fitting showed improved agreement for the optical pH measurement. All the data points fell within the area of potentiometric pH ±0.50, indicating higher accuracy and agreement with the potentiometric pH values. Thus, the polynomial fitting proved was observed to show a higher accuracy of optical pH measurement.
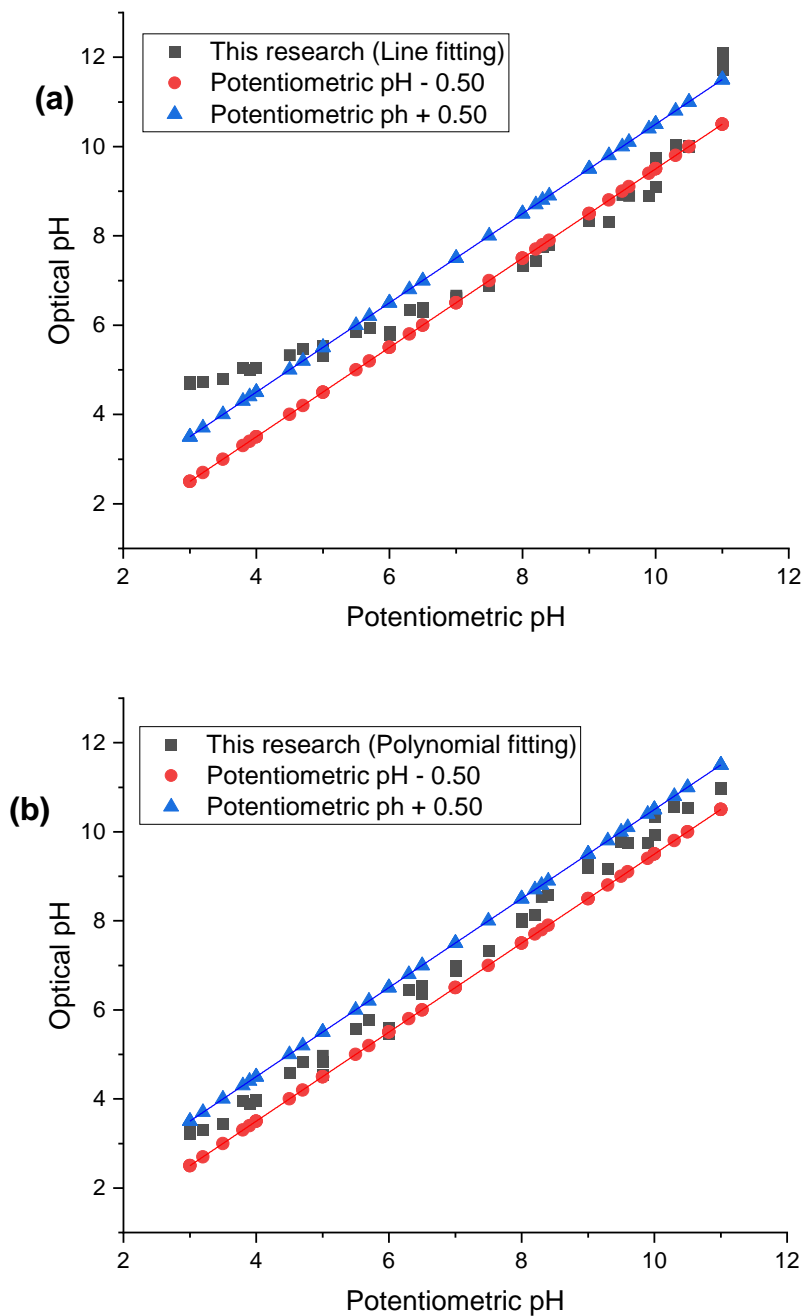
Figure 5.15: Comparison of potentiometric pH and optical pH measurements using H_3PO_4 and NaOH (a) linear fitting model (b) polynomial fitting model

This highlights the constraints of the optical system. To begin with, the optical system depends on the surface charge of the coating. Consequently, the alteration in intensity with variations in pH did not follow a linear pattern, and a second-order polynomial fitting curve yielded a notably enhanced level of precision. In brief, when comparing potentiometric pH measurements to optical pH measurements, it

becomes evident that employing the polynomial fitting method significantly enhances the accuracy of optical pH determination. The data points obtained through this approach consistently fall within the acceptable range of potentiometric pH ±0.50, affirming its precision in practical applications.

5.2.2 Optical pH measurement solution in sulphate media

The effectiveness of the AgNp/silica coated pH sensor for measuring the pH of different solutions was investigated using sulfuric acid (H_2SO_4) and sodium hydroxide (NaOH). As before, the study focused on evaluating the repeatability and reproducibility of the sensor within the same batch and across different production batches. Furthermore, the section also explains the calibration of the optical pH sensor and the results of the random pH experiment to gain insights into the accuracy of the sensor. The results are obtained from the titration experiment, and the subsequent calibration curve formed the basis for understanding the sensor's accuracy and its ability to reliably measure pH values.

The pH measurements were performed using 0.1 M sulfuric acid and 0.1 M sodium hydroxide solutions to alter the pH solutions from 3 to 11. The optical fibre coated with AgNp/silica was immersed in the solution and connected to a detector and light source. As illustrated in Figure 5.16, the intensity of light was recorded for pH values ranging from 3 to 11, using steps of pH 1. Baseline corrections were done by subtracting the I_0 (intensity with closed shutter), as mentioned in an earlier experiment. The recorded intensities were associated with their respective pH values, forming a pH calibration curve.

Similar to the previous pH experiment that investigated in phosphate and hydroxide medium, it was observed that the intensity of light increased as the pH of the solution decreased. This trend indicated an inverse relationship between pH and light intensity, where lower pH values correspond to higher light intensities. This observation was consistent with the expected behaviour of the AgNp/silica coated pH sensor, validating its performance across different acid solutions.
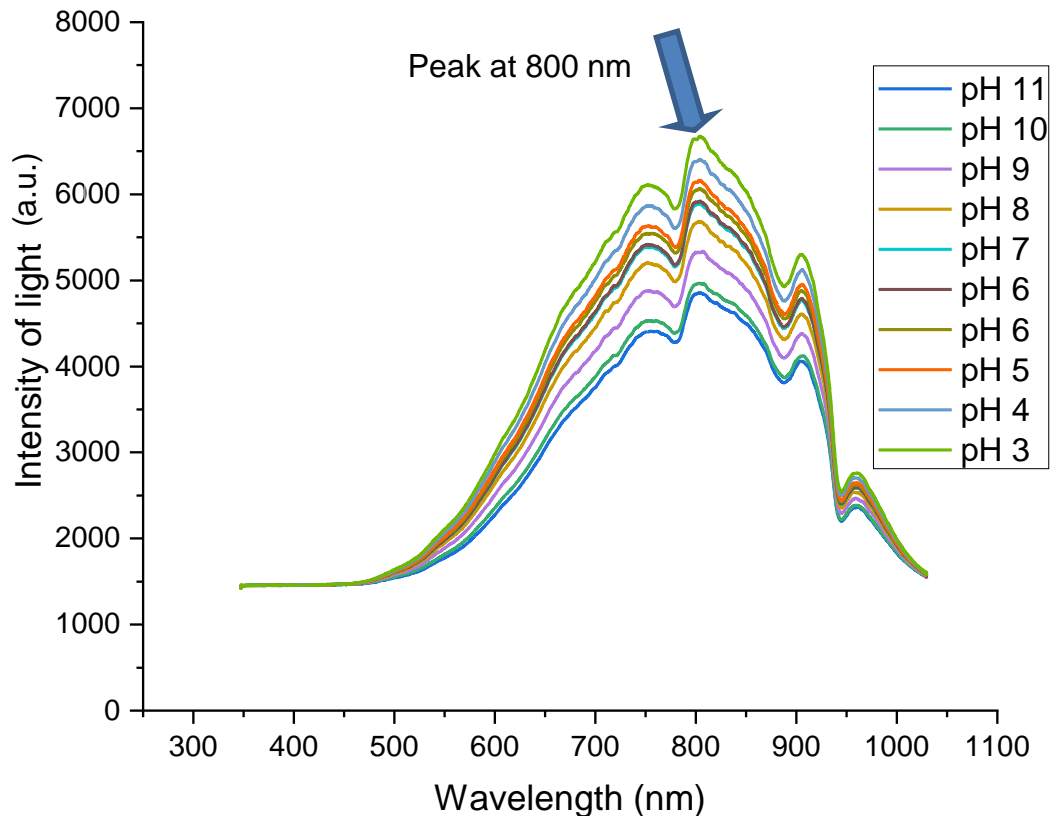
Figure 5.16: The change in intensity of light at a different wavelength of light in different pH solutions using H_2SO_4 and NaOH.

In Figure 5.16, a prominent spectral peak was detected at a wavelength of 800 nm, denoting the point of maximal alteration in light intensity. Subsequently, this variation in light intensity at 800 nm was graphically depicted in Figure 5.16. Specifically, the intensity showed at 800 nm was 4325 for a solution at a pH level of 11. Upon the acidification of the solution to a pH of 3 through the introduction of sulfuric acid, a substantial augmentation in light intensity was observed, reaching 6550 units. Notably, the transition from a pH of 11 to 3, facilitated by sulfuric acid and sodium hydroxide, manifested a discernible change in light intensity, amounting to 2225 units, as depicted in Figure 5.16. In contrast, the transition from a pH of 11 to 3, mediated by the combination of H_3PO_4 and NaOH, drew a more pronounced alteration in intensity, escalating to 7402 units, as visually represented in Figure 5.7. The changes in the intensity of light were observed to be different when the acid was changed to H_2SO_4 compared to the previous experiment. The presence of different

ions from these acids, which interact differently with the AgNp/silica coating, could be the reason for these observed changes in the intensity of light absorbed.

The protons from sulfuric acid can interact with silica surfaces through the protonation of the silanol groups. The chemical reaction is shown below the interactions between the sulfuric acid and silica surfaces [261]:

$$Si−OH + H_2SO_4 \rightarrow Si−OH_2^+ + HSO_4^- \qquad (5.11)$$
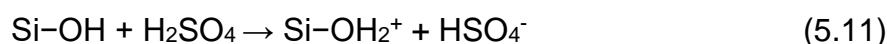
Sulfuric acid protonates silanol groups on the silica surface, forming positively charged sites ($Si-OH_2^+$) and hydrogen sulphate anions (HSO_4^-). This protonation can lead to the formation of positively charged sites on the surface, effectively increasing the positive surface charge density [261]. The extent of protonation depends on the acid concentration and the pH of the solution. At low pH, the surface may carry a positive charge due to the protonation of silanol groups.

5.2.2.1 Analysis of optical properties

The results showing the intensity of light at a specific wavelength of 800 nm for pH values ranging from pH 11 to pH 3 are shown in Figure 5.17 (a), where the intensity of light is plotted against the corresponding pH values. The analysis of these data was conducted utilizing three distinct optical fibres, all of which were fabricated during the same production batch. Additionally, Figure 5.17 (b) illustrates the normalised data, ranging from 0 to 100, for better visualisation and comparison. Upon analysing the data, it was observed that the intensity of light exhibited significant variations across the pH range. The change in intensity from pH 11 to pH 10 was measured to be 28, from pH 10 to pH 9 was 16, from pH 9 to pH 8 was 11, from pH 8 to pH 7 was 14, from pH 7 to pH 6 was 7, from pH 6 to pH 5 was 7, from pH 5 to pH 4 was 9, and from pH 4 to pH 3 was 8. Notably, the change in intensity of light was observed to be higher in alkaline solutions (pH 11 to pH 7) compared to acidic solutions (pH 7 to pH 3). This observation suggests that the pH sensor's response, as indicated by the intensity of light, is more pronounced in alkaline conditions. As the pH of the solution becomes more acidic, the change in intensity of light tends to decrease. The data presented in Figure 5.17 provides the relationship between pH and the intensity of light detected by the AgNp/silica coated pH sensor.

The substantial variation in light intensity across different pH values indicates the sensor's sensitivity to pH changes, showing the variation at low and high pHs.
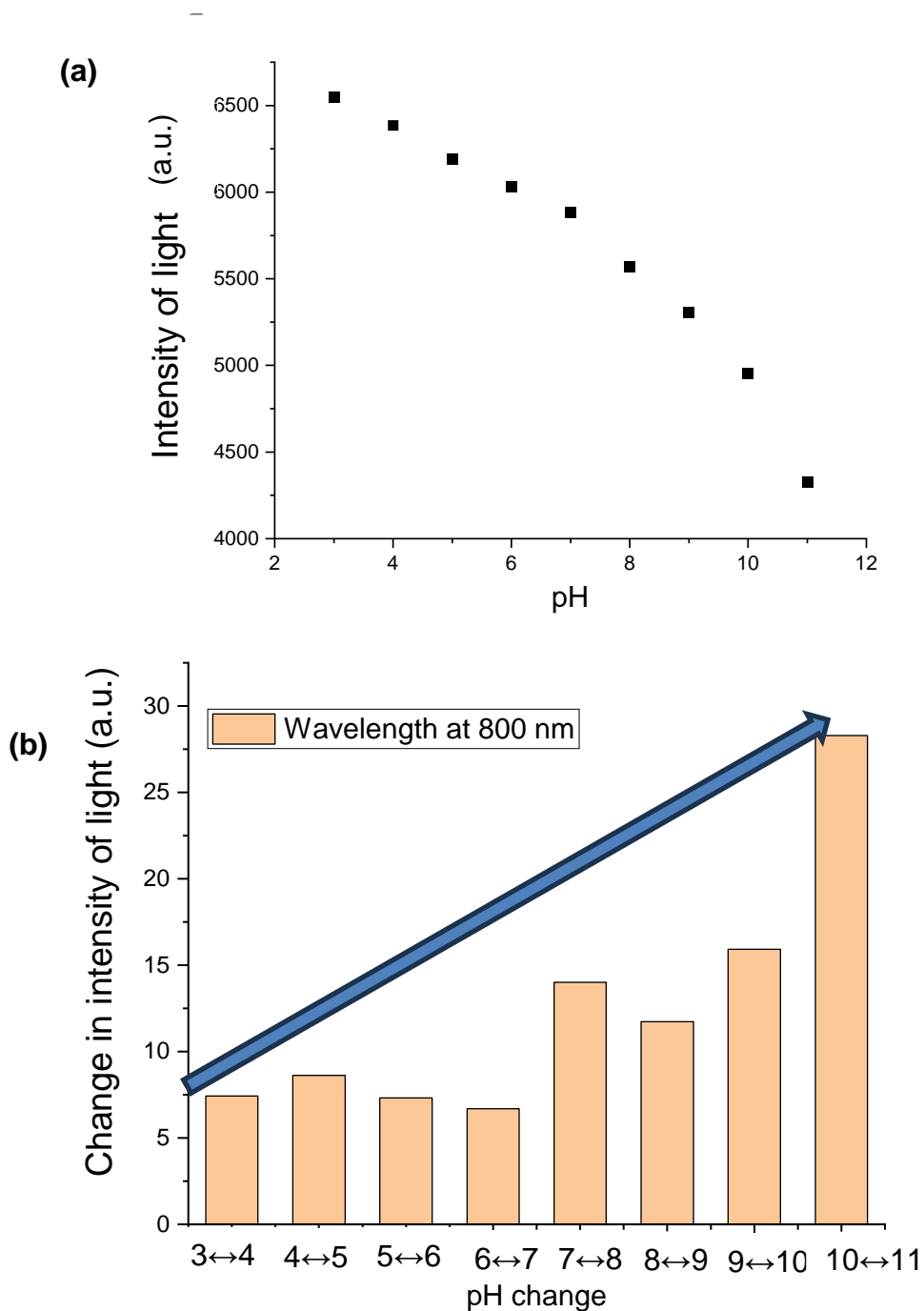
Figure 5.17 : (a) The change in intensity of light at 800 nm, (b) the change in intensity of light at the wavelength 800 nm of light in different pH solutions from pH 3 to 11 using H_2SO_4 and NaOH.

5.2.2.2 Repeatability and reproducibility analysis

To assess the reproducibility of the pH sensor, an investigation was conducted using H_2SO_4 and NaOH. In a single batch, three different optical fibres were prepared simultaneously, ensuring they underwent the same production process. The variations in intensity measurements were examined across different pH solutions using these three distinct optical fibres, and the results are illustrated in Figure 5.18 (a). The analysis of the data revealed that the intensity of light exhibited reproducibility among the three samples prepared in the same batch. The measurements obtained from each optical fibre sensor showed remarkable similarity, indicating that the sensors were consistent and reliable when manufactured together. This observation provides evidence of the reproducibility of the pH sensor's performance within the same batch.

Moreover, Figure 5.18 (b) illustrates a notable characteristic in the form of an error bar, signifying an intensity value within the range of ± 50 units, which is closely linked to the response observed in the three optical fibre samples. This reduced error bar signifies a high degree of agreement and consistency in the intensity measurements obtained from each sensor. The narrow spread further supports the reproducibility and reliability of the pH sensor's performance when the same batch is used. By evaluating the reproducibility of the pH sensor's measurements using three optical fibre samples prepared in the same batch, the study confirms the consistency and accuracy of the sensor's response. The close agreement between the measurements and the reduced variability provides sufficient evidence of the pH sensor's reliable performance, enhancing confidence in its practical application for pH measurement.

Figure 5.18: The change of intensity in different pH solutions using three different optical fibres prepared using H_2SO_4 and NaOH (a) in the same batch, (b) showing the error bar.

In the next set of experiments, the optical response in pH measurement was investigated using optical fibres prepared in different batches. It was observed that the optical fibres prepared in different batches exhibited different responses, as shown in Figure 5.19. This disparity in response can be attributed to slight variations that may occur during the preparation of the optical fibres in different batches, leading to differences in the batch production of the optical fibre pH sensor. Although the intensities varied among the different batches, a consistent trend in the intensity of light was observed across all batches. Specifically, the lowest intensity of light was recorded at pH 11, and as the pH of the solution decreased, the intensity increased. For instance, at pH 11, the intensity at 800 nm was measured to be 4373, 4847, and 4122 for batches 1, 2, and 3, respectively. Conversely, when the pH of the solution was reduced to 3, the intensity of light increased, measuring 6566, 7258, and 6368 for batches 1, 2, and 3, respectively.

By calculating the average change in intensity for each batch, it was determined that the average change in intensity per pH unit was 274/pH, 301/pH, and 280/pH for batches 1, 2, and 3, respectively. Notably, the average change in intensity across all batches fell within a similar range when sulfuric acid (H_2SO_4) and sodium hydroxide (NaOH) solution was used. The results indicate that while there are variations in the intensity measurements between different batches of optical fibres, the overall trend and average change in intensity remain consistent. This suggests that the optical response to changes in pH is reliable across different batches, demonstrating the robustness and suitability of the optical fibre pH sensor for pH measurements using H_2SO_4 and NaOH, even when there are differences within batches across different methods. It has the potential to reduce the variation in light intensity during batch production by setting up a dedicated experimental apparatus for both the sol-gel preparation and optical fibre etching processes, motivated to maintain as consistent conditions as possible for replication.
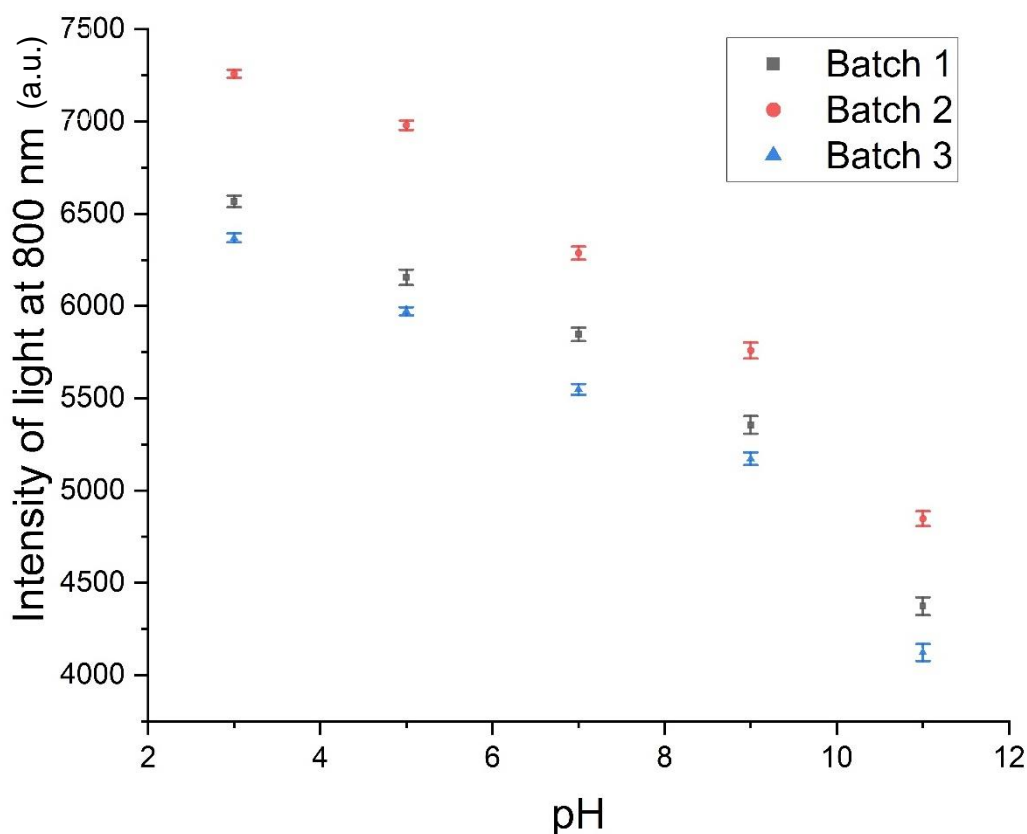
Figure 5.19: The change in intensity in different pH solutions using H_2SO_4 and NaOH across 3 different batches

5.2.2.3 Calibration of sensor in sulphate and hydroxide media

As before, the optical pH sensor was calibrated using five different solutions with pH values of 3, 5, 7, 9, and 11. To establish the calibration curve, the intensity of light at the wavelength of 800 nm was recorded for each solution, as illustrated in Figure 5.20. Two different fitting methods, namely linear fitting and polynomial fitting were employed to create the calibration curves. In the linear fitting, the recorded data points were fitted with a straight line, and the coefficient of determination (R^2) was calculated to assess the goodness of fit. The resulting R^2 value was found to be 0.93, as shown in Figure 5.20 (a). However, further analysis was performed using polynomial fitting, which involved fitting the data points with a higher-order polynomial curve. This approach led to an improved coefficient of determination (R^2) of 0.99, as shown in Figure 5.20 (b). The higher R^2 value obtained with the polynomial fitting indicated a more precise and accurate representation of the data used for calibration, providing a stronger correlation between the intensity of light and the corresponding pH values. The procedure for deriving the fitting equations for

linear and second-order polynomial regression is explained in Appendix I, revealing the manner in which these equations are derived from experimental raw data.

The equation used for the linear fitting is shown in equation 5.12:

$$y = -0.003 * x + 26.899 \qquad (5.12)$$

Also, the equation used for the polynomial fitting is shown in equation 5.13:

$$y = -1.35197\text{E} - 06 * x^2 + 0.0111 * x - 11.7431 \qquad (5.13)$$
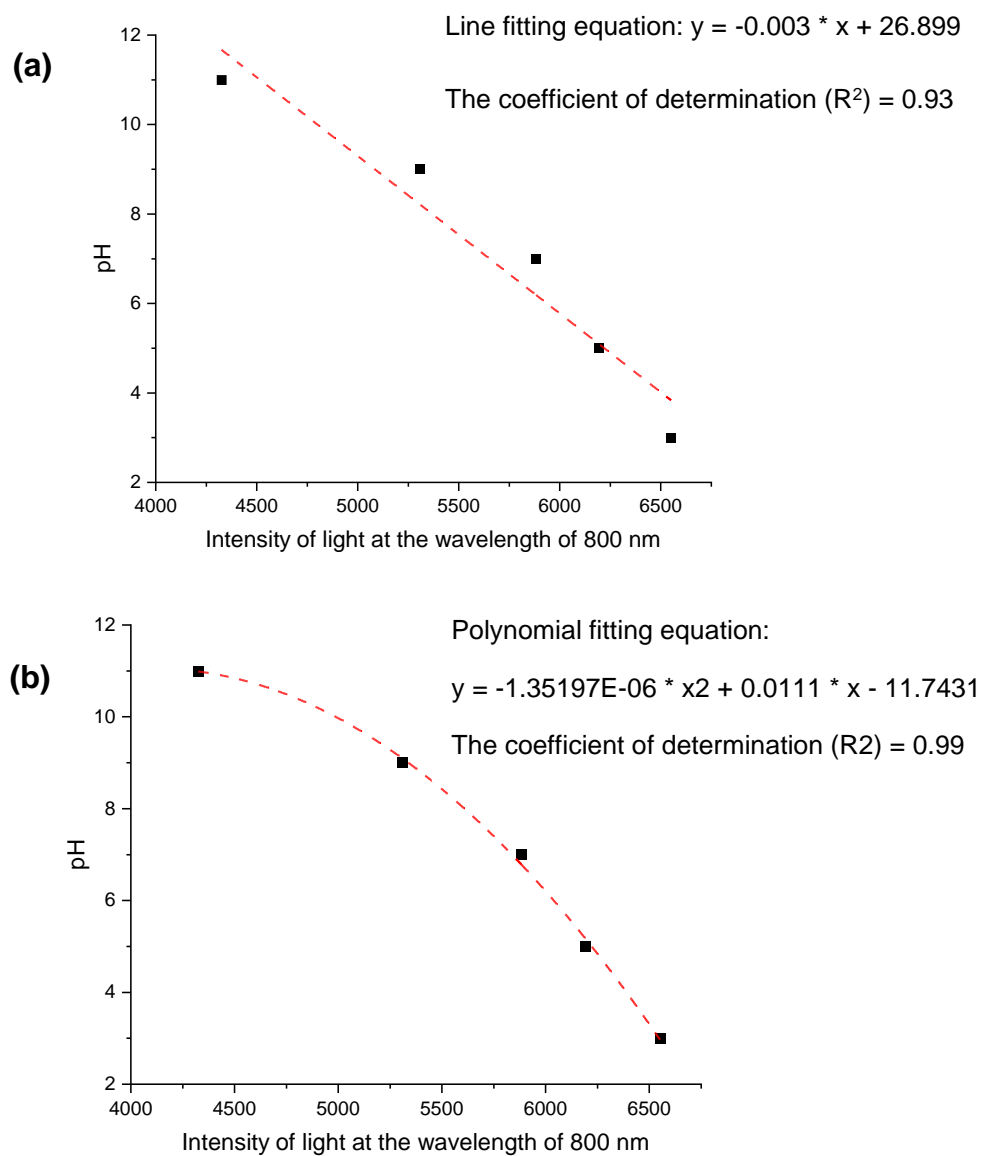
Figure 5.20: The pH calibration curve using H_2SO_4 and NaOH (a) linear fitting (b) polynomial fitting.

The effectiveness of each fitting approach for optical pH measurement was assessed by investigating the linear and polynomial fitting methods. The higher R^2 value obtained with the polynomial fitting suggested that it offered a superior calibration curve, exhibiting better accuracy and reliability in predicting pH values based on the intensity of light measured by the sensor.

5.2.2.4 Verification of optical pH measurement

In this section, a randomised pH measurement was undertaken by changing the pH of the aqueous solution within the range of pH 3 to 11 through the controlled addition of sulfuric acid (H_2SO_4) and sodium hydroxide (NaOH). This involved recording the intensity of light using the optical fibre and determining pH from the calibration curve and comparing the value against pH using a potentiometric pH meter, which served as the reference pH measurement. The recorded intensities were converted to optical pH using the calibration equations shown in Figure 5.20 (a) and (b), as detailed in Appendix J.

The results of the random experiment were plotted using the linear equation (depicted by black data points) and the polynomial equation (represented by red data points) in Figure 5.21. Also, a reference ideal line (blue line) was included in the plot, representing the equality between optical pH and potentiometric pH values. By analysing the position of the data points in relation to the ideal line, it can be determined if the optical pH values are higher or lower than the potentiometric pH values. Data points below the ideal line indicate that the optical pH values obtained are systematically lower than the corresponding potentiometric pH values, while data points above the ideal line indicate that the optical pH values obtained are higher.

In Figure 5.21, a noticeable distinction can be observed between the black data points obtained from the line fitting calibration and the ideal line. These data points are scattered far below and away from the ideal line, indicating lower accuracy in the optical pH measurements obtained using the line fitting calibration when compared to the potentiometric pH values. On the other hand, the red data points obtained from the polynomial fitting calibration cluster closely around and near the ideal line in Figure 5.21. This close proximity to the ideal line signifies a higher level of accuracy

225

in the optical pH measurements when compared to the potentiometric pH values. The alignment of these data points with the ideal line indicates that the optical pH values obtained using the polynomial fitting calibration exhibit minimal deviation from the potentiometric pH values.
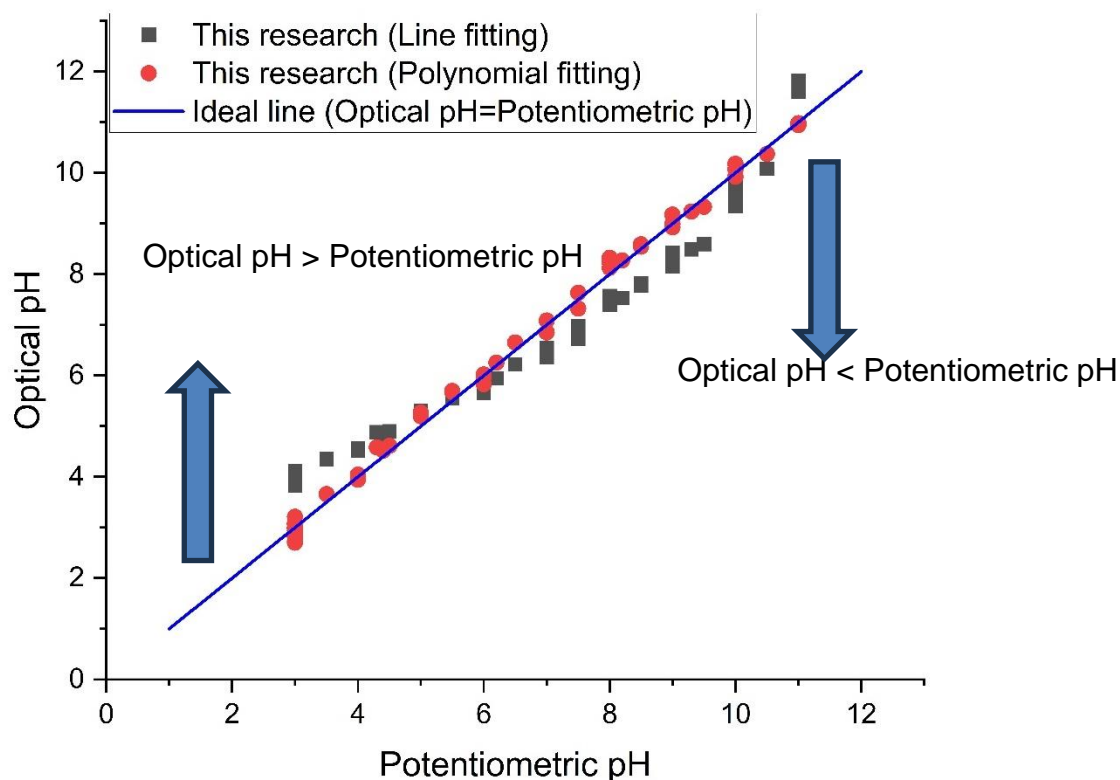
Figure 5.21: Comparison of calculation of optical pH measurement (using H_2SO_4 and NaOH) between using the line fitting and polynomial fitting with the ideal line where optical pH = potentiometric pH

Furthermore, two graphs were plotted to visualise the relationship between potentiometric pH and optical pH using the converted pH values obtained from the calibration equations. Figure 5.22(a) presents the graph generated using the results from the linear model, while Figure 5.22(b) shows the graph based on the polynomial model. To assess the accuracy of the optical pH measurements, two lines offset by ±0.5 pH value were included from the potentiometric pH. The area between these two lines represents the tolerance range of ±0.50 pH, indicating the acceptable accuracy level of the optical pH in comparison to the potentiometric pH method. The data plotted in Figure 5.22(a) clearly indicates poor accuracy for the optical pH

measurements, which were obtained using linear fitting. Many of the data points were outside the area defined by the potentiometric pH ±0.50 range, suggesting significant deviations from the actual pH values. However, Figure 5.22(b) demonstrates a better agreement in the optical pH measurements using the polynomial model. All the data points are located within the area of potentiometric pH ±0.50 pH, indicating a higher level of agreement with the potentiometric pH values. This observation highlights the enhanced accuracy achieved through the use of the polynomial fitting calibration method.
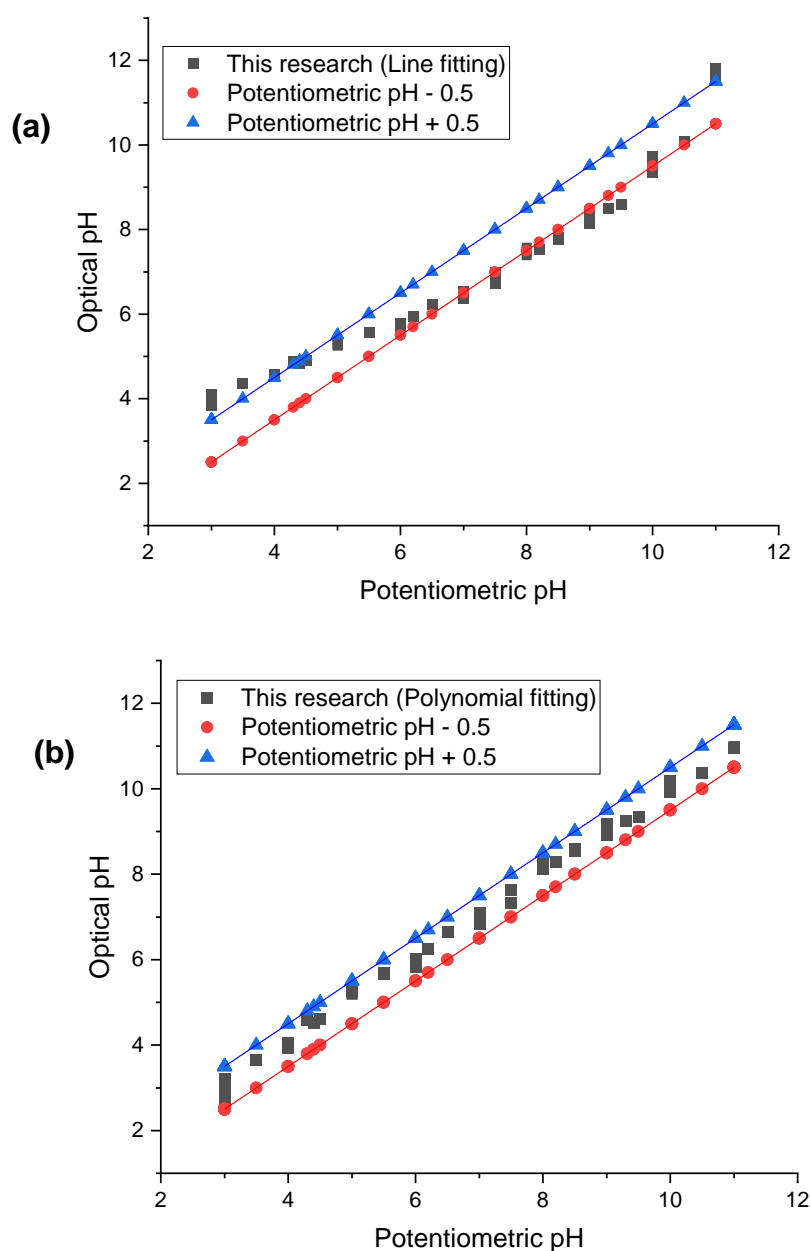
Figure 5.22: Comparison of results of potentiometric pH with optical pH using the H_2SO_4 and NaOH (a) linear model, (b) polynomial model.

In summary, the results showed the importance of selecting an appropriate fitting calibration curve for optical pH measurements. The polynomial model, in this case, offers significantly improved accuracy compared to the linear model. Choosing the best-fitting calibration curve is crucial for achieving higher precision in pH measurements using optical sensors, increasing the reliability and usability of the measurement system.

5.2.3 Optical pH measurement solution in chloride media

In this section, the effectiveness of the AgNp/silica coated pH sensor will be further investigated by assessing its performance in chloride media, which was obtained using hydrochloric acid (HCl) and sodium hydroxide (NaOH). The aim is to assess the sensor's reliability and accuracy across various chemical concentrations and pH. The repeatability and reproducibility of the sensor were assessed within the same batch and different production batches to evaluate its consistency and stability. As before, the section describes into optical pH calibration and random experiments to gain insights into the pH sensor's accuracy.

The results of the pH measurement experiment are presented in Figure 5.23. The experiment involved titrating 0.1 M hydrochloric acid and 0.1 M sodium hydroxide while immersing the AgNp/silica coated optical fibre into the solution. The optical fibre was connected to a detector and a light source to record the intensity of light. The baseline corrections were carried out on all the intensities of light. The pH values ranging from pH 3 to pH 11 were measured at intervals of 1 unit, as indicated in Figure 5.23. As before, it was observed that as the pH of the solution decreased, the intensity of light increased. This behaviour aligns with the findings of the previous experiment in phosphate and sulphate media. Notably, the graph in Figure 5.23 clearly illustrates a gradual decrease in light intensity as the pH increased from 3 to 11.
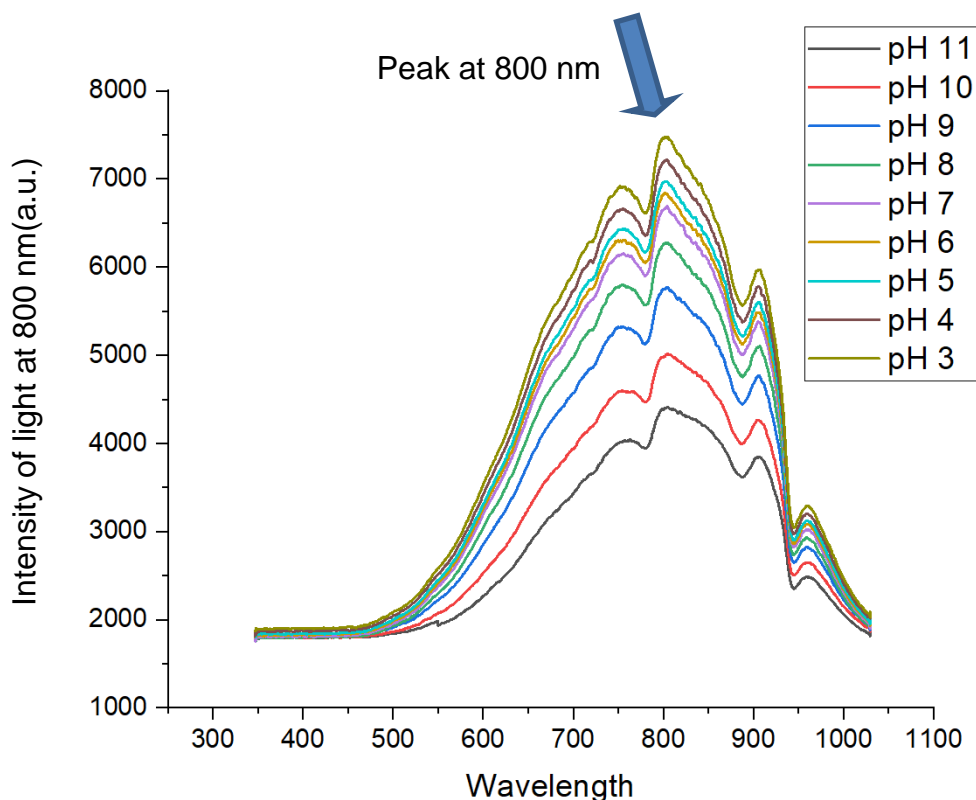
Figure 5.23: The change in intensity of light at a different wavelength of light in different pH solutions using HCl and NaOH.

The results obtained in Figure 5.23 showed a consistent peak representing the light intensity at 800 nm, similar to previous experiments. This peak represents the highest magnitude of changes in light intensity absorbed. To explore further, the change in intensity, specifically at the wavelength of 800 nm was investigated and plotted in Figure 5.24. In the initial measurement, the intensity of light at 800 nm was recorded as 4389 for a solution with a pH of 11. However, as the pH was reduced to 3 using hydrochloric acid, the light intensity increased substantially to 7462. The change in intensity is to 3073 when the pH of the solution decreases from 11 to 3.

Again, protons (H^{+}) can react with the silanol groups on the surface, leading to the formation of water and chlorosilanes [262,263]. The chemical reaction is shown below the interactions between the hydrochloric acid and silica [264]:

$$SiO_2 + 4HCl \rightarrow SiCl_4 + 2H_2O \tag{5.14}$$
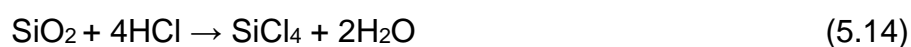
This can result in the removal of some silanol groups, reducing the overall surface charge of the silica. The removal of silanol groups decreases the number of ionisable sites on the surface, thereby reducing the surface's ability to hold a charge [262,265].

5.2.3.1 Analysis of optical properties

The intensity of light at a wavelength of 800 nm was measured in the pH solution ranging from pH 11 to pH 3, and the results are shown in Figure 5.24 (a). For comparison, the data was normalised from 0 to 100, and it is shown in Figure 5.24 (b). From the analysis of the changes in intensity, it can be observed that the transition from pH 11 to pH 10 resulted in a change of 25 units. Similarly, the change from pH 10 to pH 9 exhibited a change of 22 units, while the transition from pH 9 to pH 8 showed a change of 13 units. Subsequently, the change decreased to 10 units from pH 8 to pH 7, 8 units from pH 7 to pH 6, 8 units from pH 6 to pH 5, 10 units from pH 5 to pH 4, and 6 units from pH 4 to pH 3.

Intensity changes follow a similar pattern observed in previous experiments. Notably, there is a higher change in intensity in alkaline solutions, whereas the change in intensity decreases as the pH of the solution decreases. Specifically, in acidic conditions, the change in intensity ranges from 8 to 10 units per pH change. However, at pH 11, the change in intensity is considerably larger, ranging from 20 to 30 units. In summary, the results demonstrate a consistent trend in the change of intensity at a wavelength of 800 nm across the pH range. The changes in intensity are more pronounced in alkaline solutions and decrease as the pH becomes more acidic.
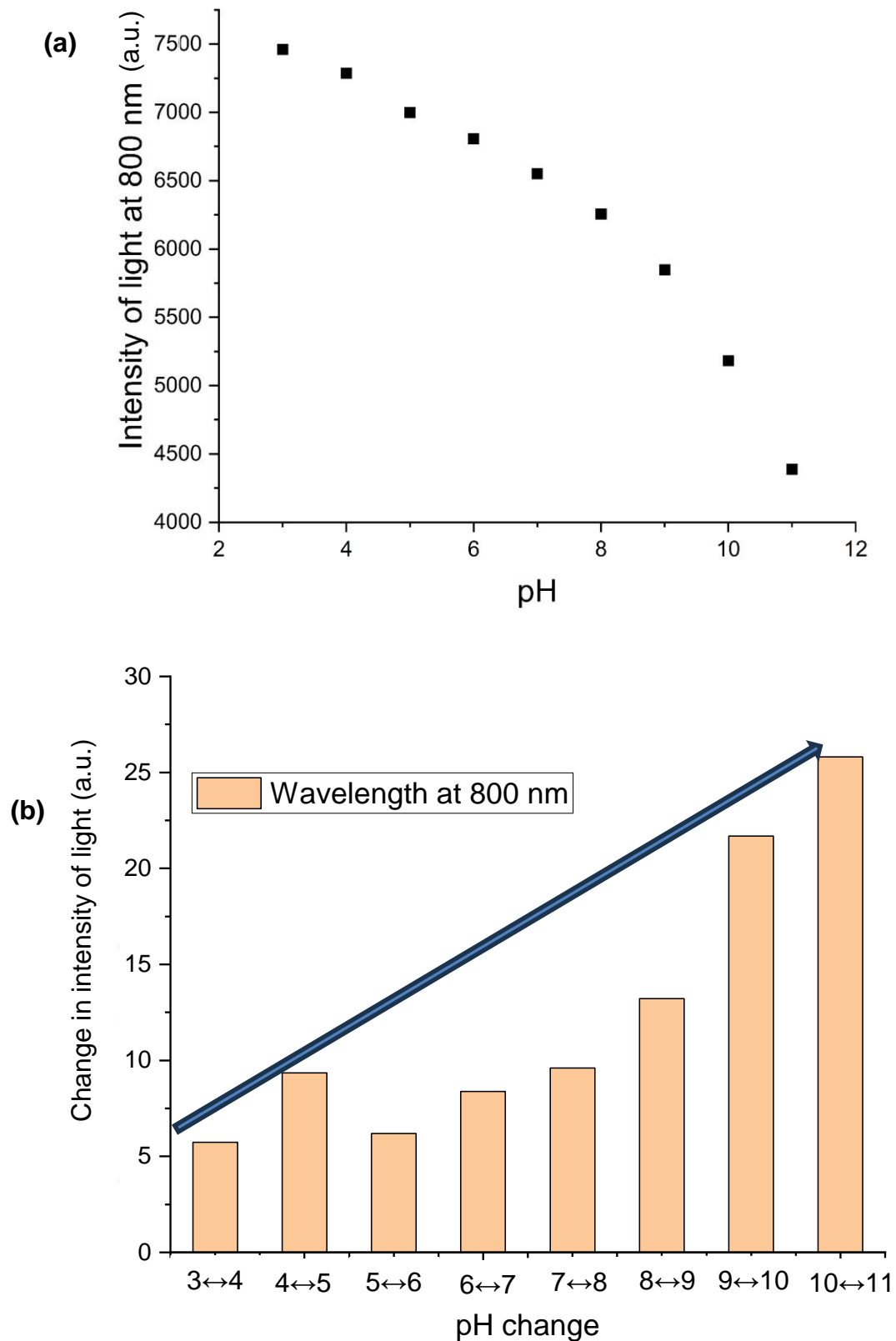
Figure 5.24 : (a) The change in intensity of light at the wavelength 800 nm, (b) the change of intensity in different pH solutions from pH 3 to 11 using HCl and NaOH at the wavelength 800 nm of light in different pH solutions from pH 3 to 11.

5.2.3.2 Repeatability and reproducibility analysis

In line with previous experiments, the reproducibility of the pH sensor was examined using hydrochloric acid (HCl) and sodium hydroxide (NaOH) solutions. Initially, the performance of the sensor within a batch production was evaluated by preparing three different optical fibres during the same production batch. The change in intensity of the sensor is then observed in various pH solutions using these three distinct optical fibres. The results of this investigation are illustrated in Figure 5.25 (a).

Figure 5.25 (a) displays the change in intensity for each of the three optical fibres across different pH solutions. It can be observed that the reproducibility of the optical fibres is excellent within the three samples. Despite using different optical fibres, the responses of the sensors exhibit remarkable similarity. This indicates that the manufacturing process for these fibres within the same production batch is consistent and reliable. Furthermore, Figure 5.25 (b) presents the corresponding error bars associated with the response of the three optical fibre sensors. The results indicate good reproducibility when tested in HCl and NaOH solutions. The consistent responses of the three optical fibre samples, along with the small error bars (average intensity ± 55 units), demonstrate the reliability and stability of the sensor within the same production batch. Notably, the error bars are considerably small, indicating a lower degree of variability in the measurements obtained from the three samples. This indicates a high level of reproducibility within the batch production, as the responses of the optical fibres exhibit consistent and accurate measurements across the pH range.
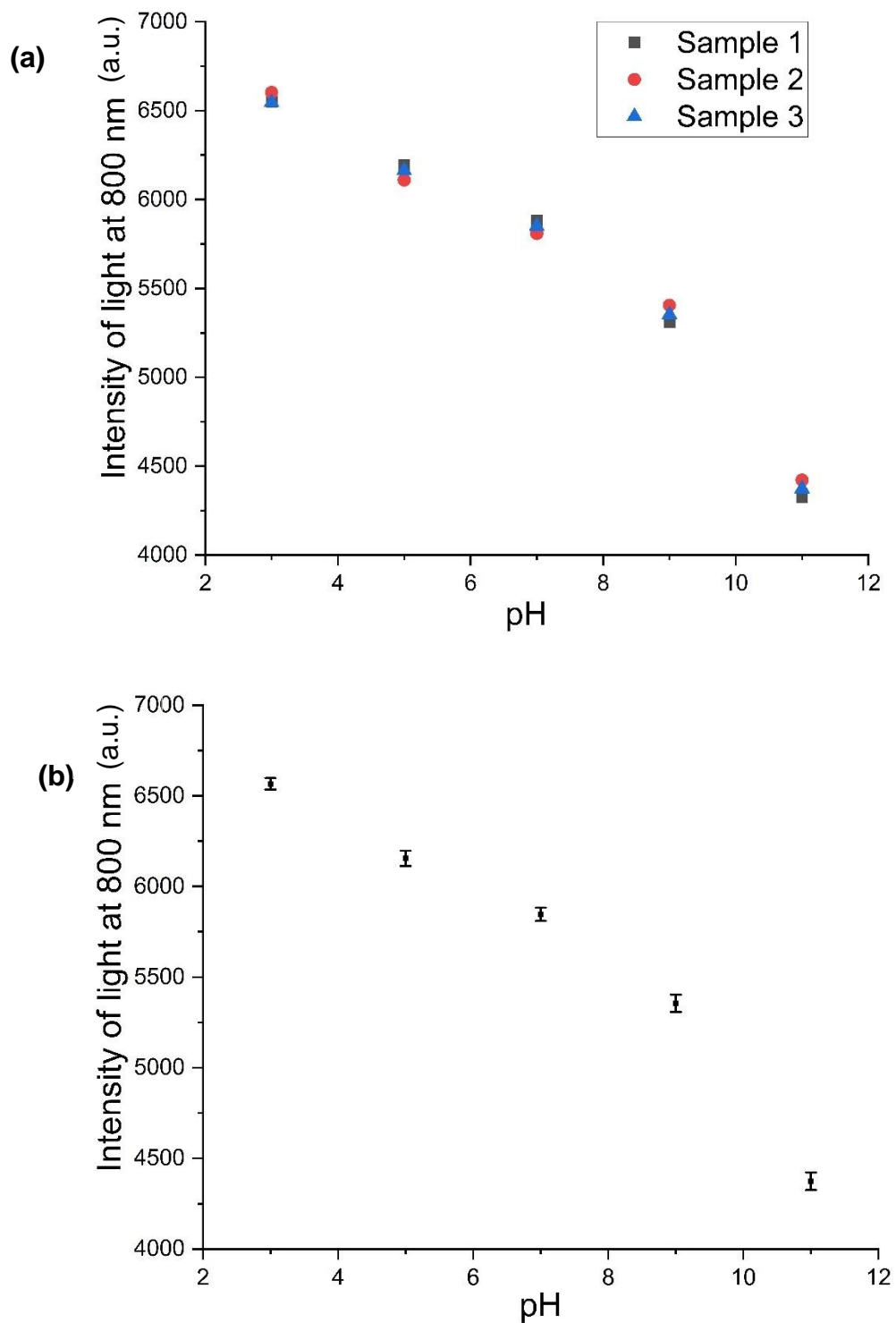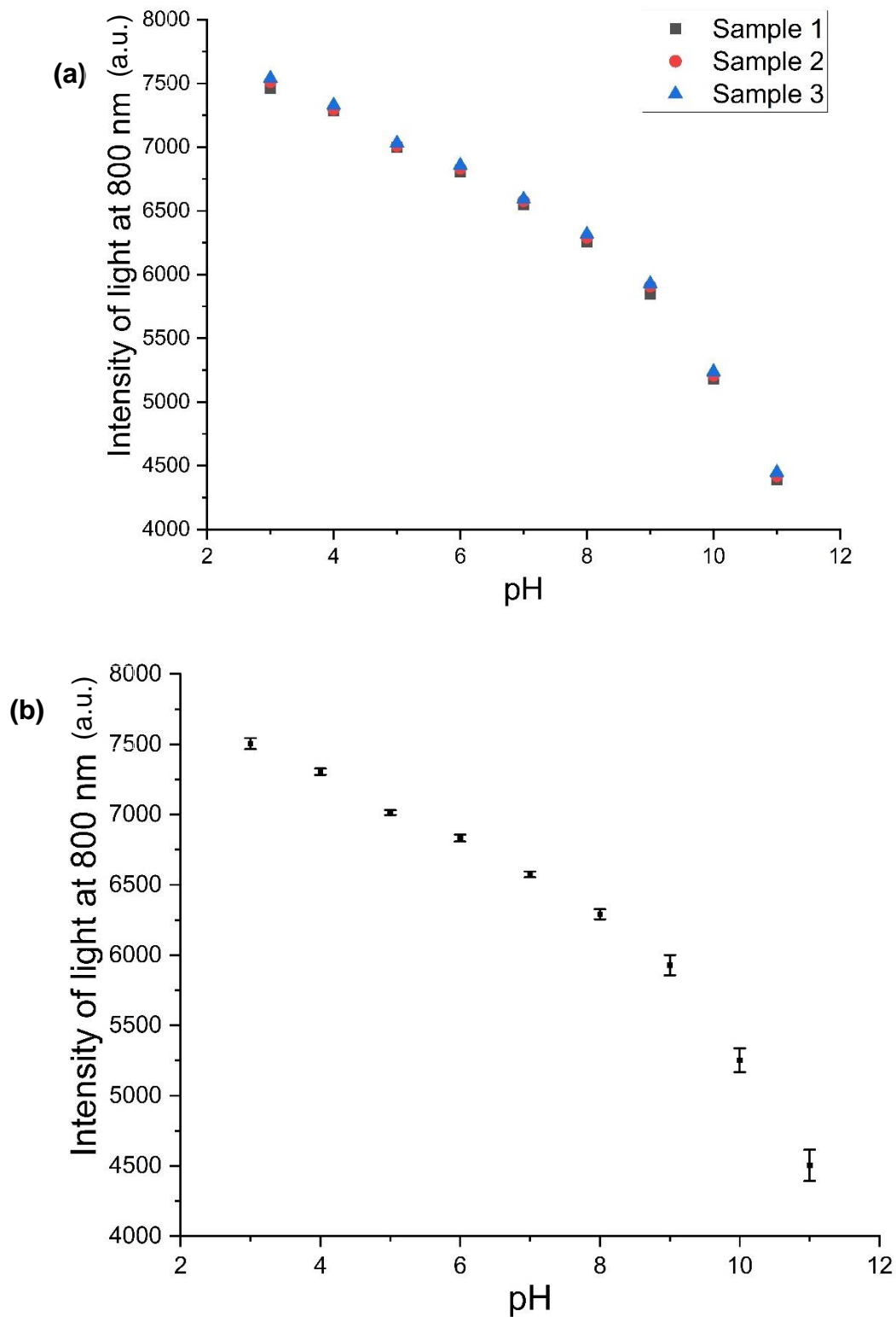
Figure 5.25: The change of intensity in different pH solutions using three different optical fibres prepared using HCl and NaOH (a) in the same batch, (b) showing the error bar.

In the second set of experiments, the optical response in pH measurement was investigated using optical fibres prepared in different batches of chloride media. In each batch, there were prepared 3 samples The optical fibres prepared in different batches exhibited varying responses, as shown in Figure 5.26. Similar to previous experiments, there was a change in the intensity of light observed in the batch production of optical fibre pH sensors. The trend of the intensity of light absorbed was consistent across all batches, indicating a similar behaviour in response to pH changes. However, the actual intensities recorded for the same pH values differed among the batches.

For the three different batches, the intensities at 800 nm for pH 11 were recorded as 4503, 5202, and 5583, respectively. As the pH of the solution was reduced to 3, the intensity at 800 nm of light increased to 7504, 8201, and 8530 for batches 1, 2, and 3, respectively. Calculating the average change in intensity per pH unit, the results for batches 1 to 3 were found to be 375/pH, 374/pH, and 368/pH, respectively.
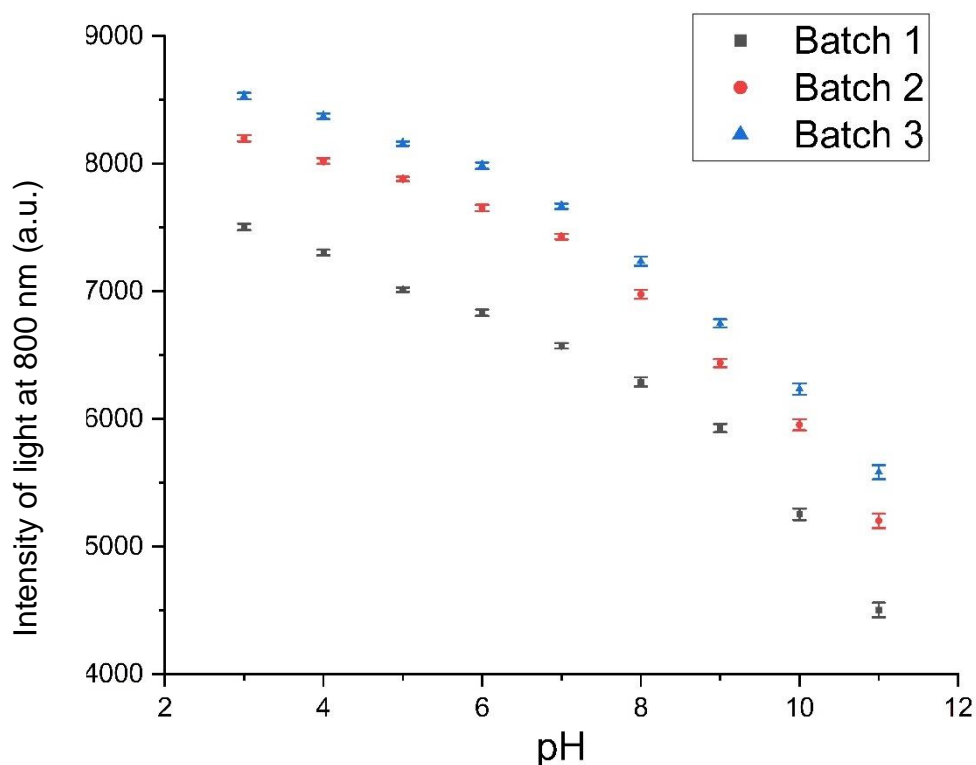
Figure 5.26: The change in intensity in different pH solutions using HCl and NaOH for the 3 different batches.

These findings demonstrate that the optical fibres prepared in different batches exhibit variation in their responses to pH changes. While the trend of change at 800 nm in intensity was consistent across all batches, the specific intensities recorded for each pH value differed among the batches. Nevertheless, the average rates of change in intensity for all batches using chloride media exhibit similar behaviour, providing confidence in the overall performance of the pH sensors.

5.2.3.3 Calibration of sensor in chloride and hydroxide media

The calibration process was carried out to assess the performance of the AgNp/silica coated pH optical fibre and further provide a basis for the conversion of optical response to pH. The experiment involved the calibration of the pH sensor using hydrochloric acid (HCl) and sodium hydroxide (NaOH) solutions across five different pH values: 3, 5, 7, 9, and 11. The intensities of light at a wavelength of 800 nm were recorded for each solution, and the results are shown in Figure 5.27.

In Figure 5.27, a calibration curve is constructed using both linear and polynomial fittings. The linear fitting yielded a coefficient of determination (R^2) of 0.93, as shown in Figure 5.27 (a). This indicates a reasonably good fit between the measured intensities and the pH values. However, to further improve the calibration, a polynomial fitting was employed. With this fitting approach, the coefficient of determination (R^2) significantly increased to 0.99, as shown in Figure 5.27 (b). This indicates that the performance of the sensor for pH measurement could best be explained by a polynomial model. The procedure for deriving the fitting equations for linear and second-order polynomial regression is explained in Appendix K, revealing the manner in which these equations are derived from experimental raw data.

The calibration equation using the linear fitting includes the following:

$$y = -0.002 * x + 23.55 \tag{5.15}$$

While the calibration equation using the polynomial fitting includes the following:

$$y = -7.90663\text{E} - 07 * x^2 + 0.00679 * x - 3.52392 \tag{5.16}$$

Both the linear and polynomial fittings were analysed to determine the optical pH measurement capabilities of the sensor. The high coefficient of determination (R^2) obtained with the polynomial fitting indicates a strong correlation between the measured intensities of light at 800 nm and the corresponding pH values. The calibration curves, generated through line fitting and polynomial fitting, demonstrate the cross check of the optical pH measurement.
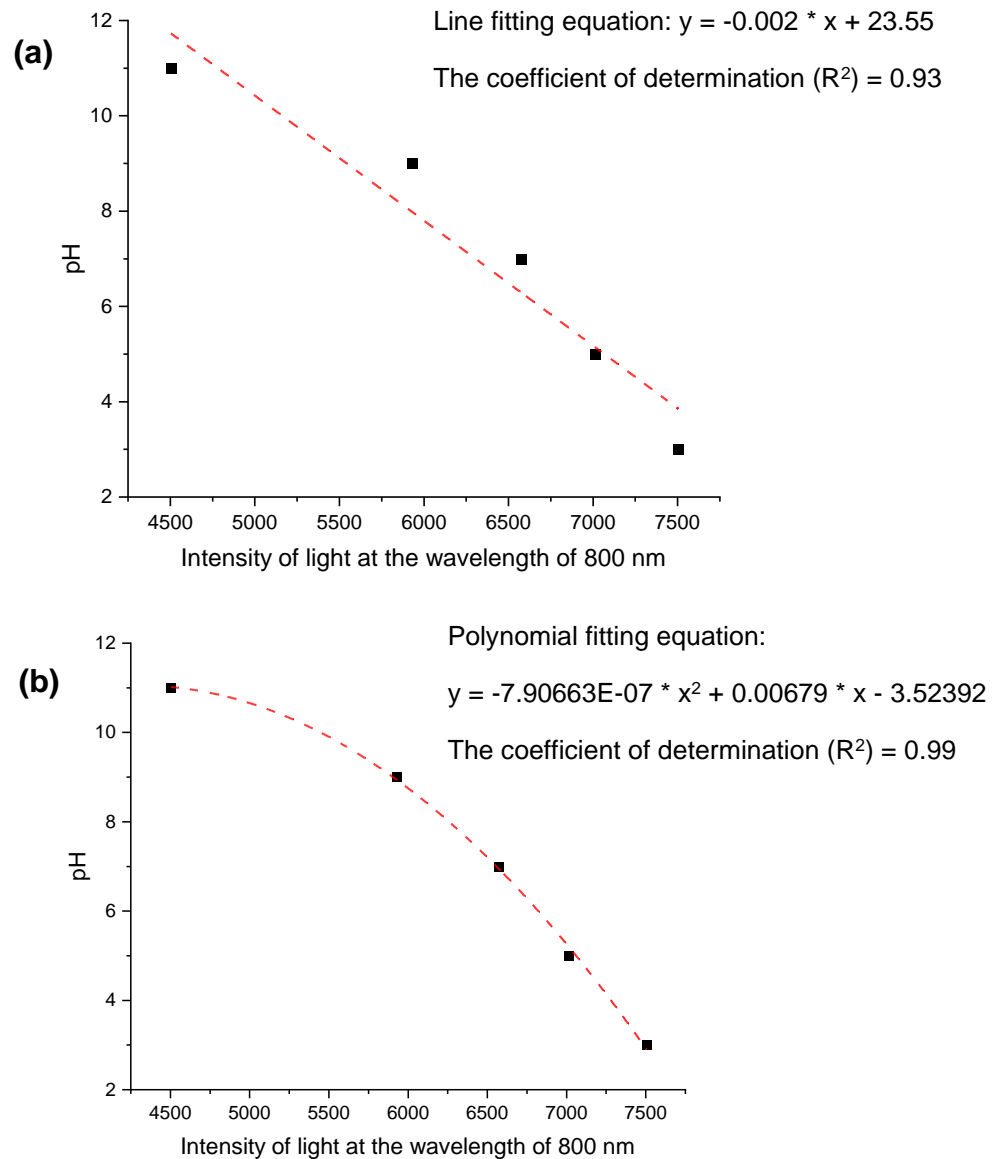
Figure 5.27: The pH calibration curve using HCl and NaOH (a) linear fitting (b) polynomial fitting.

5.2.3.4 Verification of optical pH measurement

In this section, a set of random pH experiments were conducted where the pH was randomly varied from pH 3 to 11 using hydrochloric acid (HCl) and sodium hydroxide (NaOH). The intensity of light at 800 nm was recorded, along with pH readings obtained from a potentiometric pH meter. Detailed data and calculations regarding optical pH using both models can be found in Appendix L.

From the results, the same observation as previous experiments was obtained. The polynomial model showed better accuracy compared to the linear model, as shown in Figure 5.28. When compared to the potentiometric pH readings, the optical pH measurements produced with the linear fitting are less accurate, as seen by their scattering considerably below and away from the ideal line. In contrast, as shown in Figure 5.28, the red data points derived from the polynomial model tend to be closer and aligned along the ideal line. When compared to the potentiometric pH values, optical pH readings are more precise when they are near the ideal line. When plotted against the ideal line, this data shows that the polynomial model yields optical pH values that are quite similar to the potentiometric pH readings.
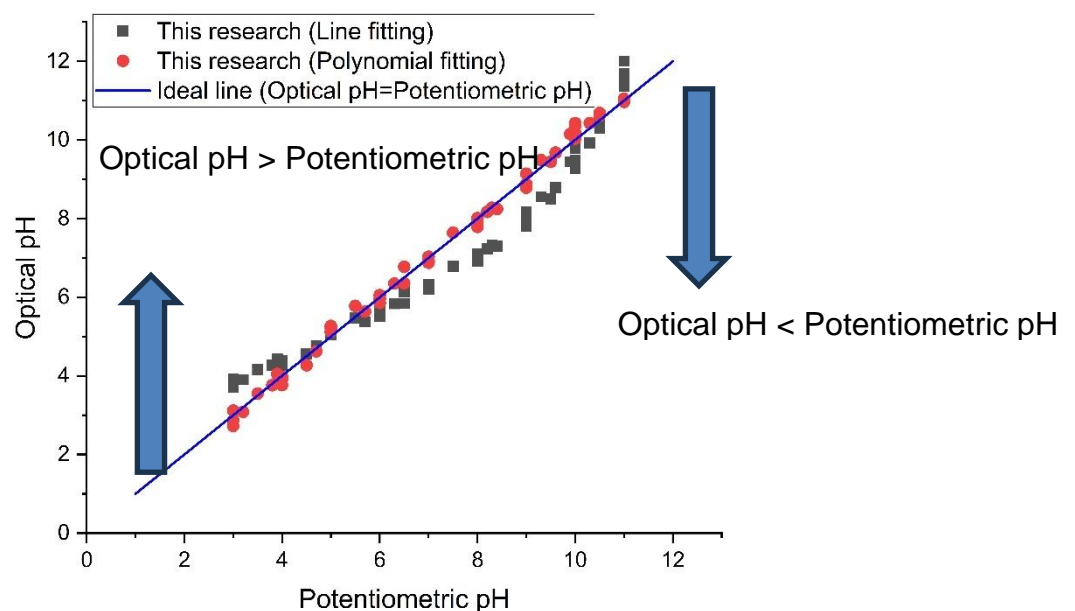
Figure 5.28: Comparison of accuracies of optical pH measurement (using HCl and NaOH) between the linear/polynomial calibration models and the ideal line where optical pH is equal to the potentiometric pH.

Figure 5.28 displays the calibration equations used to determine the best fit for the data from the random experiment, using a linear and a polynomial model. The graph also includes a reference line (blue) that indicates when the optical pH and the potentiometric pH are equal. The optical pH readings may be compared to the potentiometric pH values by looking at where the data points fall in reference to the ideal line. If the data point is below the ideal line, the acquired optical pH value is less than the corresponding potentiometric pH value, and if it is above the line, the obtained optical pH value is more than the potentiometric pH value.

In order to investigate the accuracy of the sensor, two graphs were plotted to compare potentiometric pH versus optical pH using both linear and polynomial fittings. These graphs are presented in Figure 5.29. Additionally, two lines offset by ± 0.5 pH values from the potentiometric pH were added to provide a measure of accuracy for the optical pH. Figure 5.29 showed that when the linear calibration model was used, the data points showed poor agreement with potentiometric pH readings. However, with the polynomial model, the accuracy significantly improves. All the data points fell within the area defined by potentiometric pH ± 0.50, indicating that the polynomial model offers better accuracy in pH measurement.

It is evident from the previous experiments that the polynomial model provides a more accurate pH measurement for all the acid solutions tested. This improved accuracy showed prospects for enhancing the precision and reliability of pH measurements. In summary, the random pH experiment using HCl and NaOH, along with the comparison of potentiometric pH and optical pH using linear and polynomial fitting, revealed varying levels of accuracy. The data points demonstrated poor accuracy with the linear calibration model, while the polynomial model showed a significantly improved accuracy. These findings indicate the importance of selecting the appropriate calibration curve to ensure accurate pH measurements.
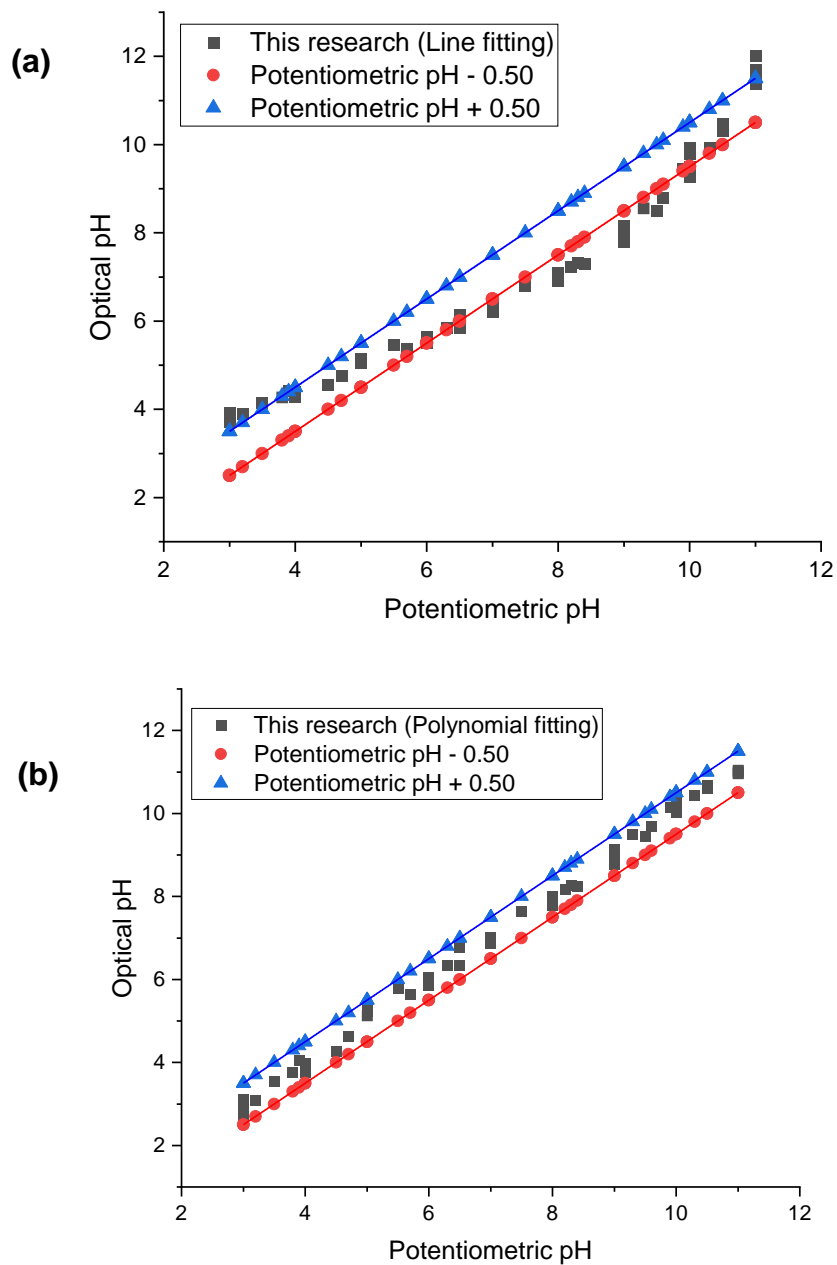
Figure 5.29: The pH measurement in comparison with potentiometric pH using HCl and NaOH (a) linear fitting equation, (b) polynomial fitting equation.

5.2.4 Comparison of the sensitivity of optical pH measurement in different media

Throughout all the previous measurements, extensive investigations and data analyses were performed on the change in light intensity under different media, including phosphate, sulphate and chloride using corresponding acids. The change in intensity from these experiments was combined into a single plot to facilitate comparison to check for variations in observed change in intensity, as shown in Figure 5.30 (a), and another graph plots the intensity of light, as shown in Figure 5.30 (b). The present dataset underwent analysis encompassing all chemical compounds, utilizing three distinct optical fibres, all of which were derived from a uniform batch preparation process.

As shown in Figure 5.30 (a), in the presence of different ions using different acids, different light intensity changes. In phosphate media, the light intensity change was 7402 when transitioning from pH 11 to 3. Similarly, in sulphate media the change in intensity amounted to 2225 under the same pH transition. In chloride media, the change in intensity amounted to 3073 under the same pH change. The highest change in intensity was observed with phosphoric acid, while the lowest change was observed using sulfuric acid.

Figure 5.30(b) presents the comparison of normalised data for the intensity of light obtained from optical pH measurement in all previous experiments. Across all the experiments, a similar trend of intensity change was observed. In acidic conditions, the change in intensity was lower compared to alkaline conditions. In alkaline solutions, a higher magnitude of the change in intensity was observed, which could be interpreted as greater sensitivity.
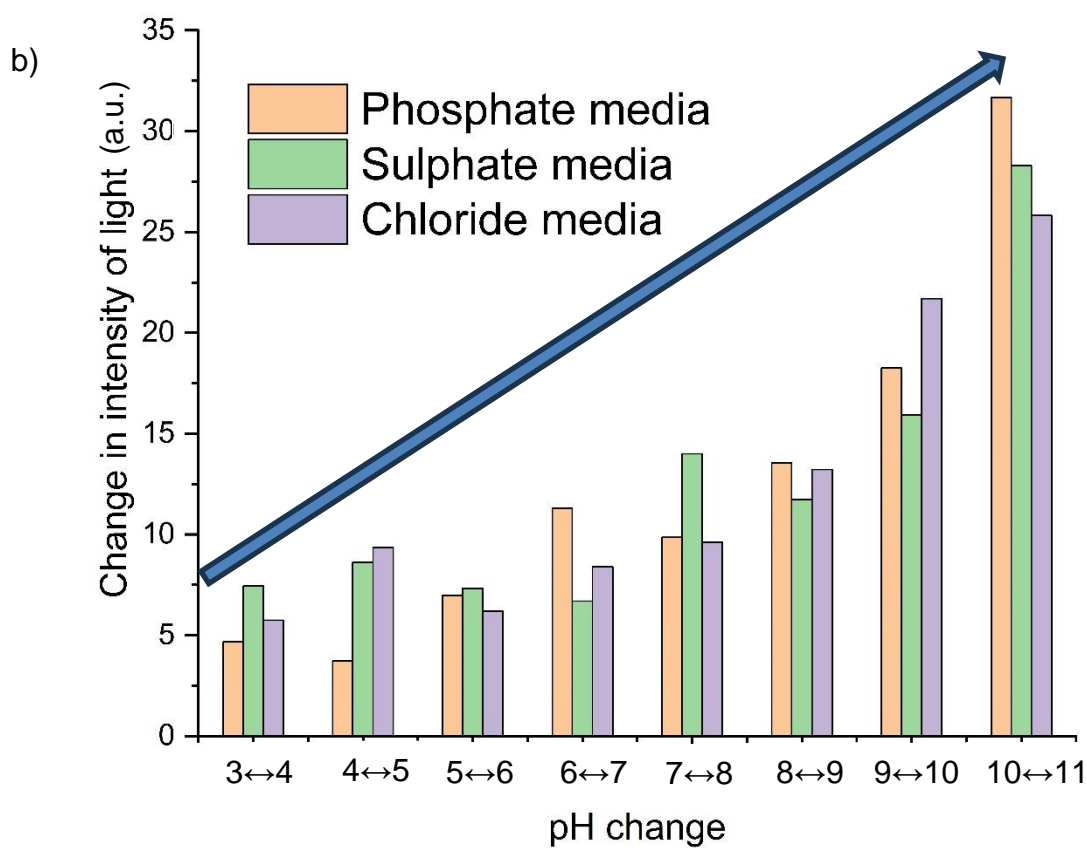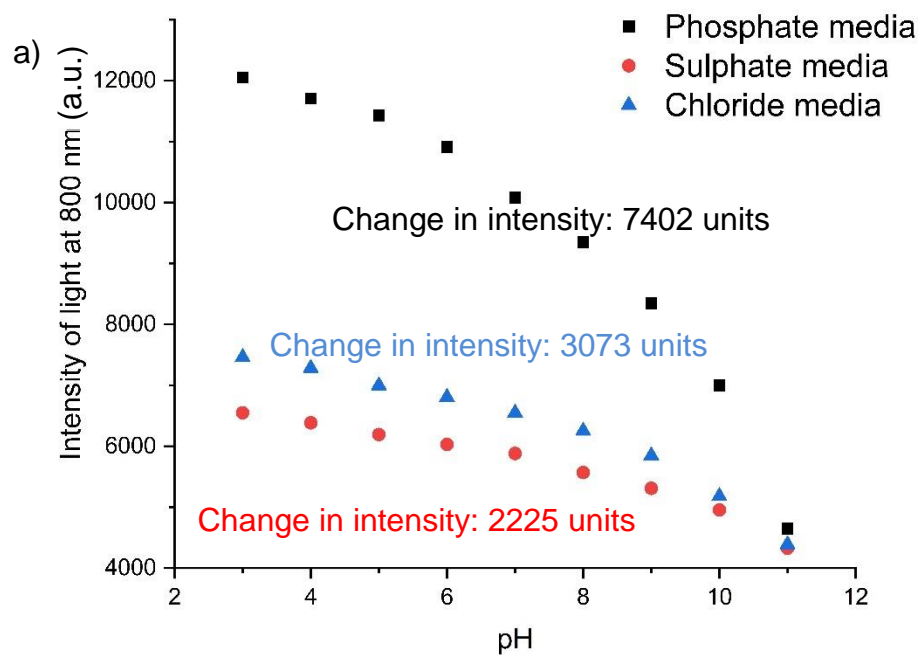
Figure 5.30: A comparison of the change in intensity of light in phosphate, sulphate and chloride media.

These findings indicate that the response of the sensor, in terms of changes in light intensity, varies depending on the acid used. The dissimilarities in the ions present in different acids might lead to distinct interactions with the AgNp/silica coating. Consequently, the reactions occurring on the surface of the coating in the presence of different acids result in higher changes in light intensity using H_3PO_4 compared to HCl and H_2SO_4. In summary, the observed differences in the changes in light intensity for different acids indicate the influence of chemical composition on the behaviour of the AgNp/silica coated pH sensor.

5.3 Durability test of AgNp/silica coated optical fibre as a sensor

The stability of the AgNp/silica coated optical fibre as a pH sensor was examined through a series of experiments. The same optical fibre was used for optical pH measurements on multiple days. Specifically, the test was repeated on the first, second, third, fifth and tenth day after the fabrication of an AgNp/silica coated optical fibre in phosphate media. Each experiment was performed in triplicate, as in Figure 5.31. After each experiment, the coated optical fibre was rinsed with deionized water, dried, and subsequently reused in the following days and so on.

In Figure 5.31 (a), light intensity measurements were recorded at different pH levels over a span of 10 days. On day 1, the intensity was recorded at 4790 units at pH 11 and 12023 units at pH 3. This translates to an average change in intensity of 904 units per unit change in pH. Subsequently, on day 2, the average change in light intensity exhibited a slight increase, with values of 5102 units at pH 11 and 12208 units at pH 3, resulting in an average change of 888 units per unit change in pH, which is 2 % less than first day sensitivity. As the study progressed to subsequent days, the trend of reduced sensitivity persisted. On day 3, the average change in light intensity was measured at 825 units per unit change in pH, and it is 9 % less compared to the first day sensitivity. This trend further continued, with an average change of 788 units per unit change in pH (13 % less) observed on day 5 and a subsequent decrease to 650 units per unit change in pH (28 % less) recorded on day 10, as shown in Figure 5.31 (b).

In effect, the test showed that the AgNp/silica coated optical fibre decreased in sensitivity over time. The average change in intensity per pH change gradually decreased, indicating a reduced response of the sensor with prolonged usage.
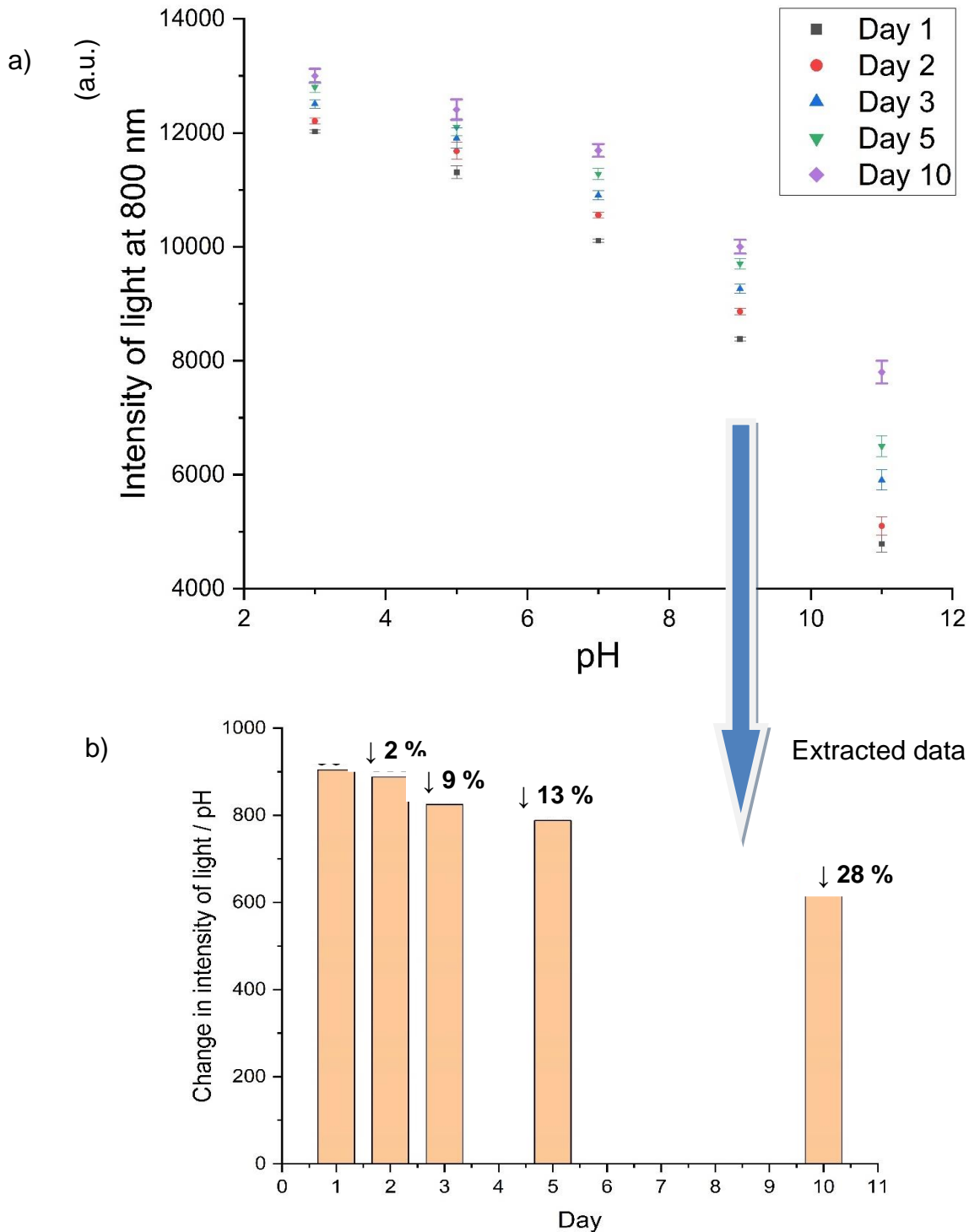
Figure 5.31: (a) The change in intensity of light using the AgNp/silica coated optical fibre as a sensor and (b) showing the change of intensity /pH on day-by-day calibration.

Micrographic images (Figure 5.32 (a) and (b) were taken to examine the AgNp/silica coated optical fibre's diameter on day 1 and day 10, respectively. On day 1, the diameter of the coated optical fibre was measured to be 115 microns. However, upon inspection of the micrographic image taken on day 10, it was observed that the diameter of the coated optical fibre had reduced to 110 microns. These micrographic images provide visual evidence that the coating of the optical fibre underwent dissolution during the course of the experiments. The reduction in diameter indicates a loss of material due to the dissolution of the coating, which would allow more leakage of light and lower the overall intensity. As a consequence of the coating dissolution, the average change in intensity per pH was gradually reduced over time.

In summary, the micrographic images clearly depict the change in diameter of the AgNp/silica coated optical fibre between day 1 and day 10. The reduction in diameter suggests that the coating experienced some degree of dissolution during the experiments. Consequently, this dissolution resulted in a decrease in the average change in intensity per pH and contributed to the loss of sensitivity in the coating.
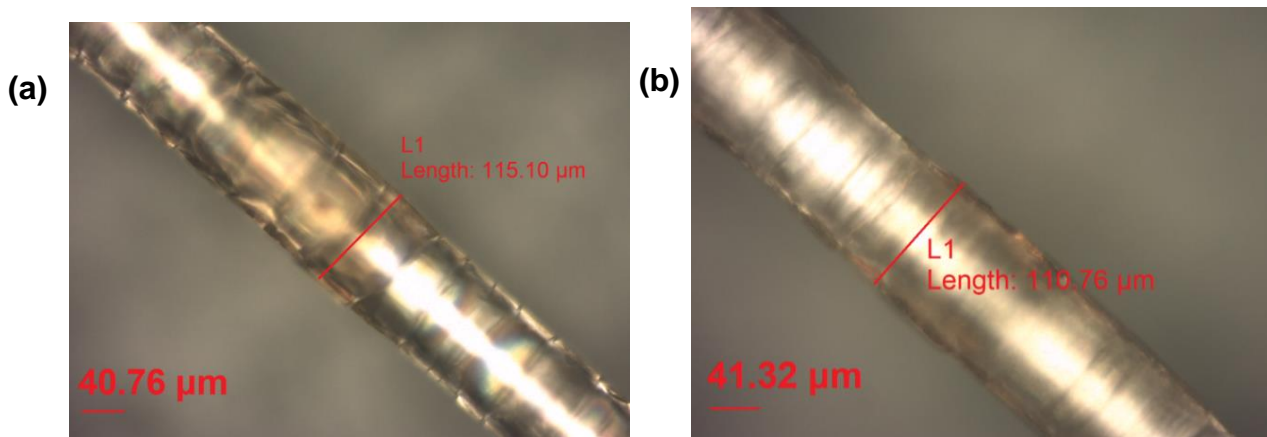
Figure 5.32: Micrographic image showing AgNp/silica coated optical fibre diameter during the stability test (a) day 1, (b) day 10.

5.4 Measurement of pH using etched and silica coated optical fibres as control

To further investigate the cause leading to changes in the sensitivity of the optical fibre and to determine if this was caused by the loss of AgNps or dissolution of the silica matrix, experiments of silica only coated fibre for pH detection were carried out. For this, a control experiment to gain insight into the individual contributions of the silica coating and Ag nanoparticles in the optical pH measurement. The experimental design involved two parts: pH measurements using an etched optical fibre without any coating on the etched area and pH measurements using an optical fibre with only a silica coating on the etched area, without the presence of Ag nanoparticles. By comparing these results, one can distinguish the roles of the silica coating and Ag nanoparticles in the pH measurement process could be ascertained.

As before, in the first part of the experiment, pH measurements were performed using an etched optical fibre without any coating on the etched area. This provided a baseline measurement to assess the influence of the silica coating and Ag nanoparticles. The results obtained from the control experiment allowed for a direct comparison with the subsequent measurements involving the coated optical fibres. In the second part of the experiment, pH measurements were carried out using an optical fibre with only a silica coating applied to the etched area, excluding the presence of Ag nanoparticles. This enabled the assessment of the effect of silica coating only on the pH measurement. By comparing these results with the previous measurements, the specific contribution of the silica coating could be ascertained. These measurements should show the effects of the silica coating only. When these data are compared against those obtained with AgNp/silica coatings, then one can understand the separate roles of the nanoparticles and matrix on the optical pH measurement.

5.4.1 Measurement of pH in test solution using etched optical fibre

The initial control experiment involved investigating on etched optical fibre to investigate the effect of silica coating. When the etched optical fibre was placed in water, it was observed that more light was transmitted through the core of the fibre compared to air. This phenomenon is illustrated in Figure 5.33 (a). The difference in transmission can be attributed to the variation in refractive indices between air

245

(refractive index of 1.00) and water (refractive index of 1.33). Since water has a higher refractive index, indicating a denser medium, it prevents light leakage through the core of the optical fibre. Consequently, more light intensity was observed when the etched fibre was immersed in water.

However, despite the change in light transmission with the presence of water, there was no corresponding change in the intensity of light when the pH of the solution was altered. In the control experiment, the intensity of light at 800 nm was monitored, consistent with previous investigations. Figure 5.33 (b) demonstrates that there was no noticeable change in the intensity of light as the pH of the solution varied. This lack of change can be attributed to the absence of any coating on the core of the optical fibre. Without a coating, there is no mechanism for the pH of the solution to influence the intensity of light transmitted through the fibre. The control experiment involving the etched optical fibre revealed that the presence of water affected light transmission through the fibre, but the absence of any coating on the core of the fibre prevented any change in light intensity corresponding to variations in pH. These findings highlight the critical role of the coating in facilitating optical pH measurements by enabling the pH of the solution to influence the intensity of light transmitted through the fibre and that without it the system is dysfunctional.
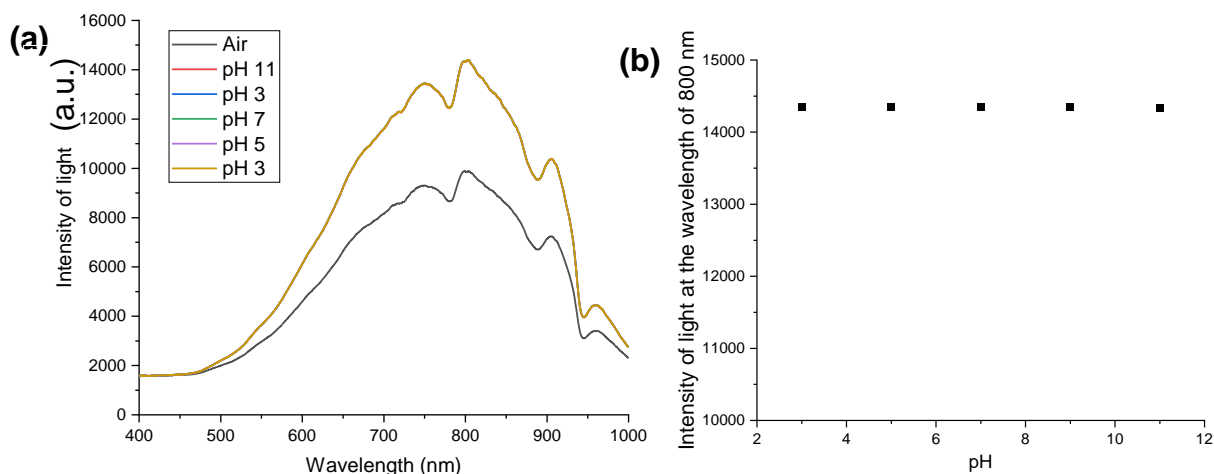
Figure 5.33 : (a) The pH experiment in phosphate media on etched optical fibre, (b) the change in intensity of light at the wavelength of 800 nm.

5.4.2 Measurement of pH of solutions using the silica-only coated optical fibre

In this section, pH measurements were conducted using optical fibres with only the silica coating on the core, this serves as the control measurement. The experiments employed phosphate media and three optical fibres were employed. The intensity of light at a wavelength of 800 nm was recorded for pH values ranging from 3 to 11, and the results, along with error bars, were plotted in Figure 5.34 (a). Upon examining Figure 5.34 (a), it became evident that the variation as quantified by error bars associated with the light intensity using only silica-only coating was relatively higher. The change in intensity was more pronounced in alkaline solutions, but the changes were not uniform in acidic conditions. A graph was plotted with the comparison of the change in intensity using three different configurations: optical fibre with an etched core only, optical fibre with only a silica coating on the core, and optical fibre with an AgNp/silica coating on the core as in Figure 5.34 (b),

The comparison clearly illustrates that without any coating, there was no observable change in light intensity. However, when only a silica coating is applied to the core of the optical fibre, a change in intensity was observed, even though these are variable and have greater uncertainty compared to the AgNp/silica coating. This suggests that the presence of silver nanoparticles in the AgNp/silica coating contributes to a stable and reliable response to pH changes in the solution. The results highlight that the silica coating solely can exhibit pH sensitivity, although its effectiveness is limited and associated with higher uncertainties. On the other hand, the inclusion of silver nanoparticles in the AgNp/silica coating provides a more repeatable and reproducible signal, as evidenced by the lower standard deviation. This indicates that the presence of silver nanoparticles enhances the stability and reliability of the pH sensor for pH measurement.
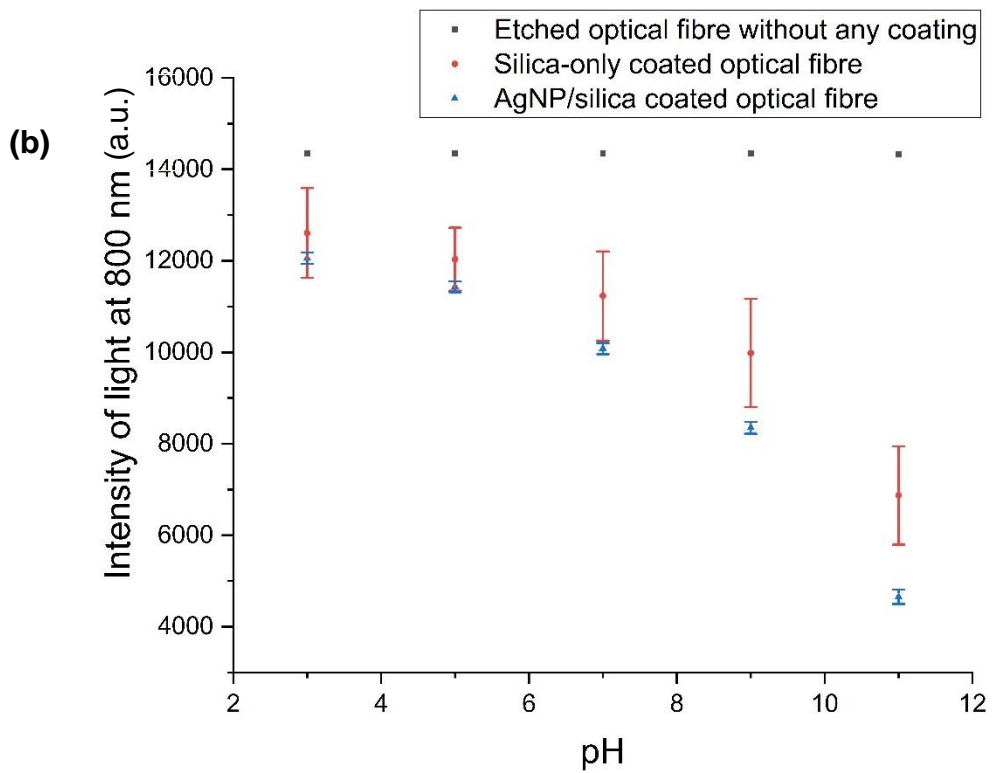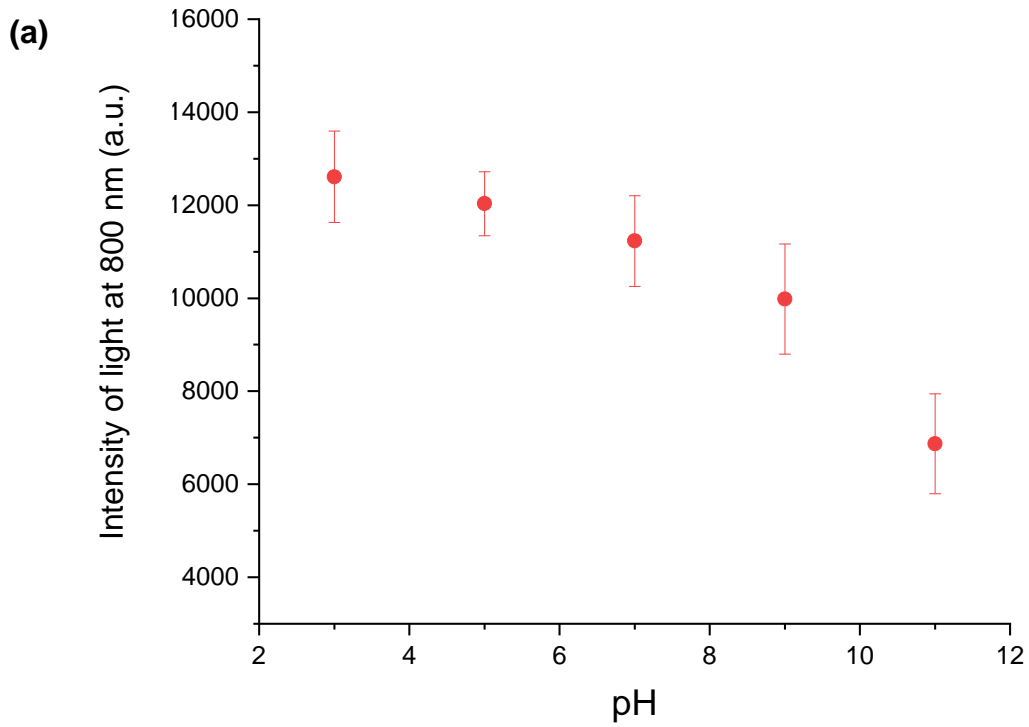
Figure 5.34: (a) The pH measurement in phosphate media with silica-only coated optical fibre, (b) a comparison of the pH measurements showing the change in intensity of light at 800 nm using the etched optical fibre, silica-only coating and AgNp/silica coated optical fibre.

This section involved the conversion of light intensity data into transmittance values. These transmittance values were analysed using pH 3, set at 100% as the reference point. The results are presented in Figure 5.35 (a). The purpose of this analysis is to compare our work with the literature. In the literature, transmittance was considered with the lowest pH solution as the reference. The analysis of Figure 5.35 (a) reveals that transmittance values exhibited lower values in acidic conditions. This indicates that the silica coating had lower sensitivity in acidic solutions compared to alkaline solutions. Conversely, transmittance showed a more significant change in alkaline solutions, indicating higher sensitivity of the coating in such conditions. Interestingly, these findings align with the report of Lu *et al.* [180], who also investigated pH measurement using only a silica coating. In their report, pH measurements were performed using an acidic solution and a pH range of 6 to 12. A comparison of their results and the experimental results is shown in Figure 5.35 (b).

In summary, the conversion of the pH measurement data to transmittance values revealed that the silica coating exhibited lower sensitivity in acidic conditions compared to alkaline conditions. This observation is consistent with the report of Lu *et al.* [180], who demonstrated the pH sensitivity of silica coatings in alkaline solutions. The findings highlight the distinct response of the silica coating under different pH conditions and further validate the results obtained in this study.
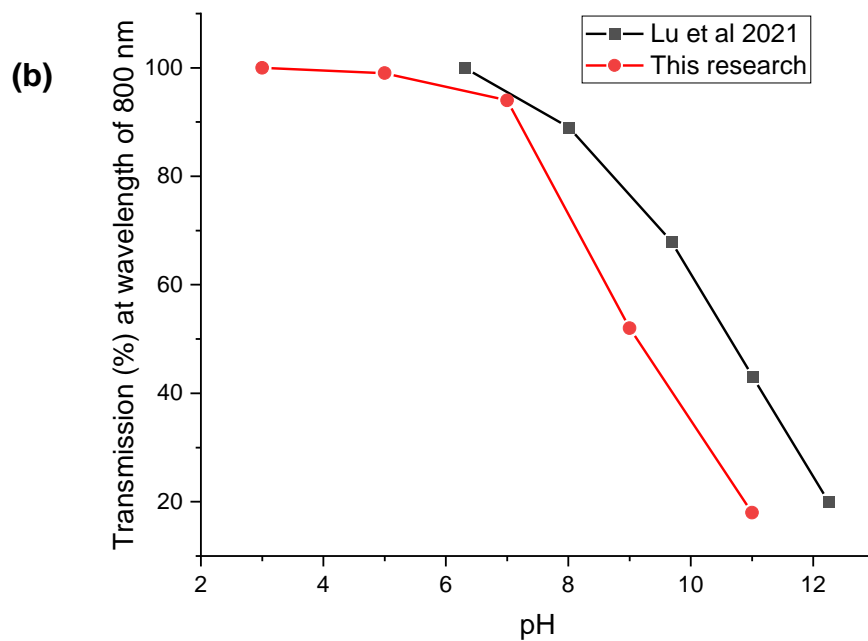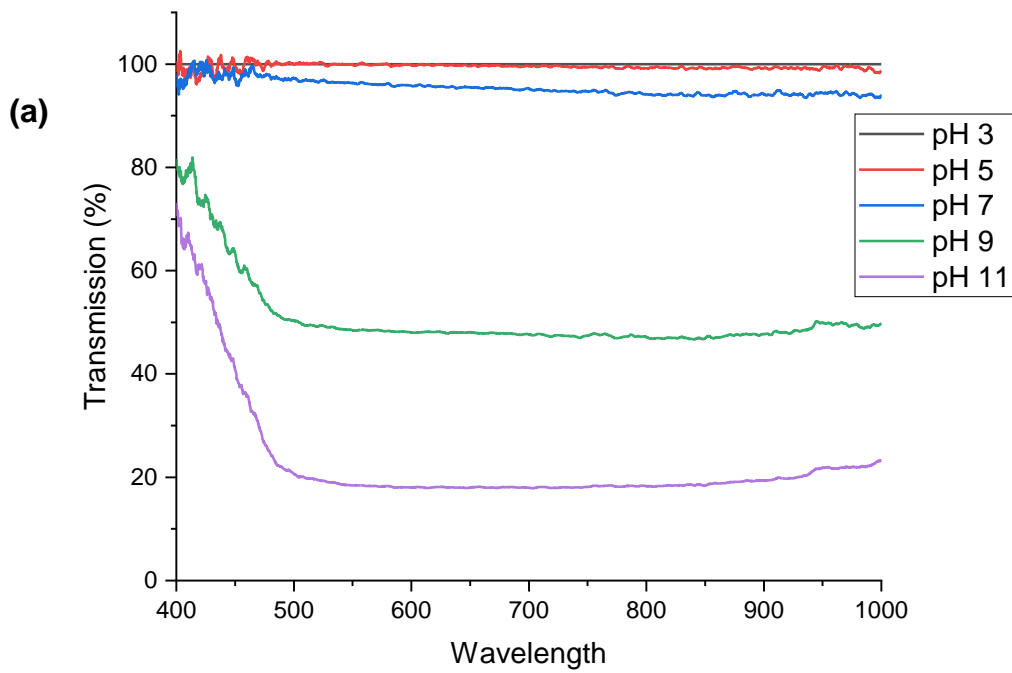
Figure 5.35 : (a) The Transmittance vs wavelength using silica coated optical fibre in different pH solutions, (b) A comparison of pH experiments using only silica coating with reports in the Lu *et al.* [180].

5.5 Chapter Conclusions

It was observed that the AgNp/silica coated optical fibre demonstrated promising sensor performance for pH measurement under ambient temperature conditions. The sensitivity of this optical pH sensor exhibited good responses in terms of reproducibility and repeatability over a short period of time. However, it should be noted that repeatability was only achieved when the optical fibres were manufactured within the same batch. Variations in batch manufacturing occurred due to the involvement of human operators in processes such as gel preparation, etching procedures on the optical fibre, multiple dip coatings, heat treatment, and sensor connection. Despite these challenges, the successful fabrication of the AgNp/silica coated optical fibre was achieved on a laboratory scale. These findings contribute to the ongoing exploration of the roles of silica and metal nanoparticles in pH sensing and provide insights for the development of advanced optical pH sensors. In summary, this study explains the intricate interplay between acid properties, silica stability, and resultant changes in light intensity.

Individual calibrations were required for different chemical conditions, highlighting the need for recalibration when changing chemicals to achieve accurate pH measurements. In preparation for the experiment, a calibration procedure was conducted using five data points at pH values of 3, 5, 7, 9, and 11. Fitting curves were established through both linear and polynomial fitting methods. Subsequently, pH values were determined using these fitting curves in conjunction with the optical technique. The calibration curve of the optical pH measurement technique was best fitted with a second-order polynomial, providing the best fit and offering a ±0.50 accuracy compared to potentiometric pH measurement.

It was observed that the optical response differed depending on the chemical used. In solutions prepared from different acids but having the same pH, the interactions between the different ions and the AgNp/silica coating varied, leading to changes in surface energy. The distinct behaviours observed can be attributed to the diverse ion compositions within different acids, leading to unique interactions with the AgNp/silica coating. This difference in interaction subsequently drives divergent reactions on the coating's surface, resulting in more pronounced changes in light

intensity when exposed to phosphate media compared to chloride and sulphate media.

It was observed that the change in intensity of light varied when the same pH level was changed in different media. The primary reason for this variation may be the different surface charges of the coating in different media, resulting in varying changes in light intensity. It is essential to highlight that this sensor's calibration is limited to the specific media it was calibrated for. Different calibrations are required for different media. Moreover, considering the observed dissolution of the coating, it is advisable to perform a calibration prior to the experiment to minimise errors in pH measurements.

In the literature, among the three media studied: phosphate, sulphate, and chloride media, the dissolution rate of silica was observed to be the lowest in phosphate. This could be attributed to the weaker acid of phosphoric acid, which imparts a milder impact on the breakdown of the silica structure. The relatively greater stability of silica in phosphoric acid appears to be the driving factor behind the more pronounced changes in light intensity observed throughout the experiments. On the other hand, the aggressiveness of sulfuric acid, characterised by the dissociation into hydrogen ions (H^+) and sulphate ions (SO_4^{2-}), leads to a more potent attack on the silica structure [266]. It was also reported in the literature that silica becomes more vulnerable to sulfuric acid and less in phosphoric acid [266], which agrees with the findings of this research. The AgNp/silica optical pH sensor may depend on the surface charge principle. Adding protons (H^+) or hydroxyl ions (OH^-) to change the pH of the solution alters the surface charge of the coating, which plays a central role in changing the intensity of light.

In this study, the pH measurement using AgNp/silica coated optical fibre was investigated under various chemical conditions, including phosphate, chloride and sulphate media. This work was motivated, in part, by the aim to determine the roles of silica and metal nanoparticles in pH monitoring. In the experiments conducted, the silica coating demonstrated pH sensitivity; however, the optical sensitivity was not repeatable with fluctuating pH levels in the solution. Conversely, the incorporation of AgNp into the silica coating resulted in improved consistency in optical pH sensitivity.

The improvement of signal stability through the incorporation of metal nanoparticles within the silica coating was observed, thus accentuating the advantageous function of metal nanoparticles in pH-sensing contexts. This phenomenon facilitated the attainment of consistent and reproducible data sets. Nevertheless, the potential impact of metal nanoparticles (e.g., AuNp or AgNp) on the acceleration of surface cracking within silica matrices was not subjected to investigation. Moreover, the comparative evaluation solely focused on pH sensitivity between metal nanoparticle-infused silica and pristine silica coatings, neglecting an assessment of the coating's surface morphology. This presents a possible opportunity for future research endeavour.

It should be noted that this study did not investigate the effect of heterogeneous systems involving the combination of different chemicals, which might be expected in real-life applications. In the oil and gas industry, the presence of different ions could affect the sensitivity of measurement. As this is a new field of study, it was necessary to focus on the effect of different ions separately rather than binary or ternary medium in order to understand the sensitivity of the sensor as well as its mechanism of operation. Having obtained the results for the single media, it would be interesting to consider the effect of the combined media in future work.

CHAPTER 6 Results: Stability and performance of AgNp/silica coated optical fibre in higher pressure and higher temperature environments

CHAPTER 6

Results: Stability and performance of AgNp/silica coated optical fibre in higher pressure and higher temperature environments

This chapter undertakes an investigation into the sensitivity of an optical fibre coated with silver nanoparticles (AgNp) embedded in a silica matrix when subjected to environments characterised by elevated temperatures and pressures, commonly referred to as high temperature and high pressure (HTHP) conditions. The existing literature prior to this inquiry lacked systematic data illustrating the effectiveness of such coatings when subjected to HTHP conditions. It is noteworthy that although a patent application is pending for the use of optical fibres coated with gold nanoparticles (AuNP) in conjunction with a silica matrix [267], a systematic exploration of the stability of the AgNp/silica-coated sensor in such demanding conditions has not been sufficiently addressed.

The experimentation began by observing the alteration of pH in solution when the solution was heated from room temperature to 70°C using potentiometric pH measurement. These experiments were used to establish a relationship between the temperature and pH of the solution. One curve utilised deionised water (pH 6.30), while the other two utilised solutions with pH 5 (prepared using phosphoric acid) and pH 9 (prepared using sodium hydroxide). These relationship equations could be useful to identify the corresponding pH at higher temperatures.

Subsequently, the HTHP experiment was conducted with the AgNp/silica-coated optical fibre immersed in deionised water at a gauge pressure of 5 bar. This experiment was aimed to simulate the conditions in which the sensor may encounter at elevated pressure in the oil and gas industry. For further evaluation of coating stability, the sensor was also subjected to cycles of pressures varying to 2 bar, simulating cyclical pressure changes. In addition, the stability of the coating was evaluated in acidic conditions (pH 5 prepared using phosphoric acid) and basic conditions (pH 9 prepared with sodium hydroxide). In the concluding phases of the investigation, the optical fibre coated with AgNp/silica was evaluated for its stability in an artificial sea water environment. This evaluation was essential for determining how the coating would perform in a more realistic and sea-water environment.

Throughout the chapter, comprehensive observations of the gauge pressure maintained during each experiment were recorded to determine the coating's response to HTHP conditions and various environmental factors.

In essence, the following items will be discussed in this chapter:

• The changes in pH when the solution was heated from temperature to 70°C.

• A trend of calibration curve relating pressure to temperature using deionised water. This would be compared against the standard steam tables. This calibration will be used to determine the sensor performance using phosphate-based (pH of 5) and hydroxide-based (pH of 9) solutions.

• Check the stability of the AgNp/silica optical fibre sensor at high temperature and high pressure (HTHP) in deionised water under a pressure of 5 bar.

• Check the suitability and stability of the AgNp/silica optical fibre sensor at higher temperatures and pressures when it has been subjected to cyclical pressure changes of 1 bar and 2 bar.

• Check the suitability and stability of the optical sensor in an acidic solution (pH 5) prepared with phosphoric acid and basic solution (pH 9) prepared using sodium hydroxide.

• The stability of the optical fibre coated with AgNp/silica in an artificial seawater at 2 bar.

6.1 pH measurement at higher temperature

The first experiment was aimed at examining the pH changes in the solutions as the temperature was raised from room temperature of 293 K (20°C) to 343 K (70°C). To achieve this, three different solutions were prepared. This includes deionised (DI) water with an initial pH of 6.3, an acid solution prepared using phosphoric acid (H_3PO_4) with a pH of 5, and an alkaline solution prepared from sodium hydroxide (NaOH) with a pH of 9. All the pH data were measured, and recorded the potential difference using a potentiometric pH meter while heating the solution.

In Chapter 1, the equation denoted as (1.16) was introduced as a means to determine the pH of a solution based on the measured potential difference. It is worth noting that this equation (1.16) exhibits a temperature (T) dependency.

$$pH(X) = pH(S) + \frac{Ex - Es}{2.3026 * RT / F} \qquad (1.16)$$

Where E_X = measured potential of solution (V),

E_S = measured potential of standard solution (V),

R = molar gas constant (8.3144 J mol^{-1} K^{-1})

T = Temperature (K),

F = Faraday constant (96485 C mol^{-1})

pH = the pH of the standard solution is 7

Consequently, by utilising the recorded values of potential difference and temperature, it becomes feasible to compute the pH of the solution, as exemplified in Table 6.1.

Table 6.1 : Calculation pH of different solutions at higher temperature using the potentiometric technique.

Temperature (K)	Acid solution (pH 5)		Basic solution (pH 9)		Deionised water (pH 6.3)	
	Potential difference (V)	Calculated pH	Potential difference (V)	Calculated pH	Potential difference (V)	Calculated pH
293	0.1160	5.00	-0.1160	9.00	0.040	6.30
303	0.1260	4.90	-0.1020	8.70	0.051	6.15
313	0.1430	4.70	-0.0715	8.15	0.062	6.00
323	0.1520	4.63	-0.0385	7.60	0.074	5.85
333	0.1620	4.55	-0.0130	7.20	0.092	5.60
343	0.1700	4.50	-0.0040	7.06	0.104	5.47

The data points for pH values, as presented in Table 6.1, were plotted to explore how the pH varied with increasing temperature for solutions with pH 5 and 9, along with deionised (D.I.) water, as shown in Figure 6.1. It is evident that the pH of each solution decreased as the temperature reached 343 K. This trend was observed across all solutions, including D.I. water (pH 6.3), the acid solution (pH 5), and the alkaline solution (pH 9). Specifically, when the DI water solution was heated from room temperature (293 K) to 343 K, its pH dropped from the initial value of 6.30 to 5.45. Similarly, the acid solution, with an initial pH of 5, experienced a shift in pH to 4.50 at the elevated temperature of 343 K. Likewise, the alkaline solution, which initially had a pH of 9, exhibited a change in pH to 7.06 under the same elevated temperature conditions. These results strongly indicate that as the temperature increased, there was a significant and consistent decrease in the pH of all the solutions under investigation. The pH, which is a measure of the acidity or alkalinity of a solution, exhibited a pronounced downward trend with the temperature rise.
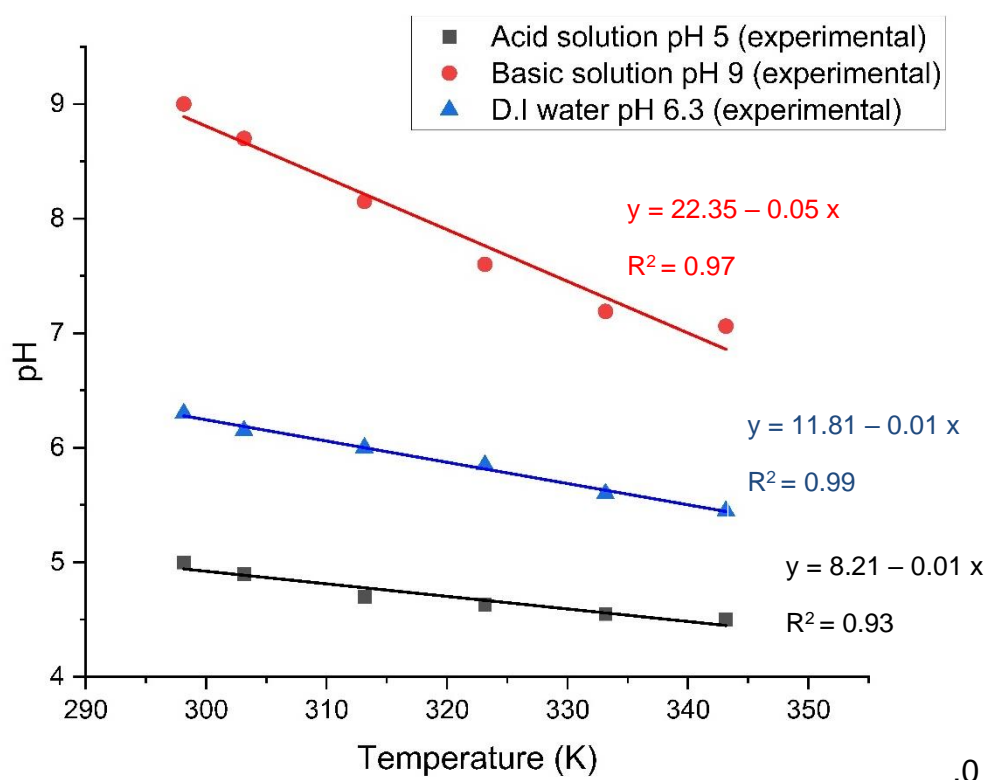
 Figure 6.1: The graph showing the change of pH with an increase in temperature up to 343 K for the acidic solution of pH 5, basic solution of pH 9, and deionised water of pH 6.3 at room temperature, respectively.

258

The fitted curve showing the pH changes was plotted at a higher temperature of 343 K for the acidic solution prepared using phosphoric acid (pH 5), the basic solution using sodium hydroxide (pH 9), and deionised water (pH 6.3). These fittings allow the prediction of the pH at higher temperatures. From the calibration model shown in Figure 6.1, the 'x' represents the temperature (K) and 'y' represents the pH of the solution. The fitting equations are provided below:

For the solution of pH 5 prepared using phosphoric acid:

$$y = 8.21 - 0.01x \qquad (6.1)$$

For the solution of pH 9 prepared using sodium hydroxide:

$$y = 22.35 - 0.05x \qquad (6.2)$$

For deionised water with a pH of 6.3:

$$y = 11.81 - 0.01x \qquad (6.3)$$

6.2 Performance and stability of AgNp/silica coated optical fibre at higher temperature and higher pressure conditions

This section presents a comprehensive investigation into the performance and suitability of the AgNp/silica-coated optical fibre in high temperature and high pressure (HTHP) conditions. The primary goal was to assess the coating resilience under these conditions and determine its potential applicability in various chemical environments. As mentioned, to simulate the HTHP conditions, a specialised high pressure vessel was utilised for the experiments. The coated optical fibre was placed within the vessel, and the temperature was gradually increased. When the temperature was increased, the pressure of the solution was increased. A hot plate was employed to heat the solution to increase the temperature and pressure of the solution.

The first high-pressure experiment was conducted using deionised water as the medium. This step was crucial to evaluate the coating's resistance to the applied pressures (or temperatures). Subsequently, a series of experiments were carried out using different chemical environments. Throughout these experiments, as mentioned, only gauge pressure readings were recorded, and temperature were

259

calculated from a correlation presented in the next section. This key correlation was crucial in deriving the corresponding temperature values for each experiment conducted under varying pressure conditions. The compiled dataset of pressure-temperature relationships facilitated the development of a calibration curve, thus serving as a valuable tool for inferring the temperature in future experiments solely based on gauge pressure readings.

Earlier, it was mentioned that the pressure sensor was reset to 0 bar at room temperature (25 °C or 298 K). In all the experiments, the 0 gauge pressure was used as a baseline, representing the total pressure at 25 °C. Gauge pressure was considered for all calculations and data analysis. The aim of this experiment was to assess the stability of AgNp/silica in HTHP experiments, and this calibration curve would convert gauge pressure to temperature. Therefore, the reported pressure in this study solely represents the gauge pressure within the vessel.

6.2.1 Calibration results showing the relationship between gauge pressure vs. temperature in the HTHP vessel

These tests were aimed at obtaining a calibration curve of gauge pressure vs temperature, which, for deionised water has one to one relationship. Additionally, this investigation involved comparing the acquired data with that of standard steam for comparative analysis. During the subsequent HTHP experiments, only gauge pressure was measured. This calibration curve enabled one to obtain the temperature of the solution. The calibration graphs of gauge pressure vs temperature were plotted for the solution of deionised water (pH 6.3), an acidic solution with a pH of 5 using phosphoric acid, and a basic solution with a pH of 9 using sodium hydroxide. In order to ensure that the results could be replicated accurately, the experiments were carried out in triplicate. In addition, a polynomial fitting was also drawn for each condition. To enable the conversion of gauge pressure measurements to the corresponding temperature values, a polynomial model was developed for each specific condition. These equations allow one to determine the temperature from experimental pressure values, as illustrated in Figure 6.2. These tests serve the purpose of establishing a reliable relationship between gauge pressure and temperature.

According to the Gibbs Phase Rule, which explains the thermodynamic equilibrium among distinct phases, there is a reduction in the count of independent variables. In the specific case of the steam/water equilibrium system, where only H_2O is present and two phases, liquid and vapor, coexist, the Gibbs Phase Rule dictates that there is only one degree of freedom. This reduction in degrees of freedom arises from the equivalence of chemical potentials between the phases in equilibrium, which effectively decreases the number of independent variables by one for each equivalence. For instance, the chemical potentials of the liquid and vapor phases are functions of both temperature (T) and pressure (P). However, when these phases reach equilibrium, their chemical potentials become equal. Consequently, if either pressure or temperature is held constant, the other variable is unequivocally determined by this equilibrium. In other words, when liquid coexists in equilibrium with vapor at a specified pressure, the temperature is determined by the equated chemical potentials and is termed the equilibrium temperature. Similarly, at a given temperature, the vapor pressure is uniquely determined by the same equivalence relationship.

a)

Fitting equation:

$y = -0.5321x^4 + 7.7303x^3 - 40.49x^2 + 102.15x + 300.6$
$R^2 = 0.99$

b)

c)
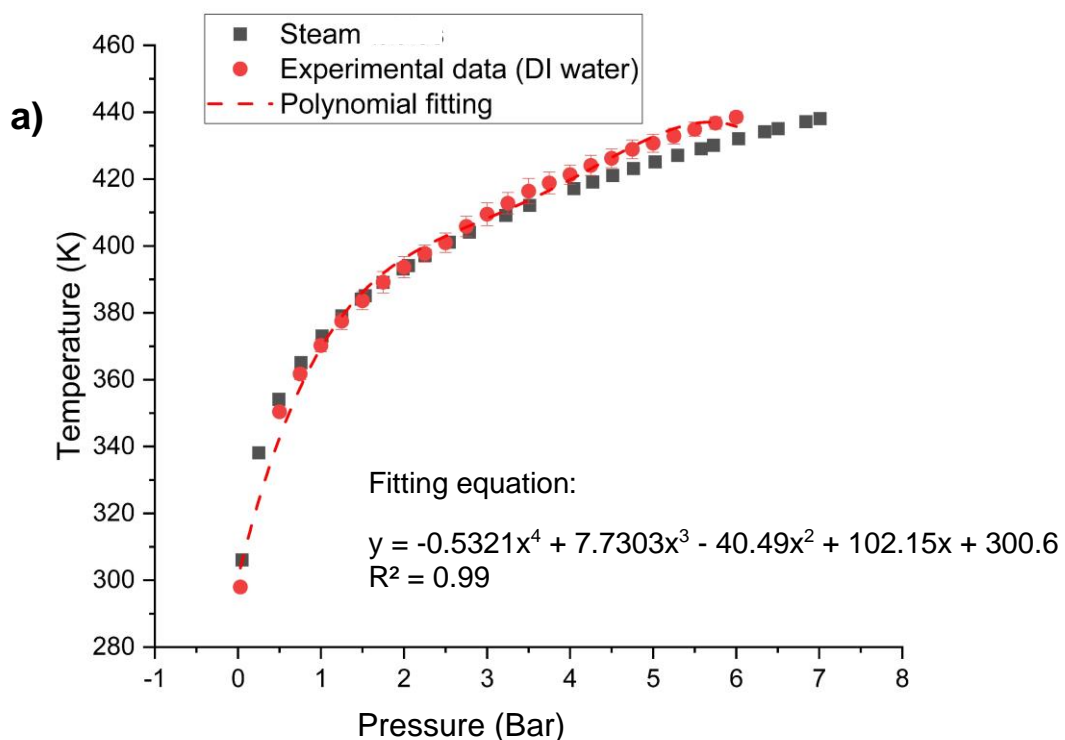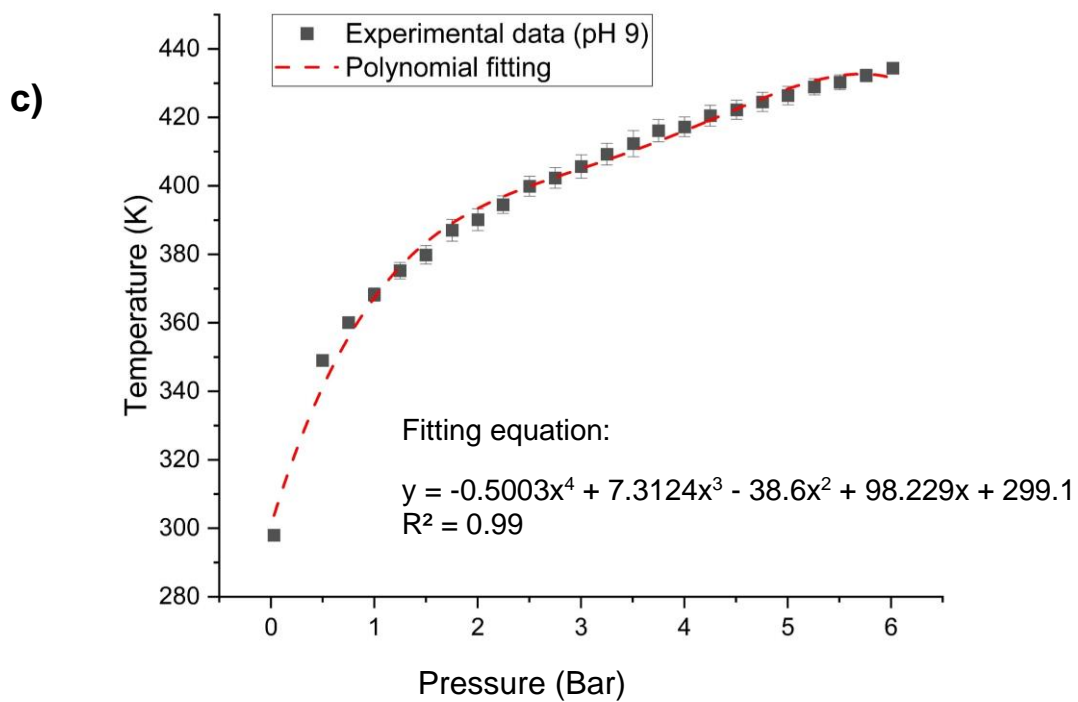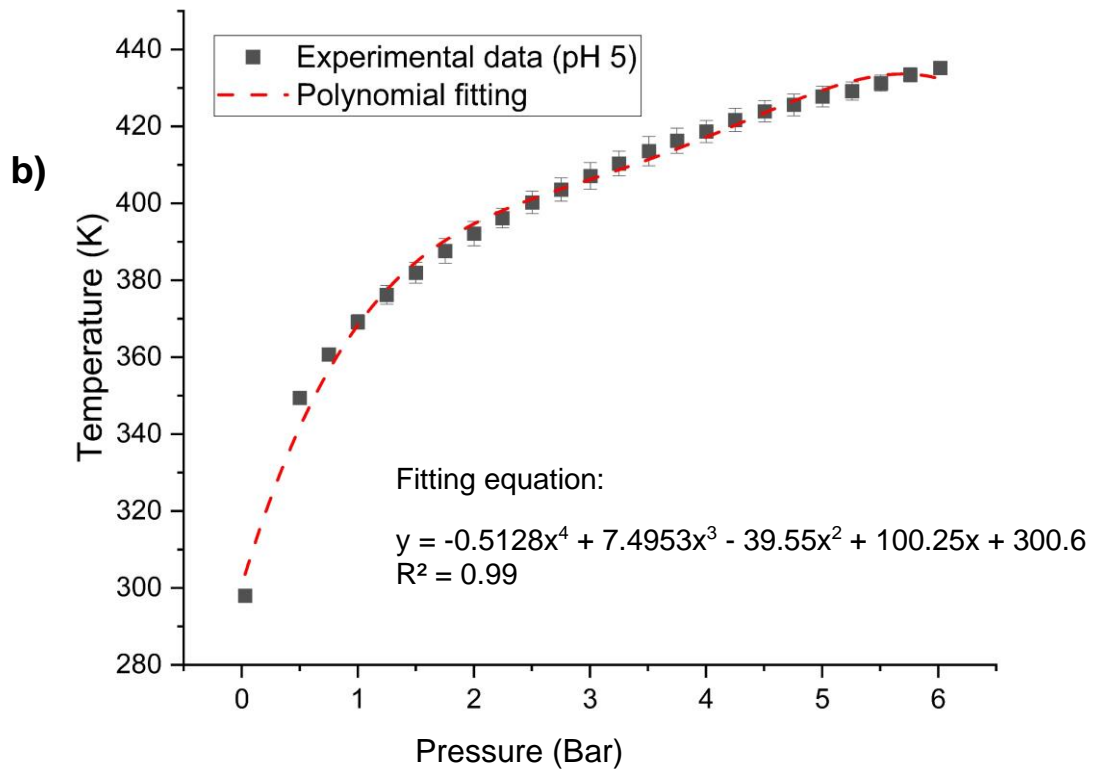
Figure 6.2: The calibration curve of gauge pressure vs. temperature using (a) deionised water at pH 6.3, (b) acidic water at pH 5 prepared using phosphoric acid, and (c) alkaline solution at pH 9 prepared using sodium hydroxide.

Figure 6.2 (a) illustrates the calibration curve for the deionised water of the pH 6.3 system. To evaluate its accuracy, the experimental data points were compared with values obtained from the standard steam tables [268,269], which is considered an ideal relationship between pressure and temperature. As shown in Figure 6.2 (a), the data from steam tables and those obtained experimentally in the HTHP vessel are in excellent agreement up to 3.5 bar and in good agreement up to 6.0 bar. This provides confidence that using a pressure reading (using the gauge) can provide a reasonable value for solution temperature.

An analytical fourth-order polynomial model was used to fit data points to obtain between gauge pressure (P) and temperature (T) for deionized water, as shown below:

$$T = -0.5321 * P^4 + 7.7303 * P^3 - 40.49 * P^2 + 102.15 * P + 300.6 \quad (6.4)$$

Where T is the temperature (K), and P is the gauge pressure (Bar).

Using equation 6.4, when the gauge pressure is 1, 2, 3, 4, and 5 bar, respectively, the temperatures are 371 K, 397 K, 409 K, 420 K, and 433 K. According to the steam table, the temperature at 5 bar should be 424 K where in this experiment it was calculated 433 K. This comparison indicates a slight deviation between the experimental results and the ideal steam table values which are observed at higher pressure.

The next calibration curve was plotted for the solution of a phosphate acidic solution of pH 5 prepared from phosphoric acid, as shown in Figure 6.2 (b). A forth-order polynomial model was plotted to obtain the relationship below:

$$T = -0.5128 * P^4 + 7.4953 * P^3 - 39.55 * P^2 + 100.25 * P + 300.2 \quad (6.5)$$

Using equation 6.5, when the gauge pressure is 1, 2, 3, 4, and 5 bar, respectively, the temperatures are 370 K, 395 K, 406 K, 417 K, and 430 K.

Similarly, the calibration curve was plotted for the basic solution with pH 9 prepared from sodium hydroxide, as shown in Figure 6.2 (c). A forth-order polynomial model was used to obtain the relationship below:

$$T = -0.5003 * P^4 + 7.3124 * P^3 - 38.6 * P^2 + 98.229 * P + 299.1 \qquad (6.6)$$

From equation 6.6, when the gauge pressure is 1, 2, 3, 4, and 5 bar, respectively, the temperatures are 367 K, 392 K, 403 K, 414 K, and 427 K.

The data show that there are slight differences in the fitting parameters depending on the pH.   The calibration curves were subsequently employed to compute temperature based on the gauge pressure measurements.

6.2.2 Effect of Pressure and Temperature on AgNp/silica coating

In the beginning, the focus of the investigation lay in using the AgNp/silica-coated fibre under to determine pH at a maximum gauge pressure of 5 bar in order to evaluate the sensor performance and stability under such elevated pressure levels. Specifically, close attention was paid to detecting any potential dissolution or degradation of the coating that could occur at this high-pressure threshold and drift in pH values.

This aspect is one of the novelties of the current study because there are almost no reports on the stability of such material, and it would also provide information on the lifetime of such sensors in HTHP conditions. Thereafter, the study expanded its investigation to assess the AgNp/silica coating's behaviour under cyclical gauge pressure conditions of 1 bar to 2 bar. These conditions involved deionised water with a pH of 6.3, an acidic solution with a pH of 5 (prepared using phosphoric acid), an alkaline solution with a pH of 9 (using sodium hydroxide), and finally artificial seawater. Assessing the coating's response under these diverse chemical conditions also provides valuable insights into its potential applications in real oil and gas scenarios where it may encounter different types of solutions.

Similar to the previously mentioned information, it was stated that the pressure sensor was reset to 0 bar at room temperature (25 °C or 298 K). In all the HTHP experiments, the 0 gauge pressure was used as a baseline, representing both the pressure of 1 atmosphere and the gauge pressure at 25 °C. Only the gauge pressure was taken into account for all calculations and data analysis. Therefore, the reported pressure in this study exclusively reflects the gauge (g) pressure within the vessel, where the gauge pressure at 298 K (25 °C) was considered as the reference 0 gauge pressure.

In the execution of high-temperature high-pressure (HTHP) experiments, monitoring protocols were implemented to record both gauge pressure and light intensity at one-minute intervals. Following this, the gauge pressure, typically set at 5 bar, 2 bar, or 1 bar in accordance with experimental specifications, was sustained for a duration of 30 minutes, as it demonstrated stability in pressure readings. This procedural step facilitated the attainment of a stabilized condition for both the pressure and optical sensors at each designated pressure level. The principal objective of this investigation was to fabricate and evaluate the sensitivity and efficacy of an optical fibre pH sensor as a dynamic instrument, with a particular focus on assessing its sensitivity under varying pressure and chemical conditions. It is noteworthy that the elevation of pressure within the pressure vessel was achieved through the utilization of a hot plate, though without precise control over the heating rate. Following the heating phase, the hot plate was deactivated to allow for the gradual return of the pressure vessel to ambient room temperature through natural cooling processes.

6.2.2.1 Experiment at gauge pressure 5 Bar using deionised water

In this section, the AgNp/silica-coated fibre was tested under high pressures of about 5 bar (g) while immersed in deionised water. This experiment was conducted three times using three different coated fibres, all prepared from the same batch to ensure consistency and reliability of the results. To measure the response of the coated fibre to varying pressures, the relative intensity of light at a wavelength of 800 nm was recorded and monitored. Figure 6.3 shows the relationship between the gauge pressure and the corresponding relative intensity of light. To convert the gauge pressure readings into temperature values, it was employed the calibration fitting

equation 6.4. As a result, it was determined that the corresponding temperature during the experiment was 433 K for 5 bar of gauge pressure.

Analysis of the results indicates that the intensity of light at the 800 nm wavelength changed with increasing gauge pressure during the heating cycle, as shown in Figure 6.3. This observation indicated that there was a notable change in light intensity as the pressure was raised to 4.5 bar (g). The sensitivity of the coated fibre showed good performance up to 3 bar (g), after which it started to decline. Surprisingly, when the pressure was increased beyond the threshold of 4.5 bar (g), there was no further response from the coated fibre. After continuing up to a pressure of 5 bar (g), the system was cooled. During the cooling cycle, the intensity of light at the 800 nm wavelength displayed remained constant. This means that the coated fibre did not exhibit any significant change in light intensity as the pressure and temperature slowly decreased. This hysteretic behaviour has never been reported by previous researchers since it has never been attempted.
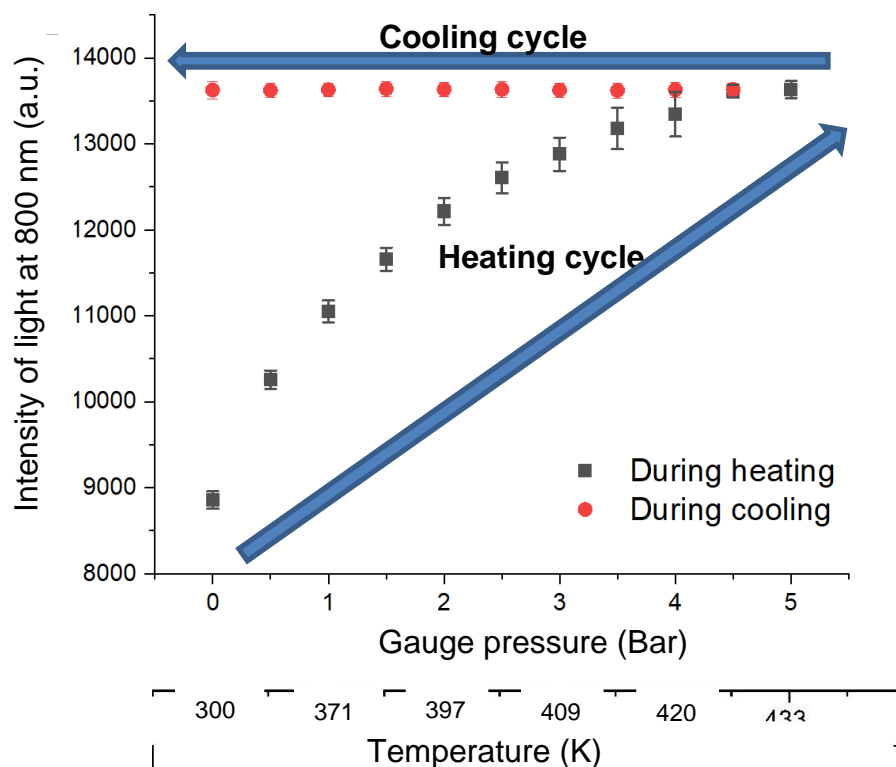
Figure 6.3: Results showing the stability of AgNp/silica coating in deionised water at 5 bar (gauge pressure).

To investigate the unusual behaviour of the sensor, an examination of optical fibre was conducted using a high-resolution optical microscope was carried out. This experiment involved measuring the diameter of the coated fibre the diameter of the coated optical fibre before and after the high-pressure experiment. The findings of this experiment are presented in Figure 6.4. Prior to the experiment, there was a visible coating of AgNp/silica on the optical fibre. However, after the experiment, where a pressure of 5 bar (g) and a temperature of 433 K was reached, a change was observed. The AgNp/silica coating is completely dissolved, resulting in a reduction in the diameter of the optical fibre, which was measured to be 103 microns after the experiment, as shown in Figure 6.4.

Further verification was carried out using an optical microscope to view the diameter of the coated optical fibre before and after the experiment, as shown in Figure 6.4. Before the experiment, there was a coating on the core of the optical fibre. However, after the experiment at 5 bar (g), it was found that the diameter of optical fibre was observed to be 103 microns, verifying the microscopic observation.

With the dissolution of the coating, the optical fibre was exposed directly to the surrounding medium with a loss of transmitted light, which caused a significant decline in the sensing capabilities of the coated fibre during the cooling phase. The dissolution of the coating at the gauge pressure of 5 bar explains why there was no change in the intensity of light during the cooling cycle. The decline in the sensitivity above 3 bar (g) could be an indication of the dissolution of the coating. As the dissolution of coating is a gradual process, more investigation was necessary to understand the dissolution rate at different pressures, which is presented in the forthcoming sections.
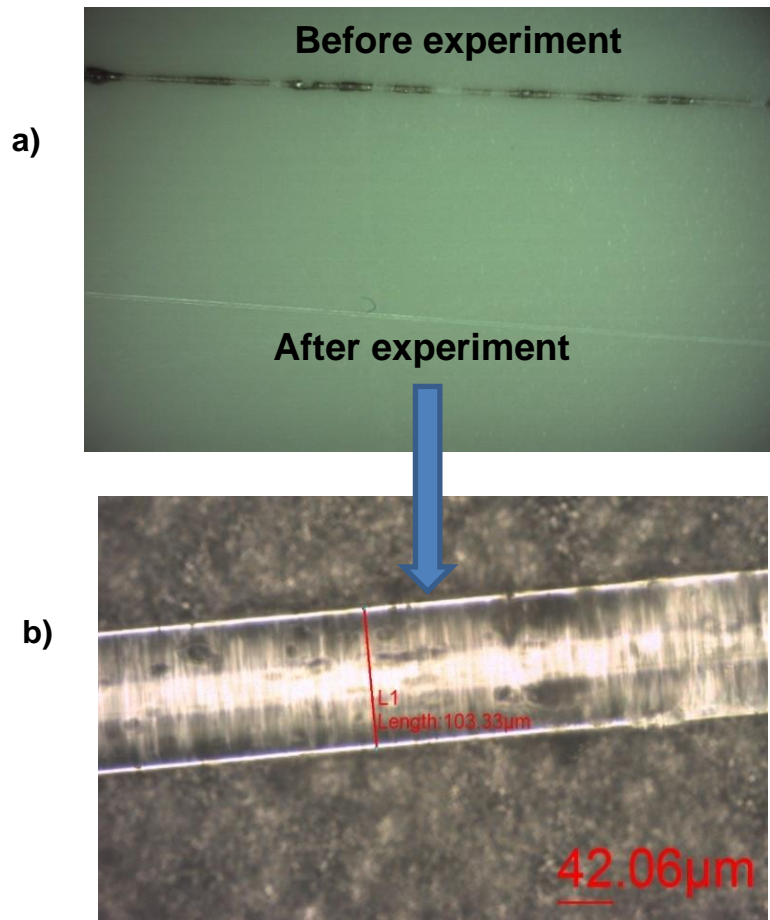
Figure 6.4: (a) The micrographic image of AgNp/silica coating before and after the experiment at 5 bar using deionised water, (b) the micrographic image of optical fibre showing the diameter after the experiment.

6.2.2.2 Experiment at the gauge pressure of 2 bar using deionised water

The preceding results demonstrated that the AgNp/silica coating was incapable of withstanding the elevated pressure of 5 bar (g). Consequently, this section delves into an investigation of the coating's stability under a pressure lower than 5 bar (g). As mentioned, it was observed that the coating exhibited higher dissolution at the pressure of 3 bar (g). Therefore, further experiments were carried out to determine at what pressures and temperatures this dissolution takes place. In an effort to do this, the coated optical fibre was subjected to a pressure of 2 bar (g). 2 bar (g), which corresponds to temperatures of 397 K according to the calibration curves. All experiments were carried out at a pressure of 2 bar (g). In these experiments, the

optical fibre was subjected to the heating and cooling cycles, and the change in the intensity of light was measured.
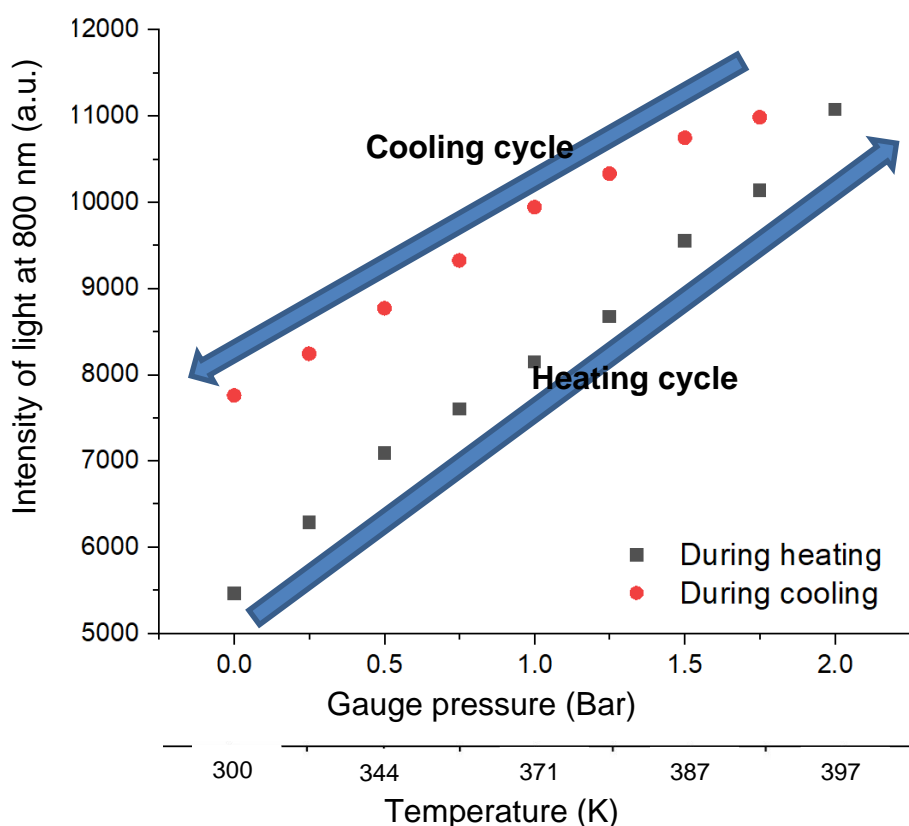
Figure 6.5: The stability of AgNp/silica coating of HTHP experiment at a gauge pressure of 2 bar using deionised water.

The results shown in Figure 6.5 indicate the changes in light intensity as a function of pressure and temperature measured at a wavelength of 800 nm, particularly during a heating and subsequent cooling cycle. At an initial pressure of 0 bar (g), the recorded intensity of light stood at 5463 units. However, as the pressure was increased to 2 bar (g) during the heating cycle, the intensity of light exhibited a substantial increase, ultimately reaching 11074 units, showing that light intensity increases during the heating phase. Conversely, during the cooling cycle, a reverse trend was observed. The intensity of light decreased as the gauge pressure and temperature were lowered. Nevertheless, upon complete cooling of the pressure vessel to room temperature, the recorded light intensity stabilised at 7758, a value

much higher than the original of 5463. Ideally, it would be expected that the intensity of light would revert to its initial value, but this was not the case.

The deviation in the light intensity from its original baseline at a gauge pressure of 0 bar (g) suggests a potential interaction or alteration of the coating material. It is possible that some dissolution or modification of the coating material occurred at increased pressure and temperature, hindering the full restoration to the original value. To interpret this phenomenon further, a micrographic examination showing the diameter before and after the experiment was also carried out. This is shown in Figure 6.6 and shows the changes in coating structure that may have contributed to the change in light intensity.

Figure 6.6 illustrates the results of a micrographic analysis undertaken to assess changes in the diameter of a coated optical fibre before and after subjecting it to a cycle of increasing and decreasing the temperature and gauge pressure of 2 bar. Figure 6.6(a) shows a difference in the colouration of the coating because of the loss of coating of AgNp/silica on the optical fibre during the HTHP experiment. The initial diameter of the AgNp/silica-coated optical fibre measured approximately 115 microns. Upon examination post-experimentation, it was ascertained that the optical fibre's diameter had undergone a reduction to 110 microns, as measured in Figure 6.6(b). At the applied pressure of 2 bar (g), a slight dissolution of the coating was observed, measuring approximately 2.5 microns in diameter. This dissolution of the coating layer could be the cause of increased light intensity and departure from its initial state.
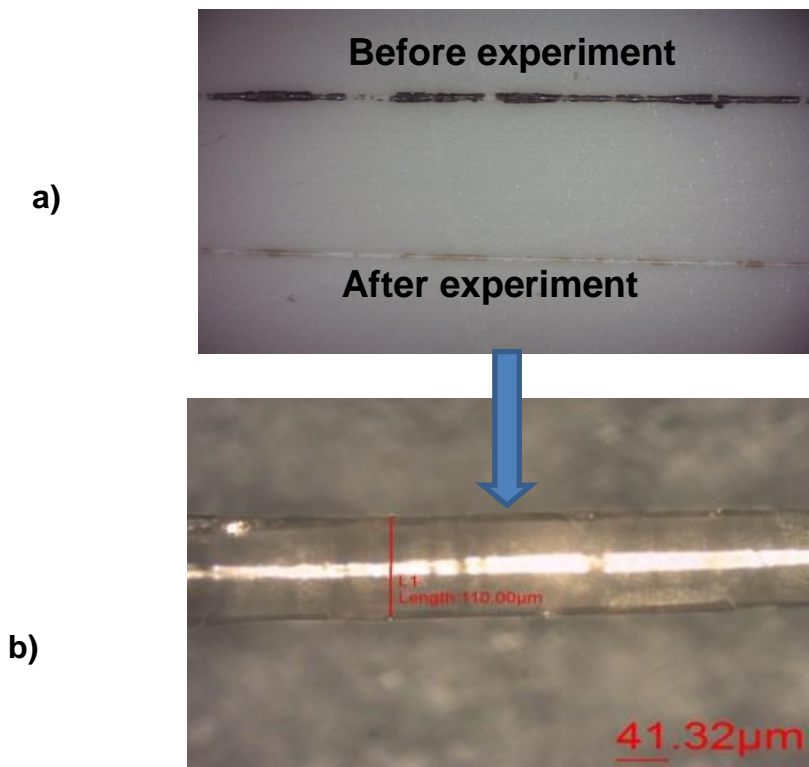
Figure 6.6: (a) The micrographic image of AgNp/silica coating before and after the experiment at 2 bar (g) using deionised water, (b) the micrographic image of an optical fibre showing the diameter after the experiment.

To evaluate the stability of the AgNp/silica coating, the experimental protocol involved subjecting the coated optical fibre to consecutive heating cycles to achieve a pressure of 2 bar (g), followed by subsequent cooling to room temperature. This cyclic process was repeated two times to assess the coating stability across a number of cycles, as graphically depicted in Figure 6.7.

As mentioned for the single cycle, the same dissolution of the coating was observed when the gauge pressure was raised to 2 bar with a corresponding increase in temperature to 397 K. In an effort to delve deeper into this phenomenon, a subsequent heating and cooling cycle was conducted on the same optical fibre. This was undertaken with the primary objective of examining if the dissolution continued in subsequent cycles.
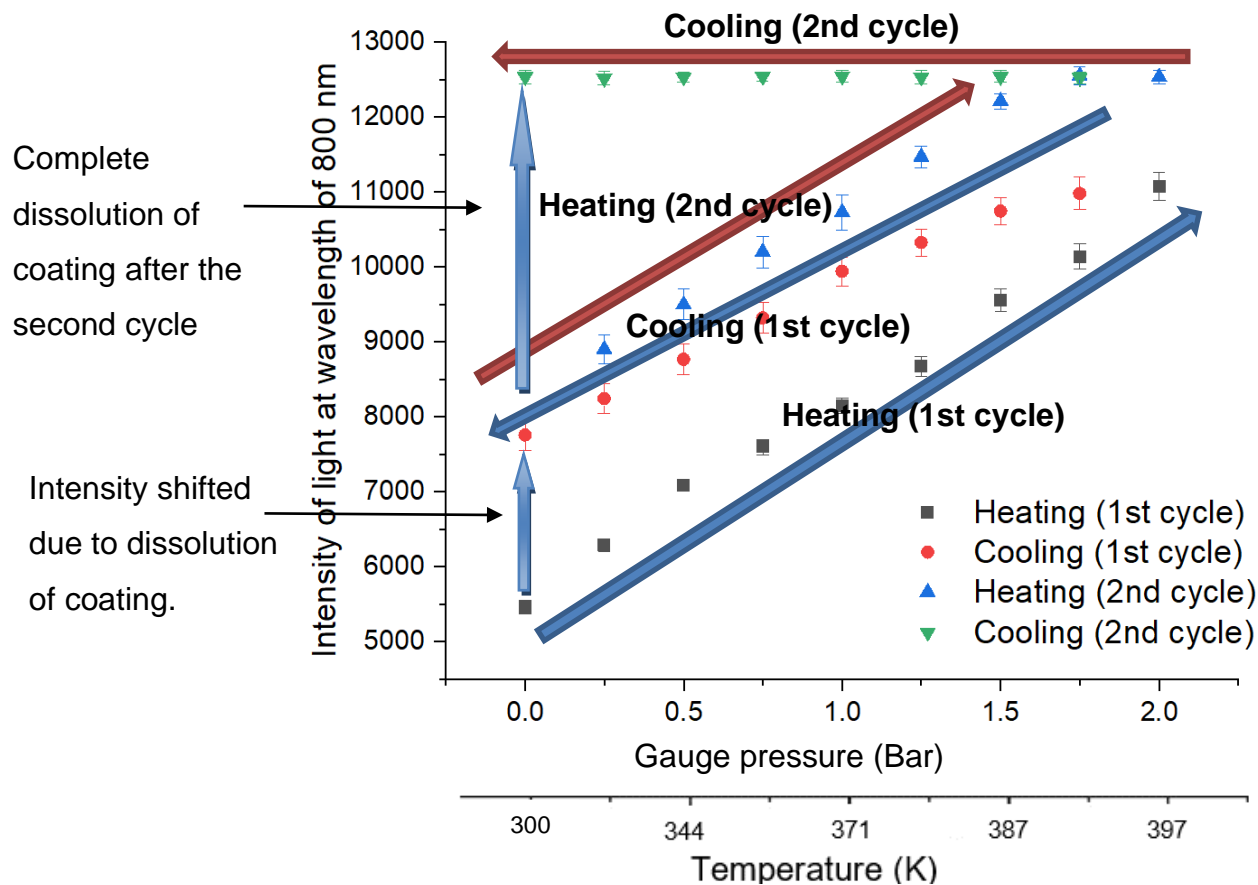
Figure 6.7: The stability of AgNp/silica coating at 2 bar (g) for two cycles using deionised water.

As explained in the preceding section, the dissolution of the coating led to a noticeable change in the light intensity. Specifically, this alteration was shifted from its original value, which was recorded at a pressure level of 0 bar (g) at the end of the cooling cycle. As graphically depicted in Figure 6.7. Subsequent analysis has revealed a notable change in light intensity during the second heating cycle, which was not observed in the first cycle. This phenomenon is characterised by measuring the change in light intensity throughout the entirety of the second heating cycle, which signifies a sustained degradation of the coating at the aforementioned pressure threshold of 1.5 bar (g). Throughout the cooling stage of the second cycle, there was an absence of any discernible changes in light intensity, showing that the coating had dissolved. Therefore, one may conclude that after two successive cycles, including a heating and cooling cycle at a pressure of 2 bar (g), the complete dissolution of the coating was observed. On the other hand, the complete dissolution of the coating was observed just after one cycle at a pressure of 5 bar (g). It could be

summarised that the dissolution of the coating is dependent on pressure and is faster at higher pressures.

6.2.2.3 Experiment at gauge pressure 1 bar using deionised water

In earlier experiments, dissolution was shown to occur at a pressure of 2 bar (g). The objective was to determine the pressure and temperature regime in which the optical fibre could remain stable. Therefore, a lower pressure of 1 bar (g) was chosen to monitor if there was any dissolution in the coating at this lower pressure. Similar to the previously conducted HTHP experiment, the pressure was initially raised to 1 bar (g) and then cooled to 0 bar (g) while the intensity of light was recorded, as shown in Figure 6.8.
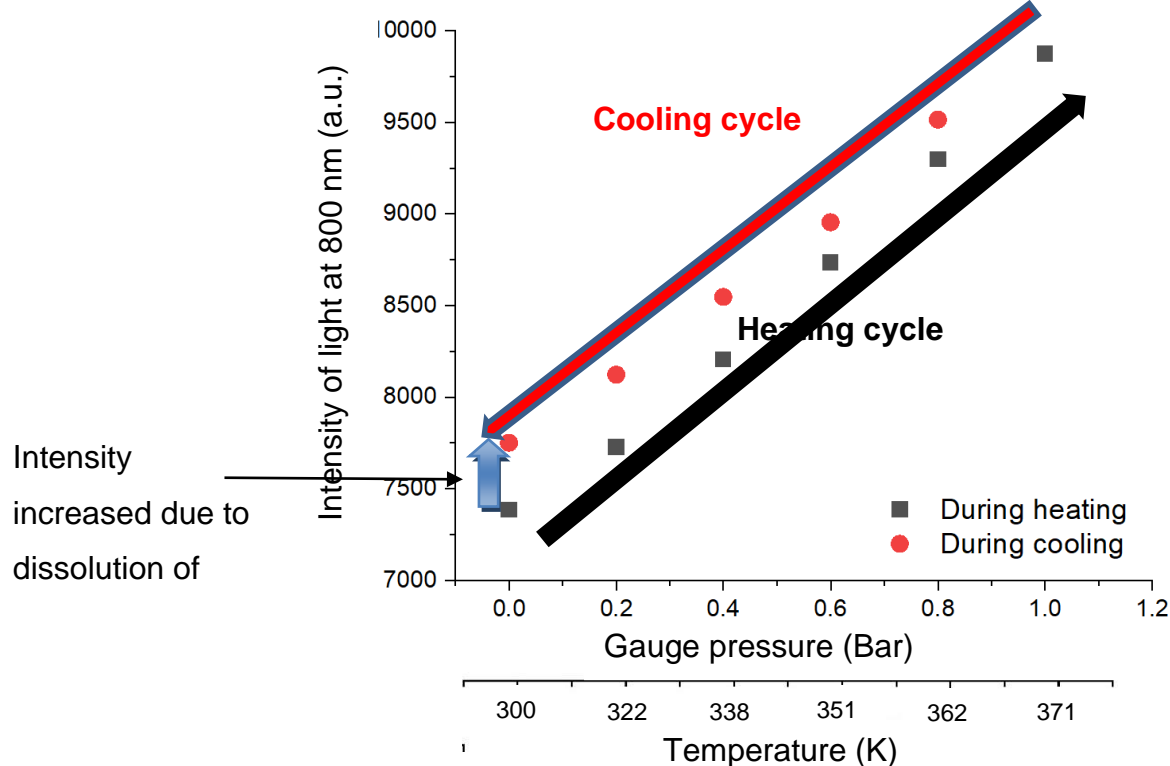
Figure 6.8: The stability of AgNp/silica coating at a gauge pressure of 1 bar in deionised water.

As before, during the heating cycle, the test carried out at 1 bar (g), an increase in the intensity of light at a wavelength of 800 nm was observed, as shown in Figure 6.8. The intensity of light during the heating cycle was recorded at 7384 units when the gauge pressure was at its base, at 0 bar; however, this intensity reached at 9874 units when the pressure reached 1 bar (g). At the end of the cycle, there was a shift

273

in the intensity of light. Upon completion of the cooling phase, the intensity was measured to be 7,750 units, an increase of 366 units. The substantial change in intensity at a gauge pressure of 0 bar suggests the possibility of dissolution or modification in the coating material. Both pre and post-experimental microscopic examinations were conducted to evaluate the diameter measurements, as was done earlier.
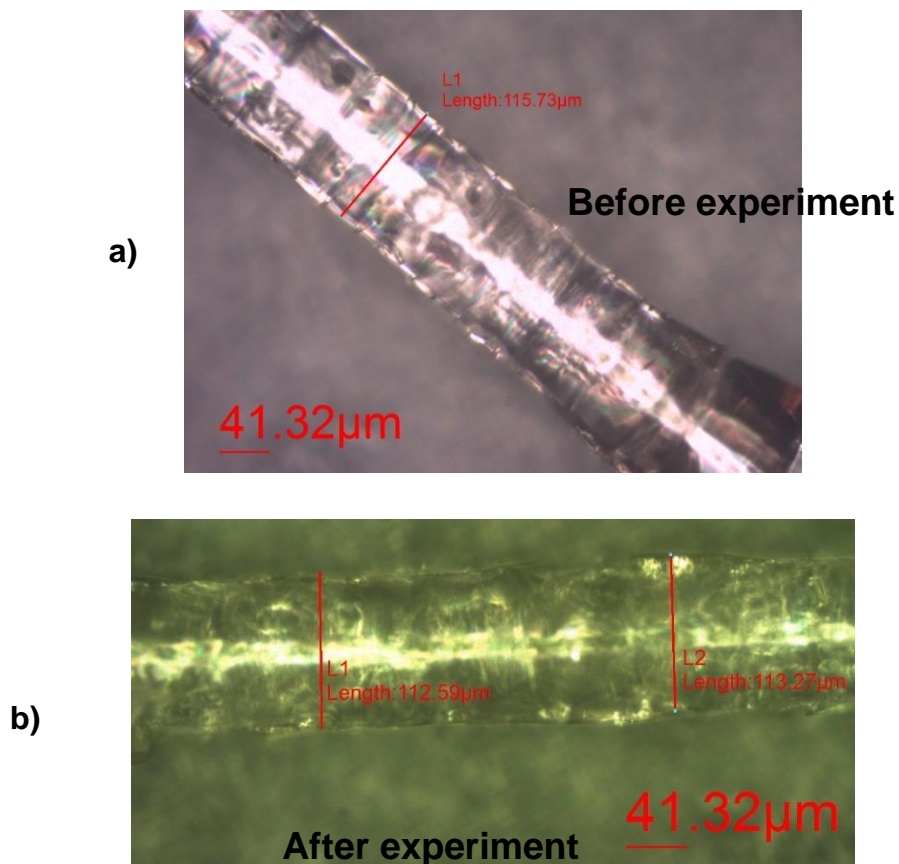
Figure 6.9: The micrographic image of AgNp/silica coating (a) before and (b) after the experiment at a pressure of 1 bar (g) using deionised water.

A micrographic inspection was conducted to compare the diameter of the coated optical fibre before and after the HTHP tests carried out at a constant pressure of 1 bar (g). The findings of this comparative analysis are visually represented in Figure 6.9. An initial application of coating material around the core of the optical fibre resulted in a diameter of 115 microns. Figure 6.9 illustrates that after temperature (and pressure) cycles, the observed diameter of the optical fibre measures approximately 112 microns. Notably, the coating thickness has decreased by approximately 1.5 microns, showing that dissolution had taken place.

To facilitate a more comprehensive examination of the coating's stability, a series of experiments were conducted, involving three successive cycles of heating and cooling, each performed under a pressure of 1 bar (g).
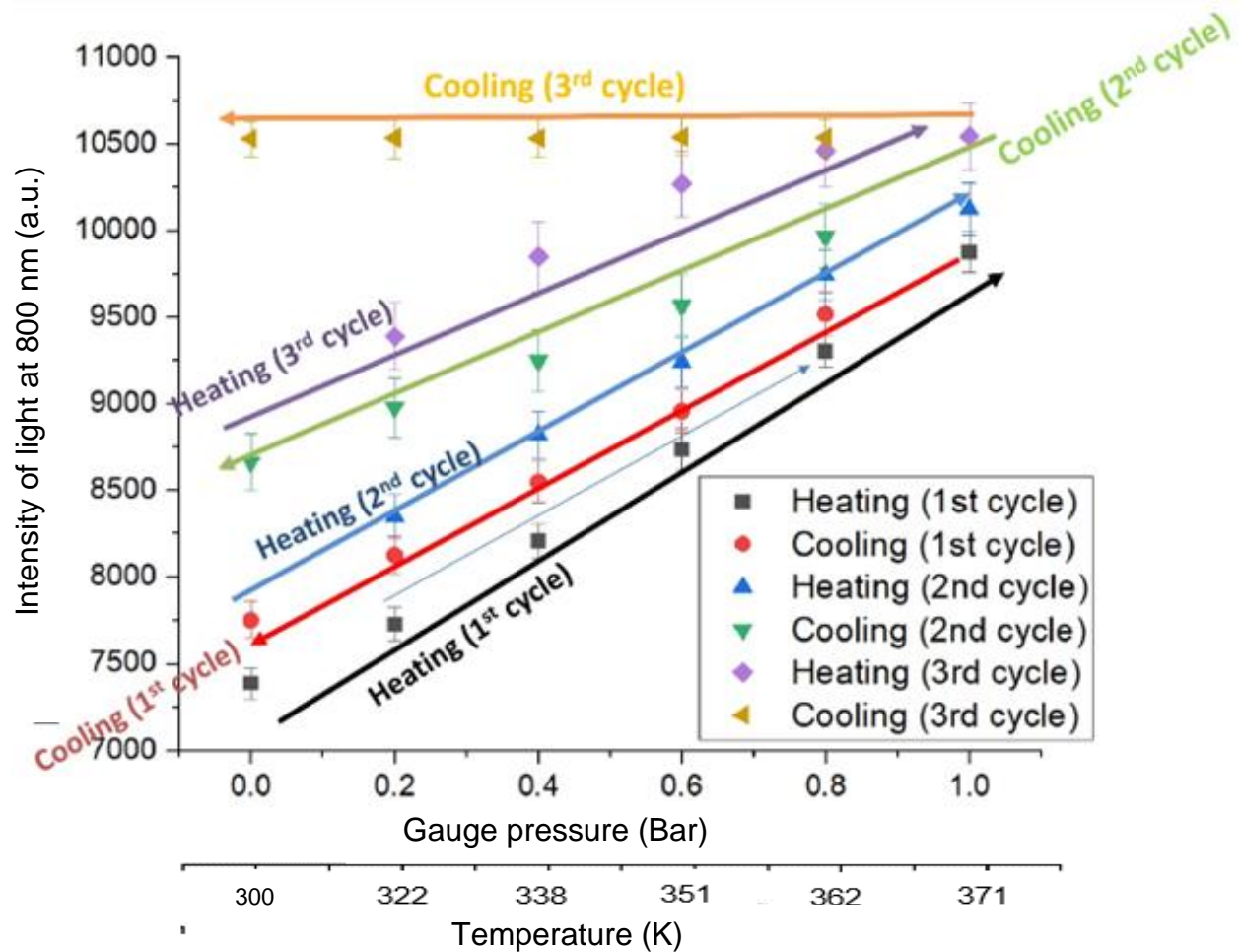
Figure 6.10: Results showing the stability of AgNp/silica coating at pressure 1 bar (g) for multiple cycles using deionised water.

A series of heating and cooling cycles were conducted thrice on the same optical fibre, as illustrated in Figure 6.10. Throughout this test, a progressive increase in light intensity is observed during each heating cycle and cooling cycle. During the third heating cycle, a significant reduction in sensitivity was notably observed when compared to the preceding cycles. Remarkably, after the completion of this third heating cycle, there is no change in the intensity of light, showing that optical properties were lost. It was found that the loss of sensitivity is due to the dissolution of the coating. The experiment conducted at 1 bar (g) provides evidence that

elevated temperatures and pressures contribute to the dissolution of the AgNp/silica coating.

In summary, it can be concluded that the AgNp/silica coating was affected by dissolution at high pressure and high temperature. Complete dissolution was observed when the experiment was conducted at 5 bar (g). Subsequently, when the pressure was reduced to 2 bar (g), it was observed that the sensor continued to work for the second cycle, although there was reduced sensitivity after the first cycle. Moreover, when the experiment was conducted at a pressure of 1 bar (g), a lower rate of dissolution on the coating was observed, allowing for the conduct of 3 cycles of the experiment. Gradual decreases in sensitivity were observed after each cycle, including the heating and cooling. This phenomenon can be attributed to the partial dissolution of the coating material, which occurred during the experiment. It is evident that at lower pressures, the dissolution of the coating occurs at a slower rate compared to conditions at 2 bar (g) and 5 bar (g) of pressure.

6.2.2.4 Effect of Pressure and Temperature on optical properties in different chemical environments

In this section, the AgNp/silica-coated optical fibre is assessed under different chemical conditions, such as acidic, basic, and artificial seawater. These experiments will provide a better understanding of the stability of the AgNp/silica coating under high-temperature and high-pressure (HTHP) conditions. All experiments will be conducted at a pressure of 2 bar (g).

6.2.2.4.1 Experiment at a gauge pressure of 2 bar in a basic solution of pH 9 prepared with sodium hydroxide

In the context of high-temperature and high-pressure (HTHP) studies, an investigation was undertaken to assess the stability of a composite coating of AgNp/silica when exposed to a basic solution. Similarly, optical fibres coated with the aforementioned AgNp/silica composite were subjected to experimental conditions involving a gauge pressure of 2 bar, involving cyclic heating and subsequent natural

cooling process, all conducted under ambient pressure conditions of 0 bar (g), as shown in Figure 6.11. This section's primary objective is to evaluate the stability exhibited by optical fibres coated with AgNp/silica when immersed in a basic solution with a pH level of 9. The solution of pH 9 was prepared using the sodium hydroxide.
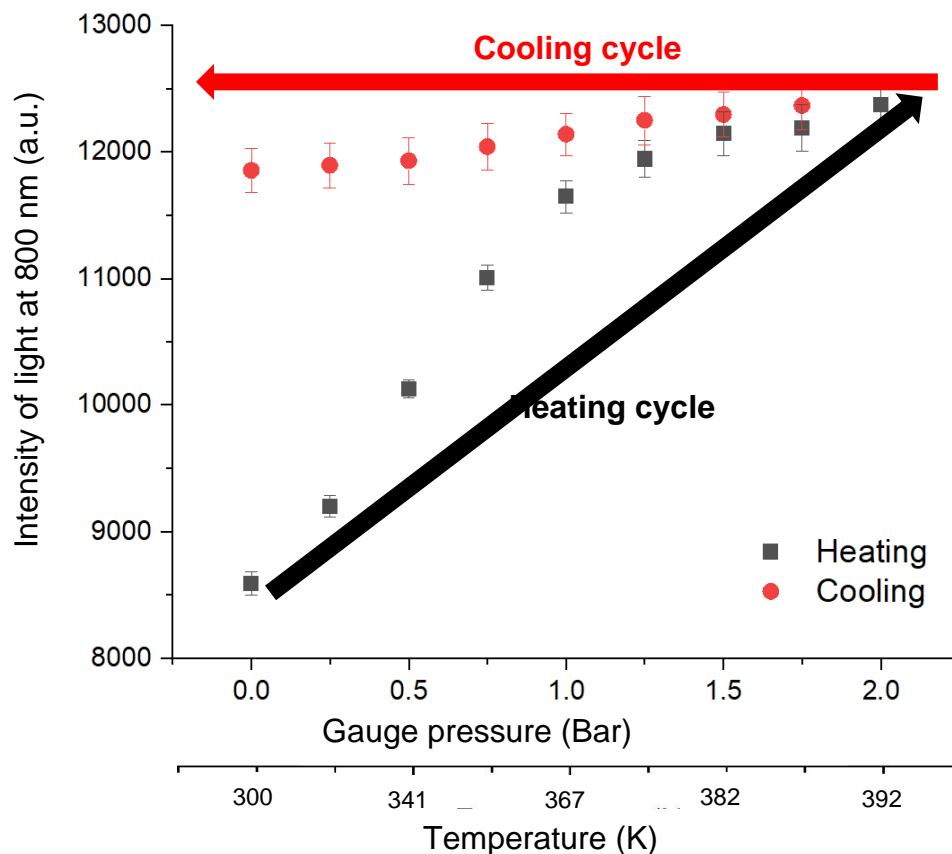
Figure 6.11: Results showing the stability of AgNp/silica coating at a pressure of 2 bar (g) using a base solution of pH 9 prepared from sodium hydroxide.

Figure 6.11 is a representation of the experimental results, in which the gauge pressure was systematically increased to 2 bar throughout the heating cycle, associated with measurements of light intensity taken at a wavelength of 800 nm. The acquired data revealed an interesting trend in the behaviour of light intensity during the heating cycle. Specifically, it was observed that light intensity exhibited a consistent increase up to the pressure of 1 bar (g). Beyond this point, the rate of change in intensity exhibited a diminishing trend, suggesting increased instability at this point. The experiment was to continue until the pressure reached a pressure of 2 bar (g).

Subsequently, during the cooling phase, a minimal response was observed, accompanied by a larger error margin. This reduction in sensitivity was indicative of a substantial degree of coating dissolution during the heating phase. It is worth noting that the etching of the optical fibre in this research necessitated the utilisation of a concentrated sodium hydroxide solution, as previously discussed in the preceding chapter. Remarkably, as the temperature of the sodium hydroxide solution was elevated, an observable correlation emerged between temperature and etching rate. Higher temperatures increased the aggressiveness of the sodium hydroxide solution, leading to an increase in the dissolution rate of the coating material.

Furthermore, a comprehensive micrographic analysis was conducted to assess the diameter measurements of the optical fibre before and after the experimental procedure. These analyses will be discussed in the subsequent paragraphs of this section and the subsequent section.
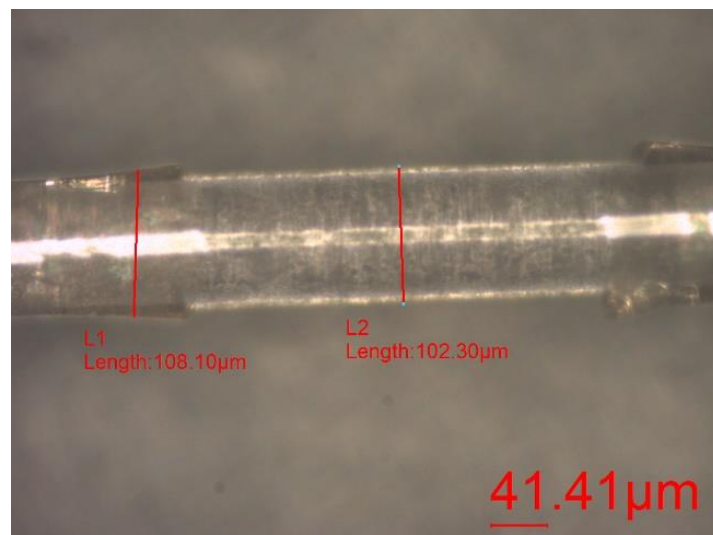
Figure 6.12: The micrographic image of AgNp/silica coating after the experiment at a pressure of 2 bar (g) using an alkali with a pH of 9 prepared using sodium hydroxide.

A micrographic examination was conducted to assess the post-HTHP experimental changes in the diameter of the coated optical fibre, specifically at the gauge pressure of 2 bar. The micrographic representations of the diameter of optical fibre are presented in Figure 6.12. From the results, it could be observed that in certain segments of the optical fibre, the diameter was about 108 microns. However, in other regions, a complete dissolution of the coating was evident. It is noteworthy that the dissolution process was not uniformly distributed across the entire surface of the

coating. This non-uniform dissolution pattern can be attributed to the pronounced aggressiveness exhibited by sodium hydroxide under HTHP conditions, which substantially augmented the rate of dissolution.

6.2.2.4.2 Experiment at a gauge pressure of 2 bar in an acidic solution with a pH of 5 prepared using phosphoric acid

In this section, an examination was conducted to assess the stability of the AgNp/silica coating under a pressure of 2 bar (g) within an acidic solution of pH 5, which was prepared using phosphoric acid, as depicted in Figure 6.13. The primary objective of this experimental investigation was to assess the stability of the AgNp/silica-coated optical fibre under various chemical conditions. This effort aims to provide a comprehensive understanding of the limitations of the coating and its implications for sensor performance.
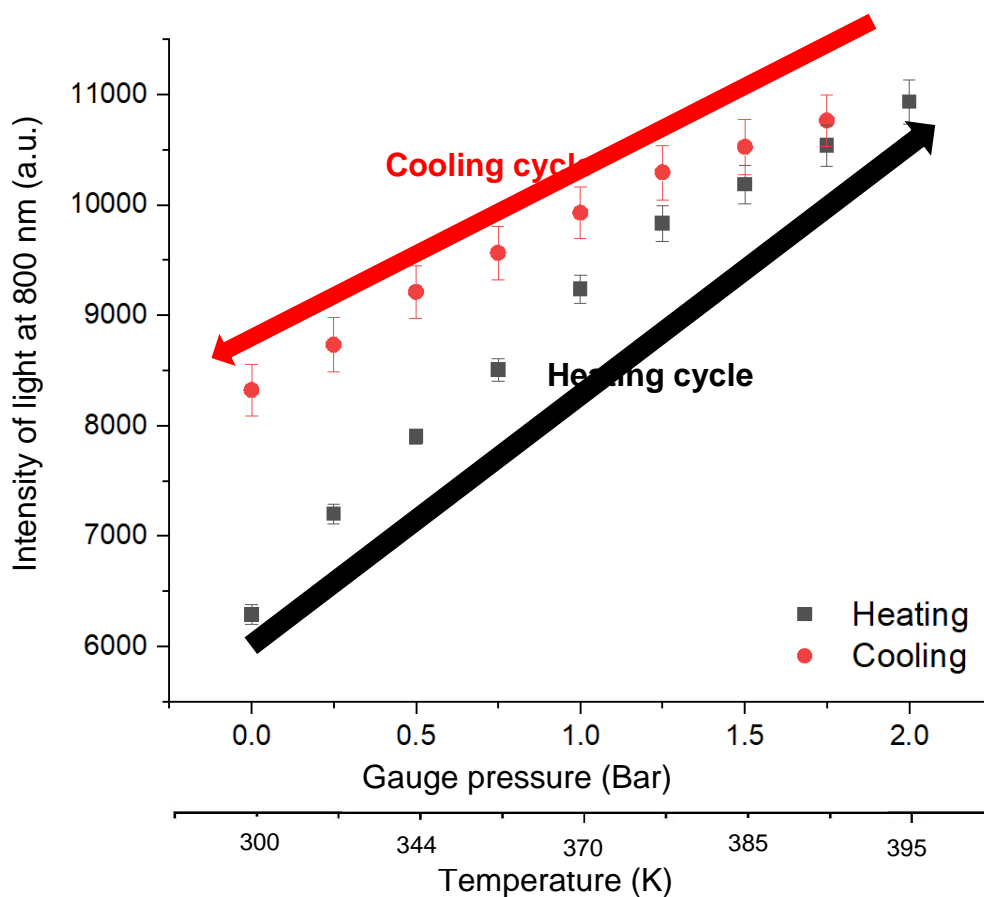
Figure 6.13: Results showing the stability of AgNp/silica coating at a pressure of 2 bar (g) using an acidic solution of pH 5 prepared using phosphoric acid.

Figure 6.13 provides the results of the observed changes in light intensity at a wavelength of 800 nm under the HTHP experiment at a pressure of 2 bar (g). Specifically, this investigation was conducted at a pressure of 2 bar (g), employing a solution with a pH of 5, in which phosphoric acid was used. The results revealed a distinctive pattern in the behaviour of light intensity throughout the heating cycle, notably stabilising at the pressure of 2 bar (g). At this point, the intensity of light, as measured at a wavelength of 800 nm, was recorded to be 6289 units.

The cooling cycle was executed after the heating phase, during which the pressure was gradually decreased. A decline in light intensity was noted with the reduction in pressure. The intensity of light reached 8321 units when the pressure had receded to 0 bar (g), marking the completion of the cooling cycle. Notably, the observed light intensity did not revert to its initial value, signifying the occurrence of coating dissolution. Importantly, it is worth noting that the degree of dissolution observed in this study was not as severe as that encountered in a comparative investigation employing a base solution with a pH level of 9.

To further elucidate the findings of this experiment, a comprehensive micrographic analysis was conducted, encompassing measurements of diameter both before and after the experimental procedures. Further discussions explaining their implications will be presented in the subsequent sections.
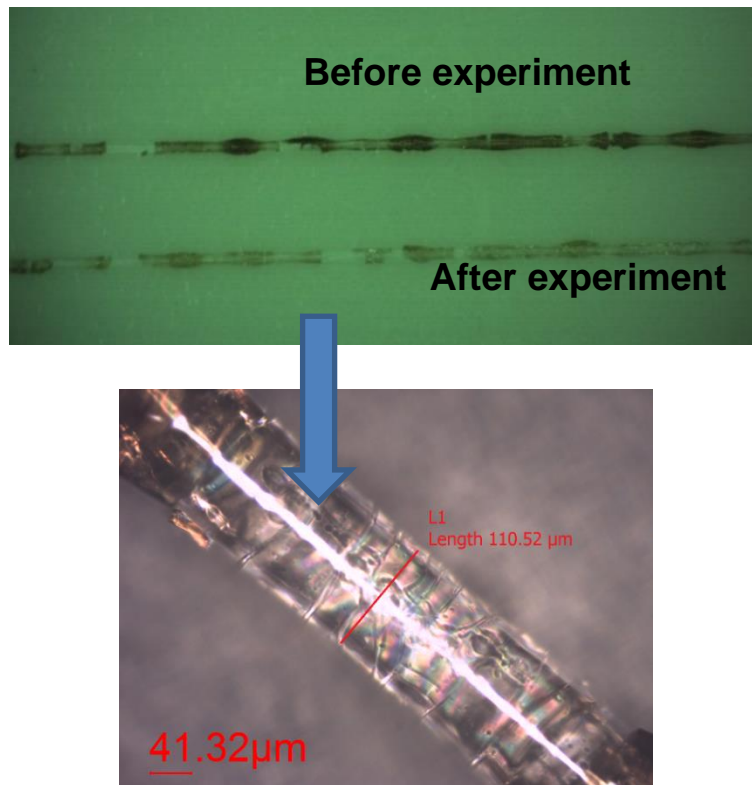
Figure 6.14: The micrographic image of AgNp/silica coating after the experiment at a pressure of 2 bar (g) using an acidic solution of pH 5 prepared from phosphoric acid.

A micrographic examination was conducted to assess the diameter of the coated optical fibre both before and after subjecting it to an HTHP test at a pressure of 2 bar (g), employing a pH 5 acidic solution containing phosphoric acid. The micrographic representations of this investigation are provided in Figure 6.14. Following the experiment, it was ascertained that the optical fibre's diameter measured approximately 110 microns. Notably, the dissolution rate in the acidic solution closely resembled that observed during experiments conducted with deionised water. Conversely, the dissolution of the AgNp/silica coating was more pronounced in the alkaline solution when compared to the acidic solution and deionised water.

6.2.2.4.3 Experiment at a gauge pressure of 2 bar using artificial seawater

This section aims to evaluate the performance and stability of an optical fibre coated with AgNp/silica under more realistic chemical conditions, aligning with the envisaged application of this sensor within the oil and gas industry. The primary objective of this experiment was to provide an insightful assessment of the stability exhibited by the AgNp/silica coating when subjected to an environment simulating artificial seawater. This is crucial for understanding the behaviour of the AgNp/silica-coated optical fibre in conditions representative of its intended use.

Figure 6.15 presents the results showing the stability of the AgNp/silica coating when subjected to a pressure of 2 bar (g) within an artificial seawater environment. The composition of the artificial seawater adhered to the ASTM standard D1141-98, with a formulation involving the addition of 0.613 M of NaCl, 54.65 mM of $MgCl_2 \cdot 6H_2O$, and 28.82 mM of Na_2SO_4 to deionised water, thus replicating a close composition of the salinity and ionic composition of natural seawater.

Prior to subjecting the AgNp/silica-coated optical fibre to artificial seawater conditions, other experiments were carried out to assess the performance of the coating in distinct environments. These included deionised water with a pH of 6.3, an acidic solution with a pH of 5, and an alkaline solution with a pH of 9. These diverse chemical conditions were selected deliberately to facilitate a comprehensive comparative analysis of the stability of the optical fibre coated with AgNp/silica. By conducting these experiments under various chemical conditions, valuable insights into the limitations inherent to both the coating material and the sensor itself could be obtained. This holistic approach to investigating the stability of the AgNp/silica-coated optical fibre contributes to a deeper understanding of its performance characteristics, ultimately advancing our knowledge of its potential applications within the oil and gas industry.
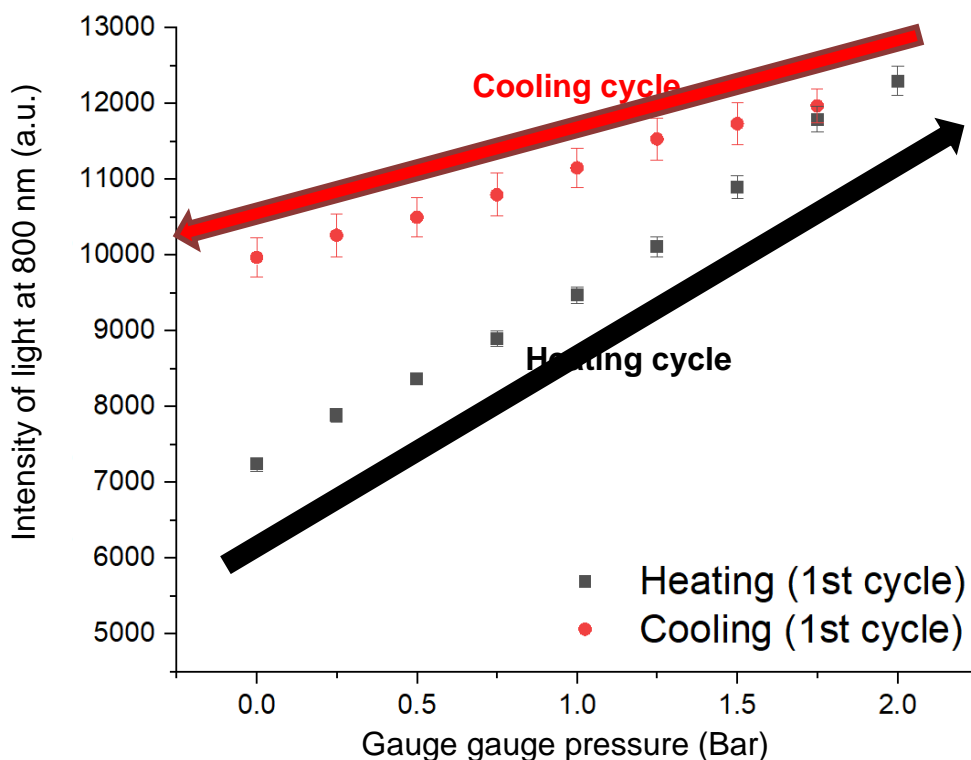
Figure 6.15: Results showing the stability of AgNp/silica coating at a pressure of 2 bar (g) using artificial seawater.

The findings from these observations are visually represented in Figure 6.15. This result illustrates that a discernible alteration in light intensity occurred at a wavelength of 800 nm when an artificial seawater solution was used at a pressure of 2 bar (g). The data reveals a consistent change in light intensity throughout the entire duration of the heating cycle, reaching a peak intensity of 7235 units at the 800 nm wavelength.

Subsequently, as the system transitioned into the cooling cycle, a noticeable decline in light intensity was observed with the reduction in pressure. On completion of the cooling cycle, the light intensity was recorded at 9967 when the pressure had returned to 0 bar (g). This outcome suggests that the coating had undergone dissolution, as the intensity did not revert to its initial state. Nevertheless, it is important to note that a substantial portion of the coating was dissolved in acidic conditions or deionised water environments. A comprehensive examination of the diameter measurements through micrographic analysis conducted both before and after the experimental procedures is shown in Figure 6.16. This analysis was

conducted pre- and post-experimentation, enabling a thorough evaluation of the dissolution of the coating.
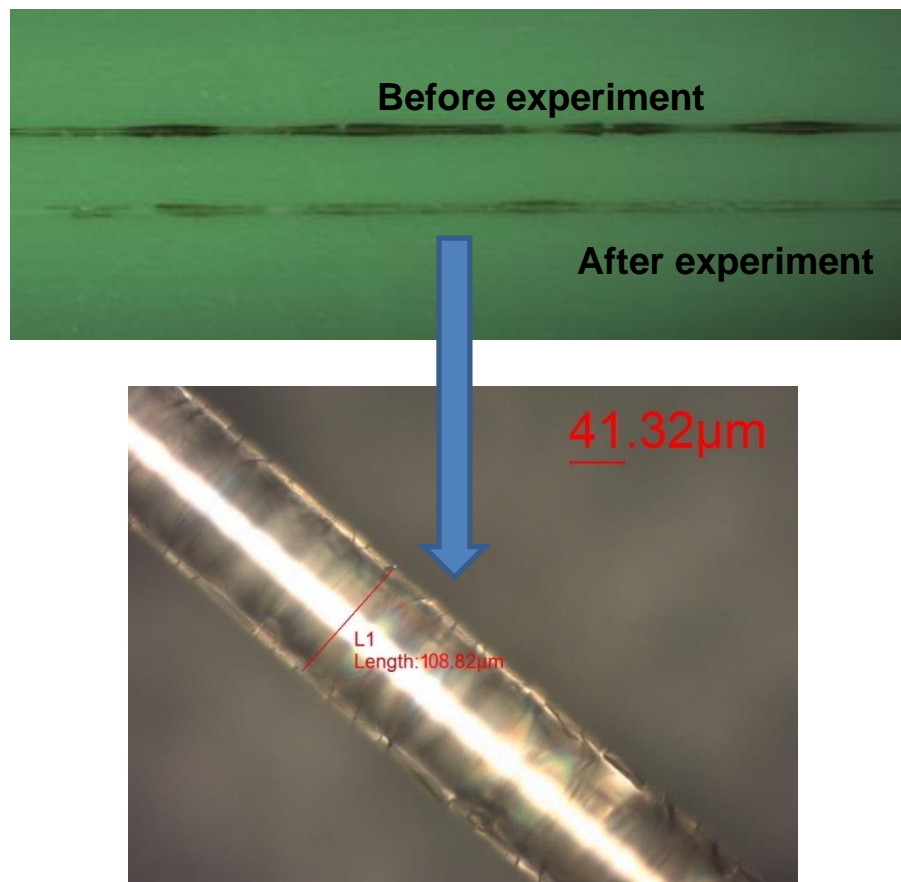
Figure 6.16: The micrographic image of AgNp/silica coating after the experiment at a pressure of 2 bar (g) using artificial seawater.

A micrographic inspection of the coated optical fibre was carried out both before and after the HTHP experiment, which was carried out at a pressure of 2 bar (g) in artificial seawater. This was carried out to determine the diameter of the coated optical fibre. The micrographic images can be seen in Figure 6.16, and the results of the experiment showed that the diameter of the optical fibre was approximately 108 microns in diameter. It seems that the dissolution was almost the same as the average, which is higher than what was demonstrated in the experiment that employed deionised water or acidic water. The alkaline solution demonstrated the largest degree of dissolution of the AgNp/silica coating, in contrast to the results of any other trials that were conducted using an acidic solution, seawater, or deionised water.

6.2.3 Experiment at a temperature of 323 K (50 °C)

Previous tests were conducted using specialised equipment designed for optical pH measurements under controlled room temperature conditions. In this section, the experimental protocol involved a controlled heating of the solution to maintain a constant temperature of 323 K (50 °C). This was achieved by adding phosphoric acid (H_3PO_4) and sodium hydroxide (NaOH) to the solution, allowing for a precise manipulation of its pH levels. The selection of a temperature of 323 K (50 °C) for the duration of the experiment over three consecutive days was driven by the observation that higher temperatures and pressures led to increased dissolution of the coating material.

In addition, a potentiometric pH probe was integrated into the apparatus within this experimental setup. This integration enabled continuous monitoring of the pH levels within the solution through the use of the potentiometric pH probe. Due to the fact that the system had a maximum 8 number of usable parts, a high-pressure closed-lid system was not implemented in the conducted experiments. Given the relatively low experimental temperature, pressure measurements are anticipated to be within 1 atm. The principal objective of the project was to analyse the dissolution or loss of coating under reduced temperature conditions. Consequently, this approach facilitated the investigation into the stability of the AgNp/silica-coated optical fibre pH sensor under the specific conditions of 323 K (50 °C), as illustrated in Figure 6.17.

The stability of the pH sensor based on AgNp/silica-coated optical fibres was systematically investigated through a series of experiments conducted at a temperature of 50 °C over three consecutive days, as shown in Figure 6.17. Results indicate that on the initial day of experimentation (day 1), the sensor exhibited a consistent and reproducible optical response about variations in pH, with a small variability as illustrated by the error bar. Specifically, on day 1, the average light intensity was found to vary by 875 units per pH change.

However, as the experiment progressed to day 2, a significant decline in the average light intensity per unit pH change was observed, with the value decreasing to 824 units per pH, and it is 6 % less sensitivity compared to the first day. Furthermore, the error bars associated with the data points noticeably expanded on day 2, suggesting increased variability and uncertainty in the measurements. This downward trend in

both the average change in light intensity and the increased error bars continued into day 3, where the average change in intensity further reduced to 768 units per pH change, which is 12 % less sensitivity from the first day. Similarly, the data collected on day 3 displayed an even greater degree of variability, as reflected by the large error bars.
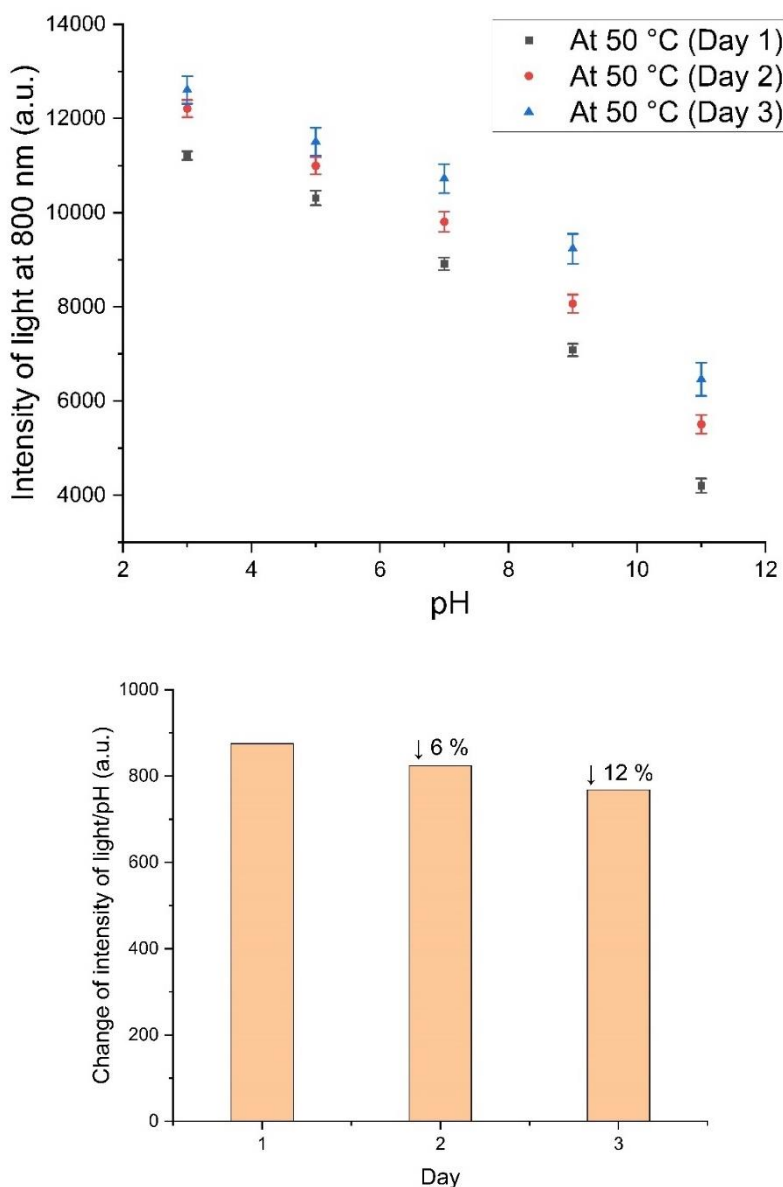
Figure 6.17: (a) Results showing the stability of AgNp/silica coated optical at the temperature of 50 °C, (b) showing changes in the sensitivity for 3 days.

The stability experiment conducted at room temperature, as explained in section 5.3, revealed a sensitivity decline on a daily basis due to the dissolution of the coating. Additionally, a similar sensitivity decline was observed when experiments were

conducted at a temperature of 323 K (50 °C). The key difference between these two experiments is the higher rate of sensitivity decline observed at 323 K compared to room temperature. At room temperature, there was a 2% reduction in sensitivity, while at 323 K, the sensitivity was reduced by 6%. Furthermore, a 9% reduction in sensitivity was observed at room temperature, whereas a 12% reduction was noted at 323 K. These observed changes in the sensor's performance are consistent with the findings discussed in the preceding chapter, which highlighted the susceptibility of the AgNp/silica coating to dissolution when exposed to aqueous systems. Interestingly, experiments conducted at an elevated temperature of 323 K appeared to accelerate the dissolution process, as indicated by a significant reduction in the rate of change in intensity. This suggests that higher temperatures may exacerbate the dissolution rate compared to what was observed under room temperature conditions. Further analysis and investigation are needed to comprehensively understand the underlying mechanisms driving this phenomenon.

6.2.4 Comparison of stability of AgNp/silica coating with similar studies in the literature

This section compares the stability of AgNp/silica under high temperature and high pressure (HTHP) conditions in various chemical environments with similar reports available in the literature. Notably, the existing literature on this subject matter is limited, thereby necessitating a reliance primarily on our empirical findings rather than drawing extensive comparisons with prior research. However, it is pertinent to mention that a recent study by Spitzmüller *et al.* [270] has contributed valuable insight into the stability of silica coating, particularly within a pH range ranging from 3 to 11. Their work elucidates the profound influence of solution pH on the dissolution rate of silica coatings. Specifically, their observations indicate that acidic solutions (pH 3 to 6) induce only minimal dissolution of silica, whereas solutions with a pH between 7 and 9 exhibit a moderate level of dissolution. Importantly, higher pH values correspond to a more pronounced rate of silica coating dissolution.

This investigation, conducted under HTHP conditions, yielded results that are similar to those of Spitzmüller *et al.* [270] Moreover, in this study, it was possible to quantify the change in coating diameter before and after exposure to HTHP conditions, which

provided the rate of the dissolution of the coating during these trials. Consequently, it was possible to compare the dissolution rates using three distinct media: deionised water, an acidic solution with a pH of 5, and an alkaline solution with a pH of 9. The rate of dissolution was found to be equivalent in both the acidic solution and deionised water, showing that pH 5 does not significantly affect the dissolution rate at room temperature. Conversely, the utilisation of an alkaline solution with a pH of 9 led to a higher dissolution rate. These findings corroborate the observations reported by Spitzmüller et al. [270].
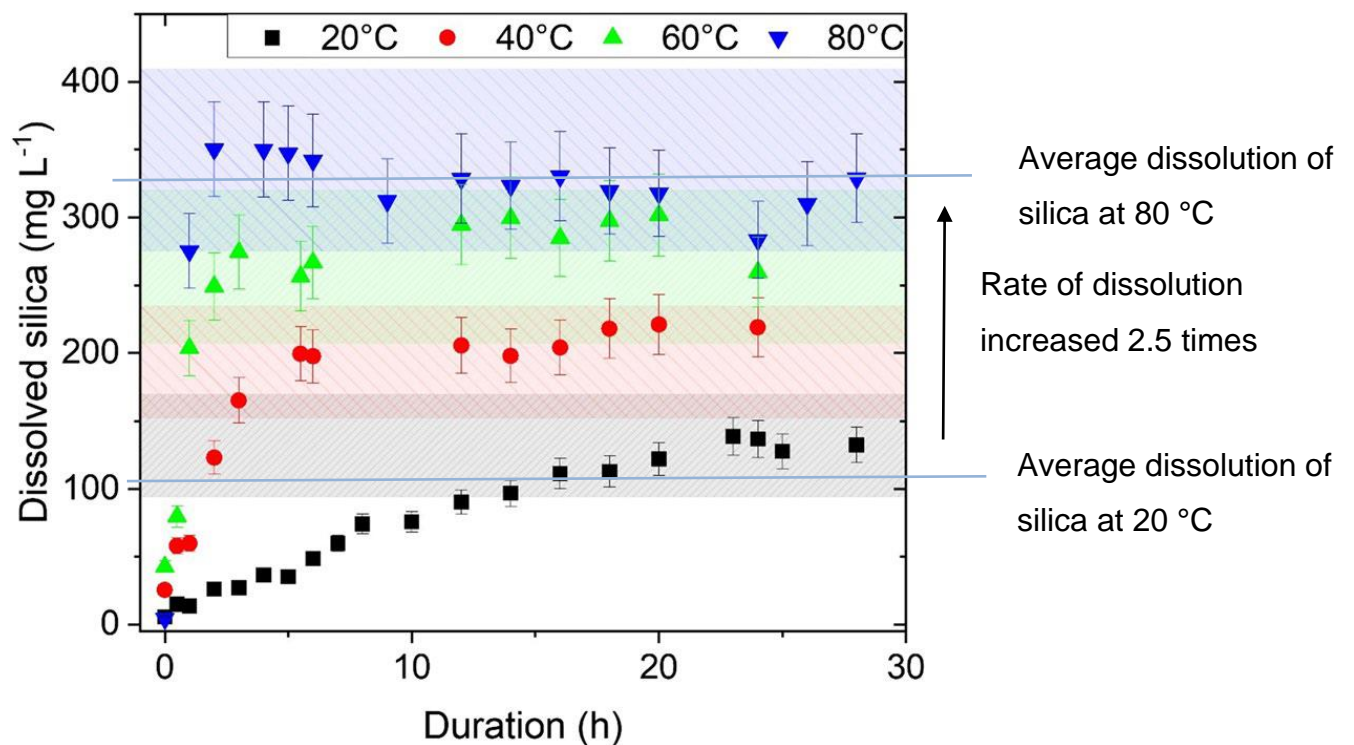
Figure 6.18: The data showing the dissolution of silica at higher temperatures [270].

As illustrated in Figure 6.18, Spitzmüller *et al.* [270] also investigated the dissolution rate at elevated temperatures, reaching up to 80°C. Their results demonstrated a substantial increase in the dissolution rate at higher temperature, almost 2.5 times higher at 80°C compared to 20°C. Numerous scholarly works have documented a recurring observation about enhancing dissolution rates concomitant with elevated solution temperatures [271–273]. Our observations align with the established understanding in the literature that silica dissolution rates generally escalate with increasing temperature. Consequently, it is reasonable to anticipate even greater

dissolution rates when temperatures reach 100°C and 150°C. In our investigation, a similar temperature-dependent trend was observed. At ambient temperature, there was only minimal dissolution of the coating. However, as the temperature increased to 50°C, a slight increase in the dissolution rate was observed, which was further magnified at 100°C and 150°C. With rising temperatures, a gradual but consistent acceleration in the rate of dissolution became evident.

The literature indicates that silica dissolves at room temperature [231,234,274,275], but there is limited information available at higher temperature. Since silica dissolution occurs at room temperature, it was anticipated that this process would accelerate at elevated temperatures. Furthermore, the dissolution rate was expected to be significantly higher in alkaline solutions due to the presence of aggressive hydroxyl groups, which break the silica bonds at higher temperatures. This observation was consistent with the etching process of the fibre coating in this research, where higher concentrations of hydroxyl solutions were used as etching agents. Consequently, it was noted that the etching rate of optical fibres increased with rising temperatures. Therefore, it was observed that the dissolution rate of the AgNp/silica coating in alkaline solutions at higher temperatures and pressures was higher than that in acidic solutions and deionised water. In summary, the findings are consistent with both Spitzmüller *et al.* [270] and the broader literature, demonstrating the influence of pH and temperature on the dissolution rate of silica coatings, particularly under HTHP conditions.

Wang *et al.* [158] also reported pH data at 80 °C (353 K) using the AuNp/silica coating. They recorded the transmittance at 550 nm while changing the pH in the solution, as shown in Figure 6.19. In their report, AuNp/silica-coated optical fibres were used, while this study utilised AgNp/silica-coated optical fibres as the pH sensor. Although the author did not report any information about the dissolution of the coating as a limitation, their data reveal a loss in the intensity of light, which, according to the findings of the current work, is caused by the dissolution of the coating. As shown in Figure 6.19, at the beginning of the experiment, the transmission was 0.60 for a pH of 5.52, but after 1700 seconds, when the pH of the solution was 5.60, the transmission increased to 0.80. Similar findings for AgNp/silica

coating were observed in the current research, and it was revealed that the reduction in sensitivity was due to the dissolution of the coating. As a result, the sensor lost its sensitivity, and this is why the intensity of light could not return to its original position. Wang *et al.* [158] have not reported on the stability, durability or lifetime of their AuNp/silica fibre optic sensors.
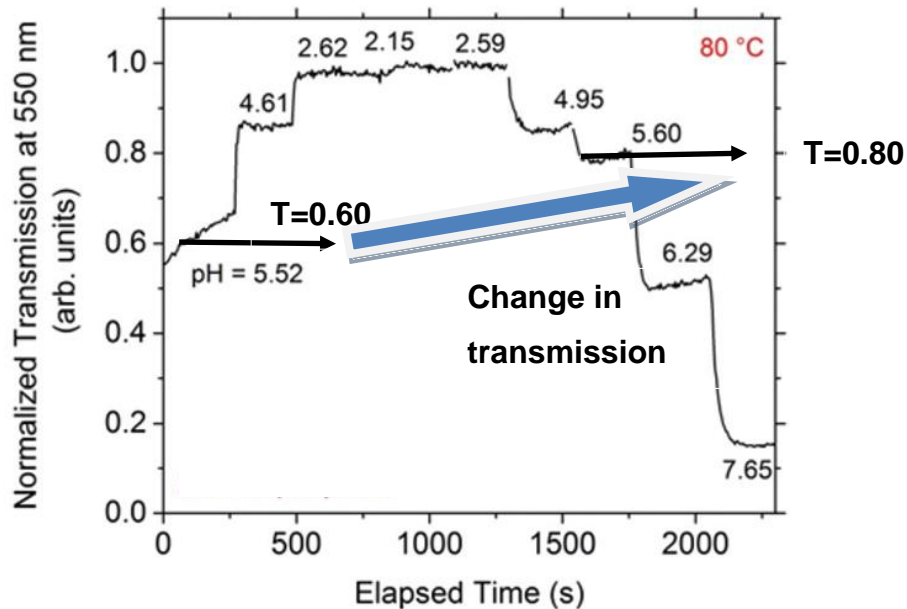
Figure 6.19: A plot showing the change in transmission at randomly varied pH levels using an Au/silica-coated optical fibre at 80°C (353 K) [158].

6.2.5 Proposed model of dissolution of AgNp/silica coating

As discussed in the previous section, a higher dissolution rate was observed with increasing pressure and temperature. These HTHP environments could be due to accelerated chemical, mechanical or a combination of their effects. For example, high-pressure conditions can alter the ionic strength of the solution, affecting chemical equilibrium and reactivity. Changes in ionic strength can promote dissolution by influencing the solubility of silica. Furthermore, the pH of the surrounding medium can also play a significant role in the dissolution of silica coatings. Silica is particularly susceptible to dissolution in acidic or alkaline environments. Under high pressure, the concentration of protons (H^+) or hydroxide ions (OH^-) changes, altering the pH of the solution and impacting the stability of the silica coating.

Furthermore, reaction rates are well known to increase exponentially with increasing temperatures. High-pressure environments might impose mechanical stress on the silica coating. Cracks were observed on the coating when examining the surface using SEM. This external mechanical stress can weaken the coating, accelerating the overall dissolution process of the AgNp/silica coating on the optical fibre. A model illustrating the dissolution of the coating in a high-pressure, high-temperature (HTHP) environment is shown in Figure 6.20.
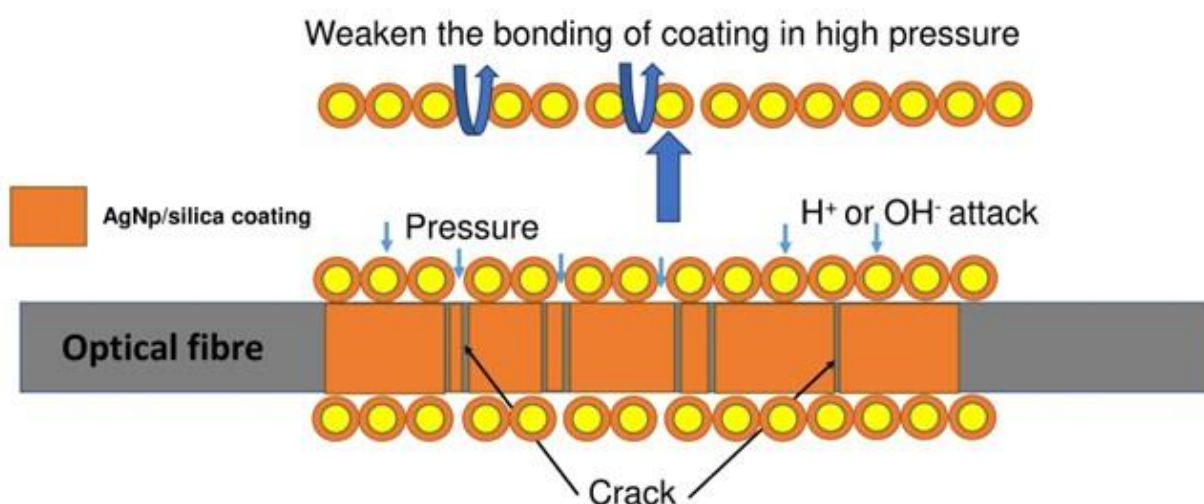
Figure 6.20 : Proposed mechanism for the dissolution of AgNp/silica coating under high pressure conditions.

6.3 Conclusion of this chapter

In this chapter, the stability of the AgNp/silica-coated optical fibre in high temperature, high pressure (HTHP) environments was explored. A set of pH measurements with increasing temperatures showed that it can significantly influence the equilibrium of the solution. Specifically, increasing the solution's temperature promotes the forward reaction, resulting in a more favourable equilibrium. This phenomenon is attributed to the well-established effect of temperature on pH equilibria. Consequently, an increased quantity of protons (H^+) is generated, leading to a discernible shift in the solution's pH towards lower values.

HTHP experiments for investigating the stability of AgNp/silica coating showed dissolution of the AgNp/silica coating was observed. This dissolution was observed consistently across all trials, impeding the ability of accurate pH measurement. Notably, when the solution temperature was raised, there was a corresponding increase in the dissolution rate of the AgNp/silica coating. The coating exhibited better stability at lower temperatures, such as 50 °C, compared to that at 100 °C or 150 °C. The temperature increase was directly correlated with an augmentation of dissolution. It was also noted that the rate of dissolution varied depending on the chemical environment.

The dissolution rate was increased when the solution was more in alkaline solution. The mere presence of this alkaline medium brought about a significant acceleration in the dissolution process. This acceleration was primarily attributed to the heightened concentration of hydroxyl ions in the solution. Hydroxyl ions are well known to react and dissolve. Consequently, the dissolution rates in this media were much greater than those in deionised water and acidic solution. Further results were noted when the experimental setup incorporated artificial seawater at a gauge pressure of 2 bar. Under these conditions, the dissolution of the coating exhibited an acceleration compared to deionised water but less than the alkaline solution.

Throughout this HTHP studies, measurements were constrained by the dissolution of the AgNp/silica coating. This posed a considerable obstacle in the ability to establish an optical calibration for pH measurements. Constructing a reliable calibration curve necessitates obtaining a consistent, repeatable, and reliable optical signal, which was not possible. The dissolution of the coating, induced by the rigorous heating and cooling cycles associated with HTHP conditions, resulted in significant variation in the intensity of the emitted light. Consequently, the assessment of the sensitivity of the pH sensor sensitivity under HTHP conditions remains a challenge, given the inherent limitations of the coating.

It is worth noting that a prior study reported the use of an AuNP/silica-based optical fibre sensor that operated effectively at a temperature of 80 °C, with no mention of any issues related to coating dissolution as a limitation [158]. Their own data reveal that the transmission was changed at the same pH.

The sensor faced a significant challenge due to the dissolution of its coating. Originally designed to operate effectively under high temperature and high pressure (HTHP) conditions, it displayed promising performance at room temperature, particularly within the pH range of 5 to 9. The susceptibility of the sensor to extreme pH values, either very high or very low, accelerated the dissolution process. Addressing the dissolution issue through future research could potentially unlock the full potential of sensors for HTHP applications.

In conclusion, this investigation into the stability of the AgNp/silica-coated optical fibre in HTHP environments has illuminated the pivotal role of temperature in altering the equilibrium of the solution and, consequently, the pH level. Furthermore, the dissolution of the coating, notably influenced by temperature and chemical environment, emerged as a predominant constraint in our HTHP studies, rendering the establishment of an optical calibration for pH measurements in these conditions a formidable undertaking.

CHAPTER 7 : Conclusion and Future Work

Chapter 7: Conclusions and Future Work

7.1 Conclusions

This study focused on the preparation of an AgNp/silica-based sensor that could be used to measure the pH of solutions. Initially, the primary goal was to develop an optical fibre pH sensor capable of functioning effectively in high-temperature and high-pressure (HTHP) environments, specifically tailored for the demanding conditions of the oil and gas industry. This attempt was prompted by the lack of a reliable method for pH measurement in such settings. The first major challenge experienced was selecting the appropriate materials, while the second challenge involved adapting optical fibres for this purpose. A prior research effort had been reported using an optical fibre pH sensor, functioning at 80 °C, using an AuNP/silica coating. This research served as the state-of-the-art, offering a promising approach [90,94,95]. However, given the high expense of gold, it was necessary to explore other options, such as the potential of replacing gold with silver nanoparticles, which is considered to be a more cost-effective alternative. Incorporating silver nanoparticles within a silica matrix for pH sensing was a completely new area which has not been investigated before and represents a novel area of interest.

The initial stages of this project were characterised by the preparation of colloidal silver nanoparticles and silica gel as separate entities. The stability of the colloidal silver nanoparticle solution was of a requirement, and this was successfully achieved by employing sodium borohydride as the reducing agent and tri-sodium citrate as the stabilising agent. In parallel, the preparation of silica gel involved the use of tetraethyl orthosilicate (TEOS) as the precursor of silica, in conjunction with ethanol and nitric acid serving as catalysts. These preliminary steps laid the foundation for the subsequent development of the AgNp/silica composite.

In the initial attempt, the integration of silver nanoparticles into silica gel failed to yield a satisfactory AgNp/silica coating with requisite adhesion to the glass slide substrate. This inadequacy may be attributed to the presence of various chemical agents utilized during the synthesis of silver nanoparticles, which potentially impeded the sol-gel process employed for the preparation of the AgNp/silica coating. However, this problem was solved by employing a sol-gel method and the strategic incorporation of additional silver nitrate and the requisite silica gel, thereby achieving

success in creating a satisfactory AgNp/silica composite. This was achieved by balancing and optimising various factors, including gelation temperature and heat treatment procedures. Maintaining a gelation temperature of 35°C for 48 hours and subjecting the composite to heat treatment at 200°C for 2.5 hours led to an optimal adhesion between the coating and the glass substrate. The thickness of the coating was increased by the introduction of multiple dip-coating cycles to enhance the thickness of the AgNp/silica coating.

The successful incorporation of the AgNp in a silica matrix and the achievement of a significant adhesion of the composite to a glass slide marked a significant milestone in this project. This protocol was then transferred to the preparation of optical fibres. This necessitated precise etching of the fibre core to expose the region where the coating would be applied. In this study, the use of hydrofluoric acid (HF) for etching purposes [90,94,276,277] was replaced by 7 M sodium hydroxide (NaOH) at 125 °C, offering a safer alternative.

A series of optimization experiments conducted in this study explained that a core diameter ranging between 103 to 105 microns constitutes a pivotal factor in achieving the desired pH sensitivity for measurement purposes. This specific range of core diameter facilitates the retention of an optimal quantity of light within the optical fibre, thereby facilitating crucial interactions between the AgNp/silica coating and the ions present in the solution. Subsequent to this determination, the configuration of both the light source and detector underwent tuning to maximize sensitivity, a pivotal aspect in optical pH measurements. The delicate equilibrium between the voltage of the light source and the integration time of the detector was calibrated to attain optimal sensitivity. Following numerous iterations, a configuration featuring a light source voltage of 6.5 V and an integration time of 5 ms emerged as the most suitable combination for achieving accurate and sensitive pH measurements within the scope of this study. However, it is essential to note that the observed correlation between core diameter and sensitivity is specific to the optical fibre utilised in this investigation, and may vary with alterations in fibre models. Additionally, the selection of parameters for the light source and spectrophotometer is contextual to this particular research, optimized in consideration of the system's connections and light loss characteristics.

The research then delved into pH measurement using the AgNp/silica-coated optical fibre under ambient temperature conditions. It was shown that the optical response was dependent on the chemical media, even when solutions exhibited the same pH values. This phenomenon was attributed to the interaction between other ions and the AgNp/silica coating. Consequently, the need for individual calibrations when transitioning between different chemical solutions became apparent to ensure the precision and reliability of pH measurements. Among the acids examined, phosphoric acid stood out as the most suitable choice for calibration due to its milder acidic strength and lower dissolution rate of silica.

The incorporation of silver nanoparticles into the silica coating yielded substantial improvements in the consistency and stability of the optical pH sensor. These metallic nanoparticles provided the surface with enhanced charge characteristics, thereby generating data that was remarkably consistent and reproducible. A noteworthy finding was that the silica coating solely could effectively modulate light intensity in response to changes in pH, with the presence of silver nanoparticles enhancing the sensor's reproducibility. The attainment of a reasonable accuracy level, within a range of ±0.5 pH units compared to that determined using potentiometric pH measurement, served as evidence of the response of AgNp/silica-coated optical fibre pH sensor under ambient conditions.

The sensor performance was subsequently evaluated in high-temperature and high-pressure (HTHP) environments. One of our initial objectives was to design an optical fibre pH sensor for such demanding conditions, but this task proved to be challenging. Implementing the optical fibre in high-pressure, high-temperature (HTHP) experiments posed a significant risk due to its fragility. Despite numerous attempts, a laboratory-scale experimental apparatus capable of operating in high-temperature and high-pressure (HTHP) settings was successfully developed using an AgNp/silica coated optical fibre. The pressure vessel were calibrated the temperature and pressure, verifying the results against steam tables. Next, it was investigated the stability and performance of the AgNp/silica coating on optical fibre up to 5 bar.

This research unveiled an imposing challenge, the dissolution of the AgNp/silica coating. As temperatures increased, the rate of dissolution accelerated ultimately resulting in a complete dissolution at 433 K (gauge pressure 5 bar). Stability experiments conducted at a lower temperature of 397 K (gauge pressure 2 bar) highlighted similar dissolution rates, regardless of the presence of deionised water or acidic solutions. However, the introduction of an alkaline solution, particularly artificial seawater, had an accelerated effect on the dissolution process, underlining the coating's vulnerability to differing chemical environments.

The investigation progressed to a phase of durability assessment predicated upon the uniformity of the coating. This phase involved subjecting the AgNp/silica-coated optical fibre to a series of acidic and alkaline conditions. Of particular note was the coating susceptibility to acidic environments, especially those characterized by a pH below 3, which resulted in instances of coating loss [231,234,235,275,278]. Analyses utilizing energy-dispersive X-ray spectroscopy (EDX) provided revealing insights into significant compositional variations, notably alterations in the concentrations of silicon (Si), silver (Ag), and oxygen (O) under acidic conditions. These variations signified the oxidation of silver constituents within the coating. Moreover, scanning electron microscopy (SEM) investigations unveiled surface cracks, prompting valid concerns regarding the coating's structural integrity. The dissolution of the coating in acidic solutions owing to the oxidation of silver nanoparticles, coupled with the observation of surface cracks, posed a risk of coating delamination consequent to inadequate surface adhesion. Despite encountering these challenges, the reproducibility of the optical fibre sensors within the same batch was demonstrated, thereby underscoring the efficacy of the pH measurements via potentiometric pH meters. Regrettably, a decrease in the coating sensitivity over time was observed due to the dissolution phenomenon. Nonetheless, the optical pH sensor exhibited promising responses at ambient temperature, thereby rendering the development of an optical pH sensor under such conditions viable.

7.2 Future work

The following are suggestions for future works that would expand the work further.

- ✓ **Exploring varied optical fibre core sizes:** An intriguing avenue for future research lies in investigating the impact of utilising optical fibres with core sizes of 105 microns. Expanding this exploration to include both larger and smaller core diameters could offer the same insight into how core size influences the sensitivity of the pH sensor. It is conceivable that altering the core diameter might result in adjustments to the interaction between the optical fibre and the AgNp/silica coating. Consequently, this endeavour may yield a broader understanding of the sensor's adaptability to different scenarios and chemical environments.

- ✓ **Incorporating polymeric binders for enhanced stability**: To address the persistent challenge of coating dissolution, particularly at room temperature and under high-pressure, high-temperature conditions, future research could delve into the incorporation of polymeric binders within the gel. These binders may serve as a protective shield, mitigating the vulnerability of the AgNp/silica coating to dissolution. This avenue of exploration holds great promise in fortifying the sensor's durability, even in the face of corrosive chemical environments and extreme conditions. The investigation of suitable polymeric materials and their application within the gel matrix represents an exciting prospect in advancing the robustness of the pH sensor.

- ✓ **Expanding chemical applications for stability assessment:** Beyond the confines of the chemicals previously examined, there lies a rich terrain of diverse chemical solutions that can be explored to comprehensively assess the stability of the sensor. Expanding the scope of chemical applications will provide a more nuanced understanding of how the sensor responds to various environmental factors. Different chemicals, each possessing unique properties and reactivity, may induce distinct behaviours in the sensor. By subjecting the sensor to a broader array of chemical conditions, researchers can develop a comprehensive profile of its adaptability and resilience. This

expansion not only enhances the sensor's versatility but also contributes to its real-world applicability across a myriad of scenarios.

- ✓ **Studying surface morphology and chemistry:** Another avenue for future investigation involves conducting a comprehensive analysis of the sensor's surface morphology and chemistry. Delving into the intricacies of how the surface of the AgNp/silica coating evolves under varying conditions promises a wealth of valuable insights. This exploration can be facilitated through the utilisation of advanced techniques, such as scanning electron microscopy (SEM) and surface analysis tools. By closely scrutinising the dynamics of surface charge and alterations in chemical composition, researchers can achieve a deeper understanding of how the coating interacts with its surrounding environment. Moreover, this research has proposed that the alteration of surface charge, induced by changes in pH, plays a pivotal role in the pH sensing mechanism. Therefore, there is an opportunity to investigate the study of surface charge and its interactions with different ions with the AgNp/silica coating. These analyses may yield critical information that can improve coating stability and sensitivity.

These suggestions not only expand the horizons of the current work but may open doors to exciting possibilities. Investigating varying optical fibre core sizes, introducing polymeric binders, expanding the range of chemical applications, and scrutinising surface morphology and chemistry all represent new avenues for further research.

References

1. Galster H. PH Measurement: Fundamentals, Methods, Applications, Instrumentation. VCH; 1991.

2. Gold V. PH Measurements: Their Theory and Practice. Methuen; 1963. (Methuen's monographs on chemical subjects).

3. Wencel D, Abel T, McDonagh C. Optical chemical pH sensors. Anal Chem. 2014 Jan;86(1):15–29.

4. Lin J. Recent development and applications of optical and fiber-optic pH sensors. TrAC Trends in Analytical Chemistry. 2000;19(9):541–52.

5. Korostynska O, Arshak K, Gill E, Arshak A. Review Paper: Materials and Techniques for In Vivo pH Monitoring. IEEE Sens J. 2008;8(1):20–8.

6. Le Grand HE. Lavoisier's oxygen theory of acidity. Ann Sci. 1972 Jun 1;29(1):1–18.

7. Finston HL, Rychtman AC. A new view of current acid-base theories. 1982;216.

8. Nivaldo J. Tro. Introductory Chemistry. Pearson Education, Incorporated; 2023.

9. Mandeep Dalal. A Textbook of Physical Chemistry Volume 1. Amazon Digital Services LLC - KDP Print US. Amazon Digital Services LLC - KDP Print US; 2018.

10. Khan MI, Mukherjee K, Shoukat R, Dong H. A review on pH sensitive materials for sensors and detection methods. Microsystem Technologies. 2017;23(10):4391–404.

11. Avolio R, Grozdanov A, Avella M, Barton J, Cocca M, Falco F De, et al. Review of pH sensing materials from macro- to nano-scale: Recent developments and examples of seawater applications. Crit Rev Environ Sci Technol. 2022;52(6):979–1021.

12. Dickson AG. The measurement of sea water pH. Mar Chem. 1993;44(2–4):131–42.

13. Raghuraman B, Keefe MO, Eriksen KO, Tau LA, Vikane O, Gustavson G, et al. Real-Time Downhole pH Measurement Using Optical Spectroscopy. Spectroscopy. 2005;

14. Gustavson G, Ruefer S, Abdou M, Raghuraman B, Carnegie AJG, Al Hosani A, et al. Applications of Real-Time Downhole pH Measurements. 2015;

15. Understanding the Science of Ocean and Coastal Acidification | US EPA [Internet]. [cited 2022 Oct 10]. Available from: https://www.epa.gov/ocean-acidification/understanding-science-ocean-and-coastal-acidification

16. Midgley D. A REVIEW OF pH MEASUREMENT. Talanta. 1990;37(8):767–81.

17. Dickson AG. The measurement of sea water pH. Mar Chem. 1993;44(2–4):131–42.

18. Sheppard NF, Guiseppi-Elie A. pH Measurement. Measurement, Instrumentation, and Sensors Handbook. 2014 Feb 3;66-1-66–10.

19. Sheppard NF, Guiseppi-Elie A. pH Measurement. Measurement, Instrumentation, and Sensors Handbook. 2014 Feb 3;66-1-66–10.

20. Mc Naught a. D, Wilkinson a. Compendium of Chemical Terminology-Gold Book. IUPAC. 2012;1670.

21. Ed Vitz, John W. Moore, Justin Shorb, Xavier Prat-Resina, Tim Wendorff, Adam Hahn. 14.9: Indicators - Chemistry LibreTexts [Internet]. [cited 2023 Apr 22]. Available from: https://chem.libretexts.org/Bookshelves/General_Chemistry/Book%3A_ChemPRIME_(Moore_et_al.)/14%3A_Ionic_Equilibria_in_Aqueous_Solutions/14.09%3A_Indicators

22. Galster H. pH Measurement and Control. Ullmann's Encyclopedia of Industrial Chemistry. 2006;

23.   Wiley EA, Chakravarti DN, Slade KM. Measurement of pH. Curr Protoc Essent Lab Tech. 2010 Jun 1;3(1):3.2.1-3.2.16.

24.   MacInnes DA, Belcher D. Further studies on the glass electrode. J Am Chem Soc. 1931 Sep 1;53(9):3315–31.

25.   Cammann K. Fundamentals of Potentiometry. 1979;6–30.

26.   Graham DJ, Jaselskis B, Moore CE. Development of the glass electrode and the pH response. J Chem Educ. 2013 Mar 12;90(3):345–51.

27.   Gilbert-Kawai ET, Wittenberg MD, editors. Gibbs–Donnan effect. In: Essential Equations for Anaesthesia: Key Clinical Concepts for the FRCA and EDA. Cambridge: Cambridge University Press; 2014. p. 151–2.

28.   Wenzel T. Ion-Selective Electrodes [Internet]. [cited 2021 Mar 27]. Available from: https://chem.libretexts.org/Bookshelves/Analytical_Chemistry/Supplemental_M odules_(Analytical_Chemistry)/Analytical_Sciences_Digital_Library/In_Class_ Activities/Electrochemical_Methods_of_Analysis/02_Text/7%3A_Electrochemi cal_Analytical_Methods/7.1%3A_Ion

29.   A Guide To pH Measurement- - the theory and practice of laboratory pH applications. United States; 2011.

30.   Raghuraman B, Gustavson G, Mullins OC, Rabbito P. Spectroscopic pH measurement for high temperatures, pressures and ionic strength. AIChE Journal. 2006 Sep 1;52(9):3257–65.

31.   Mathews S, Raghuraman B, Rosiere D, Wei W, Colacelli S, Rehman H. Laboratory Measurement of pH of Live Waters at High Temperatures and Pressures. Proceedings of SPE International Symposium on Oilfield Chemistry. 2009;

32.   Xian CG, Raghuraman B, Carnegie AJ, Goiran PO, Berrim A. Downhole pH as a novel measurement tool in carbonate formation evaluation and reservoir monitoring. Petrophysics. 2008;49(2):159–71.

33. Van Hunnik E, Hendriksen ELJA, Pots BFM. The Formation of Protective FeCO3 Corrosion Product Layers in CO2 Corrosion. CORROSION 96. 1996. p. NACE-96006.

34. Yap K-M, Srinivasan S. Key Factors In Development Of A CO2/H2S Corrosion Prediction Model For Multiphase Oil / Gas Production Systems. CORROSION 2010. 2010. p. NACE-10374.

35. Raghuraman B, Xian C, Carnegie A, Lecerf B, Stewart L, Gustavson G, et al. SPE Downhole pH Measurement for WBM Contamination Monitoring and Transition Zone C haracterization. SPE Annual Technical Conference and Exhibition. 2005;

36. Fujisawa G, Yamate T. Development and applications of ruggedized VIS/NIR spectrometer system for oilfield wellbores. Photonic Sensors 2013 3:4. 2013 Oct 8;3(4):289–94.

37. Xian CG, Raghuraman B, Carnegie AJ, Goiran PO, Berrim A. Downhole pH as a novel measurement tool in carbonate formation evaluation and reservoir monitoring. Petrophysics. 2008;49(2):159–71.

38. Al-Janabi YT. Monitoring of Downhole Corrosion: An Overview. 2013;(May):19–22.

39. Børeng R, Schmidt T, Vikane O, Tau LA, Dybdahl B, Dale TI. Downhole Measurement of pH in Oil & Gas Applications by Use of a Wireline Tool. Main. 2003;

40. Raju K, Atkinson G. Thermodynamics of "Scale" Mineral Solubilities. 1. BaSO4(s) in H2O and Aqueous NaCl. J Chem Eng Data. 1988 Feb 1;33(4):490–5.

41. Li J, Tang M, Ye Z, Chen L, Zhou Y. Scale formation and control in oil and gas fields: A review. J Dispers Sci Technol. 2017 May 4;38(5):661–70.

42. Sanders L, Hu X, Mavredaki E, Eroini V, Barker R, Neville A. Assessment of combined scale/corrosion inhibitors – A combined jar test/bubble cell. J Pet Sci Eng. 2014 Jun 1;118.

43. Senthilmurugan B, Ghosh B, Sanker S. High performance maleic acid based oil well scale inhibitors—Development and comparative evaluation. Journal of Industrial and Engineering Chemistry. 2011;17(3):415–20.

44. Gu T, Su P, Liu X, Zou J, Zhang X, Hu Y, et al. A composite inhibitor used in oilfield: MA-AMPS and imidazoline. JPSE. 2013 Feb;102:41–6.

45. Sun W, Pugh D V, Smith SN, Ling S, Pacheco JL, Franco RJ. A Parametric Study Of Sour Corrosion Of Carbon Steela. CORROSION 2010. 2010. p. NACE-10278.

46. Dugstad A, Nyborg R, Seiersten M. Flow Assurance of pH Stabilized Wet Gas Pipelines. Corrosion 2003. 2003;(03314):1–19.

47. Asmara YP. The Roles of H2S Gas in Behavior of Carbon Steel Corrosion in Oil and Gas Environment: a Review. Jurnal Teknik Mesin Mercu Buana. 2018;7(1):37–43.

48. Sun W, Nesic S. A Mechanistic Model Of H2S Corrosion Of Mild Steel. CORROSION 2007. 2007. p. NACE-07655.

49. Hedges B, Chen HJ, Bieri TH, Sprague K. A Review of Monitoring and Inspection Techniques for CO2 and H2S Corrosion in Oil & Gas Production Facilities: Location, Location, Location. CORROSION 2006. 2006. p. NACE-06120.

50. Pierre R. Roberge. Handbook of Corrosion Engineering Library of Congress. Corrosion. 1999. 1130 p.

51. Linter BR, Burstein GT. Reactions of pipeline steels in carbon dioxide solutions. Corros Sci. 1999 Jan 1;41(1):117–39.

52. DE WAARD C, MILLIAMS DE. Carbonic Acid Corrosion of Steel. Corrosion. 2013 Jan 1;31(5):177–81.

53. Kan A, Tomson M. Scale Prediction for Oil and Gas Production. SPE Journal. 2012;17(02):362–78.

54. Kermani MB, Morshed A. Carbon dioxide corrosion in oil and gas production - A compendium. Corrosion. 2003;59(8):659–83.

55. Dugstad A. Fundamental Aspects of CO2 Metal Loss Corrosion - Part 1: Mechanism. CORROSION 2006. 2006. p. NACE-06111.

56. Nordsveen M, Nyborg SNR, Stangeland A. A Mechanistic Model for Carbon Dioxide Corrosion of Mild Steel in the Presence of Protective Iron Carbonate FilmsPart 1: Theory and Verification. Corrosion. 2003 May 1;59(05).

57. Videm K, Dugstad A. Corrosion of carbon steel in an aqueous carbon dioxide environment Part 1. Mater Performance. 1989;28:3.

58. Crolet JL, Thevenot N, Nesic S. Role of Conductive Corrosion Products in the Protectiveness of Corrosion Layers. Corrosion. 1998 Mar 1;54(3):194–203.

59. Zhu Z, Tajallipour N, Teevens PJ, Xue H, Cheng FYF. A Mechanistic Model For Predicting Localized Pitting Corrosion In a Brine Water-CO2 System. CORROSION 2011. 2011. p. NACE-11256.

60. Garber JD, Knierim K, Acuna J, Deokar KC. Modeling Pitting Corrosion In A CO2 System Containing Bacteria. CORROSION 2008. 2008. p. NACE-08545.

61. Sun H, Blumer D, Swidzinski M, Davis J. Evaluating Corrosion Inhibitors for Sour Gas Subsea Pipelines. 2009 Dec 7;cp-151-00060.

62. Ma H, Cheng X, Li G, Chen S, Quan Z, Zhao S, et al. The influence of hydrogen sulfide on corrosion of iron under different conditions. Corros Sci. 2000 Oct 1;42(10):1669–83.

63. Gustavson G, Eriksen KO, Raghuraman B, Vikane O, O'Keefe MD, Indo K, et al. Real-Time Downhole pH Measurement Using Optical Spectroscopy. SPE Reservoir Evaluation & Engineering. 2007;10(03):302–11.

64. Raghuraman B, Keefe MO, Eriksen KO, Tau LA, Vikane O, Gustavson G, et al. Real-Time Downhole pH Measurement Using Optical Spectroscopy. Spectroscopy. 2005;

65.   Vilarrasa V, Silva O, Carrera J, Olivella S. Liquid CO2 injection for geological storage in deep saline aquifers. International Journal of Greenhouse Gas Control. 2013 May 1;14:84–96.

66.   Głąb S, Maj-Żurawska M, Hulanicki A. pH. In: Reference Module in Chemistry, Molecular Sciences and Chemical Engineering. Elsevier; 2013.

67.   Kao CK, of Electrical Engineers I. Optical Fibre. P. Peregrinus; 1988. (IEE materials \& devices series).

68.   Nguyen TH, Venugopalan T, Sun T, Grattan KTV. Intrinsic Fiber Optic pH Sensor for Measurement of pH Values in the Range of 0.5-6. IEEE Sens J. 2016;16(4):881–7.

69.   Thorlabs. Multimode Optical Fiber [Internet]. [cited 2021 Jun 15]. Available from:
https://www.thorlabs.com/newgrouppage9.cfm?objectgroup_id=6838&pn=FG1 05UCA#6842

70.   Villar ID, Matias IR. Optical Fibre Sensors: Fundamentals for Development of Optimized Devices. Wiley; 2020. (IEEE Press Series on Sensors).

71.   Mitschke F. Fiber Optics: Physics and Technology. Springer Berlin Heidelberg; 2016.

72.   Midgley D. A REVIEW OF pH MEASUREMENT. Talanta. 1990;37(8):767–81.

73.   Azhari A, Yilman D, Chan B, Alemohammad H, Liang R, Pope M, et al. Development of fiber Bragg grating pH sensors for harsh environments. In: Fiber Optic Sensors and Applications XV. 2018.

74.   Mihailov SJ. Fiber bragg grating sensors for harsh environments. Sensors. 2012;12(2):1898–918.

75.   Ams M, Ha P, Taheri S, Clark S, Withford MJ, Bustamante H, et al. Fibre optic temperature and humidity sensors for harsh wastewater environments. Proceedings of the International Conference on Sensing Technology, ICST. 2018;2017:1–3.

76. Deepa N, Ganesh AB. Fiber optic sensor for simultaneous measurement of ph and dissolved oxygen. Applied Mechanics and Materials. 2014;573:842–7.

77. Mishra SK, Gupta BD. Surface plasmon resonance based fiber optic pH sensor utilizing Ag/ITO/Al/hydrogel layers. Analyst. 2013;138(9):2640–6.

78. Chen T, Chen KP. Fiber optic sensors for extreme environments. 2012;3529517:131.

79. Miyazaki CM, Shimizu FM, Ferreira M. Surface Plasmon Resonance (SPR) for Sensors and Biosensors. Nanocharacterization Techniques. Elsevier Inc.; 2017. 183–200 p.

80. Yamate T, Fujisawa G, Ikegami T. Optical Sensors for the Exploration of Oil and Gas. Journal of Lightwave Technology. 2017;35(16):3538–45.

81. Wang C, Ohodnicki PR, Su X, Keller M, Brown TD, Baltrus JP. Novel silica surface charge density mediated control of the optical properties of embedded optically active materials and its application for fiber optic pH sensing at elevated temperatures. Nanoscale. 2015;7(6):2527–35.

82. Su X, Wang C, Ohodnicki PR, Brown T, Keller M. Development of Fiber Optic Sensors for Downhole pH Measurement ; NETL-TRS-7- 2015. Technical Report Series; US Department of Energy, National Energy Technology Laboratory. 2015;24.

83. Wang C, Su X, Brown TD, Ohodnicki PR. Novel sensing materials for harsh environment subsurface pH sensing applications. Fiber Optic Sensors and Applications XII. 2015;9480(2015):1–6.

84. Lu F, Wright R, Lu P, Cvetic PC, Ohodnicki PR. Distributed fiber optic pH sensors using sol-gel silica based sensitive materials. Sens Actuators B Chem. 2021;340(2020):129853.

85. Bunge C-A, Beckers M, Gries T. Polymer Optical Fibres: Fibre Types, Materials, Fabrication, Characterisation and Applications. Polymer Optical Fibres. Cambridge: Elsevier Science & Technology; 2016. 1–416 p. (Woodhead Publishing Series in Electronic and Optical Materials; vol. 89).

86. Vilarrasa V;, Silva O;, Carrera J;, Olivella S. Liquid CO2 injection for geological storage in deep saline aquifers. International Journal of Greenhouse Gas Control. 2013;14:84–96.

87. Agnihotri S, Mukherji S, Mukherji S. Size-controlled silver nanoparticles synthesized over the range 5-100 nm using the same protocol and their antibacterial efficacy. RSC Adv. 2014;4(8):3974–83.

88. Caro C, M. P, Klippstein R, Pozo D, P. A. Silver Nanoparticles: Sensing and Imaging Applications. Silver Nanoparticles. 2010;(2014).

89. Solomon SD, Mozghan B, Jeyarajasingam A V., Rutkowsky SA, Boritz C, Mulfinger L. Synthesis and study of silver nanoparticles. J Chem Educ. 2007;84(2):322–5.

90. Su X, Wang C, Ohodnicki PR, Brown T, Keller M. Development of Fiber Optic Sensors for Downhole pH Measurement ; NETL-TRS-7- 2015. Technical Report Series; US Department of Energy, National Energy Technology Laboratory. 2015;24.

91. Caro C, M. P, Klippstein R, Pozo D, P. A. Silver Nanoparticles: Sensing and Imaging Applications. Silver Nanoparticles. 2010;(2014).

92. Power AC, Betts AJ, Cassidy JF. Silver nanoparticle polymer composite based humidity sensor. Analyst. 2010;135(7):1645–52.

93. Chen X, Cheng X, Gooding JJ. Multifunctional modified silver nanoparticles as ion and pH sensors in aqueous solution. Analyst. 2012;137(10):2338–43.

94. Wang C, Su X, Brown TD, Ohodnicki PR. Novel sensing materials for harsh environment subsurface pH sensing applications. Fiber Optic Sensors and Applications XII. 2015;9480(2015):1–6.

95. Wang C, Ohodnicki PR, Su X, Keller M, Brown TD, Baltrus JP. Novel silica surface charge density mediated control of the optical properties of embedded optically active materials and its application for fiber optic pH sensing at elevated temperatures. Nanoscale. 2015;7(6):2527–35.

96.	Brinker CJ, Scherer GW. Sol-Gel Science: The Physics and Chemistry of Sol-Gel Processing. Sol-Gel Science: The Physics and Chemistry of Sol-Gel Processing. 2013 Oct 22;1–908.

97.	Iler RK, K IR. The Chemistry of Silica: Solubility, Polymerization, Colloid and Surface Properties and Biochemistry of Silica. Wiley; 1979. (A Wiley-Interscience publication).

98.	Bangi UKH, Park CS, Baek S, Park HH. Improvement in optical and physical properties of TEOS based aerogels using acetonitrile via ambient pressure drying. Vol. 38, Ceramics International. 2012. p. 6883–8.

99.	Schäfer H, Milow B, Ratke L. Synthesis of inorganic aerogels via rapid gelation using chloride precursors. RSC Adv. 2013;3(35):15263–72.

100.	Azlina HN, Hasnidawani JN, Norita H, Surip SN. Synthesis of SiO2 nanostructures using sol-gel method. In: Acta Physica Polonica A. Polish Academy of Sciences; 2016. p. 842–4.

101.	Guglielmi M, Kickelbick G, Martucci A. Sol-Gel Nanocomposites. Springer; 2014.

102.	Petcu C, Purcar V, Spătaru CI, Alexandrescu E, Şomoghi R, Trică B, et al. The influence of new hydrophobic silica nanoparticles on the surface properties of the films obtained from bilayer hybrids. Nanomaterials. 2017;7(2):1–10.

103.	Innocenzi P. The Sol to Gel Transition. Switzerland: Springer International Publishing; 2016.

104.	Hench LL, West JK. The Sol-Gel Process. Chem Rev. 1990;90(1):33–72.

105.	Tamon H, Kitamura T, Okazaki M. Preparation of silica aerogel from TEOS. J Colloid Interface Sci. 1998;197(2):353–9.

106.	Milea CA, Bogatu C, Duta A. The Influence of Parameters in Silica Sol-Gel Process. Engineering Science. 2011;4(1):59–66.

107.	Li F, Xing Y, Ding X. Silica xerogel coating on the surface of natural and synthetic fabrics. Surf Coat Technol. 2008;202(19):4721–7.

108. Kozuka H. Stress evolution and cracking in sol-gel-derived thin films. Handbook of Sol-Gel Science and Technology: Processing, Characterization and Applications. Springer International Publishing AG; 2018. 275–311 p.

109. Hegde ND, Rao AV. Effect of processing temperature on gelation and physical properties of low density TEOS based silica aerogels. J Solgel Sci Technol. 2006;38(1):55–61.

110. Czarnobaj K. Preparation and characterization of silica xerogels as carriers for drugs. Drug Deliv. 2008;15(8):485–92.

111. Innocenzi P. Understanding sol–gel transition through a picture. A short tutorial. Journal of Sol-Gel Science and Technology. Springer; 2020.

112. Pope EJA, Mackenzie JD. Sol-gel processing of silica: II. The role of the catalyst. J Non Cryst Solids. 1986 Oct 2;87(1–2):185–98.

113. Twej WAA. Temperature Influence on the Gelation Process of Tetraethylorthosilicate Using Sol-Gel Technique. Twej Iraqi Journal of Science Iraqi Journal of Science. 2009;50(1):43–9.

114. Bansal NP. Influence of Several Metal Ions on the Gelation Activation Energy of Silicon Tetraethoxide. Journal of the American Ceramic Society. 1990;73(9):2647–52.

115. Li W, Seal S, Megan E, Ramsdell J, Scammon K. Physical and optical properties of sol-gel nano-silver doped silica film on glass substrate as a function of heat-treatment temperature. J Appl Phys. 2003;93(12):9553–61.

116. Pinedo A, Alcázar B, Carlos J, Rodriguez-Reyes F, Pinedo-Flores A, Alcázar° B. Protocol for the synthesis of silver nanoparticles using sodium citrate and sodium borohydride as reducing agents. 2018;(March). Available from: https://www.researchgate.net/publication/323676186

117. Mavani K, Shah M. Synthesis of Silver Nanoparticles by using Sodium Borohydride as a Reducing Agent. International Journal of Engineering Research & Technology (IJERT). 2013;2(3):1–5.

118. Dong X, Ji X, Jing J, Li M, Li J, Yang W. Synthesis of triangular silver nanoprisms by stepwise reduction of sodium borohydride and trisodium citrate. Journal of Physical Chemistry C. 2010;114(5):2070–4.

119. Alarcon EI, Griffith M. Silver Nanoparticle Applications. Springer International Publishing; 2015.

120. Jawaad RS, Sultan KF, Al-Hamadani AH. Synthesis of silver nanoparticles. Journal of Engineering and Applied Sciences. 2014;9(4):586–92.

121. Mazzonello A, Valdramidis V V., Farrugia C, Grima JN, Gatt R. Synthesis and characterization of silver nanoparticles. International Journal Of Modern Engineering Research (IJMER). 7(3):41–7.

122. Solomon SD, Mozghan B, Jeyarajasingam A V., Rutkowsky SA, Boritz C, Mulfinger L. Synthesis and study of silver nanoparticles. J Chem Educ. 2007;84(2):322–5.

123. Gakiya-Teruya M, Palomino-Marcelo L, Rodriguez-Reyes J. Synthesis of Highly Concentrated Suspensions of Silver Nanoparticles by Two Versions of the Chemical Reduction Method. Methods Protoc. 2019;2(3):1–5.

124. Jawaad RS, Sultan KF, Al-Hamadani AH. Synthesis of silver nanoparticles. Journal of Engineering and Applied Sciences. 2014;9(4):586–92.

125. Dong X, Ji X, Jing J, Li M, Li J, Yang W. Synthesis of triangular silver nanoprisms by stepwise reduction of sodium borohydride and trisodium citrate. Journal of Physical Chemistry C. 2010;114(5):2070–4.

126. Agnihotri S, Mukherji S, Mukherji S. Size-controlled silver nanoparticles synthesized over the range 5-100 nm using the same protocol and their antibacterial efficacy. RSC Adv. 2014;4(8):3974–83.

127. Gakiya-Teruya M, Palomino-Marcelo L, Rodriguez-Reyes J. Synthesis of Highly Concentrated Suspensions of Silver Nanoparticles by Two Versions of the Chemical Reduction Method. Methods Protoc. 2018;2(1):3.

128. Šileikaite A, Prosycevas I, Puiso J. Analysis of Silver Nanoparticles Produced by Chemical Reduction of Silver Salt Solution. MATERIALS SCIENCE (MEDŽIAGOTYRA). 2006;12(4):287–91.

129. Montero MA, Gennero De Chialvo MR, Chialvo AC. Preparation of gold nanoparticles supported on glassy carbon by direct spray pyrolysis. J Mater Chem [Internet]. 2009 May 12 [cited 2024 Apr 9];19(20):3276–80. Available from: https://pubs.rsc.org/en/content/articlehtml/2009/jm/b821016k

130. Sawada T, Ando S. Synthesis, characterization, and optical properties of metal-containing fluorinated polyimide films. Chemistry of Materials. 1998;10(11):3368–78.

131. Otto K, Oja Acik I, Krunks M, Tõnsuaadu K, Mere A. Thermal decomposition study of HAuCl4·3H2O and AgNO3 as precursors for plasmonic metal nanoparticles. J Therm Anal Calorim. 2014;118(2):1065–72.

132. Kajihara K. Recent advances in sol – gel synthesis of monolithic silica and silica-based glasses. Journal of Asian Ceramic Societies. 2013;1(2):121–33.

133. Li S, Wan Q, Qin Z, Fu Y, Gu Y. Unraveling the mystery of Stöber silica's microporosity. Langmuir. 2016 Sep 13;32(36):9180–7.

134. Rahman IA, Padavettan V. Synthesis of Silica nanoparticles by Sol-Gel: Size-dependent properties, surface modification, and applications in silica-polymer nanocompositesa review. J Nanomater. 2012;2012.

135. Li S, Wan Q, Qin Z, Fu Y, Gu Y. Stöber silica's microporosity: insights from thermal analysis studies. J Therm Anal Calorim. 2019 Jun 15;136(5):1895–904.

136. Li W, Seal S, Megan E, Ramsdell J, Scammon K. Physical and optical properties of sol-gel nano-silver doped silica film on glass substrate as a function of heat-treatment temperature. J Appl Phys. 2003;93(12):9553–61.

137. Badiah HI, Seedeh F, Supriyanto G, Zaidan AH. Synthesis of Silver Nanoparticles and the Development in Analysis Method. IOP Conf Ser Earth Environ Sci. 2019;217(1).

138. Baset S, Akbari H, Zeynali H, Shafie M. Size measurement of metal and semiconductor nanoparticles via UV-Vis absorption spectra. Dig J Nanomater Biostruct. 2011;6(2):709–16.

139. Homola J, Piliarik M. Surface Plasmon Resonance (SPR) Sensors. 2006. 45–67 p.

140. Amendola V, Pilot R, Frasconi M, Maragò OM, Iatì MA. Surface plasmon resonance in gold nanoparticles: A review. Journal of Physics Condensed Matter. 2017;29(20).

141. Masson JF. Portable and field-deployed surface plasmon resonance and plasmonic sensors. Analyst. 2020;145(11):3776–800.

142. Khlebtsov BN, Khlebtsov NG. On the measurement of gold nanoparticle sizes by the dynamic light scattering method. Colloid Journal. 2011;73(1):118–27.

143. Alarcon EI, Griffith M. Silver Nanoparticle Applications. Springer International Publishing; 2015.

144. Mavani K, Shah M. Synthesis of Silver Nanoparticles by using Sodium Borohydride as a Reducing Agent. International Journal of Engineering Research & Technology (IJERT). 2013;2(3):1–5.

145. Alqadi MK, Abo Noqtah OA, Alzoubi FY, Alzouby J, Aljarrah K. PH effect on the aggregation of silver nanoparticles synthesized by chemical reduction. Materials Science- Poland. 2014;32(1):107–11.

146. Pillai ZS, Kamat P V. What factors control the size and shape of silver nanoparticles in the citrate ion reduction method? Journal of Physical Chemistry B. 2004;108(3):945–51.

147. Lee KS, El-Sayed MA. Gold and silver nanoparticles in sensing and imaging: Sensitivity of plasmon response to size, shape, and metal composition. Journal of Physical Chemistry B. 2006;110(39):19220–5.

148. De Leersnyder I, Rijckaert H, De Gelder L, Van Driessche I, Vermeir P. High Variability in Silver Particle Characteristics, Silver Concentrations, and

Production Batches of Commercially Available Products Indicates the Need for a More Rigorous Approach. Nanomaterials. 2020 Jul 1;10(7):1–22.

149. Mishra SK, Gupta BD. Surface plasmon resonance based fiber optic pH sensor utilizing Ag/ITO/Al/hydrogel layers. Analyst. 2013;138(9):2640–6.

150. Deepa N, Ganesh AB. Fiber optic sensor for simultaneous measurement of ph and dissolved oxygen. Applied Mechanics and Materials. 2014;573(October):842–7.

151. Kocincova AS, Borisov SM, Krause C, Wolfbeis OS. Fiber-optic microsensors for simultaneous sensing of oxygen and pH, and of oxygen and temperature. Anal Chem. 2007;79(22):8486–93.

152. Zhu H, Liang C, Yan W, Overbury SH, Dai S. Preparation of highly active silica-supported Au catalysts for Co oxidation by a solution-based technique. Journal of Physical Chemistry B. 2006;110(22):10842–8.

153. Allafchian AR, Banifatemi SS, Jalali SAH. Synthesis and Characterization of Ag/SiO2 Nanoparticles Embedded in TPS and TEOS Sol-gel Matrix with Excellent Antibacterial Activity. Nanoscience &Nanotechnology-Asia. 2017;8(1):33–40.

154. Aati S, Aneja S, Kassar M, Leung R, Nguyen A, Tran S, et al. Silver-loaded mesoporous silica nanoparticles enhanced the mechanical and antimicrobial properties of 3D printed denture base resin. J Mech Behav Biomed Mater. 2022 Oct 1;134:105421.

155. Kelly KL, Coronado E, Zhao LL, Schatz GC. The optical properties of metal nanoparticles: The influence of size, shape, and dielectric environment. Journal of Physical Chemistry B. 2003 Jan 23;107(3):668–77.

156. Montaño-Priede JL, Coelho JP, Guerrero-Martínez A, Peña-Rodríguez O, Pal U. Fabrication of Monodispersed Au@SiO2 Nanoparticles with Highly Stable Silica Layers by Ultrasound-Assisted Stöber Method. Journal of Physical Chemistry C. 2017;121(17):9543–51.

157. Behrens SH, Grier DG. The charge of glass and silica surfaces. J Chem Phys. 2001 Sep 27;115(14):6716.

158. Wang C, Ohodnicki PR, Su X, Keller M, Brown TD, Baltrus JP. Novel silica surface charge density mediated control of the optical properties of embedded optically active materials and its application for fiber optic pH sensing at elevated temperatures. Nanoscale. 2015;7(6):2527–35.

159. Barisik M, Atalay S, Beskok A, Qian S. Size dependent surface charge properties of silica nanoparticles. Journal of Physical Chemistry C. 2014 Jan 30;118(4):1836–42.

160. Miled OB, Grosso D, Sanchez C, Livage J. An optical fibre pH sensor based on dye doped mesostructured silica. Journal of Physics and Chemistry of Solids. 2004 Oct 1;65(10):1751–5.

161. Butler TM, MacCraith BD, McDonagh C. Leaching in sol-gel-derived silica films for optical pH sensing. J Non Cryst Solids. 1998;224(3):249–58.

162. Ben-David O, Shafir E, Gilath I, Prior Y, Avnir D. Simple Absorption Optical Fiber pH Sensor Based on Doped Sol−Gel Cladding Material. Chemistry of Materials. 1997 Nov 1;9(11):2255–7.

163. Bai X, Lin C, Wang Y, Ma J, Wang X, Yao X, et al. Preparation of Zn doped mesoporous silica nanoparticles (Zn-MSNs) for the improvement of mechanical and antibacterial properties of dental resin composites. Dental Materials. 2020 Jun 1;36(6):794–807.

164. Liu L, Shinozaki K. Toughening silica glass by imparting ductility using a small amount of silver nanoparticles. Materials Science and Engineering: A. 2021 Jun 10;817:141372.

165. Masoud N, Partsch T, de Jong KP, de Jongh PE. Thermal stability of oxide-supported gold nanoparticles. Gold Bull. 2019;52(2):105–14.

166. Gould AL, Kadkhodazadeh S, Wagner JB, Catlow CRA, Logsdail AJ, Di Vece M. Understanding the Thermal Stability of Silver Nanoparticles Embedded in a-Si. Journal of Physical Chemistry C. 2015;119(41):23767–73.

167. Faustini M, Louis B, Albouy PA, Kuemmel M, Grosso D. Preparation of sol-gel films by dip-coating in extreme conditions. Journal of Physical Chemistry C. 2010;114(17):7637–45.

168. Guglielmi M, Zenezini S. The thickness of sol-gel silica coating obtained by dipping. Vol. 121, Journal of Non-Crystalline Solids. 1990.

169. Ji G, Zhao M, Ji G, Zhao M. Membrane Separation Technology in Carbon Capture. Recent Advances in Carbon Capture and Storage. 2017 Mar 8;

170. McDonagh C, Sheridan F, Butler T, MacCraith BD. Characterisation of sol-gel-derived silica films. J Non Cryst Solids. 1996 Jan 1;194(1–2):72–7.

171. Chyad RM, Jafri MZM, Ibrahim KU. Fabrication nano fiber optic by chemical etching for sensing application. Eng &TechJournal. 2015;33(6):994–1002.

172. Bashir ST, Yang L, Liggat JJ, Thomason JL. Kinetics of dissolution of glass fibre in hot alkaline solution. J Mater Sci. 2018;53(3):1710–22.

173. Iler RK, K IR. The Chemistry of Silica: Solubility, Polymerization, Colloid and Surface Properties and Biochemistry of Silica. Wiley; 1979. (A Wiley-Interscience publication).

174. Pope EJA, Mackenzie JD. Sol-gel processing of silica: II. The role of the catalyst. J Non Cryst Solids. 1986 Oct 2;87(1–2):185–98.

175. Campen RK, Pymer AK, Nihonyanagi S, Borguet E. Linking surface potential and deprotonation in nanoporous silica: Second harmonic generation and acid/base titration. Journal of Physical Chemistry C. 2010 Nov 4;114(43):18465–73.

176. Rayss J, Sudolski G. Ion adsorption in the porous sol–gel silica layer in the fibre optic pH sensor. Sens Actuators B Chem. 2002;87(3):397–405.

177. Rayss J, Sudolski G. Ion adsorption in the porous sol-gel silica layer in the fibre optic pH sensor. Sens Actuators B Chem. 2002;87(3):397–405.

178. Skold M, Revil A, Vaudelet P. The pH dependence of spectral induced polarization of silica sands: Experiment and modeling. Geophys Res Lett. 2011 Jun 1;38(12).

179. Pokrovsky OS, Golubev S V., Mielczarski JA. Kinetic evidences of the existence of positively charged species at the quartz-aqueous solution interface. J Colloid Interface Sci. 2006 Apr 1;296(1):189–94.

180. Lu F, Wright R, Lu P, Cvetic PC, Ohodnicki PR. Distributed fiber optic pH sensors using sol-gel silica based sensitive materials. Sens Actuators B Chem. 2021;340(2020):129853.

181. Kim K Do, Kim HT. Formation of silica nanoparticles by hydrolysis of TEOS using a mixed semi-batch/batch method. J Solgel Sci Technol. 2002;25(3):183–9.

182. Wang H, Qiao X, Chen J, Ding S. Preparation of silver nanoparticles by chemical reduction method. Colloids Surf A Physicochem Eng Asp. 2005;256:111–5.

183. Bastús NG, Merkoçi F, Piella J, Puntes V. Synthesis of highly monodisperse citrate-stabilized silver nanoparticles of up to 200 nm: Kinetic control and catalytic properties. Chemistry of Materials. 2014;26:2836–46.

184. SAFETY DATA SHEET : Silver nitrate. ThermoFisher Scientific. 2020;

185. Vogt C, Wondergem CS, Weckhuysen BM. Ultraviolet-Visible (UV-Vis) Spectroscopy. Springer Handbooks. 2023;237–64.

186. Tissue BM. Basics of analytical chemistry and chemical equilibria / [internet resource]. Hoboken, New Jersey : John Wiley & Sons, Inc.; 2013.

187. Karakuzu B, Temel TM, Sevil Y, Terzioglu P, Elalmis Y. Effect of acid type and gelation pH on the structural properties of silica aerogels prepared by use of rice hull biosilica. Sigma Journal Engineering and Natural Sciences. 2016;34(2):175–82.

188. Ohodnicki PR, Wang C. Optical waveguide modeling of refractive index mediated pH responses in silica nanocomposite thin film based fiber optic sensors. J Appl Phys. 2016;119(6).

189. Pelcher KE, Crawley MR, Banerjee S, Li S, Yang S, Xu S, et al. Influence of heat treatment on the microstructure and surface groups of Stöber silica. Mater Res Express [Internet]. 2023 Oct 12 [cited 2024 Mar 30];10(10):105004. Available from: https://iopscience.iop.org/article/10.1088/2053-1591/acff3e

190. Li S, Yang S, Xu S, Wan Q. Influence of heat treatment on the microstructure and surface groups of Stöber silica. Mater Res Express [Internet]. 2023 Oct 12 [cited 2024 Mar 30];10(10):105004. Available from: https://iopscience.iop.org/article/10.1088/2053-1591/acff3e

191. Tiggelaar RM, Benito-López F, Hermes DC, Rathgen H, Egberink RJM, Mugele FG, et al. Fabrication, mechanical testing and application of high-pressure glass microreactor chips. Chemical Engineering Journal. 2007 Jul 1;131(1–3):163–70.

192. Haddock HS, Shankar PM, Mutharasan R. Fabrication of biconical tapered optical fibers using hydrofluoric acid. Materials Science and Engineering: B. 2003 Jan 15;97(1):87–93.

193. Kbashi HJ. Fabrication of Submicron-Diameter and Taper Fibers Using Chemical Etching. J Mater Sci Technol. 2012 Apr 1;28(4):308–12.

194. Mysen B, Richet P. Silica. Silicate Glasses and Melts. 2019 Jan 1;143–83.

195. Guerette M, Ackerson MR, Thomas J, Yuan F, Watson EB, Walker D, et al. Structure and Properties of Silica Glass Densified in Cold Compression and Hot Compression. Scientific Reports 2015 5:1. 2015 Oct 15;5(1):1–10.

196. Green AK, Shafir E. Termination and connection methods for optical fibres embedded in aerospace composite components. Smart Mater Struct. 1999 Apr 15;8(2):269.

197. Losada MA, Domínguez-Chapman FA, Mateo J, López A, Zubia J. Influence of termination on connector loss for plastic optical fibres. International Conference on Transparent Optical Networks. 2014;

198. ThorLabs. Bare Fiber Optic Terminator [Internet]. [cited 2021 Jun 15]. Available from: https://www.thorlabs.com/newgrouppage9.cfm?objectgroup_id=8543&pn=BFT 1#8544

199. OceanOptics. USB4000 - Operating - Instructions. 2005.

200. Zaca-Morán P, Padilla-Martínez JP, Pérez-Corte JM, Dávila-Pintle JA, Ortega-Mendoza JG, Morales N. Etched optical fiber for measuring concentration and refractive index of sucrose solutions by evanescent waves. Laser Phys. 2018;28(11).

201. Thomason JL, Nagel U, Yang L, Sáez E. Regenerating the strength of thermally recycled glass fibres using hot sodium hydroxide. Compos Part A Appl Sci Manuf. 2016;87:220–7.

202. Peter William Atkins, Julio De Paula, James Keeler. Atkins' Physical Chemistry. United Kingdom: Oxford University Press; 2018.

203. J.M. Smith, Hendrick C. Van Ness, Michael Abbott, Mark Swihart. Introduction to Chemical Engineering Thermodynamics. Philippines: McGraw-Hill Education; 2017.

204. Kula C. Misra. Introduction to Geochemistry. United Kingdom: Wiley; 2012.

205. John Clifford Jones. The Principles of Thermal Sciences and Their Application to Engineering. United Kingdom: Whittles Pub.; 2000.

206. Alqadi MK, Abo Noqtah OA, Alzoubi FY, Alzouby J, Aljarrah K. PH effect on the aggregation of silver nanoparticles synthesized by chemical reduction. Materials Science- Poland. 2014;32(1):107–11.

207. Agnihotri S, Mukherji S, Mukherji S. Size-controlled silver nanoparticles synthesized over the range 5-100 nm using the same protocol and their antibacterial efficacy. RSC Adv. 2014;4(8):3974–83.

208. Badiah HI, Seedeh F, Supriyanto G, Zaidan AH. Synthesis of Silver Nanoparticles and the Development in Analysis Method. IOP Conf Ser Earth Environ Sci. 2019;217(1).

209. Šileikaite A, Prosycevas I, Puiso J. Analysis of Silver Nanoparticles Produced by Chemical Reduction of Silver Salt Solution. MATERIALS SCIENCE (MEDŽIAGOTYRA). 2006;12(4):287–91.

210. Chaudhary A, Sangani C, Ameta R. Synthesis and Characterization of Citrate Stabilized Silver Nanoparticles. Research and Reviews: Journal of Chemistry. 2022;11(3):1–4.

211. Zhao J, Zhang X, Yonzon CR, Hoes AJ, Van Duyne RP. Localized surface plasmon resonance biosensors. Nanomedicine. 2006;1(2):219–28.

212. Pinto V V., Ferreira MJ, Silva R, Santos HA, Silva F, Pereira CM. Long time effect on the stability of silver nanoparticles in aqueous medium: Effect of the synthesis and storage conditions. Colloids Surf A Physicochem Eng Asp. 2010;364(1–3):19–25.

213. Saiqa Ikram SA. Silver Nanoparticles: One Pot Green Synthesis Using Terminalia arjuna Extract for Biological Application. J Nanomed Nanotechnol. 2015;06(04):0–6.

214. Sobczak-Kupiec A, Malina D, Wzorek Z, Zimowska M. Influence of silver nitrate concentration on the properties of silver nanoparticles. Micro Nano Lett. 2011;6(8):656–60.

215. Kao CK, of Electrical Engineers I. Optical Fibre. P. Peregrinus; 1988. (IEE materials \& devices series).

216. Bunge C-A, Beckers M, Gries T. Polymer Optical Fibres: Fibre Types, Materials, Fabrication, Characterisation and Applications. Polymer Optical Fibres. Cambridge: Elsevier Science & Technology; 2016. 1–416 p. (Woodhead Publishing Series in Electronic and Optical Materials; vol. 89).

217. Cascio C, Geiss O, Franchini F, Ojea-Jimenez I, Rossi F, Gilliland D, et al. Detection, quantification and derivation of number size distribution of silver

nanoparticles in antimicrobial consumer products. J Anal At Spectrom. 2015;30(6):1255–65.

218. De Leersnyder I, Rijckaert H, De Gelder L, Van Driessche I, Vermeir P. High Variability in Silver Particle Characteristics, Silver Concentrations, and Production Batches of Commercially Available Products Indicates the Need for a More Rigorous Approach. Nanomaterials. 2020 Jul 1;10(7):1–22.

219. Bhattarai B, Zaker Y, Atnagulov A, Yoon B, Landman U, Bigioni TP. Chemistry and Structure of Silver Molecular Nanoparticles. Acc Chem Res. 2018;51(12):3104–13.

220. Benoit M, Puibasset J, Bonafos C, Tarrat N. Silica-induced electron loss of silver nanoparticles. Nanoscale. 2022 May 19;14(19):7280–91.

221. Milczarek G, Rebis T, Fabianska J. One-step synthesis of lignosulfonate-stabilized silver nanoparticles. Colloids Surf B Biointerfaces. 2013 May 1;105:335–41.

222. Banne S V., Patil MS, Kulkarni RM, Patil SJ. Synthesis and Characterization of Silver Nano Particles for EDM Applications. Mater Today Proc. 2017;4(11):12054–60.

223. SAFETY DATA SHEET : Silver nitrate. ThermoFisher Scientific. 2020;

224. Gakiya-Teruya M, Palomino-Marcelo L, Rodriguez-Reyes J. Synthesis of Highly Concentrated Suspensions of Silver Nanoparticles by Two Versions of the Chemical Reduction Method. Methods Protoc. 2019;2(3):1–5.

225. Pris M, Trzaskuś K, Kemperman AJB, Nijmeijer IrDC. Influence of different parameters on wet synthesis of silver nanoparticles. Thesis Paper at University of Twente. 2008.

226. Pillai ZS, Kamat P V. What factors control the size and shape of silver nanoparticles in the citrate ion reduction method? Journal of Physical Chemistry B. 2004;108(3):945–51.

227. Bastús NG, Merkoçi F, Piella J, Puntes V. Synthesis of highly monodisperse citrate-stabilized silver nanoparticles of up to 200 nm: Kinetic control and catalytic properties. Chemistry of Materials. 2014;26:2836–46.

228. Gorham JM, Rohlfing AB, Lippa KA, MacCuspie RI, Hemmati A, David Holbrook R. Storage wars: How citrate-capped silver nanoparticle suspensions are affected by not-so-trivial decisions. Journal of Nanoparticle Research. 2014;16(4).

229. Guglielmi M, Zenezini S. The thickness of sol-gel silica coating obtained by dipping. Vol. 121, Journal of Non-Crystalline Solids. 1990.

230. Milea CA, Bogatu C, Duta A. The Influence of Parameters in Silica Sol-Gel Process. Engineering Science. 2011;4(1):59–66.

231. Crundwell FK. On the Mechanism of the Dissolution of Quartz and Silica in Aqueous Solutions. ACS Omega. 2017 Mar 31;2(3):1116–27.

232. Bennett PC. Quartz dissolution in organic-rich aqueous systems. Geochimica et Cosmochimica Acta; (United States). 1991 Jul 1;55:7(7):1781–97.

233. House WA, Orr DR. Investigation of the pH dependence of the kinetics of quartz dissolution at 25 °C. Journal of the Chemical Society, Faraday Transactions [Internet]. 1992 Jan 1 [cited 2023 Oct 5];88(2):233–41. Available from: https://pubs.rsc.org/en/content/articlehtml/1992/ft/ft9928800233

234. Spitzmüller L, Nitschke F, Rudolph B, Berson J, Schimmel T, Kohl T. Dissolution control and stability improvement of silica nanoparticles in aqueous media. Journal of Nanoparticle Research. 2023;25(3):1–17.

235. Klause M, Rothhaar U, Bicker M, Ohling W. Dissolution of thin SiO_2-coatings – Characterization and evaluation. J Non Cryst Solids. 2010 Feb 1;356(3):141–6.

236. Lenher V, Merrill HB. The solubility of silica. J Am Chem Soc. 1917 Dec 1;39(12):2630–8.

237. DiPippo R. Geothermal Power Generation: Developments and Innovation. Geothermal Power Generation: Developments and Innovation. 2016 Jun 22;1– 822.

238. Nikaido F, Inasawa S, Tsuji Y, Yamaguchi Y. A Model of Silica Dissolution Based on Acid Dissociation of Internal Silanol. Bulletin of the Chemical Society of Japan. 2013 Mar 20;86(4):520–5.

239. Clifton W. Chemical Grouts for Potential Use in Bureau of Reclamation Projects. December 1. Applied Sciences Branch, Division of Research and Laboratory Services, Engineering and Research Center, U.S. Department of the Interior, Bureau of Reclamation; 1986. (GR (Series)).

240. Peretyazhko TS, Zhang Q, Colvin VL. Size-controlled dissolution of silver nanoparticles at neutral and acidic pH conditions: Kinetics and size changes. Environ Sci Technol. 2014 Oct 21;48(20):11954–61.

241. Molleman B, Hiemstra T. Time, pH, and size dependency of silver nanoparticle dissolution: the road to equilibrium. Environ Sci Nano. 2017 Jun 16;4(6):1314– 27.

242. Bangi UKH, Jung IK, Park CS, Baek S, Park HH. Optically transparent silica aerogels based on sodium silicate by a two step sol-gel process and ambient pressure drying. Vol. 18, Solid State Sciences. 2013. p. 50–7.

243. Maleki H, Durães L, Portugal A. An overview on silica aerogels synthesis and different mechanical reinforcing strategies. J Non Cryst Solids. 2014;385:55– 74.

244. Kozuka H. Stress evolution and cracking in sol-gel-derived thin films. Handbook of Sol-Gel Science and Technology: Processing, Characterization and Applications. Springer International Publishing AG; 2018. 275–311 p.

245. Kozuka H, Takenaka S, Tokita H, Hirano T, Higashi Y, Hamatani T. Stress and cracks in gel-derived ceramic coatings and thick film formation. J Solgel Sci Technol. 2003 Jan;26(1–3):681–6.

246. Twej WAA. Temperature Influence on the Gelation Process of Tetraethylorthosilicate Using Sol-Gel Technique. Twej Iraqi Journal of Science Iraqi Journal of Science. 2009;50(1):43–9.

247. Prasetyo AB, Handayani M, Sulistiyono E, Syahid AN, Febriana E, Mayangsari W, et al. Development of high purity amorphous silica from emulsifier silicon by pyrolysis process at temperature of 700 oC. J Phys Conf Ser. 2022;2190(1).

248. Pichtel J. Oil and gas production wastewater: Soil contamination and pollution prevention. Appl Environ Soil Sci. 2016;2016.

249. Craddock HA. Phosphorus Chemistry. Oilfield Chemistry and its Environmental Impact. 2018 Jul 16;211–31.

250. Gazulla MF, Rodrigo M, Orduña M, Ventura MJ, Andreu C. Determination of Phosphorus in Crude Oil and Middle Distillate Petroleum Products by Inductively Coupled Plasma–Optical Emission Spectrometry. Anal Lett. 2017 Oct 13;50(15):2465–74.

251. Behrens SH, Grier DG. The charge of glass and silica surfaces. J Chem Phys. 2001 Sep 27;115(14):6716.

252. Cao J, Tu MH, Sun T, Grattan KTV. Wavelength-based localized surface plasmon resonance optical fiber biosensor. Vol. 181, Sensors and Actuators, B: Chemical. 2013. p. 611–9.

253. Sincero AP, Sincero GA. Physical-Chemical Treatment of Water and Wastewater. CRC Press; 2002.

254. Khan MA, Al-Oufi M, Toseef A, Nadeem MA, Idriss H. Comparing the Reaction Rates of Plasmonic (Gold) and Non-Plasmonic (Palladium) Metal Particles in Photocatalytic Hydrogen Production. Catal Letters. 2018 Jan 1;148(1):1–10.

255. Andersson J, Svirelis J, Ferrand-Drake Del Castillo G, Sannomiya T, Dahlin A. Surface plasmon resonance sensing with thin films of palladium and platinum – quantitative and real-time analysis. Physical Chemistry Chemical Physics [Internet]. 2022 Feb 16 [cited 2024 Apr 9];24(7):4588–94. Available from: https://pubs.rsc.org/en/content/articlehtml/2022/cp/d1cp05381g

256. De Marchi S, Núñez-Sánchez S, Bodelón G, Pérez-Juste J, Pastoriza-Santos I. Pd nanoparticles as a plasmonic material: synthesis, optical properties and applications. Nanoscale [Internet]. 2020 Dec 8 [cited 2024 Apr 9];12(46):23424–43. Available from: https://pubs.rsc.org/en/content/articlehtml/2020/nr/d0nr06270g

257. Liz-Marzán LM, Giersig M, Mulvaney P. Synthesis of Nanosized Gold−Silica Core−Shell Particles. Langmuir. 1996 Sep 4;12(18):4329–35.

258. Kelly KL, Coronado E, Zhao LL, Schatz GC. The optical properties of metal nanoparticles: The influence of size, shape, and dielectric environment. Journal of Physical Chemistry B. 2003 Jan 23;107(3):668–77.

259. Shao L, Ruan Q, Jiang R, Wang J. Macroscale Colloidal Noble Metal Nanocrystal Arrays and Their Refractive Index-Based Sensing Characteristics. Small. 2014 Feb 1;10(4):802–11.

260. Tittl A, Giessen H, Liu N. Plasmonic gas and chemical sensing. Nanophotonics. 2014 Jun 1;3(3):157–80.

261. Greenwood NN, Earnshaw A. Chemistry of the Elements. Second Edi. Elsevier Science; 2012.

262. Hair ML, Hertl W. Reactions of chlorosilanes with silica surfaces. Journal of Physical Chemistry. 1969;73(7):2372–8.

263. Chung KH, Sturm JC. Chlorine Etching for In-Situ Low-Temperature Silicon Surface Cleaning for Epitaxy Applications. ECS Trans. 2007 Apr 27;6(1):401–7.

264. Spencer JN, Bodner GM, Rickard LH. Chemistry: Structure and Dynamics. 2010;880.

265. Wang Y, Nie Z, Guo Q, Song Y, Liu L. Adsorption Behaviors of Chlorosilanes, HCl, and H2on the Si(100) Surface: A First-Principles Study. ACS Omega. 2022 Nov 22;7(46):42105–14.

266. El Mourabit S, Guillot M, Toquer G, Cambedouzou J, Goettmann F, Grandjean A. Stability of mesoporous silica under acidic conditions. RSC Adv. 2012 Oct 22;2(29):10916–24.

267. Fiber Optic pH Sensor for High-Temperature and High-Pressure Environments | netl.doe.gov [Internet]. [cited 2022 Oct 11]. Available from: https://netl.doe.gov/node/11008

268. R. K. Rajput. Steam Tables and Moiller Diagrams (S.I. Units). Laxmi Publications Pvt Limited; 2009.

269. Wolfgang Wagner, Hans-Joachim Kretzschmar. International Steam Tables-Properties of Water and Steam Based on the Industrial Formulation IAPWS-IF97. Springer Berlin Heidelberg; 2008.

270. Spitzmüller L, Nitschke F, Rudolph B, Berson J, Schimmel T, Kohl T. Dissolution control and stability improvement of silica nanoparticles in aqueous media. Journal of Nanoparticle Research. 2023;25(3):1–17.

271. Crundwell FK. On the Mechanism of the Dissolution of Quartz and Silica in Aqueous Solutions. ACS Omega. 2017 Mar 31;2(3):1116–27.

272. Klause M, Rothhaar U, Bicker M, Ohling W. Dissolution of thin SiO2-coatings – Characterization and evaluation. J Non Cryst Solids. 2010 Feb 1;356(3):141–6.

273. Lenher V, Merrill HB. The solubility of silica. J Am Chem Soc. 1917 Dec 1;39(12):2630–8.

274. Pham ALT, Sedlak DL, Doyle FM. Dissolution of Mesoporous Silica Supports in Aqueous Solutions: Implications for Mesoporous Silica-based Water Treatment Processes. Appl Catal B. 2012 Sep 9;126:258.

275. Krauskopf KB. Dissolution and precipitation of silica at low temperatures. Geochim Cosmochim Acta. 1956 Aug 1;10(1–2):1–26.

276. Chyad RM, Jafri MZM, Ibrahim KU. Fabrication nano fiber optic by chemical etching for sensing application. Eng &TechJournal. 2015;33(6):994–1002.

277. Zaca-Morán P, Padilla-Martínez JP, Pérez-Corte JM, Dávila-Pintle JA, Ortega-Mendoza JG, Morales N. Etched optical fiber for measuring concentration and refractive index of sucrose solutions by evanescent waves. Laser Phys. 2018;28(11).

278. Fernando I, Zhou Y. Impact of pH on the stability, dissolution and aggregation kinetics of silver nanoparticles. Chemosphere. 2019 Feb 1;216:297–305.

APPENDICES

Appendix A: Personal Outputs

A.1 List of attended conferences

1. Sensors Technologies International conference 2021 (Oral presentation). April 2021. Sector Conferences & Exhibitions, Italy.
2. PGI Conference 2021 (Oral Presentation), October 2021, National Physical Laboratory (NPL), United Kingdom.
3. Research Celebration Day 2021: Chemical and Process Engineering. (Oral presentation). November 2021. University of Strathclyde, United Kingdom.
4. RSC Scotland and North of England Regional Electrochemistry Symposium 2020 (Poster presentation). April 2020. Newcastle University, United Kingdom.
5. PGI Conference 2019 (Poster Presentation). November 2019, National Physical Laboratory (NPL), United Kingdom.
6. Research Celebration Day 2019: Chemical and Process Engineering. (Poster presentation). September 2019. University of Strathclyde, United Kingdom.
7. Electrochem 2019 (Poster presentation). August 2019. University of Strathclyde, United Kingdom.

A.2 Papers

1. Debnath S., Chen Y-C., Green T., Hinds G., Roy S. Preparation and Characterisation of AgNp/silica based optical pH sensor, in preparation.
2. Debnath S., Chen Y-C., Green T., Hinds G., Roy S. Sensitivity of AgNp/silica based fibre optic sensor for pH measurement in different media, in preparation.

Appendix B: COVID-19 Impact Statement

While the global impact of COVID-19 cannot be denied, this section delves into how it significantly affected my research. The initial lockdown in the United Kingdom, which began in March 2020, led to the closure of the University of Strathclyde, disrupting my research timeline. Access to the laboratory was only re-established in October 2020. Given the experimental nature of my project, this interruption led to inevitable setbacks. As my experiment revolves around optical fibre, I faced limitations in meeting people to obtain the necessary connections and apparatus for my specific research requirements. Moreover, lab time had to be scheduled in advance, and during the lockdown, access to university office spaces was severely restricted. Even when office space access was reinstated, it required prior booking and was effectively rationed.

Furthermore, the pandemic brought personal challenges. My wife was diagnosed with a serious illness during the lockdown and had to undergo urgent surgery. Her condition still persists due to delayed treatment and would be taken care of after completion of this degree. Additionally, I experienced the loss of my mother, which was deeply distressing. These circumstances significantly affected my productivity, affecting both my writing progress including my mental and physical health. This, in turn, resulted in a less comprehensive dataset than I would have otherwise been able to generate. Consequently, these challenges led to delays in my writing and the final submission of my thesis.

Appendix C: Specification of pressure vessel

Model: XX6700P01 (1 gallon/3.8 lit)

Manufacturer: Millipore Corporation

Materials: Pressure vessel Type 316L stainless steel with stainless steel fittings

EPDM (ethylene propylene diene monomer) base

     Cover O-ring and vent/relief valve seal: Fluoroelastomer

Pressure: 7 bar (100 psi) maximum; not recommended for use under vacuum
without accessory closure (cat. no. P34188)

Connections: 1/4 in. NPTF

Dimensions: 22.9 cm dia. × 21.6 cm (9.0 in. × 8.5 in.)

a- Outlet dip-tube

b- Pipe plug, 1/4 in. NPT

c- Elbow, 1/4 in. NPTM/F,

d- Vessel cover, cam-lock

e- O-ring, fluoroelastomer

f- Vent/relief valve, 7 bar

g- Pressure gauge
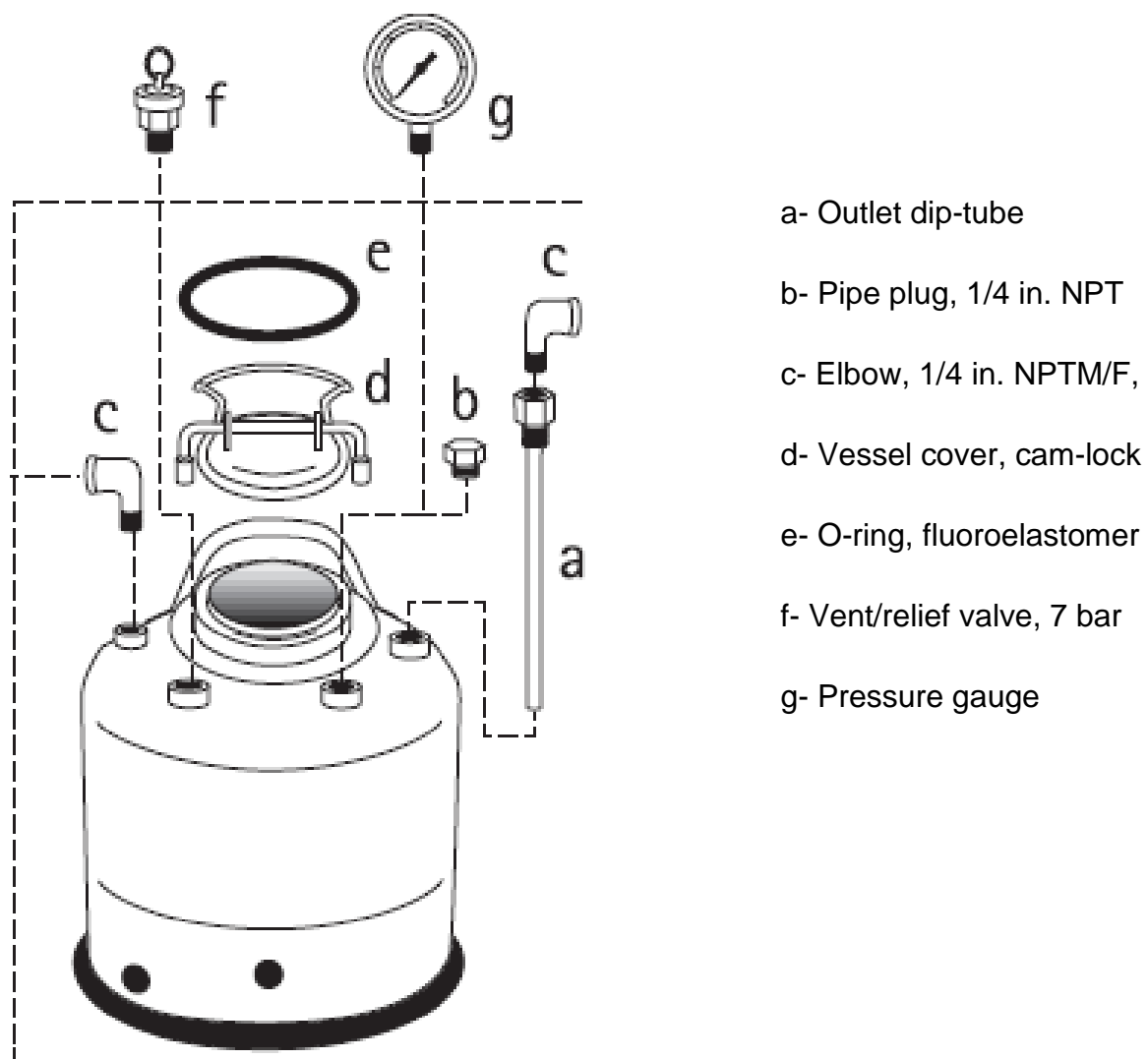
Figure A1: Manufacturer components and fittings Integrated with the pressure vessel.

Appendix D: The extraction procedure making the relationship between the wavelength of maximum extinction (λ_{max}) and the size of the silver nanoparticles as reported Agnihotri *et al.* [79]
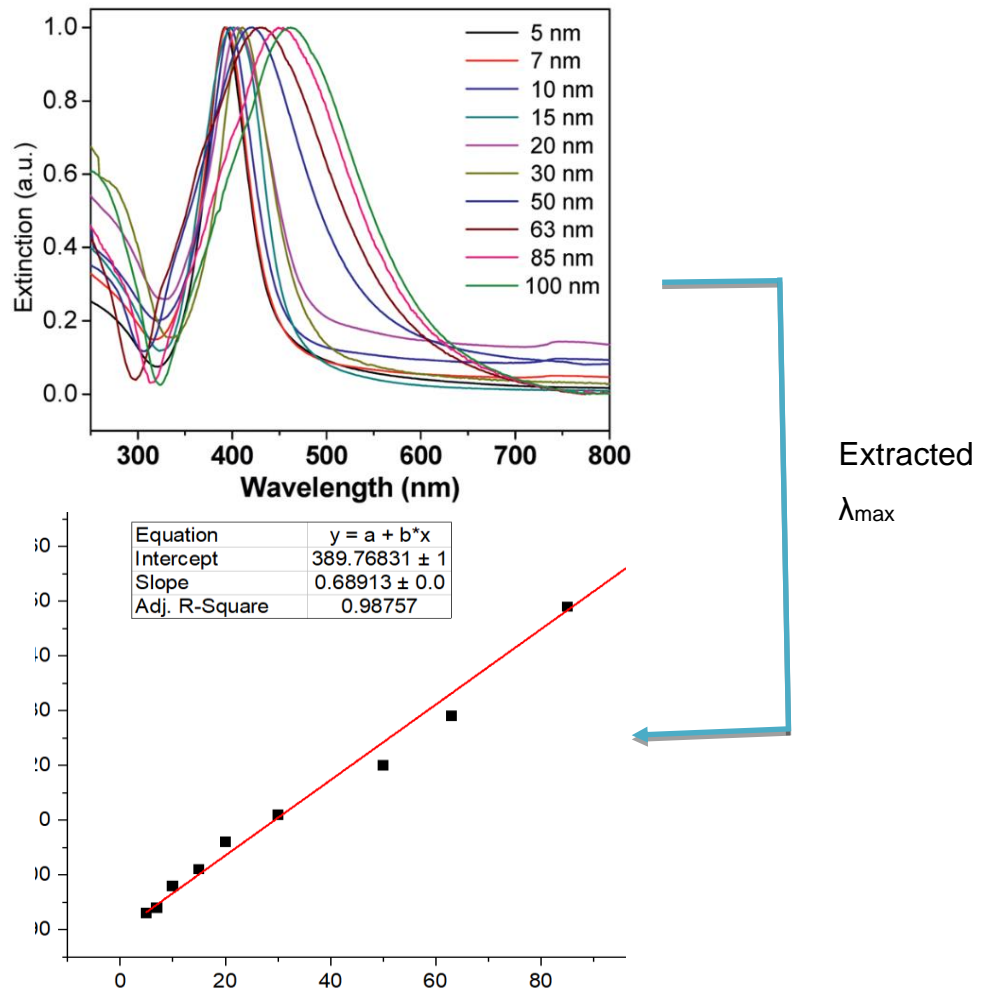
Figure A2: The relationship between the wavelength of maximum extinction (λ_{max}) and the size of silver nanoparticles [79].

From the line fitting, as shown in Figure A2, the relationship between the wavelength of the maximum extinction peak (λ_{max}) and the particle size is shown in Equation A.1

$$\lambda_{max} \text{ (nm)} = 389.77 + 0.69 * \text{Particle size (nm)} \qquad (A.1)$$

Equation A.1 could be rewritten to reflect the particle size as the subject of the formula, as shown in equation A.2.

$$Particle\ size = \frac{\lambda_{max} - 389.77}{0.69} \qquad (A.2)$$

Appendix E: Micrographic images showing the diameter of optical fibre during the 6 day test in acidic solution (pH 3), deionised water (pH 5.9) and alkaline solution (pH 11).
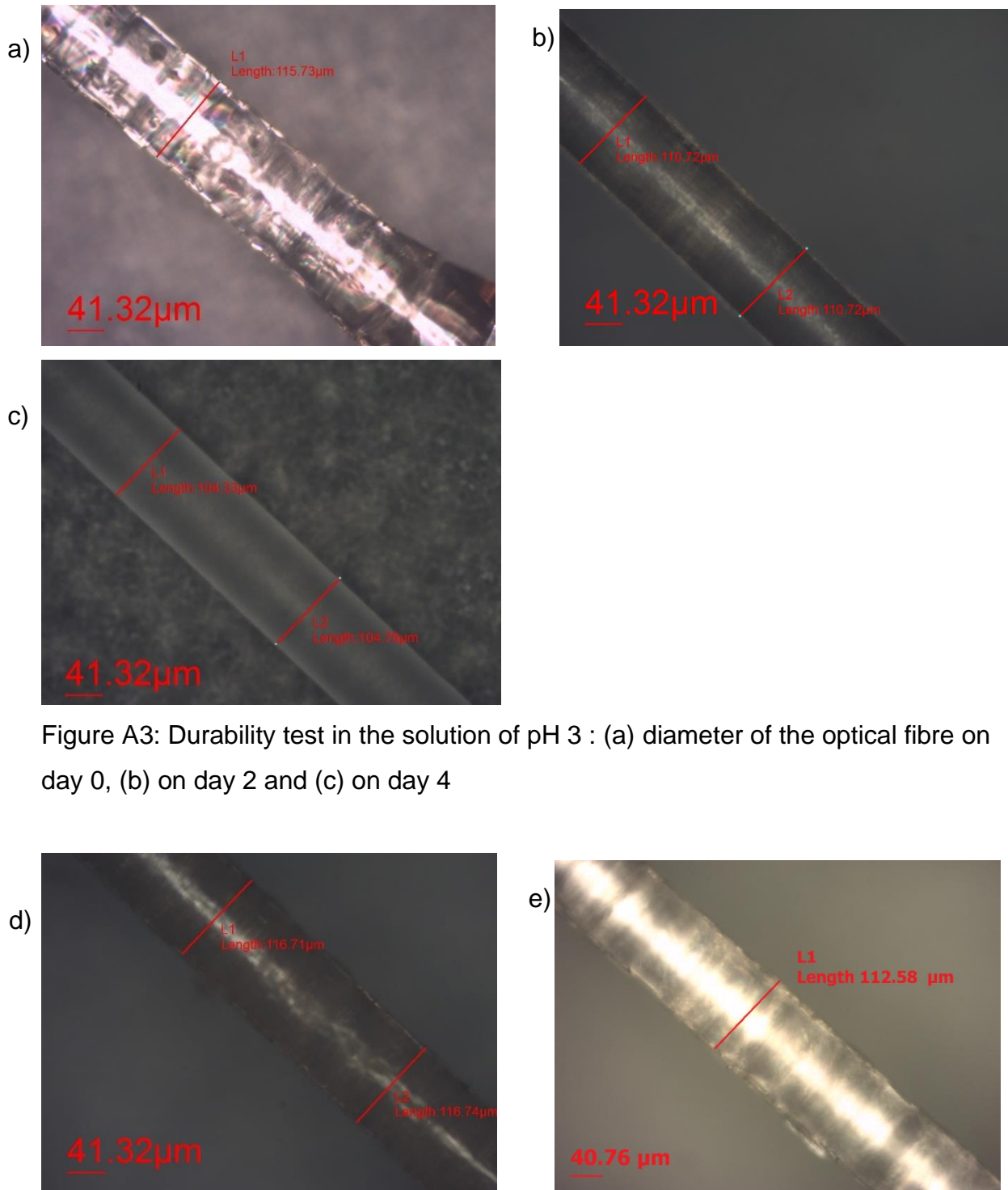
Figure A3: Durability test in the solution of pH 3 : (a) diameter of the optical fibre on day 0, (b) on day 2 and (c) on day 4

f)

41.32μm

g)

41.32μm
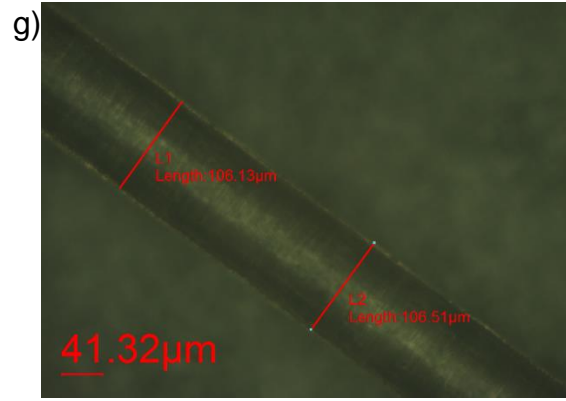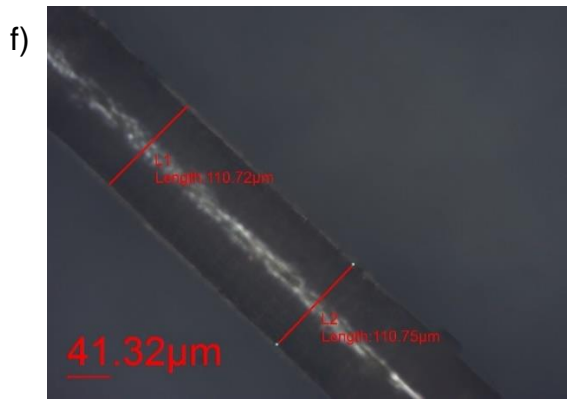
Figure A4: Durability test in the solution of pH 5.9 : (d) diameter of the optical fibre on day 0, (e) on day 2 and (f) on day 4, (g) on day 6

h)

L1
Length: 115.10 μm

40.76 μm

i)

40.76μm

j)

L2
Length:111.87μm

k)

41.32μm
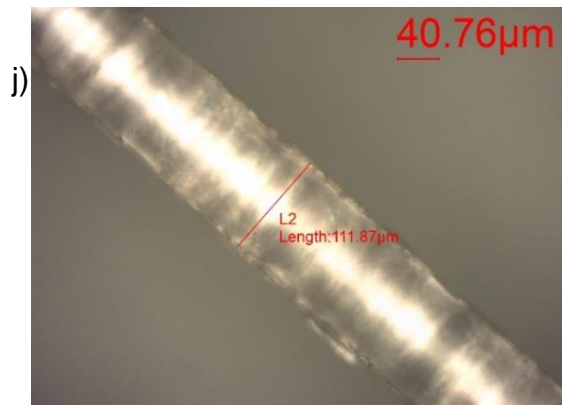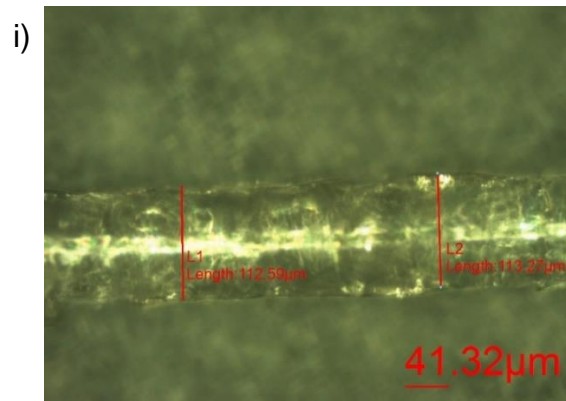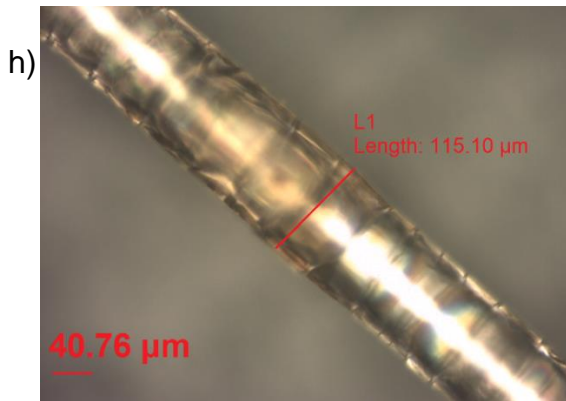
Figure A5: Durability test in the solution of pH 11 : (h) diameter of the optical fibre on day 0, (i) on day 2 and (j) on day 4, (k) on day 6

Appendix F: Intensity of light at a different voltage of light when 100 % (I_{100}) and 0 % (I_0) light were transmitted through the reference optical fibre. I represent the light transmitted through the AgNp/silica coating: (a) 2 V, (b) 2.5 V, (c) 3 V, (d) 3.5 V, (e) 4 V, (f) 4.5 V, (g) 5 V, (h) 5.5 V, (i) 6 V, (j) 6.5 V
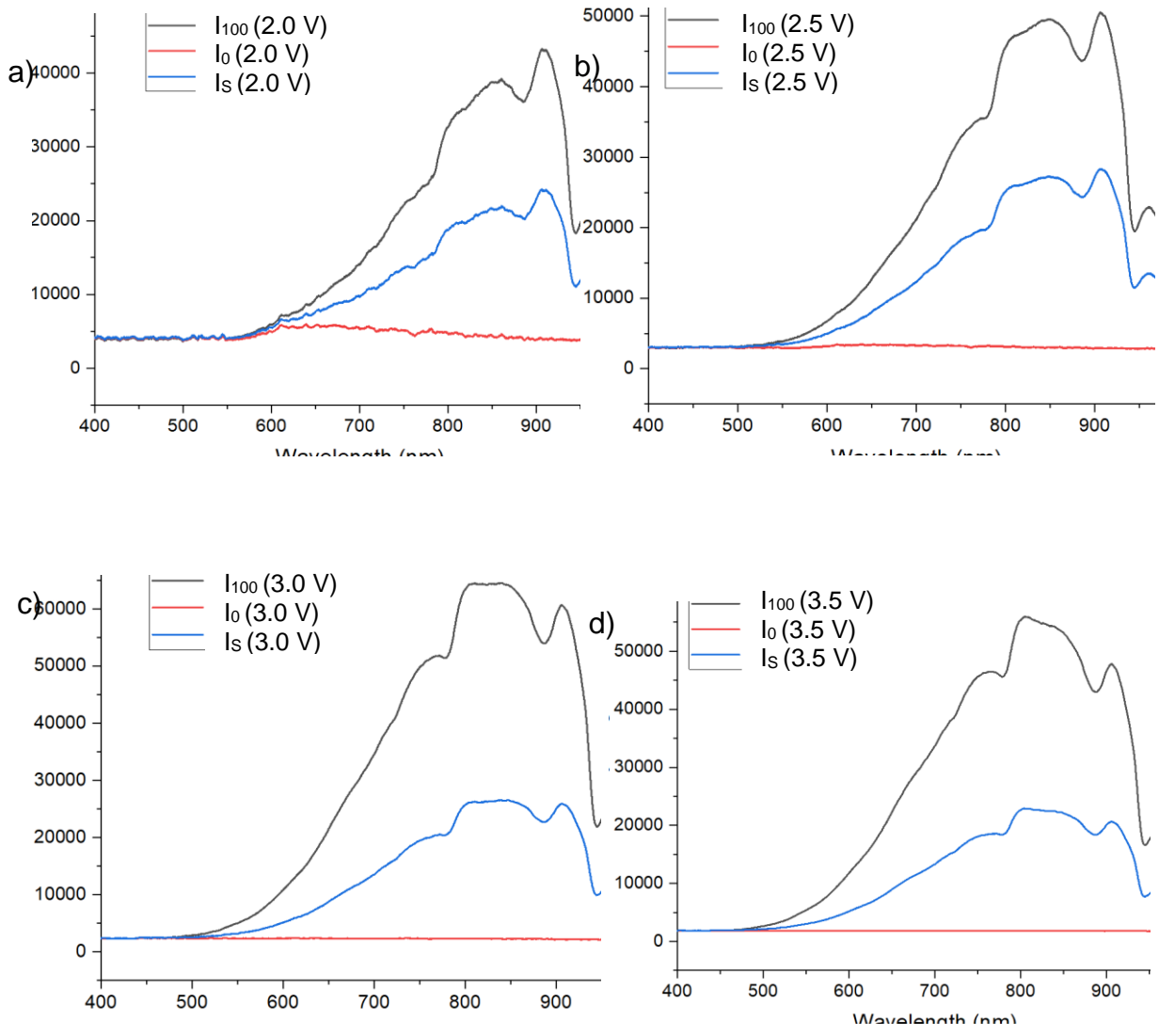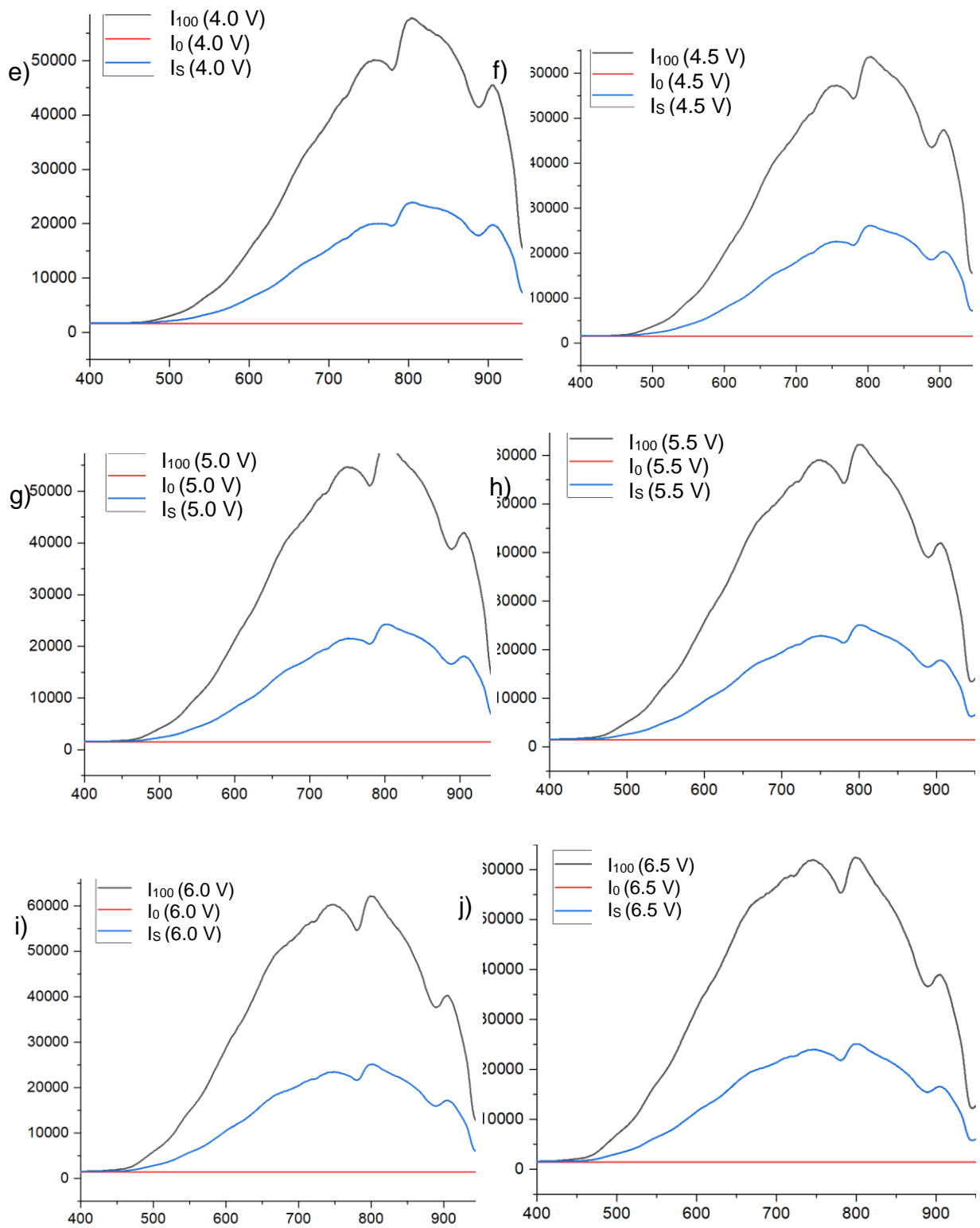
Appendix G: The linear and polynomial fittings of the intensity of light to pH when phosphoric acid (H_3PO_4) and sodium hydroxide (NaOH) were used.

The experiments involved recording the intensity of light (X) and the corresponding pH (Y), as indicated in Table A. Consequently, we calculated the values of X^2, X^3, X^4, XY, and X^2Y for use in subsequent fitting questions.

Table A: Calculation the value of X^2, X^3, X^4, XY, and X^2Y

X (Intensity)	Y (pH)	X^2	X^3	X^4	X.Y	$X^{2.}Y$
4790	11	2.29441E+07	1.09902E+11	5.26432E+14	5.26900E+04	2.52385E+08
8384	9	7.02915E+07	5.89324E+11	4.94089E+15	7.54560E+04	6.32623E+08
10112	7	1.02253E+08	1.03398E+12	1.04556E+16	7.07840E+04	7.15768E+08
11310	5	1.27916E+08	1.44673E+12	1.63625E+16	5.65500E+04	6.39581E+08
12023	3	1.44553E+08	1.73796E+12	2.08954E+16	3.60690E+04	4.33658E+08
$\sum X_i$= 46619	$\sum Y_i$= 35	$\sum X_i^2$= 4.6795E+08	$\sum X_i^3$= 4.9178E+12	$\sum X_i^4$= 5.3180E+16	$\sum X.Y$=2.91549E+05	$\sum X_i^2.Y$= 2.67401E+09

<u>For the line fitting</u>

$$A \text{ line equation: } Y = aX + b \qquad (A.1)$$

In this equation, a and b are the coefficients, and X represents the independent variable where intensity is considered.

The fitting formulas are :

$$a \sum X_i + n\, b = \sum Y_i \qquad (A.2)$$

$$a \sum X_i^2 + b \sum X_i = \sum X_i.Y_i \qquad (A.3)$$

Since there are 5 data points, then n=5. Furthermore, data from Table A was incorporated into the two equations (A1 and A2) mentioned above:

$$a * 46619 + b * 5 = 35 \qquad (A.5)$$

$$a * 4.67957E+08 + b * 46619 = 2.91549E+05 \qquad (A.6)$$

Therefore, solving the 2 equations

a = -0.001 and b= 16.743

Substituting these values into Equation A.1, the line fitting equation becomes:

$$Y = -0.001 * X + 16.743 \tag{A.7}$$

For the second-order polynomial fitting

A second-order polynomial equation: $Y = aX^2 + bX + c$ (A.8)

In this equation, a, b, and c are the coefficients of the polynomial, and X represents the independent variable where intensity is considered.

The polynomial regression formula

$$a \sum X_i^2 + b \sum X_i + n\,c = \sum Y_i \tag{A.9}$$

$$a \sum X_i^3 + b \sum X_i^2 + c \sum X_i = \sum X_i.Y_i \tag{A.10}$$

$$a \sum X_i^4 + b \sum X_i^3 + c \sum X_i^2 = \sum X_i^2.Y_i \tag{A.11}$$

Since there are 5 data points, then n=5. Put the values from Table A in the above 3 equations:

$$a * 4.67957E+08 + b * 46619 + c * 5 = 35 \tag{A.12}$$

$$a * 4.91789E+12 + b * 4.67957E+08 + c * 46619 = 2.91549E+05 \tag{A.13}$$

$$a * 5.31809E+16 + b * 4.91789E+12 + c * 4.67957E+08 = 2.67401E+09 \tag{A.14}$$

Therefore, solving the 3 equations

a = -1.57836E-07 , b= 0.00159 and c= 6.9904

Substituting these values into Equation A.8, the second-order polynomial fitting equation becomes:

$$Y = -1.57836E-07 * X^2 + 0.00159 * X + 6.9904 \tag{A.15}$$

Appendix H: The conversion of the intensity of light to optical pH using the linear and polynomial fittings when phosphoric acid (H_3PO_4) and sodium hydroxide (NaOH) were used.

Potentiometric pH	The intensity of light at the wavelength of 800nm (x)	Optical pH (y)			
		Using line fitting $y = -0.001x + 16.743$	Deviation from original (%)	Using polynomial fitting $y = -1.57836E-07x^2 + 0.00159x + 6.9904$	Deviation from original (%)
11	4652	12.09	9.91	10.97	-0.27
10	6997	9.75	-2.50	10.39	3.90
9	8348	8.39	-6.78	9.26	2.89
8	9350	7.39	-7.63	8.06	0.75
7	10079	6.66	-4.86	6.98	-0.29
6	10915	5.83	-2.83	5.54	-7.67
5	11432	5.31	6.20	4.54	-9.20
4	11709	5.03	25.75	3.97	-0.75
3	12054	4.69	56.33	3.22	7.33
11	4774	11.97	8.82	10.98	-0.18
10	7053	9.69	-3.10	10.35	3.50
9	8392	8.35	-7.22	9.22	2.44
8	9379	7.36	-8.00	8.02	0.25
7	10120	6.62	-5.43	6.92	-1.14
6	10889	5.85	-2.50	5.59	-6.83
5	11285	5.46	9.20	4.83	-3.40
4	11700	5.04	26.00	3.99	-0.25
3	12016	4.73	57.67	3.31	10.33
11	4944	11.80	7.27	10.99	-0.09
10	7066	9.68	-3.20	10.34	3.40
9	8413	8.33	-7.44	9.19	2.11
8	9407	7.34	-8.25	7.98	-0.25
7	10138	6.60	-5.71	6.89	-1.57

6	10962	5.78	-3.67	5.45	-9.17
5	11215	5.53	10.60	4.97	-0.60
4	11706	5.04	26.00	3.97	-0.75
3	11998	4.74	58.00	3.35	11.67
7.5	9852	6.89	-8.13	7.33	-2.27
6.5	10455	6.29	-3.23	6.36	-2.15
9.5	7823	8.92	-6.11	9.77	2.84
10.5	6755	9.99	-4.86	10.53	0.29
5.7	10788	5.95	4.39	5.77	1.23
8.3	8984	7.76	-6.51	8.54	2.89
3.9	11750	4.99	27.95	3.88	-0.51
4.7	11280	5.46	16.17	4.84	2.98
9.6	7845	8.90	-7.29	9.75	1.56
10.3	6707	10.04	-2.52	10.55	2.43
6.3	10402	6.34	0.63	6.45	2.38
8.4	8950	7.79	-7.26	8.58	2.14
3.8	11710	5.03	32.37	3.97	4.47
10.5	6731	10.01	-4.67	10.54	0.38
4.5	11412	5.33	18.44	4.58	1.78
9.3	8428	8.31	-10.65	9.18	-1.29
5.5	10891	5.85	6.36	5.59	1.64
9.9	7836	8.91	-10.00	9.76	-1.41
6.5	10347	6.40	-1.54	6.54	0.62
11	5028	11.71	6.45	10.99	-0.09
3.5	11954	4.79	36.86	3.44	-1.71
8.2	9300	7.44	-9.27	8.13	-0.85
3.2	12012	4.73	47.81	3.31	3.44

Appendix I: The linear and polynomial fittings of the intensity of light to pH when sulfuric acid (H_2SO_4) and sodium hydroxide (NaOH) were used.

The experiments involved recording the intensity of light (X) and the corresponding pH (Y), as indicated in Table A. Consequently, we calculated the values of X^2, X^3, X^4, XY, and X^2Y for use in subsequent fitting questions.

Table B: Calculation the value of X^2, X^3, X^4, XY, and X^2Y

X (Intensity)	Y (pH)	X^2	X^3	X^4	X.Y	$X^2.Y$
4422	11	1.95541E+07	8.64682E+10	3.82362E+14	4.86420E+04	2.15095E+08
5405	9	2.92140E+07	1.57902E+11	8.53459E+14	4.86450E+04	2.62926E+08
5808	7	3.37329E+07	1.95920E+11	1.13791E+15	4.06560E+04	2.36130E+08
6110	5	3.73321E+07	2.28099E+11	1.39369E+15	3.05500E+04	1.86661E+08
6602	3	4.35864E+07	2.87757E+11	1.89977E+15	1.98060E+04	1.30759E+08
$\sum X_i$= 28347	$\sum Y_i$= 35	$\sum X_i^2$= 1.6341E+08	$\sum X_i^3$= 9.5614E+11	$\sum X_i^4$= 5.6671E+15	$\sum X.Y$=1.8829E+05	$\sum X_i^2.Y$= 1.0315E+09

For the line fitting

Since there are 5 data points, then n=5. Furthermore, data from Table B was incorporated into the two equations (A.1 and A.2) mentioned above:

$$a * 28347 + b * 5 = 35 \qquad (A.16)$$

$$a * 1.6341E+08 + b * 28347 = 1.8829E+05 \qquad (A.17)$$

Therefore, solving the 2 equations

a = -0.003 and b= 26.899

Substituting these values into Equation A.1, the second-order polynomial fitting equation becomes:

$$y = -0.003x + 26.899 \qquad (A.18)$$

For the second-order polynomial fitting

Since there are 5 data points, then n=5. Put the values from Table B in the 3 equations of Equation 9,10 and 11:

$$a * 1.6341E+08 + b * 28347 + c * 5 = 35 \qquad (A.19)$$

$$a * 9.5614E+11 + b * 1.6341E+08 + c * 28347 = 1.8829E+05 \qquad (A.20)$$

$$a * 5.6671E+15 + b * 9.5614E+11 + c * 1.6341E+08 = 1.0315E+09 \qquad (A.21)$$

Therefore, solving the 3 equations

a = -1.35197E-06, b= 0.0111 and c= -11.7431

Substituting these values into Equation A.8, the second-order polynomial fitting equation becomes:

$$y = -1.35197E-06 * X^2 + 0.0111 * X - 11.7431 \qquad (A.22)$$

Appendix J: The conversion of the intensity of light to optical pH using the linear and polynomial fittings when sulfuric acid (H_2SO_4) and sodium hydroxide (NaOH) were used.

Potentiometric pH	The intensity of light at the wavelength of 800nm (x)	Optical pH (y)			
		Using line fitting $y = -0.003x + 26.899$	Deviation from original (%)	Using polynomial fitting $y = -1.35197E\text{-}06x^2 + 0.0111x - 11.7431$	Deviation from original (%)
11	4350	11.67	6.09	10.95	-0.45
4.4	6301	4.84	10.00	4.51	2.50
11	4333	11.73	6.64	10.96	-0.36
6.2	5986	5.94	-4.19	6.25	0.81
3	6560	3.93	31.00	2.89	-3.67
9.3	5258	8.49	-8.71	9.24	-0.65
3	6542	4.00	33.33	3.01	0.33
8.5	5463	7.77	-8.59	8.54	0.47
11	4338	11.71	6.45	10.96	-0.36
7.5	5763	6.72	-10.40	7.32	-2.40
11	4369	11.60	5.45	10.94	-0.55
3	6571	3.90	30.00	2.81	-6.33
11	4363	11.62	5.64	10.94	-0.55
5.5	6096	5.56	1.09	5.67	3.09
11	4352	11.66	6.00	10.95	-0.45
3	6511	4.11	37.00	3.21	7.00
11	4351	11.67	6.09	10.95	-0.45
3	6535	4.02	34.00	3.05	1.67
8.2	5534	7.52	-8.29	8.27	0.85
11	4326	11.75	6.82	10.97	-0.27
3	6530	4.04	34.67	3.08	2.67
11	4310	11.81	7.36	10.98	-0.18

3	6588	3.84	28.00	2.70	-10.00
11	4345	11.69	6.27	10.96	-0.36
3	6561	3.93	31.00	2.88	-4.00
11	4342	11.70	6.36	10.96	-0.36
3	6553	3.96	32.00	2.93	-2.33
11	4359	11.64	5.82	10.95	-0.45
3	6588	3.83	27.67	2.69	-10.33
4.3	6290	4.88	13.49	4.58	6.51
3	6584	3.85	28.33	2.72	-9.33
5.5	6096	5.56	1.09	5.67	3.09
11	4343	11.69	6.27	10.96	-0.36
9	5334	8.22	-8.67	8.99	-0.11
8	5521	7.57	-5.38	8.32	4.00
7	5864	6.37	-9.00	6.85	-2.14
8	5572	7.39	-7.63	8.12	1.50
11	4336	11.72	6.55	10.96	-0.36
9	5355	8.15	-9.44	8.92	-0.89
10	4902	9.74	-2.60	10.18	1.80
9	5278	8.42	-6.44	9.17	1.89
10.5	4805	10.08	-4.00	10.37	-1.24
9.5	5229	8.59	-9.58	9.33	-1.79
8	5546	7.48	-6.50	8.23	2.88
10	4951	9.56	-4.40	10.07	0.70
7	5865	6.37	-9.00	6.84	-2.29
6	6040	5.75	-4.17	5.97	-0.50
10	5013	9.35	-6.50	9.92	-0.80
8.5	5450	7.82	-8.00	8.59	1.06
7	5815	6.54	-6.57	7.08	1.14
6	6031	5.79	-3.50	6.02	0.33
5	6184	5.25	5.00	5.19	3.80
7.5	5691	6.97	-7.07	7.63	1.73
6	6068	5.66	-5.67	5.82	-3.00

5	6170	5.30	6.00	5.27	5.40
4	6395	4.51	12.75	3.94	-1.50
5.5	6093	5.57	1.27	5.69	3.45
4	6379	4.57	14.25	4.04	1.00
3	6545	3.99	33.00	2.98	-0.67
6.5	5906	6.22	-4.31	6.65	2.31
5	6175	5.28	5.60	5.24	4.80
3	6547	3.98	32.67	2.97	-1.00
4	6379	4.57	14.25	4.04	1.00
3	6532	4.03	34.33	3.07	2.33
4.5	6285	4.90	8.89	4.61	2.44

Appendix K: The linear and polynomial fittings of the intensity of light to pH when hydrochloric acid (HCl) and sodium hydroxide (NaOH) were used.

The experiments involved recording the intensity of light (X) and the corresponding pH (Y), as indicated in Table A. Consequently, we calculated the values of X^2, X^3, X^4, XY, and X^2Y for use in subsequent fitting questions.

Table C: Calculation the value of X^2, X^3, X^4, XY, and X^2Y

X (Intensity)	Y (pH)	X^2	X^3	X^4	X.Y	$X^2.Y$
4503	11	2.02770E+07	9.13074E+10	4.11157E+14	4.95330E+04	2.23047E+08
5928	9	3.51412E+07	2.08317E+11	1.23490E+15	5.33520E+04	3.16271E+08
6573	7	4.32043E+07	2.83982E+11	1.86661E+15	4.60110E+04	3.02430E+08
7013	5	4.91822E+07	3.44915E+11	2.41889E+15	3.50650E+04	2.45911E+08
7504	3	5.63100E+07	4.22550E+11	3.17082E+15	2.25120E+04	1.68930E+08
$\sum X_i = 31521$	$\sum Y_i = 35$	$\sum X_i^2 = 2.0411E+08$	$\sum X_i^3 = 1.3510E+12$	$\sum X_i^4 = 9.1023$ E+15	$\sum X.Y = 2.0647E+05$	$\sum X_i^2.Y = 1.2565E+09$

For the line fitting

Since there are 5 data points, then n=5. Furthermore, data from Table C was incorporated into the two equations (A1 and A2) mentioned above:

$$a * 31521 + b * 5 = 35 \qquad\qquad (A.23)$$

$$a * 2.0411E+08 + b * 31521 = 2.0647E+05 \qquad\qquad (A.24)$$

Therefore, solving the 2 equations

a = -0.0026 and b= 23.55

Substituting these values into Equation A.1, the second-order polynomial fitting equation becomes:

$$y = -0.0026 * X + 23.55 \qquad\qquad (A.25)$$

For the second-order polynomial fitting

Since there are 5 data points, then n=5. Put the values from Table B in the 3 equations of Equation 9,10 and 11:

$$a * 2.0411E+08 + b * 31521 + c * 5 = 35 \qquad (A.26)$$

$$a * 1.3510E+12 + b * 2.0411E+08 + c * 28347 = 2.0647E+05 \qquad (A.27)$$

$$a * 9.1023 E+15 + b * 1.3510E+12 + c * 2.0411E+08 = 1.2565E+09 \qquad (A.28)$$

Therefore, solving the 3 equations

a = -7.90663E-07, b= 0.00679 and c= - 3.52392

Substituting these values into Equation A.8, the second-order polynomial fitting equation becomes:

$$y = -7.90663E-07 * X^2 + 0.00679 * X - 3.52392 \qquad (A.29)$$

Appendix L: The conversion of the intensity of light to optical pH using the linear and polynomial fittings when hydrochloric acid (HCl) and sodium hydroxide (NaOH) were used.

Potentiometric pH	The intensity of light at the wavelength of 800nm (x)	Optical pH (y)			
		Using line fitting $y = -0.0026x + 23.55$	Deviation from original (%)	Using polynomial fitting $y = -7.90663E-07x^2 + 0.00679x - 3.52392$	Deviation from original (%)
11	4389	12.01	9.18	11.05	0.45
10	5182	9.92	-0.80	10.43	4.30
9	5849	8.17	-9.22	9.14	1.56
8	6255	7.10	-11.25	8.01	0.12
7	6550	6.32	-9.71	7.03	0.43
6	6808	5.65	-5.83	6.05	0.83
5	6998	5.14	2.80	5.27	5.40
4	7285	4.39	9.75	3.98	-0.50
3	7462	3.93	31.00	3.12	4.00
11	4510	11.69	6.27	11.02	0.18
10	5230	9.80	-2.00	10.36	3.60
9	5949	7.91	-12.11	8.89	-1.22
8	6291	7.01	-12.38	7.90	-1.25
7	6578	6.25	-10.71	6.93	-1.00
6	6833	5.58	-7.00	5.96	-0.67
5	7010	5.11	2.20	5.22	4.40
4	7298	4.36	9.00	3.92	-2.00
3	7512	3.79	26.33	2.87	-4.33
11	4612	11.42	3.82	10.97	-0.27
10	5347	9.49	-5.10	10.18	1.80
9	5988	7.80	-13.33	8.78	-2.44
8	6326	6.91	-13.63	7.79	-2.63
7	6592	6.21	-11.29	6.88	-1.71

6	6858	5.51	-8.17	5.86	-2.33
5	7032	5.06	1.20	5.13	2.60
4	7330	4.27	6.75	3.77	-5.75
3	7540	3.72	24.00	2.72	-9.33
7.5	6372	6.79	-9.47	7.64	1.87
6.5	6620	6.14	-5.54	6.78	4.31
9.5	5720	8.51	-10.42	9.45	-0.53
10.5	4976	10.46	-0.38	10.69	1.81
5.7	6912	5.37	-5.79	5.63	-1.23
8.3	6169	7.33	-11.69	8.27	-0.36
3.9	7271	4.43	13.59	4.05	3.85
4.7	7146	4.76	1.28	4.62	-1.70
9.6	5614	8.79	-8.44	9.68	0.83
10.3	5183	9.92	-3.69	10.43	1.26
6.3	6734	5.84	-7.30	6.35	0.79
8.4	6179	7.30	-13.10	8.24	-1.90
3.8	7331	4.27	12.37	3.76	-1.05
10.5	5037	10.30	-1.90	10.62	1.14
4.5	7223	4.55	1.11	4.27	-5.11
9.3	5701	8.56	-7.96	9.49	2.04
5.5	6876	5.47	-0.55	5.78	5.09
9.9	5362	9.45	-4.55	10.15	2.53
6.5	6733	5.84	-10.15	6.35	-2.31
11	4632	11.37	3.36	10.96	-0.36
3.5	7374	4.16	18.86	3.55	1.43
8.2	6204	7.23	-11.83	8.17	-0.37
3.2	7469	3.91	22.19	3.08	-3.75
10	5431	9.27	-7.30	10.03	0.30